STABILITY ANALYSIS OF THE BOILING WATER REACTOR: METHODS AND ADVANCED DESIGNS

by
Rui Hu

B.S., Nuclear Engineering (2002)
M.S., Nuclear Engineering (2005)
Shanghai Jiao Tong University, P.R. China

M.S., Nuclear Engineering (2007)
Massachusetts Institute of Technology

Submitted to the Department of Nuclear Science and Engineering
in Partial Fulfillment of the Requirements for the Degree of

Doctor of Philosophy in Nuclear Science and Engineering
at the
Massachusetts Institute of Technology

June 2010

Signature of Author .....
Rui Hu
Department of Nuclear Science and Engineering
February 9, 2010

Certified by .....
Mujid S. Kazimi
TEPCO Professor of Nuclear Engineering
Professor of Mechanical Engineering
Thesis Supervisor

Certified by .....
Jacopo Buongiorno
Carl R. Soderberg Professor of Power Engineering
Associate Professor of Nuclear Science and Engineering
Thesis Reader

Accepted by .....
Jacquelyn C. Yanch
Professor of Nuclear Science and Engineering
Chairman, Department Committee on Graduate Students

Stability Analysis of the Boiling Water Reactor: Methods and Advanced Designs

by
Rui Hu

Submitted to the Department of Nuclear Science and Engineering
in Partial Fulfillment of the Requirements for the Degree of Doctor of Philosophy
at Massachusetts Institute of Technology

Abstract

Density Wave Oscillations (DWOs) are known to be possible when a coolant undergoes considerable density reduction while passing through a heated channel. In the development of boiling water reactors (BWRs), there has been considerable concern about the effects of such oscillations when coupled with neutronic feedback. The current trend of increasing reactor power density and relying more extensively on natural circulation for core cooling may have consequences for the stability characteristics of new BWR designs. This work addresses a wide range of issues associated with the BWR stability: 1) flashing-induced instability and natural circulation BWR startup; 2) stability of the BWRs with advanced designs involving high power densities; 3) modeling assumptions in stability analysis methods; and 4) the fuel clad performance during power and flow oscillations.

To capture the effect of flashing on density wave oscillations during low pressure startup conditions, a code named FISTAB has been developed in the frequency domain. The code is based on a single channel thermal-hydraulic model of the balance of the water/steam circulation loop, and incorporates the pressure dependent water/steam thermodynamic properties, from which the evaporation due to flashing is captured. The functionality of the FISTAB code is confirmed by testing the experimental results at SIRIUS-N facility. Both stationary and perturbation results agree well with the experimental results.

The proposed ESBWR start-up procedure under natural convection conditions has been examined by the FISTAB code. It is confirmed that the examined operating points along the ESBWR start-up trajectory from TRACG simulation will be stable. To avoid the instability resulting from the transition from single-phase natural circulation to two-phase circulation, a simple criterion is proposed for the natural convection BWR start-up when the steam dome pressure is still low.

Using the frequency domain code STAB developed at MIT, stability analyses of some proposed advanced BWRs have been conducted, including the high power density BWR core designs using the Large Assembly with Small Pins (LASP) or Cross Shape Twisted (CST) fuel designs developed at MIT, and the Hitachi's RBWR cores utilizing a hard neutron spectrum and even higher power density cores. The STAB code is the predecessor of the FISTAB code, and thermodynamic properties of the coolant are only dependent on system pressure in STAB. It is concluded that good stability performance of the LASP core and the CST core can be maintained at nominal conditions, even though they have 20% higher reactor thermal power than the reference core. Power uprate does not seem to have significant effects on thermal-hydraulic stability performance when the power-to-flow ratio is maintained. Also, both the RBWR-AC and RBWR-TB2 designs are found viable from a stability performance point of view, even though the core exit qualities are almost 3 times those of a traditional BWR. The stability of the RBWRs is enhanced through the fast transient response of the shorter core, more flat power and power-to-flow ratio distributions, less negative void feedback coefficient, and the core inlet orifice design.

To examine the capability of coupled 3D thermal-hydraulics and neutronics codes for stability analysis, USNRC's latest system analysis code, TRACE, is chosen in this work. Its validation for stability analysis and comparison with the frequency domain approach, have been performed against the Ringhals 1 stability tests. Comprehensive assessment of modeling choices on TRACE stability analysis has been made, including effects of time-

spatial discretization, numerical schemes, thermal-hydraulic channel grouping, neutronics modeling, and control system modeling.

The predictions from both the TRACE and STAB codes are found in reasonably good agreement with the Ringhals 1 test results. The biases for the predicted global decay ratio are about 0.07 in TRACE results, and -0.04 in STAB results. However, the standard deviations of decay ratios are both large, around 0.1, indicating large uncertainties in both analyses. Although the TRACE code uses more sophisticated neutronic and thermal hydraulic models, the modeling uncertainty is not less than that of the STAB code. The benchmark results of both codes for the Ringhals stability test are at the same level of accuracy.

The fuel cladding integrity during power oscillations without reactor scram is examined by using the FRAPTRAN code, with consideration of both the stress-strain criterion and thermal fatigue. Under the assumed power oscillation conditions for high burnup fuel, the cladding can satisfy the stress-strain criteria in the ASME Code. Also, the equivalent alternating stress is below the fatigue threshold stress, thus the fatigue limit is not violated. It can be concluded that under a large amount of the undamped power oscillation cycles, the cladding would not fail, and the fuel integrity is not compromised.

Acknowledgements

I would like to express my sincere gratitude to the thesis advisor, Professor Mujid S. Kazimi, for his continuous support and constructive advices. Special thanks are given to Dr. Jiyun Zhao and Dr. Shih-ping Kao, for their help and fruitful discussions in the early days when I entered into this field. I sincerely thank Professor Jacopo Buongiorno for the valuable comments and to be the thesis reader.

I sincerely thank all my colleagues in Department of Nuclear Science & Engineering at MIT for the unlimited support and the friendly working atmosphere.

This work could not have been completed, without the help of many people outside MIT. Particularly, I'm grateful to:

- Dr. Masahiro Furuya at CRIEPI (Central Research Institute of Electric Power Industry) Japan, for his help in the benchmark of the FISTAB code with the experiments in SIRIUS-N facility at CRIEPI.
- Prof. Thomas Downar and Dr. Yunlin Xu at University of Michigan, for providing their sample TRACE input model for Ringhals 1 Stability Test, and the constructive discussions regarding this work.
- Dr. Dean Wang at Information Systems Laboratories, for his help in debugging the TRACE input model and offering us newer version of the TRACE code.
- Dr. Thomas Smed at Studsvik Scandpower, for providing the detailed informaiton of the Ringhals 1 Stability Test.

Table of Contents

Abstract I
Acknowledgements IV
Table of Contents V
List of Figures X
List of Tables XIV
1. Introduction 1
1.1 Motivation and Objective 1
1.2 Development of BWR technology 2
1.3 Introduction to BWR Instability Issue 5
1.3.1 Types of instabilities 5
1.3.2 Mechanisms of BWR instabilities 7
1.3.3 Analysis Methods 9
1.3.4 Safety Aspects of BWR instability 10
1.4 Literature Review 11
1.5 Scope of Work 13
Part I: Flashing Induced Instability and Natural Circulation BWR startup 17
2. Introduction of Natural Circulation BWRs and Flashing Phenomenon 18
2.1. Overview of Design Features of a Reference Natural Circulation BWR (ESBWR) 18
2.2. Mechanism of flashing induced instability 21
2.3. Previous Work 24
2.3.1. Experimental work 24
2.3.2. Analytical work 25
2.4. Scope of Part I of This Work 26
3. Development for Flashing-Induced Stability Analysis, FISTAB 28
3.1. Model Description 28
3.1.1. Governing Equations 29
3.1.2. Spatial Discretization 35
3.1.3. Steady-State Solution Scheme 36
3.2. Linear Stability Analysis in the Frequency Domain 43
3.2.1. Linear Perturbation Equations 44
3.2.2. Frequency Domain Linear Equations 53
3.2.3. Feedback and System Characteristic Equation 53
3.3. Code Benchmark 55
3.3.1. SIRIUS-N Facility Description 55
3.3.2. Comparison of steady-state results 58
3.3.3. Comparison of transient results 59
3.4. Summary 63
4. NCBWRs Start-up 64
4.1 Introduction 64
4.2 Start-up Procedure of BWRs 65
4.2.1 The start-up procedure of the Dodewaard reactor 65
4.2.2 The start-up procedure of the ESBWR 66

4.2.3 The start-up procedure of the ABWR 67
4.3 Stability analysis of ESBWR during start-up 69
4.3.1 Comparison of stationary results 72
4.3.2. Linear stability analysis 75
4.4 Start-up Procedures for NCBWRs 77
4.4.1 Literature survey on start-up procedure for NCBWRs 77
4.4.2 A simple criterion for NCBWRs start-up procedure 79
4.5 Summary 81
Part II: Stability Analyses of advanced BWR Designs 82
5. Stability of High Power Density BWR Designs 83
5.1 Introduction 84
5.2 Fuel Designs for High Power Density BWRs 84
5.2.1 Large Assembly with Small Pins Concept 84
5.2.2 Cross-Shaped Twisted Fuel Pin Design 85
5.3 Stability Analysis Method 87
5.4 Considered BWR Instability Types 89
5.4.1 Single channel thermal-hydraulics instability 89
5.4.2 Coupled neutronic regional out-of-phase instability 90
5.4.3 Coupled neutronic core-wide in-phase instability 91
5.5 Stability Analyses of High Power Density BWR Designs 93
5.5.1 Key Operating Parameters Affecting Stability 93
5.5.2 Stability Analysis Results for LASP and CST at Uprated conditions 95
5.5.3 The Effects of Power Uprates on Stability in the CST Core 97
5.6 Stability Analysis of LASP - Design Effects and Parametric Study 100
5.6.1. The Effects of Water Rods and Partial Length Rods 100
5.6.2 Sensitivity Analyses for Single Channel Stability 102
5.6.3 Sensitivity Analyses for Regional Out-of-Phase Stability 104
5.6.4 Sensitivity Analyses for Core-Wide In-Phase Stability 107
5.6.5 Pin Diameter Effects on Stability Performance 110
5.6.6 Stability Exclusion Region 111
5.7 Summary 112
6. Stability Analysis of the Reduced Moderation RBWR Designs 114
6.1 Introduction 114
6.2 Overall thermal-hydraulic characteristics of RBWRs 115
6.3 Methods Description 119
6.4 Stability Analysis of RBWR-AC 127
6.4.1 Single Channel Stability analysis 127
6.4.2 Coupled neutronics stability analysis 130
6.4.3 Reflector effects on stability analysis 131
6.4.4 Axial power shape effects on stability analysis 132
6.4.5 Neutronics modeling effects on stability analysis 134
6.5 Stability Analysis of RBWR-TB2 136
6.5.1 Single channel stability analysis 136
6.5.2 Coupled neutronics stability analysis 139
6.6 Summary 141
Part III: Stability Analysis Approach, time domain vs. frequency domain 143

7. Overview of BWR Stability Analysis Methods 145
7.1 Methods Used to Analyze BWR Instability 145
7.2 Present Capabilities of Stability Analysis Codes 149
7.2.1 Applicability to real plant conditions 149
7.2.2 Considerations on code capabilities 150
7.3 Applications of Coupled Three-Dimensional Analysis 152
7.4 Scope of Part III of This Work 154
8. Analysis of Ringhals Stability Test in the Time Domain – Model Descriptions 157
8.1 Ringhals 1 Stability Test 157
8.2 Adopted Computational Codes - TRACE/PARCS 161
8.2.1 TRACE 161
8.2.2. PARCS 162
8.3 The Decay Ratio Analysis Tool – DRACO 164
8.4 The Coupling Process 169
8.5 Thermal-Hydraulics Model 173
8.6 Neutronics Model 175
9. Analysis of Ringhals Stability Test in the Time Domain - Analyses and Results 178
9.1 Steady State Results 178
9.2 Simulation of Oscillation Transients, In-Phase 180
9.2.1 P01 Case study, transient response 181
9.2.2 P01 Case study, time window effects 184
9.2.3 Ringhals Benchmark for all test points in Cycle 14 186
9.3 Simulation of Oscillation Transients, Out-of-Phase 189
9.3.1 Simulation of asymmetric initial neutronic perturbation, using half-core symmetry TRACE model 189
9.3.2 Simulation of Parallel Channel Type of Instabilities 194
9.3.3 Out-of-phase Instability Simulation with the full-core 648-channel model 196
9.4 Numerical Scheme Effects: SI and SETS 200
9.5 Lumped channel Effects 205
9.5.1 Core channel lumping/mapping schemes 205
9.5.2 Transient responses 207
9.6 Neutronics Modeling Effects: 3D vs. 0D 211
9.6.1 Reactivity Feedback model in TRACE 211
9.6.2 Void coefficient calculation from PARCS simulation, C14P01 213
9.6.3 Transient responses under the point kinetics model 215
9.7 Control System Effects 218
9.7.1 BWR stability and control system 218
9.7.2 Transient responses after small perturbations 219
9.7.3 Transient responses after recirculation pump trip 221
9.8 Summary 225
10. Ringhals 1 Stability Test Benchmark – Frequency Domain vs. Time Domain 228
10.1 Ringhals Stability Benchmark with STAB 228
10.1.1 Model description and assumptions 228
10.1.2 Evaluation Results 230
10.2 Comparison between the Frequency Domain Approach and the Time Domain Approach 234

10.3 Summary 237
Part IV Clad performance under power oscillations 239
11. Cladding Performance under Power Oscillations in BWRs 240
11.1 Introduction 240
11.1.1 BWR Stability and Its Effect to Safety 240
11.1.2 Fuel Failure Modes 241
11.1.3 Literature Review of Fuel Performance under Power Oscillations in BWRs 242
11.1.4 Objectives of this Work 243
11.2 Description of FRAPTRAN Code 244
11.2.1 Objectives and Capability of the FRAPTRAN Code 244
11.2.2 Cladding Deformation Model 245
11.2.3 Fuel Rod Internal Gas Pressure Response Model 246
11.3 Simulation of the Power Oscillation Test, FK11 247
11.3.1 FK11 Test Description 247
11.3.2 FRAPTRAN simulation of FK-11 Power Oscillations 252
11.4 Power Oscillations under Normal BWR Operating Conditions 256
11.4.1 BWR Conditions under Normal Operation and Power Oscillations 256
11.4.2 Results of FRAPTRAN Simulation 258
11.4.3 Cladding Stress and Strain Analysis 263
11.5 Cladding Fatigue Analysis 265
11.6 Summary 267
12. Summary and Conclusions 268
12.1 Summary of Conclusions 268
12.1.1 Flashing-Induced Instability and Natural Circulation BWR Startup 268
12.1.2 Stability Analyses of Advanced BWR Designs 269
12.1.3 Stability Analysis Approach, time domain vs. frequency domain 272
12.1.4 Clad Performance under Power Oscillations 275
12.2 Recommendations for Future work 275
References: 278
Nomenclature 286
Appendixes 291
A. Supplementary Model Descriptions 292
A.1 General Drift Flux Model 292
A.2 Vapor Generation Model due to Flashing 293
A.3 Chen's Correlation 295
A.4 CISE-4 Correlation 296
References of Appendix A 297
B. A Global Newton Method to Solve the Characteristic Equation in Frequency Domain Linear Stability Analysis 298
B.1. Introduction 298
B.2. System Characteristic Equation 298
B.3. Review of Root-finding algorithms 299
B.4 The Global Newton Method for the Characteristic Equation 302
B.5 Results and Discussions 306
B.5.1. Real algebraic equations 307

B.5.2. Complex algebraic equation 307
B.5.3. System Characteristic Equation in linear stability analysis 308
B.5.4. Addressing the drawbacks of the Newton Method 309
B.6 Summary 311
References for Appendix B 312
C. Peach Bottom 2 Low Flow Stability Test Benchmark with STAB code 313
C.1 Brief Description of the PB2-LFST 313
C.2 Discussion of Results 315
References for Appendix C 318
D. Neutronic Model Description 319
D.1 Neutronic equations 319
D.2 Lamda modes expansion method 320
D.3 Neutroinc feedback 323
References for Appendix D 324
E. Decay Ratio Evaluation Methods for Stability Analysis in the Time Domain 325
References for Appendix E 329
F. The Semi-Implicit Scheme and Numerical Dissipation 330
References for Appendix F 331

List of Figures

Figure 1.1: Feedback mechanism of BWR instability 8
Figure 2.1: Schematic of Flow and Pressure Drops in a NCBWR 21
Figure 2.2: Flashing in the riser section 22
Figure 2.3: Flashing number as a function of pressure 23
Figure 3.1: Fuel pin temperature distribution profile 33
Figure 3.2: Channel spatial nodalization 35
Figure 3.3: Iteration Scheme for Steady State Solution in single-phase liquid region 38
Figure 3.4: Overall Iteration Scheme for Steady State Solution in two-phase region 40
Figure 3.5: Overall Iteration Scheme for inlet flow rate at steady state 43
Figure 3.6: Block diagram of single-channel flow feedback mechanism 54
Figure 3.7: Schematic of the SIRIUS-N Facility 56
Figure 3.8: Validation of the code at stationary conditions, at 2MPa and 228kW/m^2 59
Figure 3.9: Stability map of SIRIUS-N facility at various system pressures 60
Figure 3.10: Comparison of stability boundaries between code predictions and experiments 61
Figure 4.1: ESBWR Start-up Trajectory 67
Figure 4.2: ABWR startup sequence 68
Figure 4.3: ABWR power-flow map 68
Figure 4.4: TRACG Start-up Simulation for ESBWR: Reactor Power Trajectories 70
Figure 4.5: TRACG Start-up Simulation for ESBWR: Pressure Response 70
Figure 4.6: TRACG Start-up Simulation for ESBWR: Inlet Subcooling 71
Figure 4.7: TRACG Start-up Simulation for ESBWR: Core Inlet Flow 71
Figure 4.8: Comparison of stationary results for ESBWR Start-up, TRACG vs. FISTAB 74
Figure 4.9: ESBWR Stability Map at P=0.1 MPa 76
Figure 4.10: Scheme of the flow paths in the reactor vessel during start-up 79
Figure 4.11: Allowed flashing region in the reactor vessel for Psys < 2MPa 80
Figure 5.1: Schematic illustration of LASP core 85
Figure 5.2: The 9x9 spiral fuel assembly 86
Figure 5.3: (Left) Petals in contact; (Right) petals at their furthest distance from contact (45°) 86
Figure 5.4: Mechanism of DWO instability in a single heated channel 90
Figure 5.5: Illustration of out-of-phase stability model 91
Figure 5.6: Illustration of in-phase stability model 92
Figure 5.7: Stability sensitivity to void feedback coefficients of CST design, in-phase 98
Figure 5.8: Parametric Sensitivities of LASP Core, single-channel mode 104
Figure 5.9: Parametric Sensitivities of LASP Core, out-of-phase mode 107
Figure 5.10: Parametric Sensitivities of LASP Core, in-phase mode 109
Figure 5.11: Pin diameter effects to stability performance 111
Figure 5.12: Exclusion Region for LASP core in a Typical BWR Power/Flow Map 112

Figure 6.1: Configuration of the RBWR core and fuel assembly 116
Figure 6.2: Variation of the void fraction with flow quality for various correlations 122
Figure 6.3: Variation of the void fraction with flow quality, G=1000 kg/m^{2}s 123
Figure 6.4: Solution scheme for the inlet flow distribution among the lumped channels 125
Figure 6.5: Thermal conductivity comparison among different models..... 126
Figure 6.6: Axial power profile of RBWR-AC 128
Figure 6.7: Axial power profiles for sensitivity study in single channel stability analysis 129
Figure 6.8: Effects of axial power shape in single channel stability analysis..... 129
Figure 6.9: Axial power shape for sensitivity study 132
Figure 6.10: Axial power shape effects to decay ratio in stability analysis..... 133
Figure 6.11: Axial power shape effects to oscillation frequencies 133
Figure 6.12: Weighting function factor effects to RBWR-AC in-phase stability..... 135
Figure 6.13: Axial power profile of RBWR-TB2..... 138
Figure 6.14: Stability sensitivity to inlet orifice coefficients of RBWR-TB2, single-channel mode 139
Figure 6.15: Stability sensitivity to void feedback coefficients, in-phase mode 141
Figure 8.1: Power and flow history of the test points in cycle 14 158
Figure 8.2: Positions of LPRMs and the axis of regional power oscillation 165
Figure 8.3: Experimental signal of APRM-M at test point C14P01..... 166
Figure 8.4: LPRM11:2 Signal at Point 9 169
Figure 8.5: IRF of LPRM11:2 Signal and its fitting curve at Point 9..... 169
Figure 8.6: Typical Coupled TH/NK Code System..... 171
Figure 8.7: Coupling between TRACE and PARCS 172
Figure 8.8: TRACE Model for Ringhals 1 power plant..... 174
Figure 8.9: Planar representation of the 325 TH channels in TRACE 174
Figure 8.10: Radial composition in the PARCS input, at one axial plane..... 176
Figure 8.11: Control rod bank configurations of Ringhals 1 at cycle 14..... 177
Figure 8.12: Detector configurations of Ringhals 1 at cycle 14 177
Figure 9.1: Axial power profile of all test points at cycle 14 179
Figure 9.2: Axial power profile of C14P09 180
Figure 9.3: Radial Power distribution of C14P09..... 180
Figure 9.4: Power response after control rod perturbation, C14P01 181
Figure 9.5: Core flow response after control rod perturbation, C14P01 182
Figure 9.6: Power response after pressure perturbation, C14P01..... 183
Figure 9.7: Core flow response after pressure perturbation, C14P01..... 183
Figure 9.8: Pressure response at lower and upper pelnum after pressure perturbation, C14P01..... 184
Figure 9.9: Power response and its fitting curve after control rod perturbation, C14P01 185
Figure 9.10: Power signal and its fitting curve under pressure perturbation, C14P10... 186
Figure 9.11: IRF of Power signal and its fitting curve under pressure perturbation, C14P10..... 187
Figure 9.12: Calculated decay ratios in Cycle 14 188
Figure 9.13: Calculated oscillation frequencies in Cycle 14 188

Figure 9.14: Control rod bank configurations of Ringhals 1 at cycle 14 191
Figure 9.16: Core average power responses after initial perturbations 192
Figure 9.15: Planar representation of the PARCS model 192
Figure 9.17: Normalized (to its own steady state value) power signal during power oscillation for various initiation cases 193
Figure 9.18: 2-channel model for parallel channel instability 195
Figure 9.19: Perturbation of the inlet flow rate for the 2 channels 195
Figure 9.20: Transient flow responses of the two parallel channels 196
Figure 9.21: TRACE 648 Channel Model for Out-of-Phase Stability Analysis 197
Figure 9.22: Normalized (to its initial value) core power signal during asymmetric control rod perturbation, 648 channel model at C14P09 199
Figure 9.23: Normalized (to its own initial value) channel power signal during asymmetric perturbation, 648 channel model at C14P09 199
Figure 9.24: Axial cell size in the fuel channels 202
Figure 9.25: Axial vecolity in three typical channels, C14P04 202
Figure 9.26: Courant number along axial cells in three typical channels, C14P04 203
Figure 9.27: Core power response after pressure perturbation under different time steps and numerical methods, C14P04 204
Figure 9.28: Decay Ratios for Various Time Step Sizes at C14P04 205
Figure 9.29: Radial power distribution from TRACE/PARCS simulation, 648-chan model for C14P09 206
Figure 9.30: Channel mapping schemes for C14P09 in Ringhals 1 207
Figure 9.31: Power responses from different lumped channel models, control rod perturbation 209
Figure 9.32: Differences in radial power peaking among different channel mapping models 210
Figure 9.33: Axial power distribution differences among different channel mapping models 211
Figure 9.34:Transient core power responses under pressure perturbation, C14P01 216
Figure 9.35: Core flow rate responses under pressure perturbation, C14P01 216
Figure 9.36: Steam dome pressure response under pressure perturbation, C14P01 217
Figure 9.37: Transient core power response under control rod perturbation, C14P01 ... 219
Figure 9.38: Transient core power response under pressure perturbation, C14P01 220
Figure 9.39: Total Recirculation Pump Speed after One Recirculation Pump Trip, w and w/o Control System 223
Figure 9.40: Core Power Response after Recirculation Pump Trip, with and without Control System 224
Figure 9.41: Core Mass Flow Response after Recirculation Pump Trip, w and w/o Control System 224
Figure 9.42: Core Inlet Temperature Response after Recirculation Pump Trip, w and w/o Control System 225
Figure 10.1: Calculated decay ratios of Ringhals-1 cycle 14, Global mode 231
Figure 10.2: Calculated oscillation frequencies of Ringhals-1 cycle 14, Global mode .. 232
Figure 10.3: Calculated decay ratios of Ringhals-1 cycle 14, regional mode 232
Figure 10.4: Calculated oscillation frequencies of Ringhals-1 cycle 14, regional mode 233
Figure 11.1: Configuration of the NSRR 249

Figure 11.2: Histories of power and calculated fuel enthalpy in test FK-11 251
Figure 11.3: Histories of elongation of pellet stack and cladding, rod internal pressure and reactor power in test FK-11 251
Figure 11.4: Results of elongation of pellet stack and cladding, rod internal pressure and reactor power of FRAPTRAN simulation for test FK-11 255
Figure 11.5: Results of other parameters of FRAPTRAN simulation for test FK-11 256
Figure 11.6: Assumed history of linear heat generation rate and flow rate during BWR power oscillations 258
Figure 11.7: Results of FRAPTRAN simulation for BWR power oscillation (1) 259
Figure 11.8: Results of FRAPTRAN simulation for BWR power oscillation (2) 260
Figure 11.9: Results of FRAPTRAN simulation for BWR power oscillation (3) 261
Figure 11.10. FRAPTRAN simulation results for BWR power oscillation (4), different internal gas pressure 262
Figure 11.11: Cladding Average Temperature Changes in Power Oscillations 267
Figure B.1: Transient channel perturbation calculation by marching up the nodes 299
Figure B.2: The scheme of the global Newton method 306
Figure C.1: Test Points in the Peach Bottom-2 Low-Flow Stability Tests, [Costa, 2007] 314
Figure C.2: Axial power distributions at the four Test Points 315
Figure C.3: Comparison of decay ratios, LFST benchmark 316
Figure C.4: Comparison of oscillation frequencies, LFST benchmark 317
Figure D.1: Shapes of the fundamental and first subcritical modes 321
Figure D.2: Total neutron flux dynamics during out-of-phase oscillation 322
Figure E.1 Diagram for definitions of the decay ratio 326

List of Tables

Table 1-1: Advanced designs in large size BWR 4
Table 1-2: Common BWR Stability Analysis Codes 10
Table 2-1: Comparison of Key Features 20
Table 3-1: Comparison of SIRIUS-N Facility with a prototypical NCBWR at system pressure 0.1MPa 57
Table 3-2: Comparison of steady state results at low pressure conditions, Psys=0.2MPa 58
Table 3-3: Comparison of steady state results at high pressure conditions, Psys=2MPa. 59
Table 3-4: Benchmark Results with SIRIUS-N facility at 0.1MPa, (Experiment/Code). 61
Table 3-5: Benchmark Results with SIRIUS-N facility at 0.2MPa, (Experiment/Predicted) 62
Table 3-6: Benchmark Results with SIRIUS-N facility at 0.35MPa, (Experiment/Predicted) 62
Table 3-7: Benchmark Results with SIRIUS-N facility at 0.5MPa, (Experiment/Predicted) 62
Table 4-1: ESBWR Reactor Coolant System Geometric Data 72
Table 4-2: ESBWR Fuel Assembly Parameters 73
Table 4-3: Comparison of steady state results 74
Table 4-4: Pressure drop under various operating conditions 75
Table 4-5: Stability characteristics under ESBWR start-up 76
Table 5-1: Criteria for BWR Stability 87
Table 5-2: Design Parameters for Stability Analysis under design conditions 93
Table 5-3: Parameters in the three lumped channels of the reference core at 100% Power 95
Table 5-4: Parameters in the three lumped channels of the LASP Core at 120% Power. 96
Table 5-5: Parameters in the three lumped channels of the CST Core at 120% Power ... 96
Table 5-6: Results of stability analysis at design conditions 96
Table 5-7: Results of CST stability analysis at 100% power and uprated conditions 97
Table 5-8: Critical power ratio for the reference design and CST fuel 99
Table 5-9: Comparison of the Fuel Assembly Design for Reference and LASP Cores. 100
Table 5-10: Comparison of major hydraulics parameters 101
Table 5-11: Analysis results of decay ratio for three instability modes 101
Table 6-1: Overall Design Parameters of RBWRs and ABWR 118
Table 6-2: Specifications and Core Performance of early RBWR Designs 119
Table 6-3: Parameters for hot channel stability analysis of RBWR-AC 128
Table 6-4: Reactivity coefficients for RBWR-AC and BWR 130
Table 6-5: Results of stability analysis under design conditions 130
Table 6-6: Results of stability analysis under design conditions 131
Table 6-7: Pressure drop distribution in the single hottest fuel bundle of RBWR-AC .. 131
Table 6-8: Parameters for hot channel stability analysis, with the radial core pressure equalization occurring above the upper reflector 137

Table 6-9: Pressure drop distribution in the single hottest fuel bundle 137
Table 6-10: Reactivity coefficients for RBWR-TB2 and BWR 139
Table 6-11: Results of stability analysis under design conditions 140
Table 6-12: Parameters in the hottest assembly of RBWR-AC, RBWR-TB2 and BWR/4 142
Table 7-1: Comparison of some frequency domain codes 147
Table 7-2: Various applications of coupled NK/TH code to BWR stability analysis 156
Table 8-1: Ringhals 1 core T/H parameters 159
Table 8-2: Fuel property and heat transfer data 160
Table 8-3: Recirculation loop geometry information 160
Table 8-4: Ringhals-1 stability test conditions and results in cycle 14 161
Table 8-5: Comparison of decay ratios for all test points at Cycle 14 of Ringhals-1 166
Table 8-6: Comparison of oscillation frequencies for all test points at Cycle 14 of Ringhals-1 167
Table 8-7: Difference between DRACO predictions and the reference values 168
Table 8-8: Uncertainty in estimating the DR due to model order selection 168
Table 8-9: Main components in the TRACE input deck 175
Table 9-1: Steady state parameters from coupled calculation 179
Table 9-2: Decay ratio evaluation from power signal during CR, C14P01 185
Table 9-3: Summary of Ringhals 1 Stability Test Results in Cycle 14, In-phase 187
Table 9-4: Bias and standard deviation of the difference between calculated and reference decay ratios and oscillation frequency 189
Table 9-5: Calculated Decay ratios for C14P09, out-of-phase 200
Table 9-6: Steady-state and oscillation parameters among different mapping schemes 209
Table 9-7: Moderator density and Fuel temperature distributions at C14P01, 325-chan model 214
Table 9-8: Moderator density and Fuel temperature distribution at C14P01 with 95% flow condition, 325-chan model 215
Table 9-9: Decay ratios and oscillation frequencies at C14P01 218
Table 9-10: Decay ratios and oscillation frequencies under pressure perturbation, control system effects 221
Table 9-11: Investigations on modeling effects of coupled NK/TH code in BWR stability analysis 226
Table 10-1: Results of the Ringhals stability benchmark, global mode 230
Table 10-2: Results of the Ringhals stability benchmark, regional mode 231
Table 10-3: Bias and standard deviation between the calculated and reference global decay ratio and oscillation frequency 234
Table 10-4: Benchmark results of Ringhals 1 stability test from participants, global decay ratio 234
Table 10-5: Benchmark results of Ringhals 1 stability test from participants, regional decay ratio 234
Table 10-6: Models for Ringhals stability benchmark, STAB and TRACE 235
Table 10-7 Major modeling uncertainties in stability analysis with STAB and TRACE237
Table 11-1: Fuel design and pre-test conditions of FK-11 250
Table 11-2: Summary of conditions and results of the power oscillation test, FK-11 ... 252
Table 11-3: Difference between FK-11 pre-test and FRAPTRAN input condition 253

Table 11-4: Needed BWR/4 information for Power and flow rate calculation 258
Table 11-5: Simulation results applying to the design criterion 264
Table 11-6: Fatigue threshold stress in the literature for Zircaloy-4 cladding 266
Table B-1: Output of iteration steps, real algebraic equation 307
Table B-2: Output of iteration steps, complex algebraic equation 308
Table B-3: Output of iteration steps, system characteristic equation 309
Table B-4: Output of iteration steps, inflection point 310
Table B-5: Output of iteration steps, division by zero 310
Table B-6: Output of iteration steps, root jumping 311
Table C-1: Peach Bottom test results and conditions at the end of cycle 2 314
Table C-2: Comparison of the experimental and the predicted results 316
Table E-1: Participants and methods used in the Forsmark Stability Benchmark 329

1. Introduction

1.1 Motivation and Objective

During the development of Boiling Water Reactor (BWR) technology, there was considerable concern about the possible effect of thermal hydraulic oscillations and coupled neutronic/thermal-hydraulic instabilities. The boiling two-phase flow in the core may become less stable because of the time lag between vapor generation and pressure loss perturbation. Furthermore, in BWRs, the reactivity depends strongly on the core void fraction. Thus, when a void fraction oscillation is established in a BWR, the power oscillates according to the neutronic feedback. This feedback mechanism may under certain conditions lead to poorly damped or even long lasting (limit-cycle) power oscillations.

The current trend of increasing reactor power density and applying natural circulation for more extensive core cooling has major consequences for the stability of new BWR designs. The numerous modifications in reactor size, reactor power, fuel design, power density, discharge burnup and loading strategies changed the core stability behavior of the BWR reactor to a significant extent. In comparison to the situation in the Seventies, the exclusion region of the power-flow map, which has to be avoided due to stability concern, grew to a respectable size. Instability events had been observed more in commercial plants since 1980s.

One objective of this work is to determine the stability margin in the BWRs with evolutionary and innovative design features, such as a Natural Circulation BWR (NCBWR, e.g. General Electric's ESBWR [GE-Hitachi, 2008]) relying completely on natural convection for heat removal, the high power density BWR designs at MIT using Large Assembly with Small Pins (LASP) or Cross Shape Twisted (CST) fuel designs [Kazimi et al., 2006], and the Hitachi's RBWRs [Hitachi, 2009a, 2009b] utilizing a hard

neutron spectrum. This thesis focuses on investigation of stability against density wave oscillation under both the rated conditions and the low-pressure startup conditions.

Furthermore, a wide variety of codes and models exists that may be used to address the stability issues, ranging from sophisticated system codes, able to calculate an overall plant behavior, to very simple models. All of them have a capability to deliver results to quantify stability margins, although reliability of their predictions may be different [D'Auria et al., 1997]. Recently, the coupled codes method, which consists in incorporating three-dimensional (3D) neutron kinetics (NK) modeling of the reactor core with thermal-hydraulic (TH) system codes, has been extensively used in reactor transient analyses. However, it has been argued that numerical diffusion in the thermal-hydraulic solvers of the system codes would be detrimental to stability-related predictions, unless care is taken to exclude or limit its effects.

Thus, another objective of this work is to examine the code capability to capture key physics in a full-core 3D TH/NK model, and its effectiveness and accuracy in prediction of different stability scenarios, and the potential for the interference of numerical oscillations and physical instability.

1.2 Development of BWR technology

Substantial design and development programs are underway worldwide for further technology improvements and for development of advanced nuclear power plant designs. This development is proceeding for all reactor lines — water cooled reactors, gas cooled reactors, and liquid metal cooled reactors so that nuclear power can play an important and increasing role in global energy supply in the future. The accumulated experience is being used to develop advanced nuclear power plant designs. Sustainability, improved economic competitiveness, enhanced safety, and proliferation resistance are common goals for the advanced designs.

Considering the large effort involved in establishing new design concepts, especially for

new reactor coolant (such as SFR), and the expected replacement of existing nuclear power plants in the next twenty years, it is expected that the light water reactor will continue to play the main role in the electric power generation for many decades to come. But in order to play that role, the light water reactor will be required to have a sufficient cost advantage to compete with other electric power sources. For these reasons, Achieving economic competitiveness and high safety levels have become two of the most important objectives in the development of the near-term BWRs.

BWR plants offer a broadly developed and mature technology basis. Altogether there are 93 boiling water reactors (BWRs), including four advanced boiling water reactors (ABWRs), currently operating worldwide. Many are among the best operating plants in the world, performing in the "best of class" category. However, there is still a potential for further improvement. A list of the advanced BWR designs including type, size, design organization and status is provided in Table 1-1, from [IAEA, 2004], in which the SCPR, RMWR, and RBWR are among the category of innovative designs, others are among the category of evolutionary designs (the definitions of the evolutionary and innovative reactor designs could be found in [IAEA-TECDOC-1391, 2004]). Improved economic competitiveness and enhanced safety are common goals in these advanced designs.

In the near term most new nuclear plants will likely be evolutionary designs building on today's successful proven systems while incorporating technology advances and often pursuing economies of scale. In the longer term, development and demonstration of new, innovative designs, including their promised short construction and startup times, low capital costs, or even the potential to close the fuel cycle, could help to promote a new era of nuclear power.

Table 1-1: Advanced designs in large size BWR
(from [IAEA, 2004])

Name	Type	MWe Net	Design Organizations	Status
ABWR	BWR	1300	General Electric, USA; Hitachi Ltd. and Toshiba Corp., Japan	Operating in Japan, Under construction in Japan and Taiwan, Design certified by the U.S.NRC in USA
ABWR-II	BWR	1638	Japanese utilities, General Electric, Hitachi Ltd. and Toshiba Corp.	In design phase, commercial introduction foreseen in latter half of 2010s
BWR 90+	BWR	1575	Westinghouse Atom, Sweden	Plant design is essentially complete
ESBWR	BWR	1550	General Electric, USA	The Design Certification Application received by the U.S.NRC in 2005
SWR 1000	BWR	1250	Framatome ANP, Germany	In the U.S., the Design Certification Pre-application review by the U.S.NRC was initiated in 2002
SCPR	SCWR	950	Toshiba, et al., Japan	Representative of Super-Critical Water cooled Reactor system selected by the Generation-IV International Forum
RMWR	BWR	1300	JAERI, Japan	Design studies and experiments being performed. Small scale prototype possible by early 2010s; commercialization by 2020
RBWR	BWR	1356	Hitachi, Japan	Design studies

Besides the advanced designs summarized by IAEA in Table 1-1, Toshiba Corporation is developing AB1600, which is also a near-term ABWR. In order to achieve the main design goals of: (1) Enhance cooling capability against SA from design stage; (2) Economic competitiveness against other electric power sources: 30% power generation cost reduction from the recent ABWR; the current reference design concept includes the following design features: [Murase et al., 2006]

(1) Large rated electric power of 1600MWe,

(2) Large fuel bundle of 1.2 times as large as the current ABWR fuel bundle size,

(3) Hybrid combination between active safety system and passive safety system,

(4) Simplification of plant systems,

(5) Succession of the forced recirculation system.

Furthermore, extensive work has been done at MIT to access the feasibility of increasing the core power density of existing and future BWRs, through innovative geometry and/or the materials of the fuel assembly. The large assembly with small pins (LASP) design and the cross shape twisted (CST) fuel rod design were chose as the most promising concepts among the examined ideas [Kazimi, et al., 2006].

1.3 Introduction to BWR Instability Issue

1.3.1 Types of instabilities

1. Thermal-hydraulic instabilities

In general, several types of thermal-hydraulic instabilities may occur in a heated two-phase system. They can be classified into two broad categories: static and dynamic. The static instabilities are explained in terms of steady-state laws, whereas dynamic instabilities require the use of dynamic conservation equations. Reviews of most aspects of two-phase stability may be found in [Boure et al., 1973] and [Tong, 1997].

The common static instabilities include: flow excursion (or Leidinegg) instability, flow pattern "relaxation" instability, and geysering or chugging. All of these instability types have in common the existence of two equilibrium points, and the system tends to "jump" from one to the other [March-Leuba, 2004].

Examples of dynamic instabilities include: density wave oscillations, acoustic oscillations, pressure drop oscillations, and thermal oscillations. The acoustic oscillations have high frequencies (10-1000 Hz), dependent on the time required for pressure wave propagation in the system. Density waves travel at much lower velocity and produce oscillations with low frequencies (less than 1 Hz at BWR operating conditions), related to the transit time of the flow through the channel. The pressure drop oscillation is typically due to the dynamic interaction between channel and compressible volume, associated with very low frequency (0.1 Hz). [Boure et al., 1973]

The most common instability for commercial BWRs is the density-wave instability. This type of instability can be described as follows: given a flow perturbation, a "wave" of voids travels upward through the channel producing a pressure drop that is delayed with respect to the original perturbation. An increase in flow typically induces an increase in pressure drop and a negative feedback that tends to reduce the flow perturbation. The density-wave phenomenon, however, delays this feedback, and, at some frequency, the delay is equivalent to an 180^{o} phase lag. Thus, at this frequency, the pressure drop feedback is positive, which will increase the oscillation amplitude of the original flow and the system becomes unstable.

The two main modes of oscillation that exist for the channel thermal-hydraulic instability are single-channel and parallel-channel instabilities [March-Leuba, 2004]. In the parallel-channel mode of oscillation, the flow in one channel increases while the flow in the other channel decreases; thus, this mode of oscillation is called out-of-phase flow instability. During out-of-phase oscillations, the channel void fraction follows trends opposite to those of the flow, so that the pressure drop is the same across both channels.

Fukuda and Kobori [1979] proposed a different classification for density wave oscillations: Type-I instability (only occurring with a chimney installed) and Type-II instability. The Type-I instability is dominant when the flow quality is low, while the Type-II instability is dominant when the flow quality is high. The Type-II instability is the most commonly observed form of density wave oscillations.

2. Coupled neutronic-thermal-hydraulic instabilities

BWR instabilities could be classified based on the geometrical features of the oscillations, in which the relationships between phases and amplitudes of the oscillations at different axial and azimuthal positions in the core of a reactor are considered. Coupled neutronic-thermal-hydraulic and pure thermal-hydraulic oscillations can be distinguished, respectively. The classification results are:

- Single channel or local oscillations (pure thermal-hydraulic);
- Regional or out-of-phase oscillations (coupled neutronic-thermal-hydraulic);

- Core wide or in phase oscillations (coupled neutronic-thermal-hydraulic).

The two modes of oscillation that are commonly recognized for coupled neutronic-thermal-hydraulic are the core-wide or in-phase mode and the regional or out-of-phase mode. In the core-wide mode, the power and inlet flow of the whole core oscillate in phase for all channels. In the out-of-phase mode that has been observed in experiments and instability events worldwide, the power of half of the core oscillates out-of-phase with respect to the power of the other core half. The inlet flows of both halves of the core are also out-of-phase with respect to each other.

1.3.2 Mechanisms of BWR instabilities

The BWR instability involves two major physical processes: the neutronic process and the thermal-hydraulic process. The water inside a BWR not only functions as the coolant which removes the heat from the reactor core and keeps the fuel assembly temperature lower than safety limits, but also participates in the nuclear fission chain reactions as the moderator to slow down the fast neutrons.

The BWR thermal-hydraulic process is a complicated physical phenomenon. The process can be further divided into three dynamic processes: the fuel heat conduction, the in-core channel flow dynamics, and the out-of-core flow dynamics. For a conventional BWR, the out-of-core flow dynamic process includes the recirculation pump/loop hydraulic process and the upper plenum/separator hydraulic process. In a NCBWR, the out-of-core hydraulic processes include those inside the chimney, steam separator, and downcomer. The neutronic feedbacks from the thermal-hydraulic dynamic processes are due to the moderator density change and fuel temperature change.

The BWR instabilities may be induced by the feedback mechanism between the thermal-hydraulic and neutronic process. Without an external oscillating reactivity change, unstable oscillations or sustained power oscillations may occur between these two

dynamic processes. A typical feedback diagram of the coupling between these two processes is shown in Figure 1.1.

The density wave oscillations had been identified as the major cause of almost all the reported BWR instability incidents [Lu, 1997]. Once the density wave instability occurs, the reactivity feedback caused by delay in the change in void fraction with respect to the initial channel inlet flow perturbation. If the delay is long enough, the reactor system may become unstable. The neutron flux may oscillate with a frequency close to the inverse of the density wave time constant, which is the transport time delay of the voids traveling through the core. Under the influence of this type of instability, the core neutron flux distribution and the corresponding power distribution may oscillate in different modes. The fundamental mode of the power oscillation is the so-called core-wide in-phase mode. In this mode, the reactor power throughout the whole core oscillates in phase with the same frequency. Another mode is called the out-of-phase oscillation, in which the total reactor power may not vary greatly, but the local reactor power density changes.

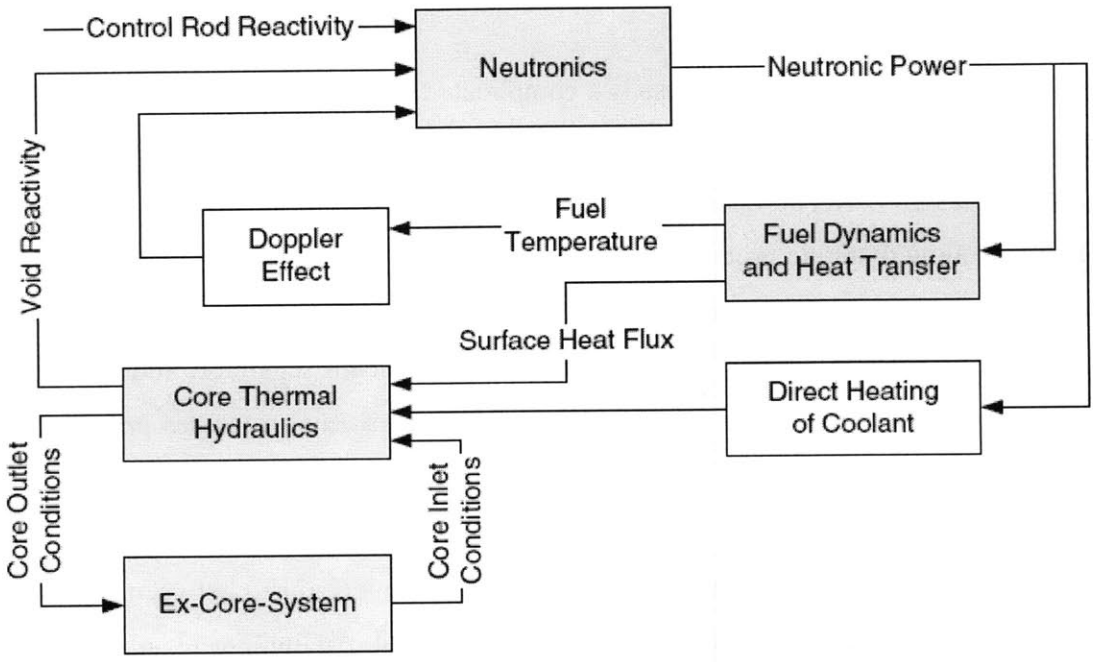

Figure 1.1: Feedback mechanism of BWR instability (From [Hanggi, 2001])

Four main interaction blocks in Figure 1.1 should be noted:

1) Core thermal hydraulics, which is often the trigger for instability mechanisms and affects power production by fission.
2) Neutron kinetics, which is directly responsible for the power variation, as a consequence of the external and the feedback reactivity perturbations.
3) Fuel dynamics and heat transfer, which act as a filter of power perturbations and introduce time delays between power production and coolant flow heating.
4) Ex-core-systems, which impose the boundary conditions to the core channels, thus influencing their stability.

BWR stability analysis would require careful modeling of all of the above four aspects.

1.3.3 Analysis Methods

Many computer programs have been developed or adopted to evaluate stability of BWRs and other boiling channel systems. Multipurpose codes solving multi-dimensional equations both for neutronics and thermal-hydraulics are now available. On the other hand, simplified codes based on Homogeneous Equilibrium Model (HEM) are still used in the same frame.

For a single uniform heated two phase flow channel, Ishii and Zuber [1970] determined the stability boundary of density wave oscillations for the system, which can be represented as a function of the dimensionless phase change number (also known as the Zuber number), N_{pch}, and the subcooling number, N_{sub}. Saha [1974] later added the non-equilibrium effects at low qualities to the stability criterion of $N_{pch} \sim N_{sub}$.

For a BWR, three are, in general, three approaches to analyze the nuclear coupled thermal-hydraulics: Frequency Domain analyses, Time Domain analyses, and Bifurcation analyses. The first two approaches are more widely used, and the examples of both can be seen in Table 1-2, noted that the details of modeling are different. A more detailed list

and code descriptions of the frequency domain and time domain codes used for BWR stability analysis can be found in [D'Auria et al., 2005].

Table 1-2: Common BWR Stability Analysis Codes

Common codes operating in the time domain					
Name	Thermal-Hydraulics			Neutronics Dimension	Developer
	Channels	Model	Eq.		
RAMONA-3B	all	D-F NE	4	3	ScandPower A/S
RELAP5/3D	a few	2 fluid	6	Point kinetics/3	INL, NRC
RETRAN-3D	4	Slip EQ	5	1	EPRI
TRACG	a few	2 fluid	6	3	GE
TRACE	a few	2 fluid	6	3	NRC

Common codes operating in the frequency domain					
Name	Thermal-Hydraulics			Neutronics Dimension	Developer
	Channels	Model	Eq.		
NUFREQ NP	a few	D-F EQ	3-5	3 simplified	RPI
LAPUR5	1-7	Slip EQ		Point kinetics	ORNL, NRC
STAIF	10	D-F NE	5	1	SIMENS
FABLE	24	Slip EQ		Point kinetics	GE
ODYSY	a few	D-F NE	5	1	GE
MATSTAB	all	D-F NE	4	3	FORSMARK AB
STAB	a few	D-F EQ	4	Point kinetics	MIT

Eq.: number of conservation equations for thermal hydraulics
D-F: drift-flux description of two-phase mixture
NE: thermal non-equilibrium between phases
Slip: non-equal gas and liquid velocities
EQ: thermal equilibrium between phases

1.3.4 Safety Aspects of BWR instability

The stability of BWR reactor systems has been of a great concern from the safety and the design point of view. In terms of safety, the concerned variables in an instability occurrence with high oscillation amplitudes are the neutron flux and the rod surface temperature. Additional problems might arise due to thermal cycling that may affect the

fuel rod integrity, making pellet-cladding interaction more probable; thermal cycling may also induce greater than normal fission product release from pellets [D'Auria, 1997]. Furthermore, sustained flow oscillations may cause forced mechanical vibration of components or system control problems, affect the local heat transfer characteristics, and may induce boiling crisis. Therefore, the designer must be able to predict the threshold of instability in order to design a reactor with substantial stability margin.

1.4 Literature Review

The broad literature on BWR-stability covers a wide range of subjects. Reviews of most aspects of neutronic coupled stability may be found in [Lahey and Moody, 1993], [D'Auria et al., 1997, 2005], and [March-Leuba, 2004]. Papers chosen in our work are briefly reviewed in the following.

According to [Lahey and Moody, 1993], from the reactor designer's viewpoint, the most important instability type in a BWR is density wave oscillations (DWO). Podowski [2003] summarized three types of DWOs. The first one is a single channel type, which means that only one channel or a small fraction of the parallel channels oscillates, while the other channels remain at steady state. This imposes a constant pressure drop boundary condition across the oscillating channel or channels. This type of DWO was also called the parallel channel type DWO by Podowski [2003]. During single channel oscillation, only a small fraction of the core flow oscillates while the bulk flow remains at steady state. Therefore, the neutronic feedback due to this small fraction oscillation can be neglected. In other words, the thermal-hydraulic dynamics is decoupled from the neutronic dynamics in the single channel oscillation. The second type is the region wide (or out-of-phase) instability. In this type of instability, about half of the core behaves out-of-phase from the other half [March-Leuba and Rey, 1993]. During the oscillation, half of the core rise in power while the other half decrease to maintain an approximately constant total core power. Also, the system adjusts flow from one half of the core to the other half while keeping the total flow rate almost constant. All channels will have the same but oscillating pressure drop [Munoz-Cobo, et al, 2002]. The third type is called the core

wide in-phase instability, where the flow and power in all channels oscillate in phase throughout the whole core.

Over the past several years, many mathematical models and computer codes have been developed, and tests have been carried out to investigate density-wave and power-void instabilities in BWRs. In the theoretical work done so far, stability analyses have usually been carried out by evaluating the decay ratios and oscillation frequencies and studying the effect of certain parameters on BWR core stability. Numerical simulations have been done to study the time evolution of certain phase variables. The results of some of these stability analyses and numerical simulations have been compared with test results or data collected from actual BWR instability incidents, and the overall agreement has been reasonably good. This overall good agreement between the computational and mathematical analyses, and the experimental tests and the actual operational BWR incidents, has led to a better understanding of the instability phenomenon.

Recently, void flashing effects received much more attention in the research of the stability of natural circulation BWRs under low-pressure start-up conditions [Inada et al. 2000, Van Bragt et al. 2002, Yadigaroglu and Askari 2005, and Furuya et al. 2004]. Thermal-dynamic properties are dependent on pressure: i.e. saturation enthalpy changes with pressure, which in turn induces the flashing phenomenon (the sudden increase of vapor generation due to the reduction in hydrostatic head). Manera et al. [2003] investigated the dynamics of a flashing bubble with wire mesh sensors in the CIRCUS facility. Furuya et al. [2004, 2006] investigated the occurrence conditions and the mechanism of flashing-induced instability experimentally in a relatively low system pressure at the SIRIUS-N facility, which simulates a prototypical natural circulation BWR. Woo et al. [2007] conducted the experimental work to investigate the stability characteristics of the NCBWR startup transients at TOSHIBA NCBWR instability facility. Although lots of experimental and numerical analysis work has been conducted in this field, mature stability analysis codes including the flashing effects are still unavailable.

Also, the nuclear industry and the scientific community turned more attention to the development of coupled 3D neutron kinetics (NK) / thermal-hydraulic (TH) system codes to simulate BWR transients and accidents. Examples of the applications in BWR stability analysis include RAMONA/MODKIN [Miró et al., 2002], TRAC-BF1/ENTRÉE [Hotta et al., 2001a, 2001b], RELAP5/PARCS [Costa 2007, Bousbia-Salah and D'Auria, 2006], and TRACE/PARCS [Xu, et al., 2009]. It is confirmed that the codes are able to capture instability and produce physically sound oscillations induced by a sufficiently strong disturbance. However, a careful control of time-space discretization to minimize numerical diffusion error is reported to be central to the successful outcome.

The detailed literature review of a specific topic within BWR stability can be found in individual chapters, including:

1) Literature review of flashing-induced instability in Chapter 2;
2) Literature review of the startup of natural circulation BWRs in Chapter 4;
3) Literature review of the stability analysis method and the applications of coupled 3D codes in Chapter 7;
4) Literature review of the fuel performance under power oscillations in Chapter 11.

1.5 Scope of Work

One part of this work include determining the stability margin in the BWRs with evolutionary and innovative design features, such as the NCBWR, the LASP and CST fuel designs for high power density BWRs, and the RBWRs, in comparison to the conventional BWR technology. It will focus on the investigation of DWO type of stabilities and the reactor safety characteristics under transients and accidents conditions. It also explores the sensitivity analysis to investigate the effects of different design features to the stability margins. As the frequency domain stability codes can be used efficiently to carry out sensitivity analyses, compared to time domain codes, a frequency domain linear stability code, STAB developed at MIT, is applied to investigate the stability performance of these advanced designs.

The stability analysis of a NCBWR at high pressure conditions was conducted in a previous work [Hu and Kazimi, 2007]. In this work, the flashing-induced instability under low pressure conditions in a NCBWR during startup is to be examined. However, for stability analysis under low pressure conditions, mature codes including the flashing effects are still unavailable. A linear stability analysis code in the frequency domain will be developed to address the issue of flashing-induced instabilities. Then, the NCBWR stability performance under startup conditions will be investigated.

The other part of this work is to examine the stability analysis methods, especially the coupled 3D TH/NK system codes, focusing on the effectiveness and accuracy in prediction of different stability scenarios, the interference of numerical oscillations and physical instability. USNRC's latest system analysis code, TRACE/PARCS, is chosen in this work. Its validation for stability analysis and the comparison against the frequency domain approach are performed against the Ringhals 1 stability tests. Various modeling effects to the stability predictions in TRACE are also examined.

Finally, the clad integrity under the power oscillations for the high burnup fuels is examined. The fuel performance under power oscillations are calculated by using the FRAPTRAN code. Then, based on the results of FRAPTRAN, the clad fatigue analysis is conducted.

The organization of the thesis includes four parts:

I. Flashing Induced Instability and Natural Circulation BWR Startup;
   - In Chapter 2, the key features of a reference NCBWR design, the flashing phenomenon, and the previous work in the literature are described.
   - In Chapter 3, a BWR stability analysis code named FISTAB is developed to address the issue of flashing-induced instability during reactor startup. Various models and solution schemes in the code are described. The functionality of the FISTAB code was confirmed by testing the experimental results at SIRIUS-N facility in Japan.

- In Chapter 4, the start-up procedure of the Dodewaard reactor and the ESBWR design are first described. Then, the stability performances of several operating points during the ESBWR start-up trajectory are examined by the FISTAB code. Finally, proposed start-up procedures for the NCBWRs in the literature are reviewed, and possible revisions to the ESBWR start-up procedure are recommended.

II. Stability Analyses of Advanced BWR Designs

- In Chapter 5, using the frequency domain code STAB, the stability analyses of the high power density large assembly design and the CST design are conducted. These designs aim to have about 20% higher power density in the BWR core over a traditional design. Three types of density wave oscillations: single-channel, out-of-phase, and in-phase oscillations have been examined. For the LASP core and the reference core, decay ratio sensitivities are evaluated against void coefficient, Doppler coefficient, inlet orifice coefficient, coolant mass flow rate, reactor thermal power, and fuel pin diameter.
- The stability performances of Hitachi's RBWRs are analyzed in Chapter 6. The RBWR aims to have about 150% higher power density in its core compared to a traditional BWR. Various design effects on stability performance are also examined, including: axial power shape, inlet orifice coefficients, reflector design, and void coefficient.

III. Stability Analysis Approach, time domain vs. frequency domain

- In Chapter 7, after a brief introduction and literature review of the methods used for BWR stability analysis, the current capabilities of the codes, latest development and research tendency, are described.
- In Chapter 8, the Ringhals 1 stability test, the coupled 3D thermal-hydraulics and neutronics code, TRACE, the decay ration analysis tool, DRACO, the thermal-hydraulics and neutronics models for the Ringhals tests, are described.
- In Chapter 9, the TRACE/PARCS code is applied to simulate the Ringhals 1 stability test. Various modeling effects on the stability predictions are examined,

including time-spatial discretization and numerical schemes, channel grouping, neutronics modeling, and control system modeling.

- In Chapter 10, the Ringhals 1 stability test is evaluated by the frequency domain code STAB. Furthermore, a detailed comparison between the frequency domain approach (i.e. STAB) and the time domain approach (i.e. TRACE) is presented.

IV. Clad Performance under Power Oscillations

- After a literature review of the fuel performance under power oscillations in Chapter 11, the power oscillation test at the NSRR (FK11) and an assumed power oscillation without scram in normal BWR operating conditions are simulated by using the FRAPTRAN code. Applying the transient results from FRAPTRAN, the clad temperature, stresses and potential failure are examined using the stress-strain criteria in ASME Code and a thermal fatigue analysis.

Part I: Flashing Induced Instability and Natural Circulation BWR startup

Contents

Part I: Flashing Induced Instability and Natural Circulation BWR startup 17

2. Introduction of Natural Circulation BWRs and Flashing Phenomenon 18
   2.1. Overview of Design Features of a Reference Natural Circulation BWR (ESBWR) 18
   2.2. Mechanism of flashing induced instability 21
   2.3. Previous Work 24
      2.3.1. Experimental work 24
      2.3.2. Analytical work 25
   2.4. Scope of Part I of This Work 26
3. Development for Flashing-Induced Stability Analysis, FISTAB 28
   3.1. Model Description 28
      3.1.1. Governing Equations 29
      3.1.2. Spatial Discretization 35
      3.1.3. Steady-State Solution Scheme 36
   3.2. Linear Stability Analysis in the Frequency Domain 43
      3.2.1. Linear Perturbation Equations 44
      3.2.2. Frequency Domain Linear Equations 53
      3.2.3. Feedback and System Characteristic Equation 53
   3.3. Code Benchmark 55
      3.3.1. SIRIUS-N Facility Description 55
      3.3.2. Comparison of steady-state results 58
      3.3.3. Comparison of transient results 59
   3.4. Summary 63
4. NCBWRs Start-up 64
   4.1 Introduction 64
   4.2 Start-up Procedure of BWRs 65
      4.2.1 The start-up procedure of the Dodewaard reactor 65
      4.2.2 The start-up procedure of the ESBWR 66
      4.2.3 The start-up procedure of the ABWR 67
   4.3 Stability analysis of ESBWR during start-up 69
      4.3.1 Comparison of stationary results 72
      4.3.2. Linear stability analysis 75
   4.4 Start-up Procedures for NCBWRs 77
      4.4.1 Literature survey on start-up procedure for NCBWRs 77
      4.4.2 A simple criterion for NCBWRs start-up procedure 79
   4.5 Summary 81

2. Introduction of Natural Circulation BWRs and Flashing Phenomenon

The first part of this dissertation, starting from this chapter, is devoted to developing a code to investigate flashing induced stability characteristics, and to examining the stability performance of natural circulation BWRs during startup. In this chapter, the key features of a reference NCBWR design, the flashing phenomenon, and the scope of this work are described.

2.1. Overview of Design Features of a Reference Natural Circulation BWR (ESBWR)

The Economic Simplified Boiling Water Reactor (ESBWR) is General Electric's latest evolution of the BWR. It is used in our analysis as a reference NCBWR. The ESBWR evolved from the design and operating experience of past BWRs, especially from innovations developed for the company's earlier ABWR and SBWR. The ESBWR is announced as a simplified reactor with a standardized design and first-rate economics [Hinds and Maslak, 2006]. Details of the ESBWR design could be found in [Hinds and Maslak, 2006], [Cheung, et. al., 1998], and [GE-Hitachi Nuclear Energy, 2008]. The stability performance of the reference NCBWR at normal operating conditions (under high pressure) was examined in the author's previous work [Hu and Kazimi, 2007].

The ESBWR relies on the use of natural circulation and passive safety features to enhance the plant performance and simplify the design. Table 2-1 (Table II in [Hinds and Maslak, 2006]) provides a comparison of key plant features for several BWR designs.

The ESBWR design achieved a major plant simplification by eliminating the external as well as the internal recirculation pumps. The use of natural circulation, along with the desire to maintain the same or better plant performance margins, resulted in the following key design features:

- Opening the flow path between the downcomer and lower plenum (elimination of internal jet pumps)
- Use of shorter fuel - resulting in a reduced core pressure drop
- Use of an improved steam separator to reduce pressure drops
- Use of a 6.61 m high chimney to enhance the driving head for natural circulation

The ESBWR core has an increased size and power level by adding more fuel assemblies. Active fuel height was decreased to 3.0 meters from a traditional 3.7 m in order to achieve the appropriate pressure drop, while the power density was maintained at 54 kW/L. The core was increased from the 872 fuel assemblies in the ABWR to 1132 fuel assemblies in the ESBWR, resulting in a thermal power rating of 4500 MWt.

The ESBWR reactor coolant system is similar to that of the operating BWRs, except that the recirculation pumps and associated piping are eliminated. Circulation of the reactor coolant through the ESBWR core is accomplished via natural circulation. The magnitude of the natural circulation flow depends on the balance between the density driving head and the pressure losses through the circulation path. Figure 2.1 shows a schematic diagram of the coolant flow path and pressure drops inside the reactor vessel [Cheung, et. al., 1998]. The driving head is proportional to the density difference between the fluid in the downcomer and the fluid inside the core shroud, or proportional to the height of the chimney/upper plenum and core. The major losses through the circulation path include those at the downcomer, core, chimney/upper plenum, and separators. The core flow varies according to the power level, as the density difference changes with changes in power levels. Therefore, a core power-flow map is only a single line and there is no active control of the core flow at any given power level.

Table 2-1: Comparison of Key Features

Parameter	BWR/4	BWR/6	ABWR	ESBWR
Power (MWt/MWe)	3293/1098	3900/1360	3926/1350	4500/1550
Vessel height/dia (m)	21.9/6.4	21.8/6.4	21.1/7.1	27.7/7.1
Fuel bundles, number	764	800	872	1132
Active fuel height (m)	3.7	3.7	3.7	3
Power density (kW/L)	50	54.2	51	54
Recirculation pumps	2 (external)	2 (external)	10 (internal)	0
Number/type of CRDs	185/LP	193/LP	205/FM	269/FM
Safety system pumps	9	9	18	0
Safety diesel generators	2	3	3	0
Alternate shutdown	2 SLC pumps	2 SLC pumps	2 SLC pumps	2 SLC accumulators
Control and instrumentation	Analog single channel	Analog single channel	Digital multiple channel	Digital multiple channel
Core damage frequency (per year)	10^{-5}	10^{-6}	10^{-7}	10^{-8}
Safety bldg vol (m^3/MWe)	120	170	180	130

CRD: Control Rod Drive; LP: Locking Piston; FM: Fine Motion.
SLC: Standby Liquid Control

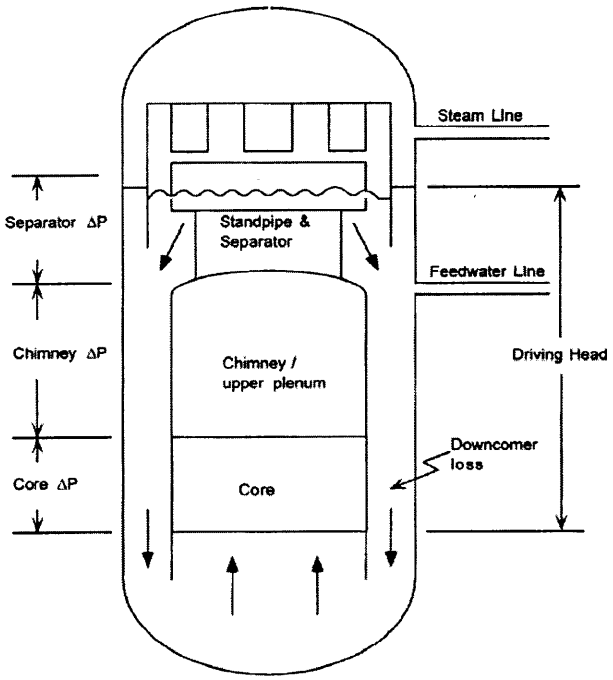

Figure 2.1: Schematic of Flow and Pressure Drops in a NCBWR

Unfortunately, the innovation in the design has introduced operational uncertainties, especially related to the start-up phase of the reactor. The instabilities in the region between single-phase and stable two-phase natural-circulation mode are mainly induced by flashing in the riser section (i.e. steam production in adiabatic conditions). The feedback between steam generation in the riser and buoyancy of the natural-circulation loop may lead, under specific conditions, to flow oscillations. These oscillations are undesirable, since they make the start-up of the reactor rather difficult and may lead to thermal fatigue and vibrations of the internal structures of the pressure vessel. The flashing phenomenon and the flow instabilities that it may induce in natural-circulation loops are of the main objects of this part of this work.

2.2. Mechanism of flashing induced instability

Flashing refers to steam production that takes place by change of phase from liquid, without the need for an external heat source. Steam production occurs due to the liquid phase becoming superheated (for instance if the local pressure decreases or if hot liquid is

transported from a higher to a lower pressure region). Flashing causes an imbalance between the driving force and pressure losses in the natural-circulation loop, giving rise to the potential for flow oscillations.

The flashing phenomenon is schematically illustrated in Figure 2.2. When the power is low, the coolant temperature increases in the heated section without reaching saturation conditions. The coolant temperature remains constant in the adiabatic section if heat exchange with adjacent flow paths can be neglected. Since at low pressure the saturation temperature is strongly dependent on pressure, the saturation temperatures at the core exit and at riser-exit locations, respectively, can differ by several degrees due to the decrease of pressure head along the axis of the system. Therefore, even if no boiling occurs in the core, void production can take place in the adiabatic section.

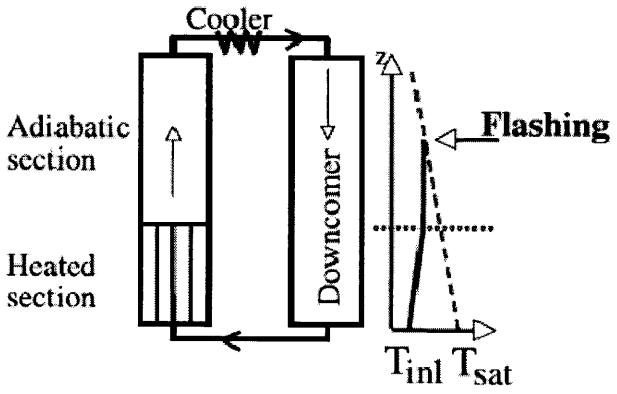

Figure 2.2: Flashing in the riser section (from [Manera and van der Hagen, 2003])

As a consequence of flashing in the adiabatic section, the natural-circulation flow rate will increase as a result of the increased buoyancy of the loop. Due to the increase in flow rate, the fluid temperature at the exit of the core will decrease, so that flashing in the riser will be suppressed. The flow rate will then decrease, and the temperature at the core exit will consequently increase, giving rise to a new flashing cycle. In this way, a self-sustained flow oscillation can take place.

A measure of the importance of flashing can be deduced by analyzing the behavior of the flashing number N_{flash} as a function of pressure. The flashing number is a function of the difference between the saturation water enthalpy at the inlet of the core and at the outlet of the riser.

$$N_{flash} = \frac{h_{f,C,i} - h_{f,R,e}}{h_{fg,C,i}} \frac{\rho_{f,C,i} - \rho_{g,C,i}}{\rho_{g,C,i}} \tag{2-1}$$

As can be seen in Figure 2.3, at pressures higher than 15 bar flashing becomes negligible.

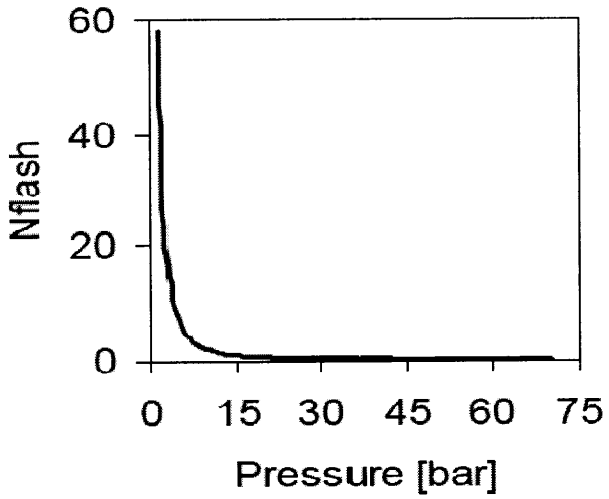

Figure 2.3: Flashing number as a function of pressure

At start-up conditions, both system pressure and heating power are low. The low system pressure implies large differences in saturation temperature between the inlet and the outlet of the adiabatic section. In ESBWR, this difference can exceed 10 K during startup, but is less than 1K at rated conditions.

For flashing type instabilities, creation and condensation of the steam is dramatic, thus the flow rate can change rapidly in intermittent and sinusoidal waves. Moreover, the flashing front (boiling boundary) may fall below the riser into the core, causing perturbations in reactivity. Thus, well-defined startup procedures are needed to avoid the instability region during the transition from single-phase to two-phase flow conditions.

Several startup procedures for different natural circulation designs have been proposed. The focus of the procedures is to avoid potential hazardous instabilities by maintaining single phase state of the natural circulation flow in the core when the system pressure is low. However, instability events caused by off-normal conditions still can not be ruled out. Therefore more extensive studies of the instability mechanism are still necessary.

2.3. Previous Work

2.3.1. Experimental work

For natural circulation systems, a series of stability experiments and tests have been conducted in laboratories and in a natural circulation driven BWR. A large volume of data has been accumulated. The flashing and flashing induced instabilities were observed in many experiments.

Most recently, Manera and van der Hagen [2003] investigated the dynamics of a flashing liquid with wire mesh sensors in the CIRCUS natural circulation loop in Delft, the Netherlands. Through visual observation, they found a complicated mode of flashing-induced instabilities. For small inlet subcooling, boiling was found to start at some point in the riser close to the top, and the flashing front traveled in both upward and downward directions. As the flow is accelerated, flashing is suppressed, but is repeated in the same way with a period of about 100 seconds. The phenomenon was explained as caused by the non-equilibrium character of flashing. They also suggested that decreasing compressible volume and increasing system pressure can stabilize the system. Furuya [2004, 2006] investigated the occurrence conditions and the mechanism of flashing-induced instability experimentally, at relatively low system pressure on another natural circulation loop, SIRIUS-N, which simulates a prototypical natural circulation BWR. Stability maps were obtained for a range of inlet subcooling and heat fluxes at system pressure of 0.1, 0.2, 0.35, and 0.5 MPa. Instability was observed to occur within a certain range of inlet subcooling. The size of the region of the instability in the N_{sub}-N_{pch} plane was reduced with increasing system pressure.

2.3.2. Analytical work

Computer simulation of the flashing induced instabilities is more limited when compared to experiments, partly due to difficulties in developing models that include the pressure dependence of water-steam thermodynamic properties. This coupling is the key for the simulation of flashing-induced instabilities under low pressure. Not many of the models that have been reported in literature, can deal with flashing-induced instabilities. Analyses can be divided into those carried out using system codes and those using reduced order models.

Inada et al. [2000] reported a simplified model based on HEM (Homogeneous Equilibrium Model) formulation, which includes flashing effect by assuming linear dependence of the saturation enthalpy on local pressure. But the single-phase natural circulation is not included (i.e. in their model the flow rate is different from zero only when steam is present in the system). They performed a frequency domain analysis. The stability boundaries follow the experimental results qualitatively, and better agreement was found under lower system pressure conditions. Van Bragt et al. [2002] extended Inada's model in the time domain by adding neutronics and heat transfer models. For simplification of the derivation of the reduced order model, linear variations of the steam quality and saturation enthalpy in the nodes were assumed. Again, inertial term in the single phase momentum equation and the time derivative term of saturation enthalpy in the energy equation were ignored.

Most recently, Askari [2008] developed a frequency domain code for BWR stability analysis, which considered the pressure dependent thermo property, and the effects of 3D power oscillation. However, the code was not applied to low pressure conditions, thus no flashing-induced instability was simulated, nor comparison with experimental results was shown.

Even state-of-the-art thermal-hydraulic system codes have often given unsatisfactory and sometimes even contradictory results. Paniagua et al. [1999] developed a modified version of RAMONA-4B that includes local pressure dependencies and an explicit numerical scheme to avoid numerical damping of the solution. Their simulations with the improved code show occurrence of geysering type instabilities, but the quantitative comparison with experimental results gives an under-prediction of the flow rate oscillation amplitude. They do not report about flashing-induced instabilities.

Cheung and Rao [2000] performed simulations of the start-up of the ESBWR with TRACG code, and claimed that no instabilities are found during the entire start-up procedure. Andersen et al. [1995] reproduced flashing-induced instabilities with TRACG and found excellent qualitative agreement with the different kinds of flow oscillations obtained experimentally at CRIEPI (Central Research Institute of Electric Power Industry, Japan). In the cases they examined, the amplitude of flow oscillations were always underestimated. No systematic quantitative comparison was reported.

Manera [2003b] simulated the experiments conducted in the CIRCUS facility which showed flashing, with a 4-equation drift flux code, FLOCAL. Generally good agreements of amplitudes, frequencies and stability maps were found.

2.4. Scope of Part I of This Work

The objective of this work is to assess the flashing-induced stability phenomena in NCBWRs, such as the ESBWR, during startup conditions. This work is applicable to regular BWRs since all BWRs can be partially operated with natural circulation during startup.

The system codes suffer from long calculation time, complicated data analyses, and embedded numerical damping problems. On the other hand, the available frequency domain codes do not allow for pressure dependent water properties and therefore are not fully reliable at low-pressure and low-power conditions. Thus, they cannot be used to

predict the behavior of natural-circulation–cooled BWRs during startup conditions and to simulate startup procedures with reasonable confidence. Therefore, a frequency domain code is developed to investigate flashing induced stability characteristics.

Zhao et al. [2005] at MIT developed a linear stability analysis code, STAB (originally called SAB), in frequency domain. In our work, the capability of the code will be extended to model the natural circulation loop and to capture the effects of flashing at low pressure conditions. The work of adding the capability to the original STAB code of modeling natural circulation loop, along with other modifications, and the stability analysis of NCBWR at high pressure conditions were completed in a previous work [Hu and Kazimi, 2007]. In this work, a BWR stability analysis code named FISTAB was developed to address the issue of flashing-induced instability.

The code is described in Chapter 3. Focus will be on the governing equations and constitutive correlations, the spatial discretization, the derivation of the perturbation equations, and the solutions schemes. After the functionality of the FISTAB code is confirmed by testing the experimental results at SIRIUS-N facility, the code is applied to ESBWR startup conditions in Chapter 4.

3. Development for Flashing-Induced Stability Analysis, FISTAB

In this chapter, a BWR stability analysis code named FISTAB (Flashing-Induced STability Analysis for BWR) was developed to address the issue of flashing-induced instability during reactor startup.

A thermal-hydraulic non-homogeneous equilibrium model (NHEM) based on the drift-flux approach, along with a lumped fuel dynamics model is incorporated in the work. The vapor generation rate is derived from the mixture energy conservation equation while considering the effect of flashing. An iterative solution scheme was developed to calculate the steady state under zero loop pressure drop boundary condition.

For linear stability analysis, a perturbation approach for calculating the pressure oscillation through flow channels was developed, along with an efficient scheme to solve the resulting perturbation equations. Then, the oscillation characteristic equation is constructed and solved by a global Newton method. From the dominant root of the characteristic equation, the decay ratio of a system is calculated and the stability characteristic is obtained.

The functionality of the FISTAB code was confirmed by testing the experimental results at SIRIUS-N facility in Japan. Both stationary and perturbation results agree well with the experimental results. In the next chapter, the code will be applied to the stability analysis of natural circulation BWRs under lower pressure startup conditions.

3.1. Model Description

Mathematical models used to describe the dynamic behavior of flashing phenomenon in a BWR system are discussed in this section. They include the fundamental two-phase flow equations, the fuel pin heat conduction equations, and the neutron point kinetics

equations. Also, the spatial discretization and steady state solution scheme are briefly explained.

3.1.1. Governing Equations

(1) Thermal Hydraulics Equations

Neglecting axial heat conduction, energy variation due to pressure changes and frictional dissipation, and shear forces due to velocity gradients in the fluid at open portions of the surface area, the mass, momentum, and energy balance equations for one-dimensional single-phase liquid flow in a coolant channel can be written as:

$$\frac{\partial \rho}{\partial t} + \frac{\partial (\rho u)}{\partial z} = 0 \tag{3-1}$$

$$\frac{\partial (\rho u)}{\partial t} + \frac{\partial (\rho u^2)}{\partial z} = -\frac{\partial p}{\partial z} - \rho g - \frac{f}{D_e}\frac{\rho u^2}{2} \tag{3-2}$$

$$\frac{\partial \rho h}{\partial t} + \frac{\partial (\rho u h)}{\partial z} = \frac{\partial p}{\partial t} + u\frac{\partial p}{\partial z} + \frac{P_h}{A_c} q''(z,t) \tag{3-3}$$

$$\rho = \rho(p,h) \tag{3-4}$$

where z is the axial coordinate in flow direction and ρ , u, p and h are the coolant density, velocity, pressure, and enthalpy, respectively. The variable q'' is the heat flux at the fuel cladding outer surface. The parameters D_e, P_h, and A_c respectively denote the hydraulic diameter, perimeter, and cross-sectional area of the coolant channel; f is the turbulent friction factor, g is the acceleration due to gravity.

The mass, momentum, and energy conservation equations are closed by the equation of state for water and steam. In this study, water/steam properties are determined using the NIST REFPROP software package [NIST, 2007]. As to the boundary conditions for these conservation equations, the constant inlet pressure, inlet enthalpy, and outlet pressure are used.

Similarly, the mass of the mixture and the vapor phase, momentum, and energy conservation

equations for one-dimensional two-phase mixture flow in the Non-Homogeneous Equilibrium Model (NHEM) can be written as:

$$\frac{\partial \rho_m}{\partial t} + \frac{\partial G_m}{\partial z} = 0 \tag{3-5}$$

$$\frac{\partial(\rho_g \alpha)}{\partial t} + \frac{\partial(\rho_g u_g \alpha)}{\partial z} = \Gamma_{tot} \tag{3-6}$$

$$\frac{\partial G_m}{\partial t} + \frac{\partial}{\partial z}\left(\frac{G_m^2}{\rho_m^+}\right) = -\frac{\partial p}{\partial z} - \rho_m g - \frac{f_m}{D_e}\frac{G_m{}^2}{2\rho_m} \tag{3-7}$$

$$\frac{\partial}{\partial t}\left(\rho_m h_m - p\right) + \frac{\partial}{\partial z}\left(G_m h_m^+\right) = \frac{G_m}{\rho_m}\frac{\partial p}{\partial z} + \frac{P_h}{A_c} q''(z,t) \tag{3-8}$$

In which,

$$\rho_m = (1-\alpha)\rho_f + \alpha\rho_g \tag{3-9}$$

$$\frac{G_m^2}{\rho_m^+} = (1-\alpha)\rho_f u_f^2 + \alpha\rho_g u_g^2 \tag{3-10}$$

$$h_m = \frac{(1-\alpha)\rho_f h_f + \alpha\rho_g h_g}{\rho_m} \tag{3-11}$$

$$h_m^+ = \frac{(1-\alpha)\rho_f u_f h_f + \alpha\rho_g u_g h_g}{G_m} \tag{3-12}$$

For simplicity, the drift flux model is chosen to model the non-homogeneous velocities of the liquid and steam. The drift flux model is based on correlations to compute the void fraction distribution at a plane and the slip in two-phase flow needed to obtain the relative velocity between the phases. Thus, the accuracy of the correlations has a decisive role in determining the correct transport of vapor along the system and, subsequently, in the prediction of the correct response of flow oscillations. The Maier and Coddington correlation, which employs a purely empirical approach to the evaluation of C_0 and V_{gj} of the drift-flux equation by [Zuber and Findlay, 1965], is used in this analysis. The description of the general drift-flux model can be found in Appendix A.

According to [Coddington and Macian, 2002], the void fraction predictions with Maier and Coddington correlation are very good, which is due to the fact that the correlation was obtained by a least squares fit to a wide range of the experimental data. The correlation is among the "best" void fraction correlations examined by Coddington and Macian [2002]. This correlation has the following form:

$$C_0 = c_1 p + c_2 \tag{3-13}$$

$$V_{gj}=(v_1 p^2+v_2 p+v_3)G+(v_4 p^2+v_5 p+v_6), \tag{3-14}$$

in which, c_1, c_2, v_1, v_2 v_3, v_4, v_5, v_6 are coefficients derived by matching experimental results.

Applying the drift-flux model to the vapor mass, mixture momentum and mixture energy conservation equations, some terms could be replaced, as shown below.

$$u_g=u_m+\frac{\rho_l}{\rho_m}V_{gj} \tag{3-15}$$

$$\frac{G^2}{\rho_m^+}=\frac{G^2}{\rho_m}+\frac{\alpha}{(1-\alpha)}\frac{\rho_f\rho_g}{\rho_m}V_{gj}^2 \tag{3-16}$$

$$G_m h_m^+ = G_m h_m + \frac{\alpha\rho_f\rho_g}{\rho_m}V_{gj}(h_g - h_l) \tag{3-17}$$

The void fraction may be also predicted from the drift flux model as:

$$\alpha = \frac{x}{C_o(x\frac{\rho_{fg}}{\rho_f}+\frac{\rho_g}{\rho_f})+\frac{\rho_g V_{gj}}{G}}. \tag{3-18}$$

Considering the flashing effects, the vapor generation rate Γ_{total} could be derived from the mixture energy conservation equation, as shown in Eq. (3-19). It is confirmed with the flashing model in [Yadigaroglu and Askari, 2005]. The details of the derivation can be found in Appendix A.

$$\Gamma_{total} = \frac{q_w'' P_h}{A_c h_{fg}} + \frac{1}{h_{fg}}\left(\frac{\partial p}{\partial t}(1-\alpha\rho_g h'_g-(1-\alpha)\rho_f h'_f)-\frac{\partial p}{\partial z}(\rho_g j_g h'_g+\rho_f j_f h'_f)\right) \tag{3-19}$$

In the above, the primes denote derivatives of the liquid and steam enthalpies with respect to the pressure along the saturation line.

Neglecting the pressure derivative term in the energy equation (3-8), $\frac{\partial p}{\partial t}+u_m \frac{\partial p}{\partial z}$, which are usually very small comparing to the heat addition, the two-phase fluid governing equations would be:

$$\frac{\partial \rho_m}{\partial t}+\frac{\partial G_m}{\partial z}=0 \tag{3-20}$$

$$\frac{\partial(\rho_g \alpha)}{\partial t}+\frac{\partial}{\partial z}(\alpha \rho_g u_m+\frac{\alpha \rho_f \rho_g}{\rho_m} V_{gj}^2)=\Gamma_{tot} \tag{3-21}$$

$$\rho_m \frac{\partial u_m}{\partial t}+\rho_m u_m \frac{\partial u_m}{\partial z}=-\frac{\partial P}{\partial z}-\rho_m g-\frac{f_m}{D_e}\frac{\rho_m u_m^2}{2}-\frac{\partial}{\partial z}\left(\frac{\alpha}{(1-\alpha)}\frac{\rho_f \rho_g}{\rho_m} V_{gj}^2\right) \tag{3-22}$$

$$\rho_m \frac{\partial h_m}{\partial t}+\rho_m u_m \frac{\partial h_m}{\partial z}=\frac{q'' P_h}{A_c}-\frac{\partial}{\partial z}\left(\alpha \frac{\rho_f \rho_g}{\rho_m} V_{gj} h_{fg}\right) \tag{3-23}$$

(2) Heat Conduction Equations

A lumped fuel dynamics model with the temperature distribution in the fuel pin developed at Brookheaven National Lab [Wulff, et al, 1984] was applied in the previous work [Hu and Kazimi, 2007]. The temperature profile in the fuel, gas gap and cladding are illustrated in Figure 3.1. The same model is applied in FISTAB.

Assuming a power polynomial for the temperature distribution in the fuel pellet, it can be given as:

$$T_f = T_o + b\xi + c\xi^2 \tag{3-24}$$

Where, $\xi \equiv \frac{r}{R_1}$, b and c are appropriate constants.

Assuming a linear temperature distribution in the thin cladding, the temperature can be given as:

$$T_c = T_2 + d\eta \tag{3-25}$$

Where, $\eta \equiv \dfrac{r - R_2}{R_3 - R_2}$ $(R_2 < r < R_3)$, and d is a constant.

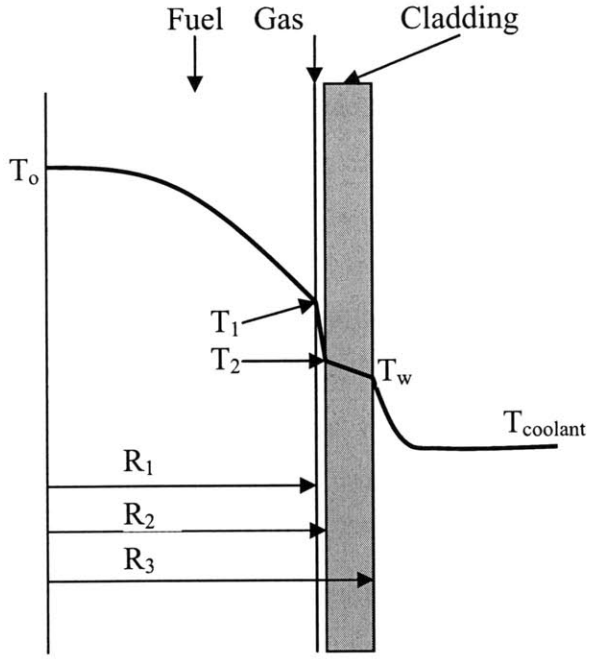

Figure 3.1: Fuel pin temperature distribution profile

Solving the Fourier heat transfer equation with the above temperature distributions, one obtains:

$$\frac{d\overline{T}}{dt} = \frac{2}{(R_3 - R_2)R_3} \frac{k_c}{(\rho c_p)_f} \frac{N_{Bi,c}}{[1 + (C_{gm} + F_{pr})N_{Bi,c}]} \times (T_{coolant} - \overline{T}) + (\frac{R_1}{R_3})^2 \frac{q'''_v}{(\rho c_p)_f} \tag{3-26}$$

Where,

$\overline{T}$: average temperature of the fuel;

$$N_{Bi,c} \equiv \frac{\overline{h}(R_3 - R_2)}{k_c} \tag{3-27}$$

$$C_{gm} \equiv (\frac{R_1}{R_3})^2 + [1 - (\frac{R_2}{R_3})^2][\frac{3(R_2 + R_3) - (R_3 - R_2)}{6(R_2 + R_3)}] \tag{3-28}$$

$$F_{pr} \equiv \frac{R_1^3}{(R_3 - R_2)R_3^2}(\frac{k_c}{4k_f} + \frac{k_c}{R_1}\frac{1}{h_{gap}}) \tag{3-29}$$

$\bar{h}$: the average heat transfer coefficient between the coolant and fuel rods;

h_{gap} : the gas conductance of the fuel gap.

From Figure 3.1, the fuel rod surface temperature, fuel pin average temperature and the coolant bulk temperature can be derived as:

$$T_w - T_\infty = \frac{\overline{T} - T_\infty}{[1 + (C_{gm} + F_{pr}) N_{Bi,c}]} \tag{3-30}$$

(3) Neutronic Equations

Currently, a neutron kinetics model is not included in the code. This is valid as long as there are no feedbacks from oscillations in the core void fraction during the startup transient. This assumption is applicable as the heating power is low enough that the boiling always starts in the long chimney region and the core is kept sub-cooled.

(4) Friction Factor and Heat transfer Correlations

In the single-phase liquid region, the friction factors can be obtained from the Blasius and McAdams relations [Todreas and Kazimi, 1990]:

For $\mathrm{Re} = 3 \times 10^4 - 10^6$:

$$f = 0.184 \mathrm{Re}^{-0.2} \tag{3-31}$$

For $\mathrm{Re} < 3 \times 10^4$:

$$f = 0.316 \mathrm{Re}^{-0.25} \tag{3-32}$$

In the two phase mixture region, the friction factor is assumed that in the HEM model for two-phase flow, which means the two-phase friction multiplier is equal to the HEM value of ρ_l / ρ_m. This assumption is valid when the pressure drop is dominated by the gravity head loss.

The pressure drop coefficients are used to account for the form pressure drop at the inlet orifice, tie-plates and spacers. For example, the pressure drop at the inlet orifice can be expressed as:

$$\Delta p_{ori} = k_{in} \frac{\rho_f u_{in}^2}{2} \tag{3-33}$$

Where k_{in} is the inlet orifice coefficient.

The Dittus-Boelter correlation is applied in this analysis to calculate the heat transfer coefficient in single-phase region, and the Chen's correlation in two-phase region. The details of Chen's correlations could be found in Appendix A. The Dittus-Boelter has the following form for the heated fluid:

$$Nu = 0.023\,\mathrm{Re}^{0.8}\,\mathrm{Pr}^{0.4}. \tag{3-34}$$

3.1.2. Spatial Discretization

The governing equations discussed in the previous section form a system of nonlinear equations. This system of nonlinear equations cannot be solved analytically, and thus needs to be solved numerically. In this section, the spatial discretization schemes employed to solve this system of equations are discussed.

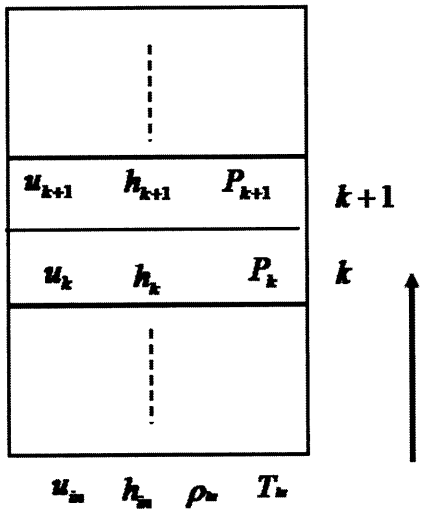

Figure 3.2: Channel spatial nodalization

To derive the finite difference approximations of the coolant conservation equations, the problem domain is divided into axial computational nodes as shown in Figure 3.2. In order to facilitate the frequency domain analysis, the finite difference equations are

derived in terms of the state variables at node surfaces such that the variables of only two meshes are coupled. Applying the upwind differencing scheme to the governing equations, the finite difference equations for coolant channel node k at single-phase liquid region are obtained as:

$$\frac{d\rho_{l,k}}{dt} = \frac{1}{\Delta z}\left(\rho_{l,k-1}u_{k-1} - \rho_{l,k}u_k\right) \tag{3-35}$$

$$\rho_{l,k}\frac{du_k}{dt} = \frac{\rho_{l,k}u_k}{\Delta z}\left(u_{k-1} - u_k\right) + \frac{1}{\Delta z}\left(P_{k-1} - P_k\right) - \rho_{l,k-1}g - \frac{f_{k-1}}{D_e}\frac{\rho_{l,k-1}u_{k-1}^{\ 2}}{2} \tag{3-36}$$

$$\rho_{l,k}\frac{dh_k}{dt} = \frac{\rho_{l,k}u_k}{\Delta z}\left(h_{k-1} - h_k\right) + \frac{P_h}{A_c}q_k'' \tag{3-37}$$

Similarly, the finite difference equations for the two-phase mixture conservation equations at each node can be derived.

3.1.3. Steady-State Solution Scheme

At steady state, all the heat generated in the fuel is deposited in the coolant, and hence the cladding-wall heat flux is directly related to the volumetric heat source. As a result, the fuel conduction equations are decoupled from the other equations. Therefore, the axial distributions of coolant and water rod temperature, pressure, density, and velocity can be determined for given inlet flow rate, inlet enthalpy (or temperature), and inlet pressure.

(1) Iteration scheme for pressure distribution in the single-phase liquid region

At steady state, the time derivatives in the conservation equations are equal to zero. Thus, the governing equations can be simplified as:

$$\frac{\partial(\rho u)}{\partial z} = 0, G \equiv const\ . \tag{3-38}$$

$$G\frac{\partial u}{\partial z} = -\frac{\partial P}{\partial z} - \rho g - \frac{f}{D_e}\frac{\rho u^2}{2} \tag{3-39}$$

$$G\frac{\partial h}{\partial z} = \frac{P_h}{A_c}q'' \tag{3-40}$$

The energy equation is decoupled from the mass and momentum equations. The liquid enthalpy distribution could be first calculated. However, as the liquid density is dependent on both the node pressure and enthalpy, $\rho = \rho(p,h)$, the distribution of velocity, density and pressure are coupled.

To solve the problem for a given inlet flow rate, the following iteration scheme is applied, as depicted by Figure 3.3.

(1) The liquid enthalpy distribution in the channel is first solved from the energy conservation equation.

(2) The pressure distribution $\tilde{P}(k)$ is first solved under the assumption of constant liquid density.

(3) Knowing the pressure distribution $\tilde{P}(k)$, the density distribution, along with the viscosity and friction factor at each node, can be obtained by using the NIST water/steam property package.

(4) Knowing the liquid density distribution, the velocity distribution can be calculated from the mass conservation equation.

(5) Then, the more realistic pressure distribution $P(k)$ can be calculated again from the momentum conservation equation with considering the density variation through the channel nodes.

(6) Comparing $P(k)$ and $\tilde{P}(k)$, if the difference between the two satisfy the convergence criteria, then the state parameters are solved at the steady state. If not, the new pressure distribution $\tilde{P}_{i+1}(k)$ is calculated from: $\tilde{P}_{i+1}(k) = (1-\theta)\tilde{P}_i(k) + \theta P_i(k)$ ($\theta = 0.9$ is currently used in the code). Go back to step (3).

Then, for each axial node, the fuel cladding and pin temperature can be determined by solving the fuel dynamics model with the boundary condition provided by the coolant temperature of each axial node.

In details, the enthalpy distribution could be calculated from the discretized equation:

$$\frac{G}{\Delta z}(h_{k-1} - h_k) + \frac{P_h}{A_c} q_k^{"} = 0 \tag{3-41}$$

The initial guess of pressure distribution is calculated from:

$$\frac{1}{\Delta z}(P_{k-1} - P_k) = \rho g + \frac{f}{D_e}\frac{\rho u^2}{2} \tag{3-42}$$

The velocity distribution is calculated from:

$$u_k = \frac{G}{\rho_k} \tag{3-43}$$

The more realistic pressure distribution is calculated from:

$$P_k = P_{k-1} - \left[G(u_k - u_{k-1}) + \rho_{l,k-1} g dz + \frac{f_{k-1}}{D_e}\frac{\rho_{l,k-1} u_{k-1}^2}{2} dz \right] \tag{3-44}$$

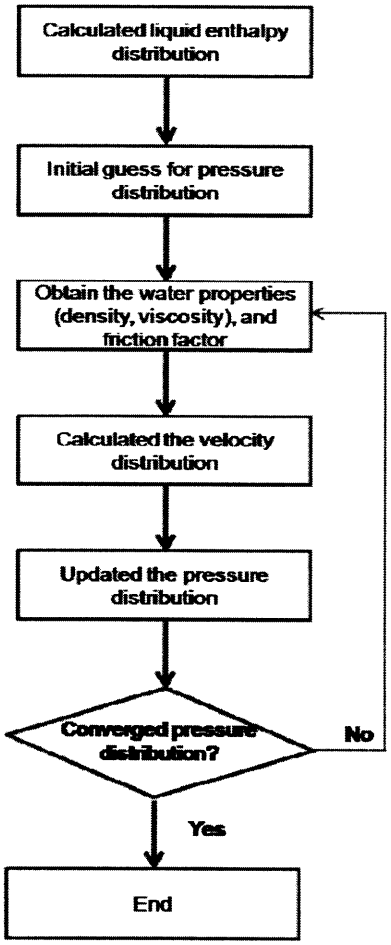

Figure 3.3: Iteration Scheme for Steady State Solution in single-phase liquid region

(2) Iteration scheme for pressure distribution in the two-phase mixture region

Similarly to the single-phase liquid region, at steady state the governing equations for the two-phase region can be simplified as:

$$\frac{\partial G_m}{\partial z} = 0 \tag{3-45}$$

$$\frac{\partial}{\partial z}(\alpha\rho_g u_m + \frac{\alpha\rho_f\rho_g}{\rho_m}V_{gj}) = \Gamma_{tot} = \frac{q''_w P_h}{A_c h_{fg}} - \frac{1}{h_{fg}}\frac{\partial p}{\partial z}(\rho_g j_g h'_g + \rho_f j_f h'_f) \tag{3-46}$$

$$\rho_m u_m \frac{\partial u_m}{\partial z} = -\frac{\partial P}{\partial z} - \rho_m g - \frac{f_m}{D_e}\frac{\rho_m u_m^2}{2} - \frac{\partial}{\partial z}\left(\frac{\alpha}{(1-\alpha)}\frac{\rho_f\rho_g}{\rho_m}V_{gj}^2\right) \tag{3-47}$$

$$\rho_m u_m \frac{\partial h_m}{\partial z} = \frac{q'' P_h}{A_c} - \frac{\partial}{\partial z}\left(\alpha\frac{\rho_f\rho_g}{\rho_m}V_{gj}h_{fg}\right) \tag{3-48}$$

The overall iteration scheme for the steady state solution in the two-phase region, depicted in Figure 3.4, is summarized below.

(1) The pressure distribution $\tilde{P}(k)$ is first solved under the assumption of constant water/steam properties at saturation conditions.

(2) Knowing the pressure distribution $\tilde{P}(k)$, the water/steam properties at saturation can be obtained by using the NIST water/steam property package.

(3) The distribution of mixture quality, void fraction, density, and velocity can be calculated from the conservation equations and constitutional correlations.

(4) Then, the more realistic pressure distribution $P(k)$ can be calculated again from the momentum conservation.

(5) Comparing $P(k)$ and $\tilde{P}(k)$, if the difference between the two satisfy the convergence criteria, then the state parameters are solved at the steady state. If not, the new pressure distribution $\tilde{P}_{i+1}(k)$ is calculated from: $\tilde{P}_{i+1}(k) = (1-\theta)\tilde{P}_i(k) + \theta P_i(k)$ ($\theta = 0.9$ is currently used in the code). Then, go back to step (2) and advance the calculation.

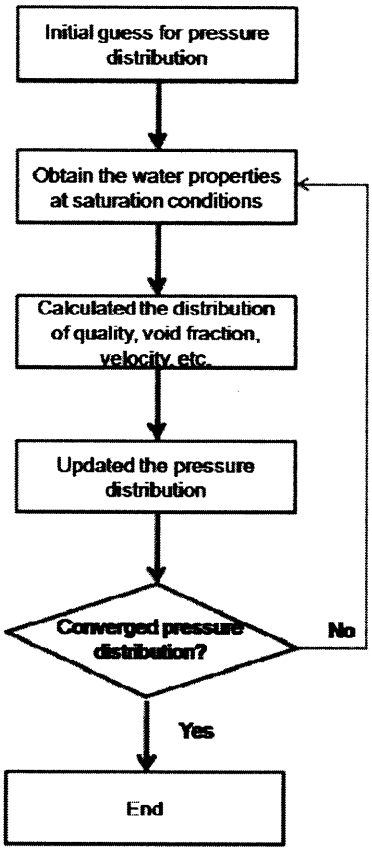

Figure 3.4: Overall Iteration Scheme for Steady State Solution in two-phase region

In the step of initial guess of pressure distribution, $\rho_f, \rho_g, h_f, h_g, v_{fg}, V_{gj}$ are independent on pressure. These values are used the same as those of the net vapor generation point, and $h_f^{'} = h_g^{'} = 0$. So, the governing equations could be simplified as [Saha, 1974],

$$\frac{\partial j}{\partial z} = \frac{\Gamma \Delta \rho}{\rho_g \rho_f} \tag{3-49}$$

$$\frac{\partial \rho_m}{\partial t} + C_k \frac{\partial \rho_m}{\partial z} + \rho_m \frac{\Gamma \Delta \rho}{\rho_g \rho_f} = 0 \tag{3-50}$$

$$\rho_m \left(\frac{\partial u_m}{\partial t} + u_m \frac{\partial u_m}{\partial z}\right) = -\frac{\partial P_m}{\partial z} - \frac{f_m}{2D_e} \rho_m u_m^2 - g\rho_m - \frac{\partial}{\partial z}\left[\frac{\rho_f - \rho_m}{\rho_m - \rho_g} \frac{\rho_f \rho_g}{\rho_m} V_{gj}^2\right] \tag{3-51}$$

$$\rho_m \left(\frac{\partial h_m}{\partial t} + u_m \frac{\partial h_m}{\partial z}\right) = \frac{q_w'' P_h}{A_c} + \frac{\partial P_m}{\partial t} - \frac{\partial}{\partial z}\left(\frac{\rho_f - \rho_m}{\rho_m} \frac{\rho_f \rho_g}{\Delta \rho} V_{gj} h_{fg}\right) \tag{3-52}$$

Where,

$$C_k = j + V_{gj} \tag{3-53}$$

$$u_m = j - (\frac{\rho_f}{\rho_m} - 1)V_{gj} \tag{3-54}$$

Thus, the initial pressure distribution can be calculated from the following steps.

a) Calculate *j(k)*.

$$j_k = j_{k-1} + \Gamma_{k-1}\frac{\rho_{fg}}{\rho_f \rho_g}dz \tag{3-55}$$

b) Calculate $\rho_{m,k}$

$$\rho_{m,k} = \rho_{m,k-1} - \left[\frac{\rho_{m,k-1}\Gamma_{k-1}}{(j_k + V_{gj})}\frac{\rho_{fg}}{\rho_f \rho_g}dz\right] \tag{3-56}$$

c) Calculate $u_{m,k}$ and α_k

$$u_{m,k} = \frac{G_m}{\rho_{m,k}} \tag{3-57}$$

$$\alpha_k = \frac{\rho_f - \rho_m}{\rho_{fg}} \tag{3-58}$$

d) From momentum equation calculated the initial guess of pressure distribution $\tilde{P}_0(k)$:

$$\tilde{P}_{0,k} = \tilde{P}_{0,k-1} - \left[G_m(u_{m,k} - u_{m,k-1}) + \rho_{m,k-1}gdz + \frac{f_{m,k-1}}{2D_e}\frac{G_m^2}{\rho_{m,k-1}}dz\right] - \left[\frac{\alpha_k}{1-\alpha_k}\frac{\rho_f \rho_g}{\rho_{m,k}}V_{gj}^2 - \frac{\alpha_{k-1}}{1-\alpha_{k-1}}\frac{\rho_f \rho_g}{\rho_{m,k-1}}V_{gj}^2\right] \tag{3-59}$$

Then, more realistic pressure distribution is calculated from the following steps.

e) Calculate the quality distribution *x(k)*.

$$x_k = x_{k-1} + \frac{\Gamma_{k-1}}{G_m}dz \tag{3-60}$$

f) Calculate the distribution of void fraction α_k

$$\alpha_k = \frac{x_k}{C_o(x_k\frac{\rho_{fg,k}}{\rho_{f,k}} + \frac{\rho_{g,k}}{\rho_{f,k}}) + \frac{\rho_{g,k}V_{gj,k}}{G_m}} \tag{3-61}$$

g) Calculated the distribution of mixture velocity and density, $u_{m,k}$ and $\rho_{m,k}$

$$u_{m,k} = \frac{G_m}{\rho_{m,k}} \tag{3-62}$$

$$\rho_{m,k} = (1-\alpha_k)\rho_{f,k} + \alpha_k \rho_{g,k} \tag{3-63}$$

h) Calculated a more realistic pressure distribution $P(k)$:

$$P_k = P_{k-1} - \left[G_m \left(u_{m,k} - u_{m,k-1}\right) + \rho_{m,k-1} g dz + \frac{f_{m,k-1}}{2D_e} \frac{G_m^2}{\rho_{m,k-1}} dz \right] - \left[\frac{\alpha_k}{1-\alpha_k} \frac{\rho_f \rho_g}{\rho_{m,k}} V_{gj}^2 - \frac{\alpha_{k-1}}{1-\alpha_{k-1}} \frac{\rho_f \rho_g}{\rho_{m,k-1}} V_{gj}^2 \right] \tag{3-64}$$

(3) Iteration scheme for channel inlet flow rate

The above calculation is given by knowing the inlet mass flow rate. However, under natural circulation conditions, the mass flow rate is decided by the flow conditions (no longer an input of the code). The magnitude of the natural circulation flow depends on the balance between the density driving head and the pressure losses through the circulation path. Figure 2.1 shows a schematic diagram of the flow path and pressure drops in the reactor. The driving head is proportional to the density difference between the fluid in the downcomer and the fluid inside the core shroud, or effectively proportional to the sum of the heights of the chimney/upper plenum and core. The major losses through the circulation path include those at the downcomer, core, chimney/upper plenum, and separators. The core flow rate varies proportionally to the power level, as the density difference changes with the power levels, and there is no active control of the core flow at any given power level. The driving head in the cold downcomer and the pressure losses in the heated side must be balanced.

$$\Delta P_{hot} = \Delta P_{cold} \tag{3-65}$$

where,

$$\Delta P_{cold} = \rho_f g (L_{core} + L_{chimney} + L_{upper-plenum} + L_{separator}) - f_{dc} \frac{L_{dc}}{De_{dc}} \frac{G_{dc}^2}{2\rho_f} \tag{3-66}$$

$$\Delta P_{hot} = \Delta P_{core} + \Delta P_{chimney} + \Delta P_{upper-plenum} + \Delta P_{separator} \tag{3-67}$$

$$\Delta P_{core} = \Delta P_{grav} + \Delta P_{acc} + \Delta P_{fric} + \Delta P_{inlet} + \Delta P_{grid} \tag{3-68}$$

$$\Delta P_{chimney} \text{ or } \Delta P_{upper-plenum} = \Delta P_{grav} + \Delta P_{acc} + \Delta P_{fric} \tag{3-69}$$

$$\Delta P_{separator} = K_{sp} \frac{G_{sp}^2}{2\rho_{sp}} + \rho_m g L_{separator} \tag{3-70}$$

Depending on the balance between the driving head and the pressure losses, the inlet mass flow rate could be calculated by iteration.

The iteration scheme for the steady state core inlet flow rate calculation is illustrated in Figure 3.5.

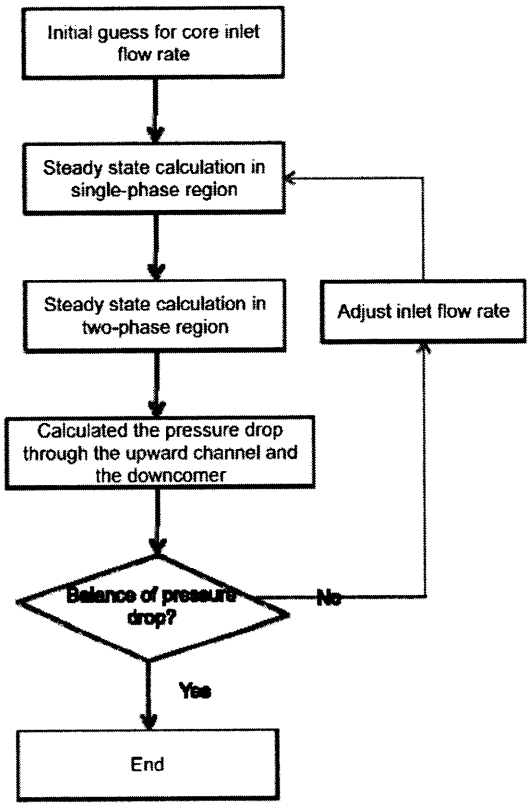

Figure 3.5: Overall Iteration Scheme for inlet flow rate at steady state

3.2. *Linear Stability Analysis in the Frequency Domain*

The frequency domain linear system of equations is obtained by linearizing the differential equations and the constitutive equations near the steady state solution, and

subsequently applying the Laplace transformation to the resulting linear equations. Each equation is linearized by representing each state variable with its steady state values and a deviation from steady state, expanding the nonlinear terms in a Taylor series, and neglecting the higher order terms. The frequency domain linear system of equations is obtained by applying the Laplace transformation to the resulting linear equations. The frequency responses of state variables to the external perturbations are determined by solving this linear system of perturbation equations. The determinant of the coefficient matrix of this system of equations is the system characteristic equation that determines the system stability.

The frequency responses of state variables and the system characteristic equation are discussed in the following sections along with the detailed derivation of the frequency domain linear system of equations.

3.2.1. Linear Perturbation Equations

(1) Single-phase liquid region perturbation equations

In order to derive the perturbation equations of the coolant conservation equations, each of density, velocity, enthalpy, pressure, and heat flux is represented by its steady state value and a deviation from steady state as:

$$\begin{aligned} \rho(t) &= \rho_0 + \delta\rho(t) \\ u(t) &= u_0 + \delta u(t) \\ h(t) &= h_0 + \delta h(t) \\ P(t) &= P_0 + \delta P(t) \\ q''(t) &= q''_0 + \delta q''(t) \end{aligned} \qquad \textbf{(3-71)}$$

By substituting these perturbation expressions into Equations (3-35) to (3-37), expanding nonlinear terms in Taylor series, neglecting higher order terms, and using upwind finite difference scheme, we obtain the linearized perturbation equations for the mass, energy, and momentum conservation equations in the single-phase region as

$$\frac{d\delta\rho_{l,k}}{dt} = \frac{1}{\epsilon z}\left(-\rho_{l,k}\delta u_k - u_k\delta\rho_{l,k} + \rho_{l,k-1}\delta u_{k-1} + u_{k-1}\delta\rho_{l,k-1}\right) \tag{3-72}$$

$$\rho_{l,k}\frac{d\delta h_k}{dt} = \frac{(h_{k-1}-h_k)}{\Delta z}\left(\rho_{l,k}\delta u_k + u_k\delta\rho_{l,k}\right) + \frac{\rho_{l,k}u_k}{\Delta z}\left(\delta h_k - \delta h_{k-1}\right) + \frac{P_h}{A_c}\delta q''_{k-1} \tag{3-73}$$

$$\rho_{l,k}\frac{d\delta u_k}{dt} = \frac{\rho_{l,k}u_k}{\epsilon z}\left(\delta u_{k-1} - \delta u_k\right) + \frac{(u_{k-1}-u_k)}{\epsilon z}\left(\rho_{l,k}\delta u_k + u_k\delta\rho_{l,k}\right) + \frac{1}{\epsilon z}\left(\delta P_{k-1} - \delta P_k\right) -$$
$$\delta\rho_{l,k-1}g - \left(\frac{\rho_{l,k-1}u_{k-1}^2}{2D_e}\delta f_{k-1} + \frac{f_{k-1}u_{k-1}^2}{2D_e}\delta\rho_{l,k-1} + \frac{f_{k-1}\rho_{l,k-1}u_{k-1}}{D_e}\delta u_{k-1}\right) \tag{3-74}$$

The oscillation of the friction factor can be calculated from the following correlation:

$$\frac{\delta f}{f} = \frac{\alpha}{\rho}\delta\rho + \frac{\alpha}{u}\delta u - \frac{\alpha\beta}{\mu}\delta h - \frac{\alpha\gamma}{\mu}\delta P \tag{3-75}$$

where α is the exponent of Reynolds number in Eq. (3-31) and (3-32), β is the partial derivative of the viscosity with respect to enthalpy at a constant pressure, and γ is the partial derivative of the viscosity with respect to pressure at a constant enthalpy. In general, γ is very small and could be neglected.

So the momentum perturbation equation changes to:

$$\rho_{l,k}\frac{d\delta u_k}{dt} = \frac{u_k(u_{k-1}-u_k)}{\epsilon z}\delta\rho_{l,k} + \frac{\rho_{l,k}(u_{k-1}-2u_k)}{\epsilon z}\delta u_k + \frac{1}{\epsilon z}\left(\delta P_{k-1} - \delta P_k\right) - \left(g + (1+\alpha)\frac{f_{k-1}u_{k-1}^2}{2D_e}\right)\delta\rho_{l,k-1}$$
$$\left(\frac{\rho_{l,k}u_k}{\Delta z} - (2+\alpha)\frac{f_{k-1}\rho_{l,k-1}u_{k-1}}{2D_e}\right)\delta u_{k-1} + \alpha\frac{f_{k-1}\rho_{l,k-1}u_{k-1}^2}{2D_e\mu_{k-1}}\delta h_{k-1} \tag{3-76}$$

The coolant density variation δρ can be obtained from a pressure-enthalpy state relation as:

$$\delta\rho = \frac{\delta\rho}{\delta h}\Big|_p\delta h + \frac{\delta\rho}{\delta P}\Big|_h\delta P = \xi\delta h + \eta\delta P \tag{3-77}$$

Eliminating $\delta\rho$ using this correlation, Equation (3-72), (3-73) and (3-74) can be reduced to:

$$\xi_k \frac{d\delta h_k}{dt} + \eta_k \frac{d\delta p_k}{dt} = \frac{1}{\Delta z}\left(-u_k \xi_k \delta h_k - u_k \eta_k \delta p_k - \rho_{l,k}\delta u_k + u_{k-1}\xi_{k-1}\delta h_k + u_{k-1}\eta_{k-1}\delta p_k + \rho_{l,k-1}\delta u_{k-1}\right) \tag{3-78}$$

$$\frac{d\delta h_k}{dt} = \frac{u_k}{\Delta z}\left[\frac{(h_{k-1}-h_k)\xi_k}{\rho_{l,k}} - 1\right]\delta h_k + \frac{u_k(h_{k-1}-h_k)\eta_k}{\rho_{l,k}\Delta z}\delta p_k + \frac{(h_{k-1}-h_k)\delta u_k}{\Delta z} + \frac{u_k}{\Delta z}\delta h_{k-1} + \frac{P_h}{\rho_{l,k}A_c}\delta q''_{k-1} \tag{3-79}$$

$$\frac{d\delta u_k}{dt} = \frac{u_k(u_{k-1}-u_k)\xi_k}{\rho_{l,k}\Delta z}\delta h_k + \frac{[u_k(u_{k-1}-u_k)\eta_k - 1]}{\rho_{l,k}\Delta z}\delta p_k + \frac{(u_{k-1}-2u_k)}{\Delta z}\delta u_k + b_{31}^k \delta h_{k-1} + b_{32}^k \delta p_{k-1} + b_{33}^k \delta u_{k-1} \tag{3-80}$$

Where,

$$b_{31}^k = \frac{1}{\rho_{l,k}}\left[\frac{\rho_{l,k-1}u_{k-1}^2}{2D_e}\left(\frac{\alpha\rho_{l,k-1}\beta_{k-1}}{\mu_{k-1}} - (1+\alpha)\xi_{k-1}\right) - g\xi_{k-1}\right]$$

$$b_{32}^k = \frac{1}{\rho_{l,k}}\left[\frac{1}{\Delta z} - \frac{\rho_{l,k-1}u_{k-1}^2}{2D_e}(1+\alpha)\eta_{k-1} - g\eta_{k-1}\right]$$

$$b_{33}^k = \frac{u_k}{\Delta z} - (2+\alpha)\frac{f_{k-1}\rho_{l,k-1}u_{k-1}}{2D_e\rho_{l,k}}$$

Substituting Eq. (3-79) into (3-78), the time derivative of pressure perturbation is obtained as:

$$\begin{aligned}\frac{d\delta p_k}{dt} = &-\frac{u_k}{\Delta z}\frac{(h_{k-1}-h_k)\xi_k^2}{\rho_{l,k}\eta_k}\delta h_k - \frac{u_k}{\rho_{l,k}\Delta z}(\rho_{l,k} + (h_{k-1}-h_k)\xi_k)\delta p_k - \frac{(\rho_k + (h_{k-1}-h_k)\xi_k)}{\Delta z\eta_k}\delta u_k \\ &+ \frac{u_{k-1}\xi_{k-1} - u_k\xi_k}{\Delta z\eta_k}\delta h_{k-1} + \frac{u_{k-1}\eta_{k-1}}{\Delta z\eta_k}\delta p_{k-1} + \frac{\rho_{k-1}}{\Delta z\eta_k}\delta u_{k-1} - \frac{P_h\xi_k}{\rho_{l,k}A_c\eta_k}\delta q''_{k-1}\end{aligned} \tag{3-81}$$

Equations (3-79), (3-80) and (3-81) form a system of linear equations for the perturbations of enthalpy, pressure, and velocity. This system of equation can be written in a matrix form as:

$$\frac{d\delta X_k}{dt} = A_k \delta X_k + B_k \delta X_{k-1} + C_k \delta q''_{k-1}, \tag{3-82}$$

where δX_k is the vector representing the enthalpy, pressure, and velocity perturbations in the node k and is defined as: $\delta X_k(t) = \left[\delta h_k(t), \delta P_k(t), \delta u_k(t)\right]^T$.

The 3×3 matrices A_k, B_k, and 3×1 vector C_k are given by:

$$A_k = \begin{bmatrix} \frac{u_k}{\Delta z}\left[\frac{(h_{k-1}-h_k)\xi_k}{\rho_{l,k}}-1\right] & \frac{u_k(h_{k-1}-h_k)\eta_k}{\rho_{l,k}\Delta z} & \frac{(h_{k-1}-h_k)}{\Delta z} \\ -\frac{u_k}{\Delta z}\frac{(h_{k-1}-h_k)\xi_k^2}{\rho_{l,k}\eta_k} & -\frac{u_k}{\rho_{l,k}\Delta z}(\rho_{l,k}+(h_{k-1}-h_k)\xi_k) & -\frac{(\rho_k+(h_{k-1}-h_k)\xi_k)}{\Delta z\eta_k} \\ \frac{u_k(u_{k-1}-u_k)\xi_k}{\rho_{l,k}\Delta z} & \frac{[u_k(u_{k-1}-u_k)\eta_k-1]}{\rho_{l,k}\Delta z} & \frac{(u_{k-1}-2u_k)}{\Delta z} \end{bmatrix} \quad \textbf{(3-83)}$$

$$B_k = \begin{bmatrix} \frac{u_k}{\Delta z} & 0 & 0 \\ \frac{u_{k-1}\xi_{k-1}-u_k\xi_k}{\Delta z\eta_k} & \frac{u_{k-1}\eta_{k-1}}{\Delta z\eta_k} & \frac{\rho_{k-1}}{\Delta z\eta_k}\delta u_{k-1} \\ b_{31}^k & b_{32}^k & b_{33}^k \end{bmatrix} \quad \textbf{(3-84)}$$

$$C_k = \begin{bmatrix} \frac{P_h}{\rho_{l,k}A_c} & -\frac{P_h\xi_k}{\rho_{l,k}A_c\eta_k} & 0 \end{bmatrix}^T \quad \textbf{(3-85)}$$

Note that all the variables in these matrices can be calculated in the steady state solutions for coolant channel nodes.

(2) Two-phase region perturbation equations

Similarly to the single-phase liquid region, by substituting the perturbation into Equations (3-5) to (3-8), neglecting higher order terms, we obtain the linearized perturbation equations for the mass, energy, and momentum conservation equations in the two-phase region as:

$$\frac{\partial\delta\rho_m}{\partial t}+\frac{\partial\delta(\rho_m u_m)}{\partial z}=0 \quad \textbf{(3-86)}$$

$$\frac{\partial\delta(\rho_g\alpha)}{\partial t}+\frac{\partial}{\partial z}\delta(\alpha\rho_g u_m+\frac{\alpha\rho_f\rho_g}{\rho_m}V_{gj})=\delta\Gamma_{tot} \quad \textbf{(3-87)}$$

$$\begin{aligned}\rho_m\frac{\partial\delta(u_m)}{\partial t}+\rho_m u_m\frac{\partial\delta(u_m)}{\partial z}+\frac{\partial u_m}{\partial z}(u_m\delta\rho_m+\rho_m\delta u_m)=&-\frac{\partial\delta p}{\partial z}-g\delta\rho_m \\ &-\delta(\frac{f_m}{D_e}\frac{\rho_m u_m^2}{2})-\frac{\partial}{\partial z}\delta\left(\frac{\alpha}{(1-\alpha)}\frac{\rho_f\rho_g}{\rho_m}V_{gj}^2\right)\end{aligned} \quad \textbf{(3-88)}$$

In which,

$$\delta\rho_m = \delta\rho_f - \delta(\alpha\rho_{fg}) = \frac{\partial\rho_f}{\partial p}\delta p - \alpha\frac{\partial\rho_{fg}}{\partial p}\delta p - \rho_{fg}\delta\alpha \tag{3-89}$$

$$\frac{\partial\delta(\rho_g\alpha)}{\partial t} = \alpha\frac{\partial}{\partial t}(\frac{\partial\rho_g}{\partial p}\delta p) + \rho_g\frac{\partial\delta\alpha}{\partial t} \tag{3-90}$$

$$\begin{aligned}\frac{\partial\delta(\alpha\rho_g u_m + \frac{\alpha\rho_f\rho_g}{\rho_m}V_{gj})}{\partial z} &= \frac{\partial}{\partial z}\{(u_m + \frac{\rho_f}{\rho_m}V_{gj})\rho_g\delta\alpha + (u_m + \frac{\rho_f}{\rho_m}V_{gj})\alpha\frac{\partial\rho_g}{\partial p}\delta p \\ &\quad + \alpha\rho_g(\delta u_m + \frac{V_{gj}}{\rho_m}\delta\rho_f + \frac{\rho_f}{\rho_m}\delta V_{gj} - \frac{\rho_f}{\rho_m^2}V_{gj}\delta\rho_m)\}\end{aligned} \tag{3-91}$$

$$\begin{aligned}\delta\Gamma_{total} &= -\frac{\delta h_{fg}}{h_{fg}^2}\left[\frac{q''P_h}{A_c} - \frac{\partial p}{\partial z}(\rho_g j_g h'_g + \rho_f j_f h'_f)\right] + \frac{1}{h_{fg}}\frac{P_h}{A_c}\delta q'' \\ &+ \frac{1}{h_{fg}}(1-\alpha\rho_g h'_g - (1-\alpha)\rho_f h'_f)\frac{\partial\delta p}{\partial t} - \frac{1}{h_{fg}}(\rho_g j_g h'_g + \rho_f j_f h'_f)\frac{\partial\delta p}{\partial z} \\ &- \frac{1}{h_{fg}}\frac{\partial p}{\partial z}(j_g h'_g\delta\rho_g + \rho_g h'_g\delta j_g + \rho_g j_g\delta h'_g + j_f h'_f\delta\rho_f + \rho_f h'_f\delta j_f + \rho_f j_f\delta h'_f)\end{aligned} \tag{3-92}$$

Where,

$$j_g = \alpha u_g = \alpha(u_m + \frac{\rho_f}{\rho_m}V_{gj}) \tag{3-93}$$

$$j_f = (1-\alpha)u_f = (1-\alpha)u_m - \frac{\alpha\rho_g}{\rho_m}V_{gj} \tag{3-94}$$

$$\delta j_g = u_m\delta\alpha + \alpha\delta u_m + \frac{\alpha\rho_f}{\rho_m}\delta V_{gj} + \frac{\alpha V_{gj}}{\rho_m}\delta\rho_f + \frac{\rho_f}{\rho_m}V_{gj}\delta\alpha - \frac{\alpha\rho_f V_{gj}}{\rho_m^2}\delta\rho_m \tag{3-95}$$

$$\delta j_f = -u_m\delta\alpha + (1-\alpha)\delta u_m - \frac{\alpha\rho_g}{\rho_m}\delta V_{gj} - \frac{\alpha V_{gj}}{\rho_m}\delta\rho_g - \frac{\rho_g}{\rho_m}V_{gj}\delta\alpha + \frac{\alpha\rho_g V_{gj}}{\rho_m^2}\delta\rho_m \tag{3-96}$$

Also,

$$\delta(\frac{f_m}{D_e}\frac{\rho_m u_m^2}{2}) = \frac{\rho_m u_m^2}{2D_e}\delta f_m + \frac{f_m u_m^2}{2D_e}\delta\rho_m + \frac{f_m\rho_m u_m}{D_e}\delta u_m \tag{3-97}$$

$$\delta\left(\frac{\alpha}{(1-\alpha)}\frac{\rho_f\rho_g}{\rho_m}V_{gj}^2\right)=\frac{\alpha}{(1-\alpha)}\frac{\rho_f\rho_g}{\rho_m}2V_{gj}\delta V_{gj}+\frac{\alpha}{(1-\alpha)}\frac{\rho_g}{\rho_m}V_{gj}^2\delta\rho_f+\frac{\alpha}{(1-\alpha)}\frac{\rho_f}{\rho_m}V_{gj}^2\delta\rho_g$$
$$-\frac{\alpha}{(1-\alpha)}\frac{\rho_f\rho_g}{\rho_m^2}V_{gj}^2\delta\rho_m+\frac{\rho_f\rho_g}{\rho_m}V_{gj}^2\frac{\delta\alpha}{(1-\alpha)^2} \quad \textbf{(3-98)}$$

Applying the upwind finite difference scheme, after some derivations, the perturbation Equations (3-86), (3-87) and (3-88) could form a system of linear equations for the perturbations of mixture velocity, pressure, and void fraction. This system of equations can be written in a matrix form as:

$$E_k\frac{d\delta X_k}{dt}=A_k\delta X_k+B_k\delta X_{k-1}+C_k\delta q''_{k-1}+D_k \quad \textbf{(3-99)}$$

Where δX_k is the vector representing the mixture velocity, pressure, and void fraction perturbations in the node k and is defined as $\delta X_k(t)=\left[\delta u_{m,k}(t),\delta P_k(t),\delta\alpha_k(t)\right]^T$.

The 3 × 3 matricesE_k, A_k and B_k and 3 × 1 vector C_k and D_k are given by:

$$E_k=\begin{bmatrix}0 & C_{\rho,k} & -\rho_{fg,k}\\ 0 & \alpha_k\eta_{fg,k}-\frac{1}{h_{fg,k}}(1-\alpha_k\rho_{g,k}h'_{g,k}-(1-\alpha_k)\rho_{f,k}h'_{f,k}) & \rho_{g,k}\\ \rho_{m,k} & 0 & 0\end{bmatrix} \quad \textbf{(3-100)}$$

$$A_k=\begin{bmatrix}a_{11}^k & a_{12}^k & a_{13}^k\\ a_{21}^k & a_{22}^k & a_{23}^k\\ a_{31}^k & a_{32}^k & a_{33}^k\end{bmatrix} \quad \textbf{(3-101)}$$

$$B_k=\begin{bmatrix}b_{11}^k & b_{12}^k & b_{13}^k\\ b_{21}^k & b_{22}^k & b_{23}^k\\ b_{31}^k & b_{32}^k & b_{33}^k\end{bmatrix} \quad \textbf{(3-102)}$$

$$C_k=\begin{bmatrix}0 & \frac{P_h}{A_c h_{fg,k}} & 0\end{bmatrix}^T \quad \textbf{(3-103)}$$

$$D_k=\begin{bmatrix}0 & 0 & \frac{\rho_{m,k-1}u_{m,k-1}^2}{2D_e}\delta f_{m,k-1}\end{bmatrix}^T \quad \textbf{(3-104)}$$

where

$$a_{11}^{k} = -\frac{\rho_{m,k}}{\Delta z}$$

$$a_{12}^{k} = -\frac{u_{m,k}}{\Delta z} C_{\rho,k}$$

$$a_{13}^{k} = \frac{u_{m,k}}{\Delta z} \rho_{fg,k}$$

$$a_{21}^{k} = -\left[\frac{\alpha_k \rho_{g,k}}{\Delta z} + \frac{(p_k - p_{k-1})}{h_{fg,k} \Delta z} (\alpha_k \rho_{g,k} h'_{g,k} + (1-\alpha_k) \rho_{f,k} h'_{f,k}) \right]$$

$$\begin{aligned} a_{22}^{k} = & -\frac{1}{\Delta z}\left[\alpha_k u_{g,k} \eta_{g,k} + \frac{\alpha_k \rho_{g,k}}{\rho_{m,k}} (V_{gj,k} \eta_{f,k} + \rho_{f,k} \frac{\partial V_{gj,k}}{\partial p} - \frac{\rho_{f,k} V_{gj,k}}{\rho_{m,k}} C_{\rho,k}) \right] \\ & - \frac{h'_{fg,k}}{h_{fg,k}^2}\left[\frac{q''_k P_h}{A_c} - \frac{(p_k - p_{k-1})}{\Delta z} (\rho_{g,k} j_{g,k} h'_{g,k} + \rho_{f,k} j_{f,k} h'_{f,k}) \right] \\ & - \frac{1}{h_{fg,k} \Delta z} (\rho_{g,k} j_{g,k} h'_{g,k} + \rho_{f,k} j_{f,k} h'_{f,k}) \\ & - \frac{(p_k - p_{k-1})}{h_{fg,k} \Delta z}\left[\frac{\alpha_k \rho_{g,k} h'_{g,k}}{\rho_{m,k}} (V_{gj,k} \eta_{f,k} + \rho_{f,k} \frac{\partial V_{gj,k}}{\partial p} - \frac{\rho_{f,k} V_{gj,k}}{\rho_{m,k}} C_{\rho,k}) \right. \\ & + j_{g,k} h'_{g,k} \eta_{g,k} + \rho_{g,k} j_{g,k} h''_{g,k} + j_{f,k} h'_{f,k} \eta_{f,k} + \rho_{f,k} j_{f,k} h''_{f,k} \\ & \left. + \frac{\alpha_k \rho_{f,k} h'_{f,k}}{\rho_{m,k}} (\frac{\rho_{g,k} V_{gj,k}}{\rho_{m,k}} C_{\rho,k} - V_{gj,k} \eta_{g,k} + \rho_{g,k} \frac{\partial V_{gj,k}}{\partial p}) \right] \end{aligned}$$

$$\begin{aligned} a_{23}^{k} = & -\frac{1}{\Delta z}\left[\rho_k u_{g,k} + \frac{\alpha_k \rho_{g,k} \rho_{f,k} V_{gj,k} \rho_{fg,k}}{\rho_{m,k}^2} \right] \\ & - \frac{(p_k - p_{k-1})}{h_{fg,k} \Delta z}\left[\rho_{g,k} h'_{g,k} (C_{u,k} + \frac{\alpha_k \rho_{f,k} V_{gj,k} \rho_{fg,k}}{\rho_{m,k}^2}) - \rho_{f,k} h'_{f,k} (C_{u,k} + \frac{\alpha_k \rho_{g,k} V_{gj,k} \rho_{fg,k}}{\rho_{m,k}^2}) \right] \end{aligned}$$

$$a_{31}^{k} = \frac{\rho_{m,k}\left(u_{m,k-1} - 2u_{m,k}\right)}{\Delta z}$$

$$\begin{aligned} a_{32}^{k} = & \frac{u_{m,k}\left(u_{m,k-1} - u_{m,k}\right)}{\Delta z} C_{\rho,k} - \frac{1}{\Delta z} \\ & - \frac{1}{\Delta z} \frac{\alpha_k V_{gj,k}}{(1-\alpha_k)\rho_{m,k}}\left[2\rho_{g,k} \rho_{f,k} \frac{\partial V_{gj,k}}{\partial p} + \rho_{g,k} V_{gj,k} \eta_{f,k} + \rho_{f,k} V_{gj,k} \eta_{g,k} - \frac{\rho_{g,k} \rho_{f,k} V_{gj,k}}{\rho_{m,k}} C_{\rho,k} \right] \end{aligned}$$

$$a_{33}^{k} = -\frac{u_{m,k}\left(u_{m,k-1} - u_{m,k}\right)}{\Delta z} \rho_{fg,k} - \frac{1}{\Delta z} \frac{\rho_{g,k} \rho_{f,k} V_{gj,k}^2}{(1-\alpha_k)\rho_{m,k}}\left(\frac{\alpha_k \rho_{fg,k}}{\rho_{m,k}} + \frac{1}{(1-\alpha_k)} \right)$$

$$b_{11}^{k} = -\frac{\rho_{m,k-1}}{\Delta z}$$

$$b_{12}^{k} = -\frac{u_{m,k-1}}{\Delta z} C_{\rho,k-1}$$

$$b_{13}^{k} = \frac{u_{m,k-1}}{\Delta z} \rho_{fg,k-1}$$

$$b_{21}^{k} = \alpha_{k-1} \rho_{g,k-1}$$

$$b_{22}^{k} = -\frac{1}{\Delta z}\left[\alpha_{k-1} u_{g,k-1} \eta_{g,k-1} + \frac{\alpha_{k-1}\rho_{g,k-1}}{\rho_{m,k-1}} (V_{gj,k-1}\eta_{f,k-1} + \rho_{f,k-1}\frac{\partial V_{gj,k-1}}{\partial p} - \frac{\rho_{f,k-1} V_{gj,k-1}}{\rho_{m,k-1}} C_{\rho,k-1}) \right]$$
$$- \frac{1}{h_{fg,k}\Delta z}(\rho_{g,k} j_{g,k} h'_{g,k} + \rho_{f,k} j_{f,k} h'_{f,k})$$

$$b_{23}^{k} = C_{u,k-1}\rho_{g,k-1} + \frac{\alpha_{k-1}\rho_{f,k-1}\rho_{g,k-1} V_{gj,k-1}\rho_{fg,k-1}}{\rho_{m,k-1}^{2}}$$

$$b_{31}^{k} = \frac{\rho_{m,k} u_{m,k}}{\Delta z} - \frac{f_{m,k-1}\rho_{m,k-1} u_{m,k-1}}{D_e}$$

$$b_{32}^{k} = \frac{1}{\Delta z} - (g + \frac{f_{m,k-1} u_{m,k-1}^{2}}{2D_e}) C_{\rho,k-1}$$
$$+ \frac{1}{\Delta z}\frac{\alpha_{k-1} V_{gj,k-1}}{(1-\alpha_{k-1})\rho_{m,k-1}}\left(2\rho_{g,k-1}\rho_{f,k-1}\frac{\partial V_{gj,k-1}}{\partial p} + \rho_{g,k-1} V_{gj,k-1}\eta_{f,k-1} \right.$$
$$\left. + \rho_{f,k-1} V_{gj,k-1}\eta_{g,k-1} - \frac{\rho_{g,k-1}\rho_{f,k-1} V_{gj,k-1}}{\rho_{m,k-1}} C_{\rho,k-1} \right)$$

$$b_{33}^{k} = (g + \frac{f_{m,k-1} u_{m,k-1}^{2}}{2D_e})\rho_{fg,k-1} + \frac{1}{\Delta z}\frac{\rho_{g,k-1}\rho_{f,k-1} V_{gj,k-1}^{2}}{(1-\alpha_{k-1})\rho_{m,k-1}}\left(\frac{\alpha_{k-1}\rho_{fg,k-1}}{\rho_{m,k-1}} + \frac{1}{(1-\alpha_{k-1})} \right)$$

Where,

$$C_{\rho,k} = \eta_{f,k} - \alpha_k \eta_{fg,k}$$

$$C_{u,k} = u_{m,k} + \frac{\rho_{f,k}}{\rho_{m,k}} V_{gj,k} = u_{g,k}$$

$$\eta_{f,k} = (\frac{\partial \rho_f}{\partial p}\Big|_h)_k$$

$$\eta_{g,k} = (\frac{\partial \rho_g}{\partial p}|_h)_k$$

(3) Fuel dynamics perturbation equations

The fuel dynamics model is coupled to the coolant thermal hydraulics model through the dynamics of the fluctuation of the fuel rods surface heat flux.

Perturbation, linearization of Equation (3-26) and combining it with Equation (3-30), one obtains:

$$\frac{d\delta\bar{T}_{pin}}{dt} = (\frac{R_1}{R_3})^2 \frac{\delta q_v'''}{(\rho c_p)_f} - \frac{2}{R_3} \frac{\delta q_w''}{(\rho c_p)_f} \tag{3-105}$$

Perturbation, linearization of Equation (3-30), and its combination with $q_w'' = \bar{h}(T_w - T_\infty)$ yields:

$$\frac{\delta q_w''}{\bar{h}} - \frac{q_w''}{\bar{h}} \frac{\delta\bar{h}}{\bar{h}} + \frac{(C_{gm} + F_{pr})(R_3 - R_2)}{k_c} \delta q_w'' = \delta\bar{T}_{pin} - \delta T_\infty \tag{3-106}$$

Perturbation and linearization of the Dittus-Boelter correlation, i.e., Equation (3-34) yields:

$$\frac{\delta\bar{h}}{\bar{h}} = 0.8 \frac{\delta\rho_\infty u_\infty + \rho_\infty \delta u_\infty}{\rho_\infty u_\infty} \tag{3-107}$$

Combining the above equations, after some rearrangement, one obtains:

$$[\frac{1}{\bar{h}} + \frac{2}{sR_3(\rho c_p)_f} + \frac{(C_{gm} + F_{pr})(R_3 - R_2)}{k_c}]\delta q_w'' = \frac{q_w''}{\bar{h}} \frac{\delta\bar{h}}{\bar{h}} + (\frac{R_1}{R_3})^2 \frac{\delta q_v'''}{(\rho c_p)_f} - \frac{\delta h_\infty}{c_{p,\infty}} \tag{3-108}$$

Set $\delta q_v''' = 0$ in Eq. (3-108), we can find the fluctuation of the fuel rods surface heat flux as a function of coolant density, velocity and enthalpy oscillations.

3.2.2. Frequency Domain Linear Equations

The frequency domain linear equations are obtained by applying the Laplace transformation to the linearized perturbation equations discussed above. For each axial node k, the coolant perturbation equations are obtained by the Laplace transformation of Eq. (3-82) or Eq. (3-99) as:

$$s\delta X_k = A_k \delta X_k + B_k \delta X_{k-1} + C_k \delta q''_{k-1} \quad \textbf{(3-109)}$$

$$\text{Or } sE_k \delta X_k = A_k \delta X_k + B_k \delta X_{k-1} + C_k \delta q''_{k-1} + D_k \quad \textbf{(3-110)}$$

Given the constant inlet boundary conditions of pressure and enthalpy, the perturbation equations can be solved by marching the node from the inlet of the flow channel. The perturbation vector δX_k could be solved as:

$$\delta X_k = (sI - A_k)^{-1} B_k \delta X_{k-1} + (sI - A_k)^{-1} C_k \delta q''_{k-1} \quad \textbf{(3-111)}$$

$$\delta X_k = (sE_k - A_k)^{-1} B_k \delta X_{k-1} + (sE_k - A_k)^{-1} C_k \delta q''_{k-1} + (sE_k - A_k)^{-1} D_k \quad \textbf{(3-112)}$$

where s is the complex variable of Laplace transform and I is the identity matrix.

3.2.3. Feedback and System Characteristic Equation

The closed loop transfer functions and the system characteristic equations are derived by taking into account the hydraulic and reactivity feedbacks. The hydraulic feedback is determined by the boundary conditions imposed on the thermal-hydraulics equations. The reactivity feedback is neglected at this time, as discussed in Section 3.1.1. The hydraulic feedback is dependent on the type of oscillations. For single-channel type of density wave oscillations, the characteristic equation is derived from the boundary conditions of constant pressure drop across the channel.

For a two-region flow channel model, the feedback mechanism can be illustrated by Figure 3.6. If $\Gamma_1(s)$ and $\Gamma_2(s)$ are the transfer functions between an inlet flow oscillation and the pressure drop oscillations corresponding to regions 1 and 2 respectively (region 1 represents single-phase liquid region, incompressible part; while region 2 represents the

two-phase region, compressible part), the system characteristic equation can be determined as follows: [Hu and Kazimi, 2007]

If δu_{ext} is the external disturbance of the inlet flow velocity and δu_F is the feedback flow velocity, the total disturbance of the inlet flow velocity is:

$$\delta u_t = \delta u_{ext} + \delta u_F \tag{3-113}$$

Recognizing that

$$\delta \Delta p_t = \delta \Delta p_1 + \delta \Delta p_2 = 0 \tag{3-114}$$

One can obtain the following relationship between δu_t and δu_{ext}:

$$\delta u_t = \frac{\Gamma_1(s)}{\Gamma_1(s)+\Gamma_2(s)} \delta u_{ext} \tag{3-115}$$

Set $\Pi(s) = \Gamma_1(s) + \Gamma_2(s)$, the system characteristic equation is:

$$\Pi(s) = 0 \tag{3-116}$$

where $\Pi(s)$ is the transfer function between an inlet flow oscillation and the channel pressure drop oscillations. For a stable system, all the eigenvalues of $\Pi(s)$ must have negative real parts.

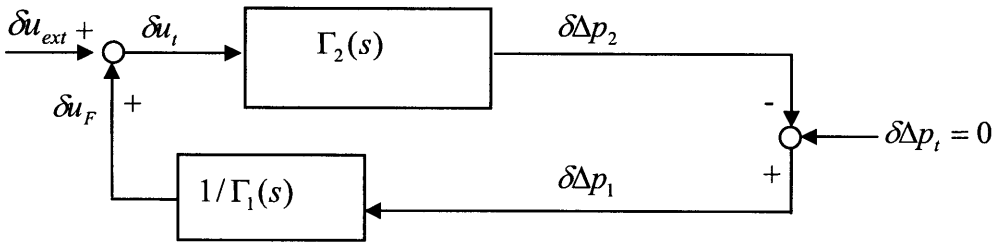

Figure 3.6: Block diagram of single-channel flow feedback mechanism

The transient response is determined by the roots of the characteristic equation. After a sufficient time, it is dominated by the root that has the largest real part. If the real part of this dominant root is positive, the response to a perturbation would grow indefinitely and

the linear system is unstable. If it is negative, the system is asymptotically stable. Oscillations introduced in the system are damped to the extent determined by the decay ratio, which is defined as the ratio between first and second peaks in the impulse response. Denoting the dominant root by λ, the decay ratio of the system can be determined as:

$$DR = e^{-2\pi|\mathrm{Re}(\lambda)/\mathrm{Im}(\lambda)|} \tag{3-117}$$

The characteristic equation is a very high order non-linear equation, often solved by the Newton-Raphson method. However, due to the poor global convergence of the Newton-Raphson method, the solution is highly dependent on the initial guess of the dominant root; and does not converge in many cases. After a review of root solving algorithms, a global Newton method is suggested and implemented in FISTAB. The test results of some simple equations and the actual characteristic equation demonstrate good global convergence of the new method. Details can be found in Appendix B.

3.3. Code Benchmark

To evaluate the reliability of the stability code FISTAB, the steady state and transient tests were evaluated by comparison to the experimental results of SIRIUS-N facility at CRIEPI in Japan.

3.3.1. SIRIUS-N Facility Description

The SIRIUS-N (SImulated Reactivity feedback Implemented into thermal-hydraUlic Stability loop for Natural circulation BWR) test facility was designed to investigate the instability characteristics in natural circulation BWRs and the role of the flashing phenomena in the mechanism of the instability. This facility is a scaled copy of a prototypical natural circulation BWR in CRIEPI (Central Research Institute of Electric Power Industry), Japan.

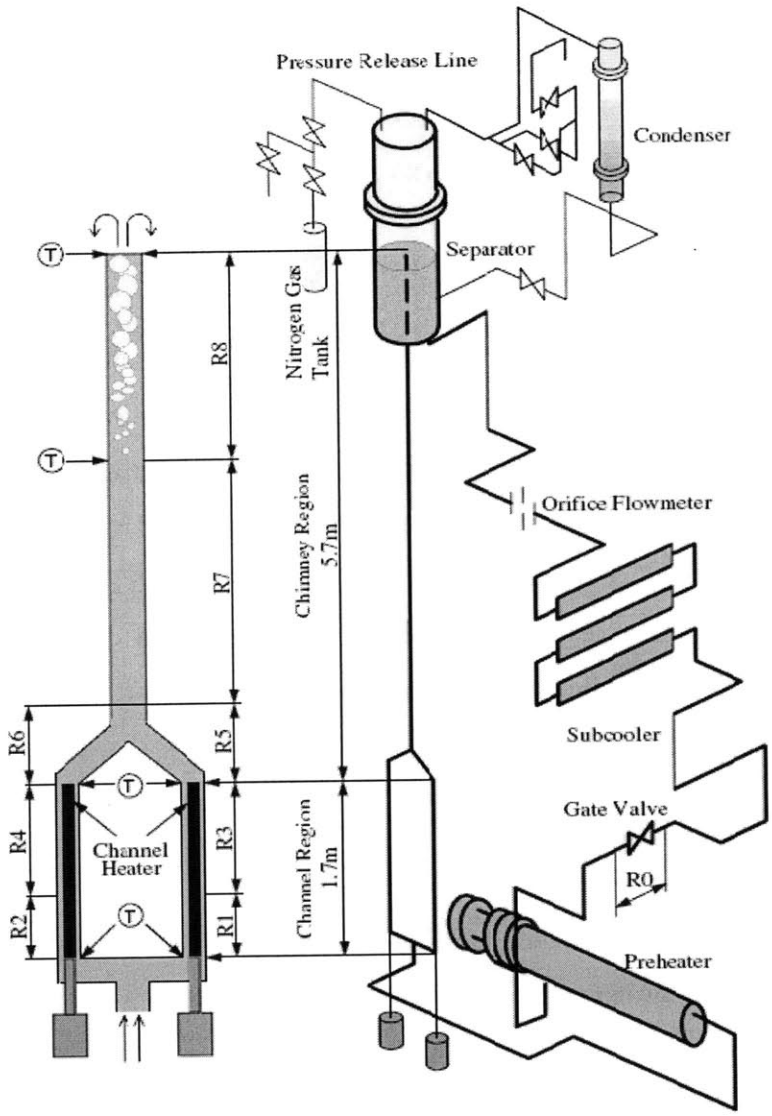

Figure 3.7: Schematic of the SIRIUS-N Facility (from [Furuya, 2006])

Figure 3.7 shows a schematic of the test facility. The thermal-hydraulic loop consists of two channels, a chimney, an upper-plenum (separator), a downcomer, a subcooler, and a preheater. The channel length, lc,is 1.7 m and the chimney length, lr, is 5.7 m, are around 70% of the actual values used in a prototypical natural circulation BWR. A heater pin is installed concentrically in each channel. The test fluid is water. More details of the SIRIUS-N facility could be found in [Furuya, 2006].

The non-dimensional parameters used for scaling of the SIRIUS-N facility are listed in Table 3-1. The Froude number and Flashing parameter are key values that determine the magnitude of flashing. These two values in the SIRIUS-N facility are approximately 70% of the values found in a prototypical natural circulation BWR. The facility height is limited within the availability of vertical space of the existing facility building. The other parameter values agree well with the actual reactor specifications.

The experimental parameters are the system pressure, heat flux and channel inlet temperature. The system pressure was maintained at a specific level by controlling the performance of the condenser. Subsequently, the channel inlet temperature was maintained at the desired value by controlling the performance of the sub-cooler.

Table 3-1: Comparison of SIRIUS-N Facility with a prototypical NCBWR at system pressure 0.1MPa

Parameters	**Prototype NCBWR**	**SIRIUS**
Flashing parameter	67	46
Froude number	1.05×10^{-3}	7.60×10^{-4}
Phase change number	11.6	13.1
Subcooling number	9	9
Non-dimensional drift velocity	1.32	1.97
Ratio of vapor to liquid densities	6.20×10^{-4}	6.20×10^{-4}
Ratio of chimney exit to channel inlet vapor densities	2.01	1.63
Friction coefficient in the channel	6.9	5.7
Orifice coefficient at the channel inlet	10~50	30
Orifice coefficient at the chimney exit	20~40	21
Non-dimensional downcomer cross sectional area	1.05	1.11
Non-dimensional chimney cross sectional area	2.59	2.47
Non-dimensional chimney length	3.34	3.38

In Table 3-1, the definition of the dimensionless parameters are:

$$N_{flash} = \frac{h_{f,C,i} - h_{f,R,e}}{h_{fg,C,i}} \frac{\rho_{f,R,i} - \rho_{g,R,i}}{\rho_{g,R,i}},$$

$$N_{Fr} = \frac{u_{in}^2}{gL_c},$$

$$N_{sub} = \frac{(h_f - h_{in})}{h_{lg}} \frac{\rho_l - \rho_g}{\rho_g},$$

$$N_{pch} = \frac{v_{lg}}{h_{lg}} \frac{q'' P_h L}{A_c u_{in}}.$$

3.3.2. Comparison of steady-state results

Very limited results are available for steady state benchmark at low pressure conditions. The available results in [Furuya, 2006] are two steady state operating conditions, as listed in Table 3-2 with the results of code predictions.

Table 3-2: Comparison of steady state results at low pressure conditions, Psys=0.2MPa

Parameters	Case 1		Case 2	
	Experimental results	Code results	Experimental results	Code results
System pressure (MPa)	0.2			
Heat Flux (kW/m^2)	53			
Inlet Temperature (°C)	101.5		121.5	
Inlet Velocity (m/s)	0.2	0.195	0.86~0.95	0.90
Void Fraction at chimney exit	0.02	0.015	0.45~0.55	0.52

To further evaluate the steady-state performance of the code, some available experimental results of the SIRIUS-N facility at high pressures are also simulated. The test results and important operating conditions are listed in Table 3-3. The inlet flow velocities of code prediction are plotted in Figure 3.8, with comparison aginst experimental results.

Table 3-3: Comparison of steady state results at high pressure conditions, Psys=2MPa

Test Case	Heat flux (kw/m^2)	Subcooling number	Inlet enthalpy (kJ/kg)	Inlet temperature (°C)	Inlet Velocity(m/s)	
					Experiment	Code prediction
1	228	2.4	854.3	200.5	0.86	0.87
2	228	3.1	838.5	197.1	0.78	0.78
3	228	4.1	815.9	192.1	0.67	0.67
4	228	5.05	794.4	187.4	0.58	0.57
5	228	6.3	766.2	181.2	0.49	0.48
6	228	6.95	751.5	178.01	0.445	0.44
7	228	8.4	718.7	170.8	0.38	0.39

It can be observed that the biases for the predicted inlet flow velocities are very small under both the low and high pressure conditions in the SIRIUS-N facility. Therefore, it can be concluded that the code FISTAB matches the experimental data reasonably well under steady-state conditions.

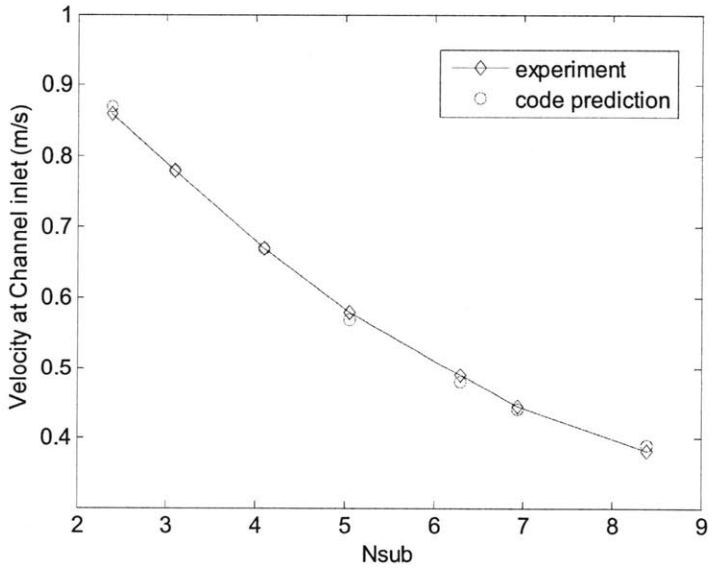

Figure 3.8: Validation of the code at stationary conditions, at 2MPa and 228kW/m^2

3.3.3. Comparison of transient results

The available transient results are the stability boundaries obtained by changing the inlet flow temperature in SIRIUS-N facility, as shown in Figure 3.9. Under every system

pressure conditions, instability occurred within a certain range of the inlet subcooling. The unstable range grows as the heat flux was increased. In this work, the stability performances of a large amount of points in the stability map in [Furuya 2006] are examined with the stability code FISTAB.

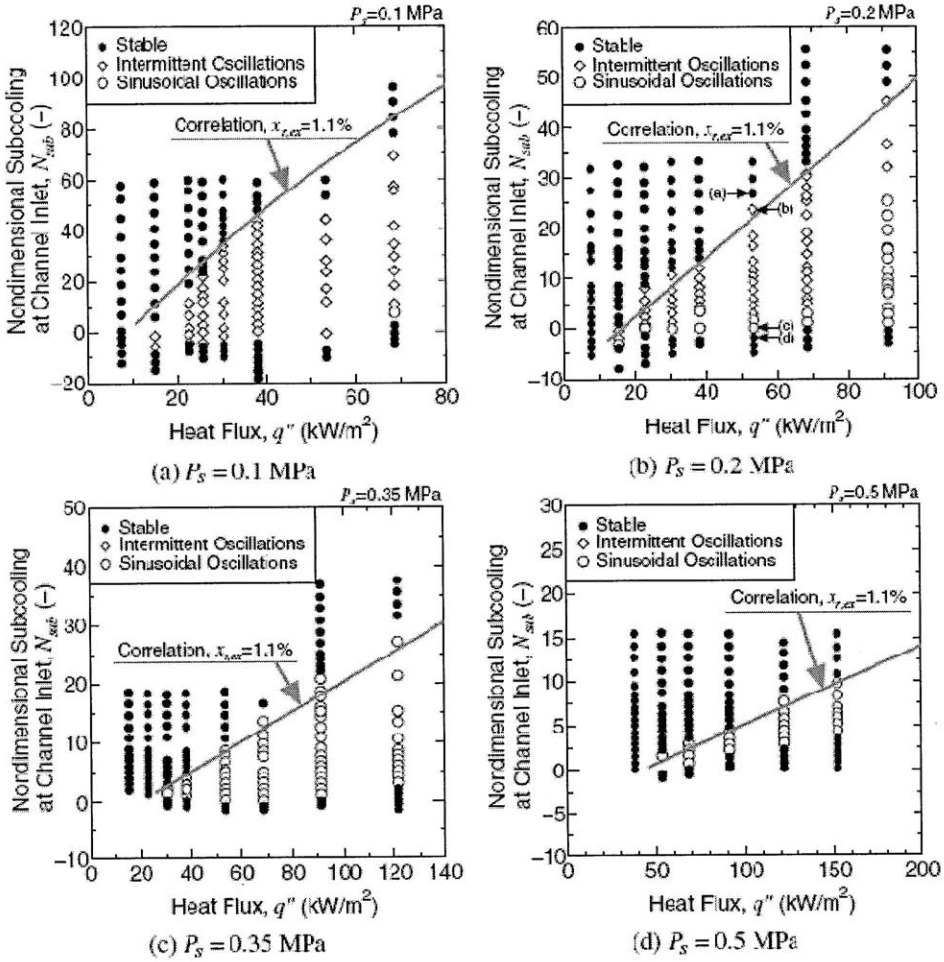

Figure 3.9: Stability map of SIRIUS-N facility at various system pressures (Fig. 2.4 in [Furuya, 2006])

The benchmark results at $P_{sys} = 0.1MPa$ are listed in Table 3-4 and Figure 3.10. It is seen in Table 3-4 that the code predictions match the experimental results in most cases, except for few operating points near the stability boundaries. Also, the code cannot predict the stability boundary well under very low sub-cooling number (i.e. high flow quality). However, this is not a problem for its application to BWR since the high quality

stability boundary is always beyond the CHF limit in BWR operating conditions. The benchmark results under other pressure conditions (0.2 MPa, 0.35 MPa, and 0.5 MPa) are listed in Table 3-5, 3-6, and 3-7, which are very similar to those shown in Table 3-4 and Figure 3.10.

Table 3-4: Benchmark Results with SIRIUS-N facility at 0.1MPa, (Experiment/Code)

Heat flux(kW/m^2) / N_{sub}	8	16	22	30	38	53	68
60	Y/Y	Y/Y	Y/Y	Y/Y	Y/Y	Y/Y	N/N
50	Y/Y	Y/Y	Y/Y	Y/Y	Y/Y	N/N	N/N
40	Y/Y	Y/Y	Y/Y	Y/Y	N/Y	N/N	N/N
30	Y/Y	Y/Y	Y/Y	N/Y	N/N	N/N	N/N
20	Y/Y	Y/Y	Y/Y	N/N	N/N	N/N	N/N
10	Y/Y	Y/Y	N/N	N/N	N/N	N/N	N/N
0	Y/N	N/N	N/N	N/N	N/N	Y/N	Y/N
-10	Y/N	Y/N	Y/N	Y/N	Y/N	Y/N	Y/N

Y: Stable; N: Not Stable

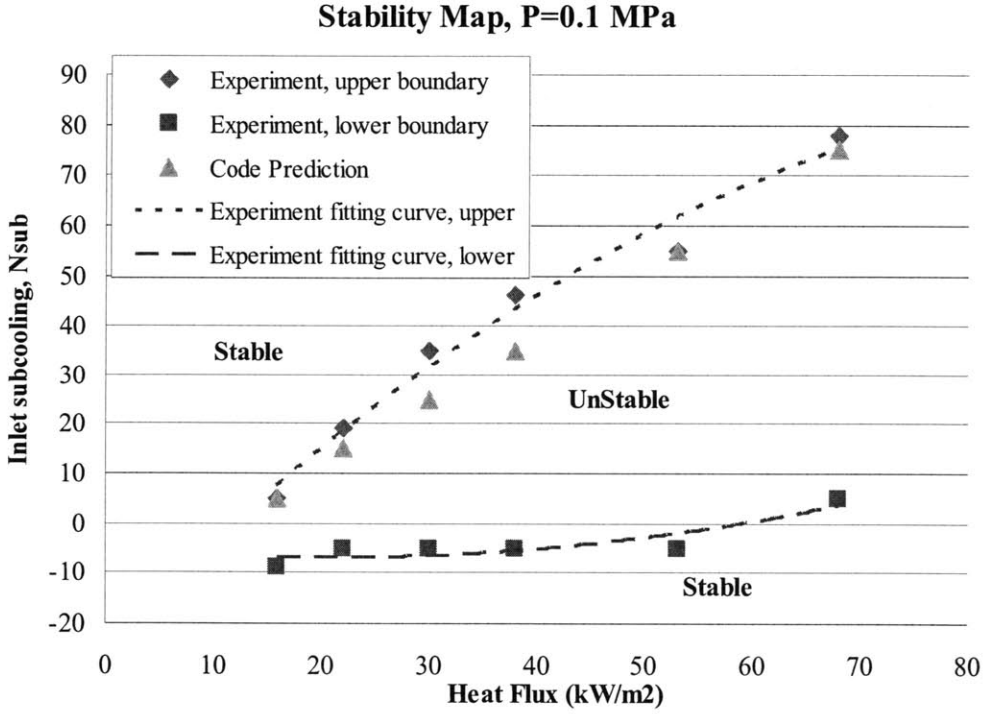

Figure 3.10: Comparison of stability boundaries between code predictions and experiments

Table 3-5: Benchmark Results with SIRIUS-N facility at 0.2MPa, (Experiment/Predicted)

Heat flux(kW/m^2) / Nsub	8	16	22	30	38	52	68	92
40	Y/Y	Y/Y	Y/Y	Y/Y	Y/Y	Y/Y	Y/Y	N/Y
30	Y/Y	Y/Y	Y/Y	Y/Y	Y/Y	Y/Y	N/Y	N/Y
20	Y/Y	Y/Y	Y/Y	Y/Y	Y/Y	N/N	N/N	N/N
10	Y/Y	Y/N	Y/N	N/N	N/N	N/N	N/N	N/N
5	Y/Y	Y/N	N/N	N/N	N/N	N/N	N/N	N/N
0	Y/Y	N/N	N/N	N/N	N/N	N/N	N/N	N/N
-5	Y/N	Y/N	Y/N	Y/N	Y/N	Y/N	Y/N	Y/N

Y: Stable; N: Not Stable

Table 3-6: Benchmark Results with SIRIUS-N facility at 0.35MPa, (Experiment/Predicted)

Heat flux(kW/m^2) / Nsub	22	30	38	52	68	92	122
25	Y/Y	Y/Y	Y/Y	Y/Y	Y/Y	Y/Y	N/N
20	Y/Y	Y/Y	Y/Y	Y/Y	Y/Y	N/Y	N/N
15	Y/Y	Y/Y	Y/Y	Y/Y	N/N	N/N	N/N
10	Y/Y	Y/Y	Y/Y	N/Y	N/N	N/N	N/N
5	Y/N	Y/N	N/N	N/N	N/N	N/N	N/N
0	Y/N	Y/N	Y/N	N/N	N/N	Y/N	Y/N

Y: Stable; N: Not Stable

Table 3-7: Benchmark Results with SIRIUS-N facility at 0.5MPa, (Experiment/Predicted)

Heat flux(kW/m^2) / Nsub	38	52	68	92	122	152
15	Y/Y	Y/Y	Y/Y	Y/Y	Y/Y	Y/Y
10	Y/Y	Y/Y	Y/Y	Y/Y	Y/Y	N/Y
7.5	Y/Y	Y/Y	Y/Y	Y/Y	N/N	N/N
5	Y/Y	Y/Y	Y/Y	N/N	N/N	N/N
2.5	Y/N	Y/N	N/N	N/N	N/N	Y/N
0	Y/N	N/N	N/N	Y/N	Y/N	Y/N

Y: Stable; N: Not Stable

It is seen in both the experimental results and the code predictions that:

1) Instability occurs within a certain range of the inlet subcooling. The unstable range enlarges as the heat flux increases.
2) It is obvious that the stable region increases in size as the system pressure goes up. Furthermore, as the system pressure increases, the region of instability shifts to a higher heat flux.

It can be concluded that the characteristics of stability boundary from code predictions agree well with the experimental results, which give us confidence to apply it to NCBWRs startup analysis.

3.4. Summary

To capture the effect of flashing on density wave oscillations in NCBWRs at low pressure startup conditions, a code named FISTAB was developed in the frequency domain. The functionality of the FISTAB code was confirmed by testing the experimental results at SIRIUS-N facility. Both stationary and perturbation results agree well with the experimental results. The stability characteristics under startup conditions for NCBWRs will be investigated in Chapter 4.

4. NCBWRs Start-up

4.1 Introduction

More and more advanced reactor designs are employing natural circulation based heat removal systems, which ensures improved safety as well as cost effectiveness, including the ESBWR [GE-Hitachi Nuclear Energy, 2008], AHWR [Sinha and Kakodkar, 2006], etc. In these designs, a long adiabatic pipe (so-called riser or chimney) is above the core to enhance the flow rate. The elimination of the recirculation systems (pumps and related piping and components) simplifies the design and excludes a whole series of transients and initiating events that can lead to accidents (pump trips, LOCAs due to failures of the external recirculation piping, etc.). However, both experimental and analytical studies had shown that such a new reactor configuration makes the system susceptible to thermal-hydraulic instabilities during the start-up phase.

Since the reactor power is very low during the start-up phase, so there are large margins with respects to thermal limits (CHF). The core should be kept in single-phase conditions before the pressurization, so the flow oscillation would not turn into a power oscillation. However, it was shown that the periods of the oscillations are relatively large and the amplitudes of temperature fluctuations are about 10 °C or lower [Manera, 2003]. Thus, questions arise if such oscillations could initiate thermal fatigue of the reactor internals, and if the mechanical vibrations of the structures might be induced by the flow oscillations. Although it is not clear whether flashing-induced oscillations are acceptable from a reactor safety point of view, appropriate start-up procedures have to be planned to avoid instabilities.

In this chapter, the start-up procedure realized at the Dodewaard reactor [Nissen et al., 1994] and the start-up procedure proposed for the ESBWR design [GE-Hitachi Nuclear Energy, 2008] are first described. Then, the stability performances of several operating points during the ESBWR start-up trajectory are examined by the FISTAB code, which is

described in Chapter 3. Finally, proposed start-up procedures for the NCBWRs in the literature are reviewed, and possible revisions for start-up procedure are recommended.

4.2 Start-up Procedure of BWRs

4.2.1 The start-up procedure of the Dodewaard reactor

The start-up procedure of the Dodewaard reactor is described by [Nissen et al., 1994] and develops as the following (for a scheme of the reactor it is suggested to refer to Figure 2.1, note that no steam separators are present in Dodewaard):

1) First, the reactor vessel contains water at about 95 °C with a water level of 2.54 m above the riser exit (the value at nominal power is 0.54 m). The water is circulated and heated up by means of the RAS (Reactor Shutdown Cooling System) heaters up to 100 °C;
2) The reactor is made critical and a heat-up rate of 45 to 55 °C/h (by fission power) is maintained. The pressure rises. When a pressure of 5 bar is reached the RWCU (Reactor Water Clean-up System) is started to keep the water level at the desired value;
3) While the pressure rises, the water level above the riser is decreased by means of the RWCU till the nominal level is reached at a pressure of 20 bar. Later on, the water level is kept constant by regulating the FW (feed water) flow. Meanwhile, the turbine bypass is used to control the pressure increase;
4) At 30 bar, the turbine is started, while pressure and power are continuously increased until the nominal values.

Measurements during start-up conditions of the Dodewaard reactor are available, though the lack of instrumentation makes the assessment of the results rather difficult. In fact, during the start-up only reactor pressure and power measurements are available [Manera, 2003]. If steam production takes place only in the riser section at low power, noise analysis of the in-core neutron detectors will not detect significant fluctuations even if flow oscillations are generated, especially in transient conditions. However, whether flow oscillations took place or not during the start-up of the Dodewaard reactor, it is striking

that no problems (mechanical vibrations, thermal stresses and fatigue) have ever been reported during the life of the reactor.

4.2.2 The start-up procedure of the ESBWR

The start-up process of the ESBWR generally follows the procedure from the Dodewaard plant [GE-Hitachi Nuclear Energy, 2008]. Figure 4.1 shows the stages of the startup process of the ESBWR, as described in the following:

1) **De-aeration Period:** the reactor coolant is de-aerated by drawing a vacuum on the main condenser and reactor vessel using mechanical vacuum pumps with the steam drain lines open. The reactor coolant is heated up to between 80°C and 90°C with the RWCU (Reactor Water Clean-up System) / SDC (Shut-Down Cooling System) auxiliary heater and decay heat. The reactor pressure is reduced to about 50 to 60 kPa.
2) **Pressurization Period:** initiated by pulling groups of control rods to criticality with the Main Steam Isolation Valves (MSIVs) either left open or closed. Fission power is used to heat the reactor water, while maintaining the water level close to the top of the separators but well below the steam lines. Steaming at the free surface starts to pressurize the reactor vessel. The core region remains subcooled due to the large static head in the chimney and separators. As the reactor heats up and pressurizes, the RWCU/SDC system heat exchangers are used to control the downcomer temperature, enhance coolant flow and reduce lower plenum stratification.
3) **Power Increase Period:** the MSIVs are reopened at the end of the Start-up Period, when pressure reaches 6.3 MPa. Subsequently, the turbine bypass valves are used to control pressure. The RPV power is increased and preparations made to roll the turbine.

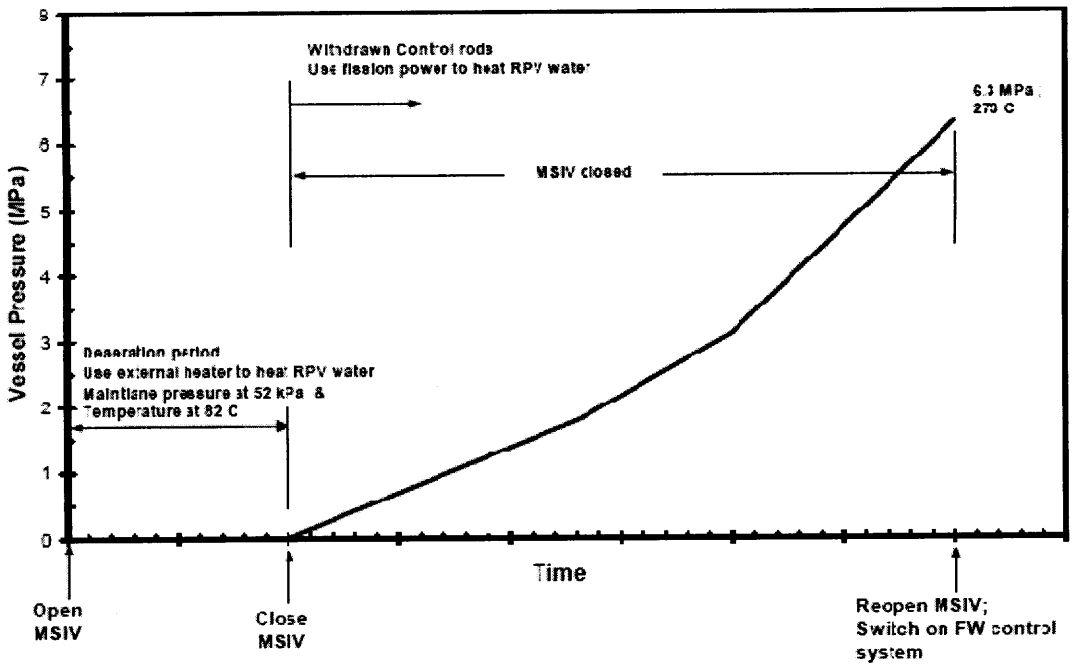

Figure 4.1: ESBWR Start-up Trajectory
(from [GE-Hitachi Nuclear Energy, 2008])

4.2.3 The start-up procedure of the ABWR

For comparison, the start-up procedure of the ABWR [GE Nuclear Energy, 2000] is also briefly described. Figure 4.2 shows the key steps in the plant startup sequence, including criticality, heatup, pressurization, turbine synchronization, and power ascension, which is similar to that of the ESBWR.

A typical ABWR start-up path in the power-flow map is given in Figure 4.3. It is shown that the ABWR starts with natural circulation in the start-up, and then operates with a minimum pump speed; after the reactor vessel is pressurized, the reactor power is increased first by removing the control rods, and then by increasing the internal pump speed. The ESBWR start-up path in the power-flow map is totally different since it relies on natural circulation during all operating conditions. There is no active control of the coolant flow in the ESBWR, as the recirculation pumps are all eliminated.

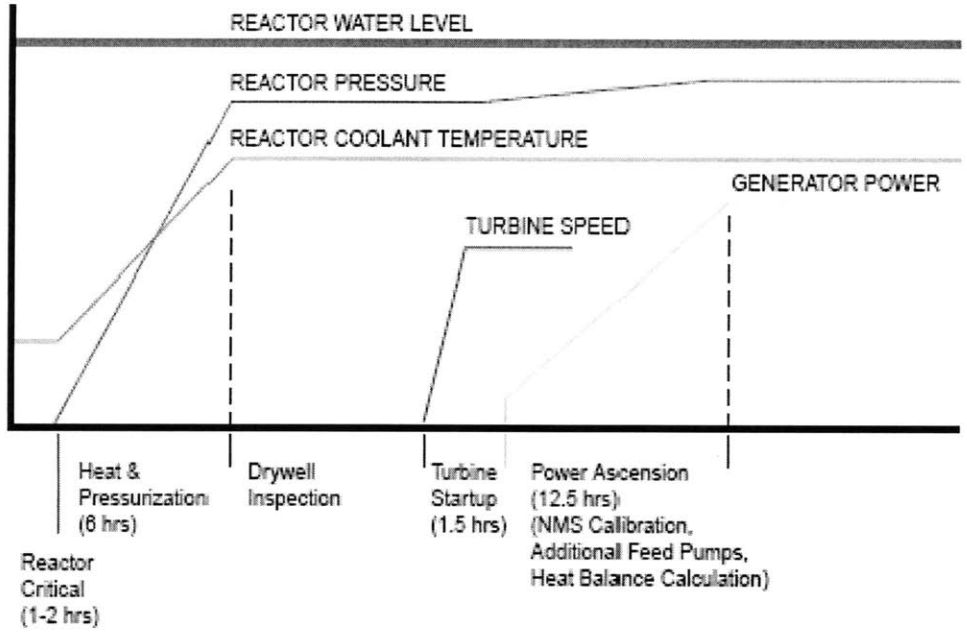

Figure 4.2: ABWR startup sequence

(from [GE Nuclear Energy, 2000])

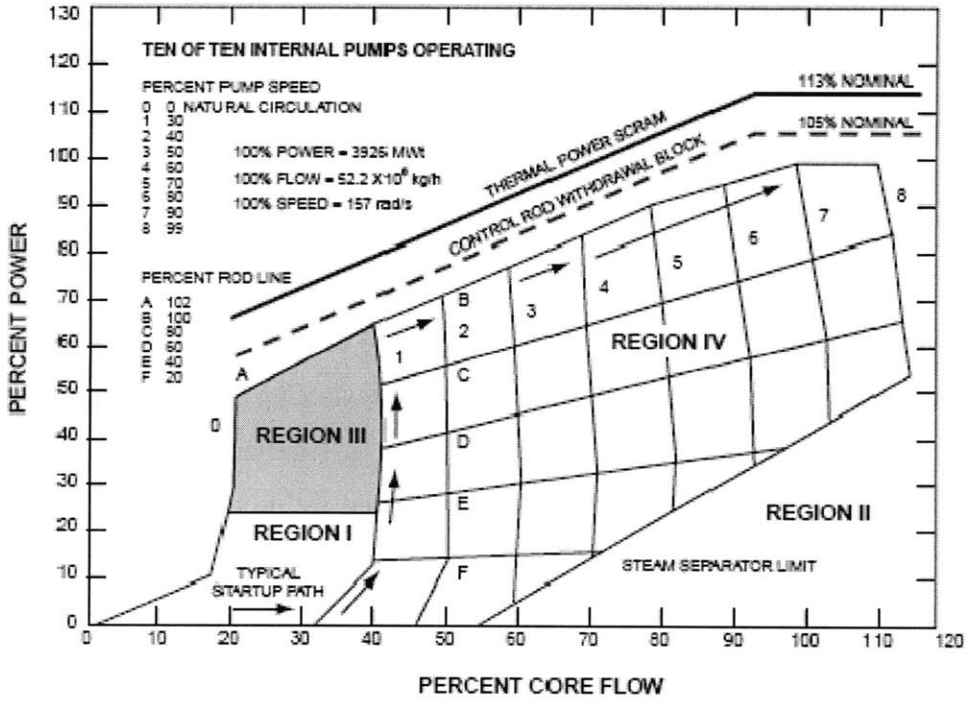

Figure 4.3: ABWR power-flow map
(from [GE Nuclear Energy, 2000])

4.3 Stability analysis of ESBWR during start-up

The startup transient for the ESBWR is simulated with TRACG and reported in [GE-Hitachi Nuclear Energy, 2008]. Important parameters trajectories are reported in figures including: reactor power, pressure, inlet subcooling, core inlet flow rate, separator void fraction, hot bundle void fraction, hot bundle exit flow rate. To examine the stability performance of the ESBWR startup, a certain number of operating points from the start-up trajectories in [GE-Hitachi Nuclear Energy, 2008] are analyzed in this work with the FISTAB code, described in Chapter 3.

These TRACG calculations were performed with imposed core power, without the neutronics feedback. This is valid as long as there are no feedbacks from oscillations in the core void fraction during the startup transient. The calculation was initiated at the end of the de-aeration period with the steam dome pressure at 52 kPa and RPV water at 82°C. The water level was maintained near the top of the separators. The MSIVs were closed to isolate the RPV. The power level was maintained constant until the pressure reached 6.3 MPa. Subsequently, the MSIVs were opened and the power level was increased in steps to achieve rated pressure at 300 MWt (6.67% of rated power). Three startup heating rates (50 MWt, 85 MWt, and 125 MWt) were considered. The lowest power level of 50 MWt corresponded to a heatup rate of 30°C/hour and is said to likely be close to the actual value for startup. The three power trajectories are shown in Figure 4.4.

Figure 4.5 shows the pressure response predicted by TRACG for the three cases. The circulating water heats up because of the core power. The heat exchangers in the RWCU/SDC system are enabled to remove part of the energy and control the core inlet subcooling. Steam generation begins at the water surface and starts to pressurize the vessel.

The core flow transient response provided by TRACG is shown in Figure 4.7. For the lowest heatup rate, the flow trace shows a minor oscillation (noise) between 3000 to 5500

s. The cause of this noise can be traced to the beginning of voiding at the top of the separators [GE-Hitachi Nuclear Energy, 2008]. The flow noise is terminated when a steady void fraction is established at the top of the separators. At higher start-up power levels of 85 MWt and 125 MWt, the flow becomes noisier, as seen in Figure 4.7.

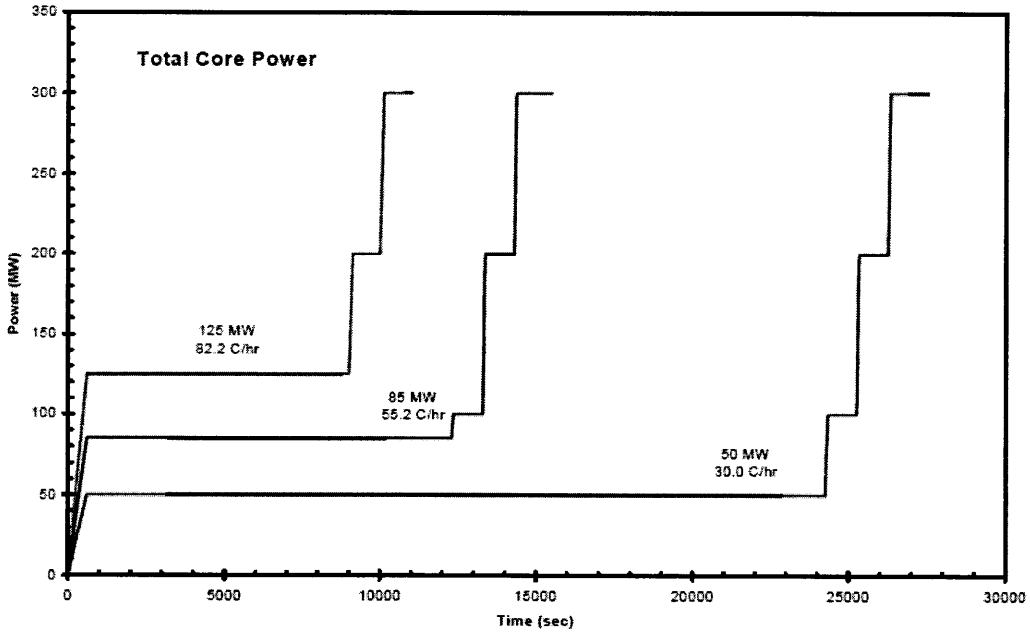

Figure 4.4: TRACG Start-up Simulation for ESBWR: Reactor Power Trajectories (from [GE-Hitachi Nuclear Energy, 2008])

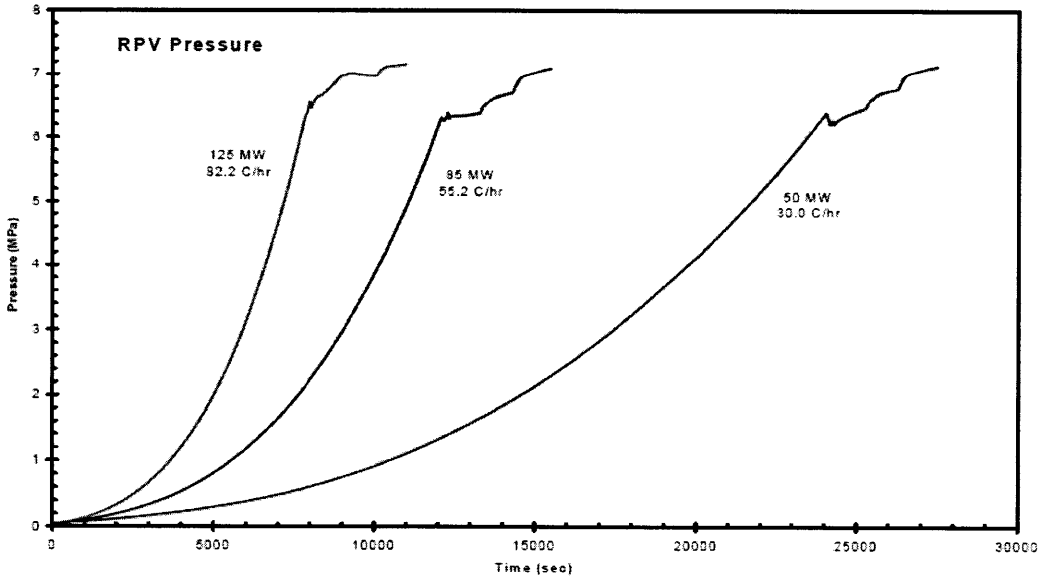

Figure 4.5: TRACG Start-up Simulation for ESBWR: Pressure Response (from [GE-Hitachi Nuclear Energy, 2008])

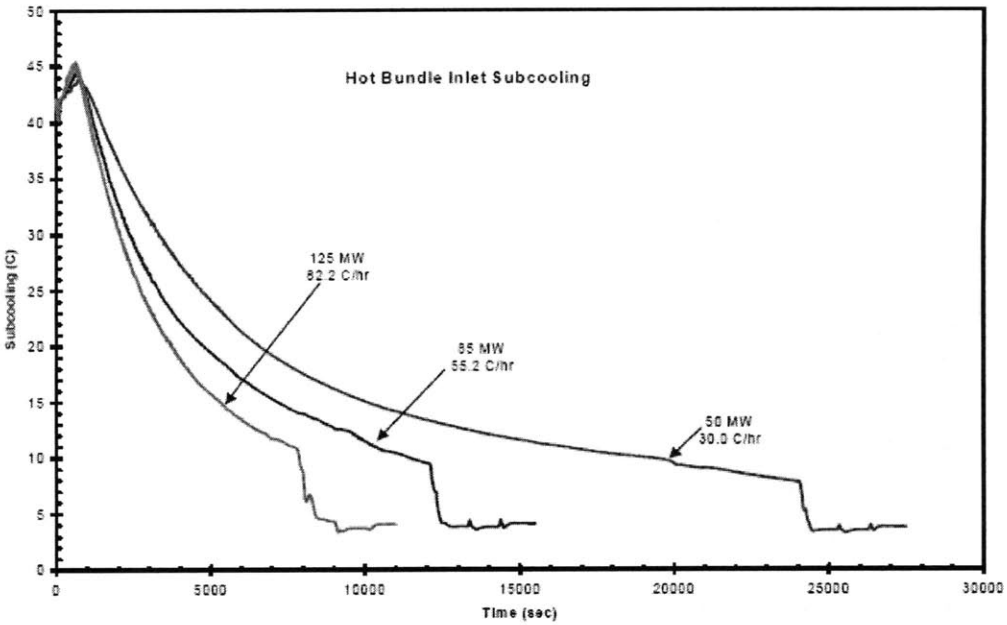

Figure 4.6: TRACG Start-up Simulation for ESBWR: Inlet Subcooling (from [GE-Hitachi Nuclear Energy, 2008])

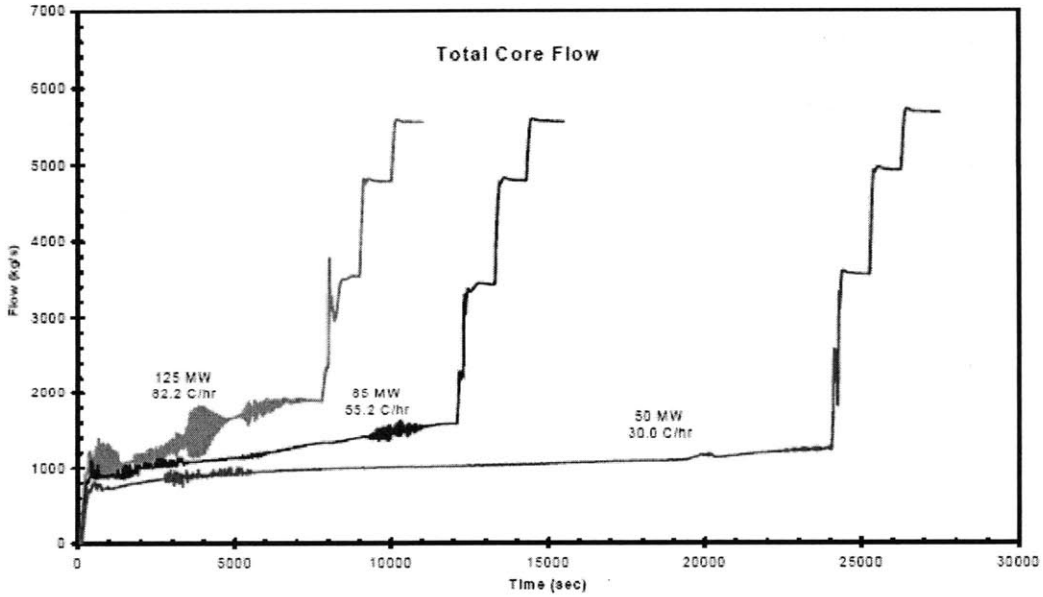

Figure 4.7: TRACG Start-up Simulation for ESBWR: Core Inlet Flow (from [GE-Hitachi Nuclear Energy, 2008])

4.3.1 Comparison of stationary results

Six operating states along the start-up trajectories of the 50 MWt heatup rate case in [GE-Hitachi Nuclear Energy, 2008], at which the steam dome pressures are at 0.1, 0.2, 0.4, 0.6, 0.8 and 1 MPa, have been analyzed by FISTAB.

The geometric data of the ESBWR used in this analysis is listed in Table 4-1 and 4-2. The detailed design information can be found in [GE-Hitachi Nuclear Energy, 2008].

Table 4-1: ESBWR Reactor Coolant System Geometric Data

	Flow Path Length (m)	**Volume of Fluid (m^3)**	**Average Flow Area (m^2)**
Lower Plenum	4.13 (Axial) 1.78 (Radial)	103	16.83
Core	3.79	96	20.22
Chimney	6.61	276 (includes upper plenum)	29.27
Upper Plenum	2.75	276 (includes chimney)	29.53
Dome	1.78 (Radial) 2.79 (Axial)	225	28.67
Downcomer	14.53	259	8.4

Table 4-2: ESBWR Fuel Assembly Parameters

Parameter	Value
Geometry	
Fuel pin lattice	Square 10x10
Assembly number	1132
Number of fuel pins per assembly	92 (78 full length, 14 partial length)
Overall length (m)	3.79
Active fuel length (m)	3.048 (2.032 for partial length rods)
Fuel pin OD (mm)	10.26
Cladding thickness (mm)	0.71
Pellet thickness (mm)	8.67
Hydraulics	
In-Channel Flow Area (m^2)	0.0093
In-Channel Hydraulic Diameter (m)	0.0098
Number of Spacers	8
Local Loss Coefficient at Inlet Orifice (Center)	42.1
Local Loss Coefficient at Orifice (Peripheral)	110
Local Loss Coefficient at Lower Tie-Plate	9.46
Local Loss Coefficient at Spacer	1.20
Local Loss Coefficient at Upper Tie-Plate	0.37
Bypass Flow Fraction of the Total Flow Rate (%)	10

First, the steady state predictions of the FISTAB code are benchmarked with the TRACG code. Giving FISTAB the input conditions of the power, inlet subcooling, and system pressure respectively in Figure 4.4, Figure 4.5, and Figure 4.6 from TRACG simulation, the predicted natural circulation flow rates are compared. The results are shown in Table 4-3 and Figure 4.8.

Table 4-3: Comparison of steady state results

Reactor heating Power	50MW			
System Pressure (MPa)	Inlet Subcooling (°C)	Core inlet flow rate (kg/s) – TRACG †	Core inlet flow rate (kg/s) - FISTAB	Relative Errors
0.1	36.6	810	925	+14.2%
0.2	29.1	900	881	-2.1%
0.4	21	970	989	+2.0%
0.6	17.5	995	1035	+4.0%
0.8	15.9	1000	1040	+4.0%
1	14.7	1005	1045	+4.0%

†: The TRACG results are read from the figure in [GE-Hitachi Nuclear Energy, 2008], an uncertainty of ±20 *kg/s* should be considered.

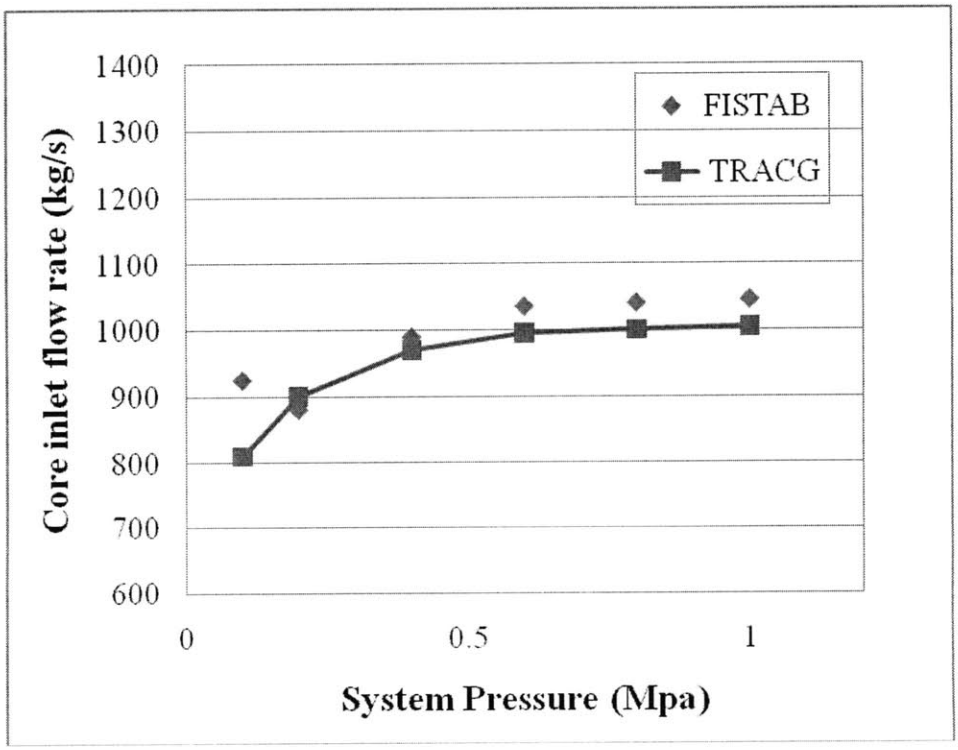

Figure 4.8: Comparison of stationary results for ESBWR Start-up, TRACG vs. FISTAB

It is seen in Figure 4.8 that the predictions of inlet flow rate from FISTAB agree well with the TRACG simulations, except for one point at P=0.1 MPa, which could be due to: 1) reading error from the report [GE-Hitachi Nuclear Energy, 2008], 2) the more

sensitive conditions at low pressure, and 3) the operating point is selected from a transient analysis by TRACG and not a steady-state condition (the process of reactor vessel pressurization is actually a slow transient).

Another interesting result from FISTAB steady-state simulation is that the pressure drop is dominated by gravity loss for all six examined points, as shown in Table 4-4. It is clearly different from the conditions under normal density wave oscillations, in which the two-phase friction pressure drop is dominant.

Table 4-4: Pressure drop under various operating conditions

Reactor Heating Power	50 MW			
System Pressure (MPa)	Inlet Subcooling (°C)	Total pressure drop (kPa)	Gravity pressure drop (kPa)	Gravity pressure drop fraction
0.1	36.6	136.3	132.6	0.973
0.2	29.1	134.6	131.0	0.973
0.4	21	131.6	127.95	0.972
0.6	17.5	129.4	125.8	0.972
0.8	15.9	127.5	123.9	0.973
1	14.7	126	122.4	0.971

4.3.2. Linear stability analysis

Using the FISTAB code, the decay ratios of the six examined point are calculated. It is shown in Table 4-5 that the decay ratios of all the examined points are very small, i.e., large margin to instability.

Table 4-5: Stability characteristics under ESBWR start-up

Reactor Heating Power	50 MW				
System Pressure (MPa)	Inlet Subcooling (°C)	Quality at chimney exit	Quality at the top node of separator	Decay Ratio	Stable
0.1	36.6	0	0.0020	0.032	Y
0.2	29.1	0	0.0022	0.053	Y
0.4	21	0	0.0026	0.065	Y
0.6	17.5	0	0.0028	0.080	Y
0.8	15.9	0	0.0029	0.098	Y
1	14.7	0.0009	0.0031	0.113	Y

Y: Stable; N: Not Stable

Furthermore, a stability map (subcooling number vs. heating power) is constructed for the system pressure at 0.1 MPa, to gain more insights of the stability performance during ESBWR startup. The stability map is constructed as follows: for a given inlet subcooling, the heating power is increased step by step until the decay ratio equals to one, results in the boundary value of the heating power. Changing the inlet subcooling to repeat the calculation procedure, the stability boundary map can be constructed. However, this procedure is very inefficient.

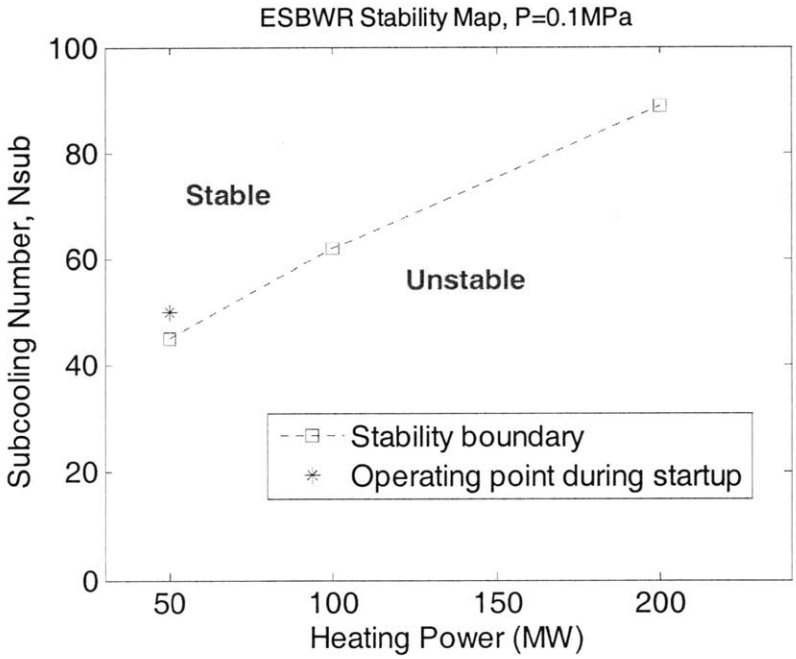

Figure 4.9: ESBWR Stability Map at P=0.1 MPa

It is shown in Figure 4.9 that the operating point is close to the stability boundary, though the calculated decay ratio is very small, which indicates that decay ratio is very sensitive to the inlet subcooling when the system pressure is very low.

It should be emphasized here that the FISTAB code is based on the perturbation theory. The built-in assumptions in the code include: 1) the oscillation amplitude is small, and 2) an initial steady-state is achieved. Thus, the code could not predict the stability behavior in a transient, which includes instability initiated by the transition from single-phase natural circulation to steady two-phase natural circulation flow.

4.4 Start-up Procedures for NCBWRs

It is not clear whether flashing-induced oscillations are acceptable, although [GE-Hitachi, 2008] claimed that the magnitude of the flow oscillations is typically very small and instability resulted from the initial flashing (transition from single-phase to two-phase natural circulation flow) is acceptable. To avoid the flashing-induced instabilities, start-up procedures for the NCBWRs in the literature are reviewed, and possible revisions to the ESBWR start-up procedure are proposed.

4.4.1 Literature survey on start-up procedure for NCBWRs

Not many proposals of start-up procedures are reported in literature, but all authors [Nayak 2000, Jiang et al., 2000, Cheung and Rao 2000, etc.] agree on the fact that the system should be pressurized before the transition to two-phase circulation is allowed.

Nayak [2000] and Jiang et al. [2000] propose to externally pressurize the system by injecting in the pressure vessel steam produced in a separate boiler or nitrogen respectively. Once the pressure in the vessel is high enough, the reactor power can be increased to achieve two-phase natural circulation. Unfortunately, the procedure suggested by Nayak [2000] needs an external boiler of adequate volume and power and the related connecting piping to the reactor vessel, while the one suggested by Jiang et al. [2000] requires an additional system for the nitrogen storage and the related connecting

piping to the reactor vessel. The external pressurization does not accomplish the requirements of simplicity that are at the base of the natural circulation BWRs design and is thus not desirable.

Cheung and Rao [2000], from the General Electric (GE) developer's team of the ESBWR concept, suggest a start-up procedure in which the reactor is made critical and is pressurized in conditions of single phase circulation, up to a pressure of 63 bar. At this pressure the transition to two-phase operation is achieved by opening the MSIVs (Main Steam Isolation Valves).

Schuster et al. [2000], on the basis of experimental results collected at the DANTON facility, state that "without external pressurization there exists no other way to reach the stable two-phase operation mode. In all cases a range of instability has to be passed". Manera [2003] re-examined their experimental results collected at the DANTON facility, and revealed that the free volume above the riser (5 m length) and the downcomer is only 10 cm high. This means that it is practically not possible to create a steam cushion in this volume without producing steam also in the riser section. Thus it is indeed impossible to start-up the facility without incurring flow instabilities if external pressurization is not supplied.

Manera [2003] proposed procedures to create the steam cushion in the steam dome, and the flashing is supposed to take place in a confined region above the riser exit, as indicated in Figure 4.10 (steam separator is missed). A collapsed water level of about 1-1.5 m above the riser is suggested during the startup, and flashing could be allowed in the last 0.5 m of the separator region to produce steam. Also proposed is the reactor power as a function of system pressure.

Gartia et al. [2008] examined several start-up procedures for the AHWR by using RELAP5. They concluded that occurrence of low pressure flow instability is unavoidable with natural circulation flow, but it is feasible to avoid low pressure instabilities during

start-up if an initial specified flow is provided by the feed water pump until the system pressure reached 50 bar.

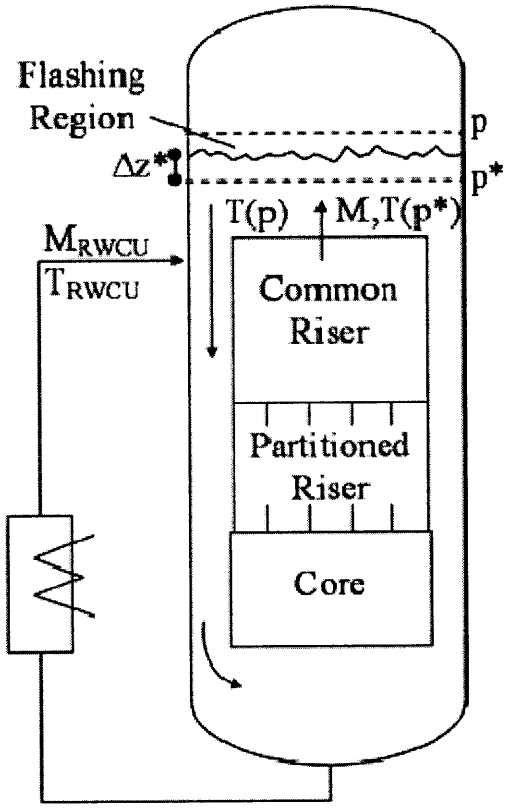

Figure 4.10: Scheme of the flow paths in the reactor vessel during start-up (from [Manera, 2003])

4.4.2 A simple criterion for NCBWRs start-up procedure

Although it is claimed that the flashing-induced instabilities in the adiabatic riser section are not grievous from a safety point of view [GE-Hitachi Nuclear Energy 2008, Gartia et al., 2008], the proposed criterion is intended to avoid two-phase flashing flow in the riser before the pressurization of the reactor vessel (above 15 bar).

Thus, only single-phase natural circulation is allowed in the core and riser, but flashing would occur above the riser, in the upper part of the separator, as the same philosophy in [Manera, 2003], and in [GE-Hitachi, 2008], although not clearly stated. The allowed flashing region is between lines A and B in Figure 4.11, in which line A is the bottom of the separator and line B is at the height of the steam line.

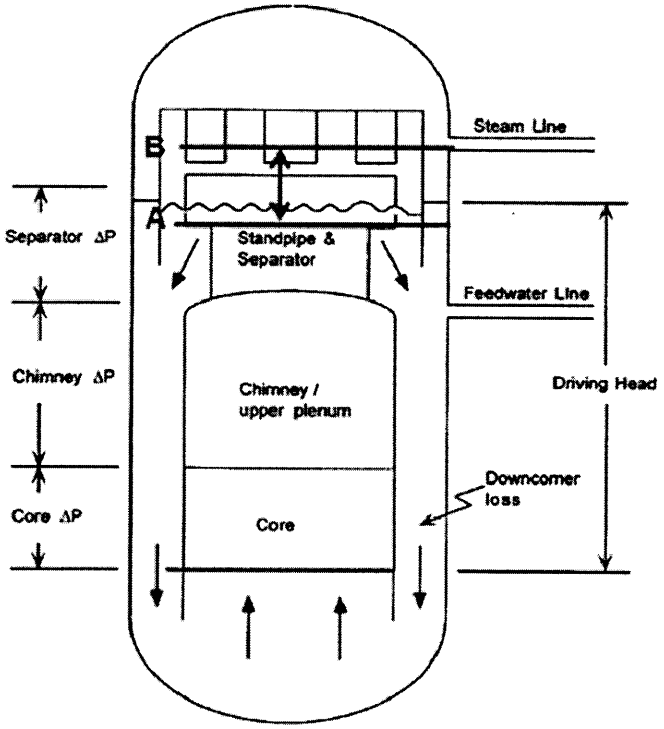

Figure 4.11: Allowed flashing region in the reactor vessel for Psys < 1.5 MPa

The initial water level in the vessel before the reactor becomes critical is also between lines A and B. The reactor power $\dot{Q}$ has to satisfy,

$$\dot{m}(h_{f,sd} - h_{in}) \leq \dot{Q} \leq \dot{m}(h_{f,sep,in} - h_{in}) \qquad \textbf{(4-1)}$$

Where $\dot{m}$ is the core flow rate, h_{in} is the core inlet enthalpy, $h_{f,sep,in}$ is the liquid saturation enthalpy at inlet of the separator, and $h_{f,sd}$ is the liquid saturation enthalpy at the steam dome pressure.

There is another relationship between the core flow rate and power based on the momentum and energy conservation equations for single-phase natural circulation flow.

Once the initial state (steam dome pressure, core inlet subcooling, and water level) is chosen for the startup procedure, the heatup rate could be chosen based on Eq. (4-1). The

inlet subcooling can be adjusted by the RWCU system during the start-up. Thus, the reactor vessel will be pressurized through the flashing above the water level. The proposed criterion can be neglected once the vessel pressure is high enough (above 15 bar).

4.5 Summary

Both experimental and analytical studies in the literature have shown that NCBWRs are susceptible to flashing-induced instabilities during start-up. To examine the stability characteristics of NCBWRs during startup, the proposed ESBWR start-up procedure are examined by the FISTAB code. It is confirmed that the examined operating points along the ESBWR start-up trajectory are stable.

However, the FISTAB code is based on linear perturbation theory, and the transition from single-phase to two-phase natural circulation flow induced by flashing could not be modeled in FISTAB. Then, a simple criterion is proposed for the NCBWRs start-up, in which flashing is only allowed above the riser and below the steam line (in essence the upper separator region).

Further investigation of the NCBWRs start-up with a system code such as RELAP5 or TRACE would be necessary to examine the transient responses under various start-up procedures.

Part II: Stability Analyses of advanced BWR Designs

Contents

Part II: Stability Analyses of advanced BWR Designs 82
5. Stability of High Power Density BWR Designs 83
5.1 Introduction 84
5.2 Fuel Designs for High Power Density BWRs 84
5.2.1 Large Assembly with Small Pins Concept 84
5.2.2 Cross-Shaped Twisted Fuel Pin Design 85
5.3 Stability Analysis Method 87
5.4 Considered BWR Instability Types 89
5.4.1 Single channel thermal-hydraulics instability 89
5.4.2 Coupled neutronic regional out-of-phase instability 90
5.4.3 Coupled neutronic core-wide in-phase instability 91
5.5 Stability Analyses of High Power Density BWR Designs 93
5.5.1 Key Operating Parameters Affecting Stability 93
5.5.2 Stability Analysis Results for LASP and CST at Uprated conditions 95
5.5.3 The Effects of Power Uprates on Stability in the CST Core 97
5.6 Stability Analysis of LASP - Design Effects and Parametric Study 100
5.6.1. The Effects of Water Rods and Partial Length Rods 100
5.6.2 Sensitivity Analyses for Single Channel Stability 102
5.6.3 Sensitivity Analyses for Regional Out-of-Phase Stability 104
5.6.4 Sensitivity Analyses for Core-Wide In-Phase Stability 107
5.6.5 Pin Diameter Effects on Stability Performance 110
5.6.6 Stability Exclusion Region 111
5.7 Summary 112
6. Stability Analysis of the Reduced Moderation RBWR Designs 114
6.1 Introduction 114
6.2 Overall thermal-hydraulic characteristics of RBWRs 115
6.3 Methods Description 119
6.4 Stability Analysis of RBWR-AC 127
6.4.1 Single Channel Stability analysis 127
6.4.2 Coupled neutronics stability analysis 130
6.4.3 Reflector effects on stability analysis 131
6.4.4 Axial power shape effects on stability analysis 132
6.4.5 Neutronics modeling effects on stability analysis 134
6.5 Stability Analysis of RBWR-TB2 136
6.5.1 Single channel stability analysis 136
6.5.2 Coupled neutronics stability analysis 139
6.6 Summary 141

5. Stability of High Power Density BWR Designs

Substantial design and development programs are underway worldwide for further technology improvements in LWRs and for development of advanced nuclear power plant designs. Considering the large effort of establishing new design concepts, especially for the new reactor coolant (such as SFR), and the expected replacement of existing nuclear power plants in the next twenty years, it is expected that the light water reactor will play the main role in the electric power generation for many decades to come.

A list of advanced BWR designs [IAEA, 2004] including type, size, design organization and status was summarized by IAEA, provided in Table 1-1, in which the SCPR, RMWR, and RBWR are among the category of innovative designs, others (such as ESBWR) are among the category of evolutionary designs. Improved economic competitiveness and enhanced safety are the common goals in these advanced designs. Also, extensive work has been done at MIT to assess the feasibility of increasing the core power density of existing and future BWRs, through innovative geometry and/or the materials of the fuel assembly. The large assembly with small pins (LASP) design and the cross shape twisted (CST) fuel rod design were chosen as the most promising concepts among the examined ideas [Kazimi, et al., 2006].

The advanced designs, however, could have major consequences for the stability performance. Since the design changes will persist due to economic reasons and/or concerns of sustainable nuclear power, the instability potential needs to be addressed. In this chapter and the next one, the stability performance of several advanced BWR designs will be assessed, focusing on the key design effects. In Chapter 5, the stability analyses of the high power density large assembly design and the CST design were conducted. The stability performance of Hitachi's RBWRs is described in Chapter 6.

5.1 Introduction

The large assembly with small pins (LASP) design and the cross shape twisted (CST) fuel rod design are the two most promising fuel designs for high power density BWRs among the examined options at MIT. Besides the consideration of the Minimum Critical Power Ratio (MCPR), the stability of the flow against density wave oscillations is important to ascertain under all expected operating conditions.

The objective of this work is to determine the margin for stability of operation in BWRs with high power density designs: the LASP design and CST fuel design, in comparison to the conditions in conventional BWRs. The focus is on investigation of stability against density wave oscillation.

5.2 Fuel Designs for High Power Density BWRs

5.2.1 Large Assembly with Small Pins Concept

Figure 5.1 shows a schematic illustration of the LASP core compared to the reference core which has the current 9x9 fuel [Karahan et al., 2007]. The LASP core concept is based on replacing four traditional assemblies and the associated water gap regions between them with a single large assembly, so that the number of assemblies of the LASP core is ¼ that of the reference core. The LASP has a 22×22 square lattice, in which the traditional BWR cylindrical UO_2 fuelled zircaloy clad fuel pin design is retained. This study assumed that the reactor thermal power of the reference core is uprated by 20 % using the LASP fuel. Out-of-core components, for example the reactor pressure vessel, steam separators, and jet pumps, are assumed to be the same as the reference plant. The total core height, active fuel height, partial length rod height, channel power factor (radial peaking factor) as well as power to flow ratio in each channel are also set equal to those of the reference core.

Since the inter-assembly water gap area is reduced, twenty-five water rods are placed within the assembly to maintain neutron moderation and to accommodate 25 finger-type control rods, similar to PWRs. However, the control rods are still inserted through the

same penetrations from the bottom of the RPV. The total number and positions of the control rod mechanisms are not changed from the reference core, so existing BWRs can be retrofitted with this new fuel assembly concept.

The LASP core adopted a smaller fuel pin and larger pitch-to-diameter ratio than the reference core. These modifications create larger margin to dryout and thus open the possibility for power density uprate. Although the fuel to moderator ratio has been preserved, the higher pitch-to-diameter ratio results in a larger void reactivity coefficient. According to the 3D neutronic simulation in [Karahan et al., 2007], the LASP has 25 % more negative void reactivity coefficient and 35 % more negative Doppler coefficient than those of the reference core.

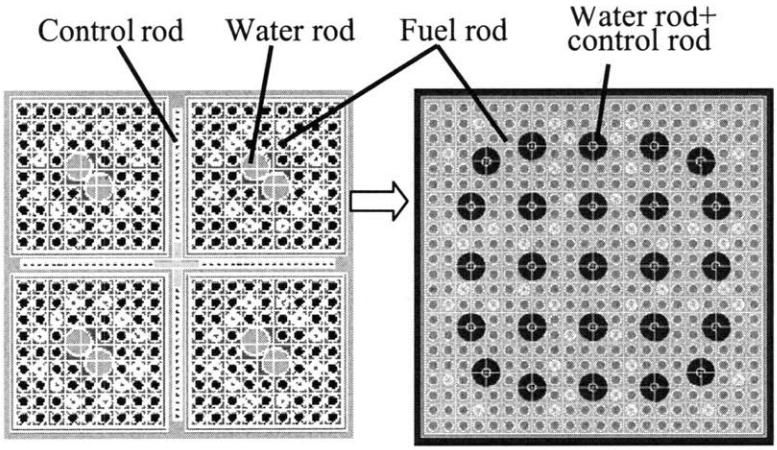

(a) Four current 9x9 assembly (b) LASP assembly

Figure 5.1: Schematic illustration of LASP core (from [Karahan et al., 2007])

5.2.2 Cross-Shaped Twisted Fuel Pin Design

The CST fuel assembly design is based on a modification of the General Electric BWR 9x9 reference assembly, maintaining the same assembly wall dimensions, number of fuel pins, and overall fuel mass. This fuel assembly is highly distinctive in its axially-twisted pin, whose cross-sectional geometry resembles a cross (or a 4-petaled flower), but retains the UO_2 pellet and zircaloy clad in the fuel pin. As shown in Figure 5.2, the spiral pins fill an assembly in a tight bundle such that the petals of neighboring pins contact each

other at their outer-most extent in a self-supporting lattice, without the presence of grid spacers. The twisted fuel pin could have a 40% increase in surface area over a traditional cylindrical pin. [Conboy et al., 2007]

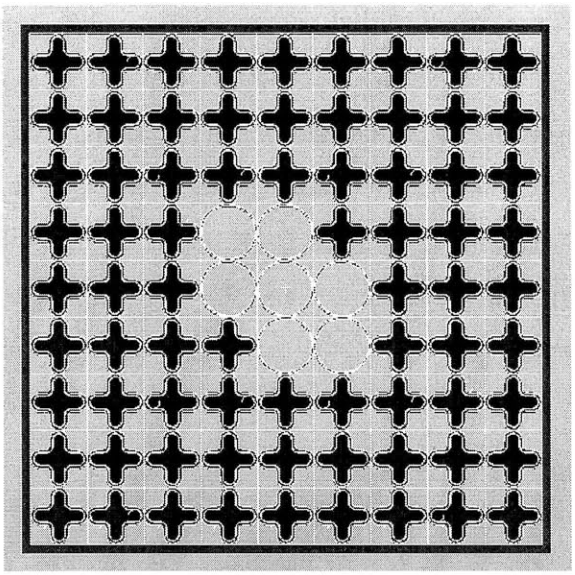

Figure 5.2: The 9x9 spiral fuel assembly
(from [Conboy et al., 2007])

As shown in Figure 5.3, the petals come into contact with one-another once for every 90° axial-twist, and remain out of contact until the next 90° twist has been completed further along the length of the pin.

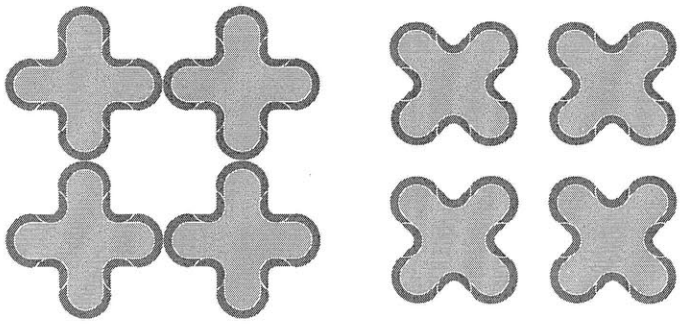

Figure 5.3: (Left) Petals in contact; (Right) petals at their furthest distance from contact (45°)
(from [Conboy et al., 2007])

5.3 Stability Analysis Method

A wide range of time domain codes and frequency domain codes can be used to evaluate the stability performance of a reactor. As frequency domain methods can be used more efficiently to carry out sensitivity analyses compared to time domain codes, a frequency domain linear stability code, STAB, was developed to investigate BWRs stability at MIT. It was confirmed that the STAB code shows good agreement with low flow stability test results at Peach Bottom 2 (BWR/4) reactor [Zhao, et al., 2005], which is re-examined in Appendix C. The STAB code was also applied to ESBWR design which has Partial Length Rods (PLRs), and achieved reasonable results [Hu and Kazimi, 2007].

In stability analyses using the frequency domain method, reactor stability is judged by the perturbation decay ratio. The decay ratio is defined as the ratio between the first and second peaks of the system oscillation in the impulse response. A reactor is stable if the decay ratio is below 1.0. However to allow for uncertainties and varying operating conditions the acceptance criteria used by GE for ESBWR is 0.5 for the single channel thermal-hydraulics instability and 0.8 for regional and core-wide instability [GE-Hitachi Nuclear Energy, 2008]. We adopt these conservative criteria in this work for the LASP core. Table 5-1 summarizes the criteria used in this study.

Table 5-1: Criteria for BWR Stability

Instability mode	Criterion
Single channel thermal-hydraulics	Decay ratio is below 0.5
Regional out-of-phase	Decay ratio is below 0.8
Core-wide in-phase	Decay ratio is below 0.8

To determine the quality and void distribution, either the Homogeneous Equilibrium Model (HEM) or the Non-Homogeneous Equilibrium Model (NHEM) based on the Bestion drift flux correlation [Bestion, 1990] can be selected in STAB. HEM is applied in this analysis as the HEM predictions are always more conservative in predicting the stability conditions compared to the non-homogeneous models. In the drift flux model, the vapor velocity is always higher than that of the liquid. Thus, the void fraction would be smaller in the heterogeneous model for the same equilibrium quality as the

homogeneous model. Also, to be conservative, the two-phase friction multiplier is assumed to be twice the HEM value of ρ_l / ρ_m.

A lumped fuel dynamics model with the temperature distribution in the fuel pin developed at Brookhaven National Lab [Wulf et al., 1984] is applied, as described in Chapter 3. The fuel dynamics model is coupled to the coolant thermal-hydraulics model through the dynamics of the fluctuation of the fuel rod's surface heat flux.

The thermal-hydraulic model is then coupled to the neutronic dynamic model through the fuel Doppler reactivity feedback and coolant density reactivity feedback. The point kinetics model is used for the neutronics in the code. For core-wide effects, both the radial and axial power distributions are taken into account. The effects of reactivity changes are summed up by weighting the local reactivity changes by the square of the local power fraction. A detailed description of the neutronics model in the STAB code can be found in [Zhao et al., 2005] and [Hu and Kazimi, 2007], as given in Appendix D.

For out-of-phase type instability, the subcritical modes can become unstable under certain conditions even when the fundamental mode is stable. To obtain the first subcritical neutronic dynamic mode, the modal expansion method for point kinetics equation based on the so-called λ modes was applied. The subcritical reactivity ρ_m^s can be calculated using the formula derived by [March-Leuba and Blakeman, 1991]:

$$\rho_m^s = D\nabla B^2 / \nu\Sigma_f \qquad \textbf{(5-1)}$$

Where,

D: diffusion coefficient

Σ_f : fission macroscopic cross section

ν : number of neutrons per fission

∇B^2 : the geometric buckling difference between the fundamental and mth mode

The details of STAB code could be found in [Hu and Kazimi, 2007].

5.4 Considered BWR Instability Types

According to [Lahey and Moody, 1993], the most important instability types that are of interest in the BWR technology are the density wave oscillations (DWO). In this work, three types of density wave oscillations: single-channel, regional (also called out-of-phase), and core-wide (or in-phase), are all analyzed. Each of these three instability modes is briefly described in this section.

5.4.1 Single channel thermal-hydraulics instability

The BWR fuel assembly is contained in a channel box to manage coolant distribution among different assemblies. Consequently, a small fluctuation in the flow rate of any single channel will not affect the total flow rate of the remaining channels. Therefore, a constant pressure drop boundary condition can be imposed on that single channel. Also, the neutronic feedback due to flow fluctuation of a single channel will not affect the whole core neutronic properties. So, a single channel can oscillate on its own without the neutronic feedback. The mechanism of single channel DWO in a parallel channel system can be illustrated by Figure 5.4. In single channel thermal-hydraulics stability analyses, only the hottest channel is evaluated because the hottest channel is expected to show the highest tendency for the instability phenomena.

If some external forces or disturbances create a small change in the inlet flow, the local coolant density in the compressible coolant in the channel will experience a fluctuation, and a density wave will propagate towards the exit along with the flow. This density wave will cause the local pressure drop to fluctuate or oscillate with some time delay with respect to the inlet flow. In some situations, the channel total pressure drop may experience an 180° phase lag with respect to the inlet flow as shown in Figure 5.4. The exit pressure may attempt to decrease, but the constant external pressure boundary condition of a parallel channel system such as a BWR core will then generate an inlet velocity feedback to the oscillating channel, which will attempt to increase the flow increment amplitude of the initial flow forcing the system to become unstable.

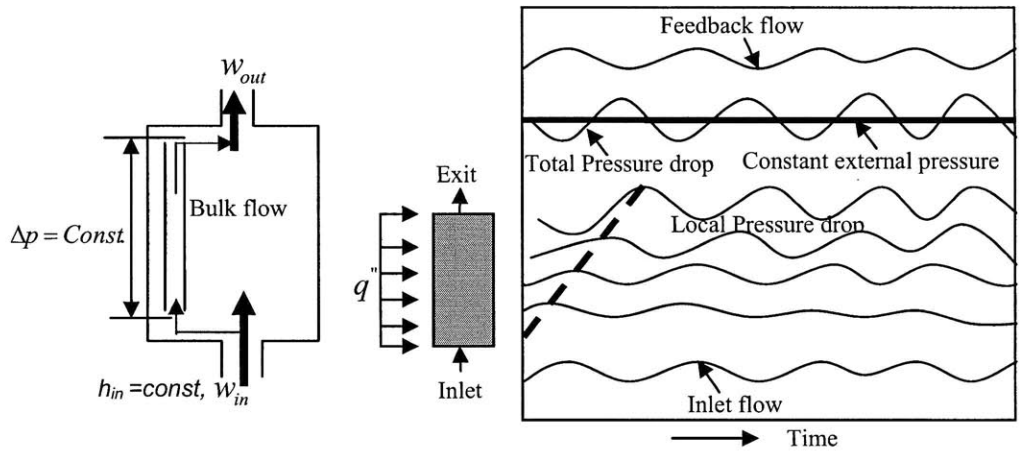

Figure 5.4: Mechanism of DWO instability in a single heated channel

5.4.2 Coupled neutronic regional out-of-phase instability

Regional out-of-phase oscillations in BWRs have been observed in some reactors during stability tests and also during start up conditions. In the tests at Caorso plant in Italy [Gialdi, et al., 1985], local power oscillations as large as 70% occurred while the average reactor power oscillated by only 12%. For automatic safety systems in BWRs that rely on total power measurements to scram the reactor, large amplitude out-of-phase oscillations can occur without reactor scram.

In regional out-of-phase instability, about half of the core behaves out-of-phase from the other half. During the oscillation, half of the core rises in power while the other half decreases to maintain an approximately constant total core power. Also, the system adjusts flow from one half of the core to the other half while keeping the total flow rate almost constant. The thermal-hydraulics and neutronic models for out-of-phase stability analysis are illustrated in Figure 5.5. As seen in Figure 5.5, the core model includes two regions, each representing one half of the core. Each region is modeled as consisting of three subregions depicting the hot, middle and low power assemblies.

Using the TRAC/BF1 code, Hotta et al. [2001a] analyzed the effects of thermal-hydraulic regional representation on BWR out-of-phase stability, and found that the stability is not sensitive to the number of lumped channels in the core. Using the STAB code, Zhao et al.

[2005] also reached the same conclusion, provided there are at least three zones in each region of the modeled core. Using the point kinetics model in the STAB code, the neutronic feedback is controlled by the core average properties (void fraction and fuel temperature). Since the core thermal hydraulic lumping approach will not change the core average properties, the BWR out-of-phase stability is not sensitive to the degree of core channel lumping, provided that the peak power assemblies as well as the average power assemblies and the inlet orifice groups are represented. Thus, using three subregions for each half of the core appears to be the most concise choice that includes the important physical effects.

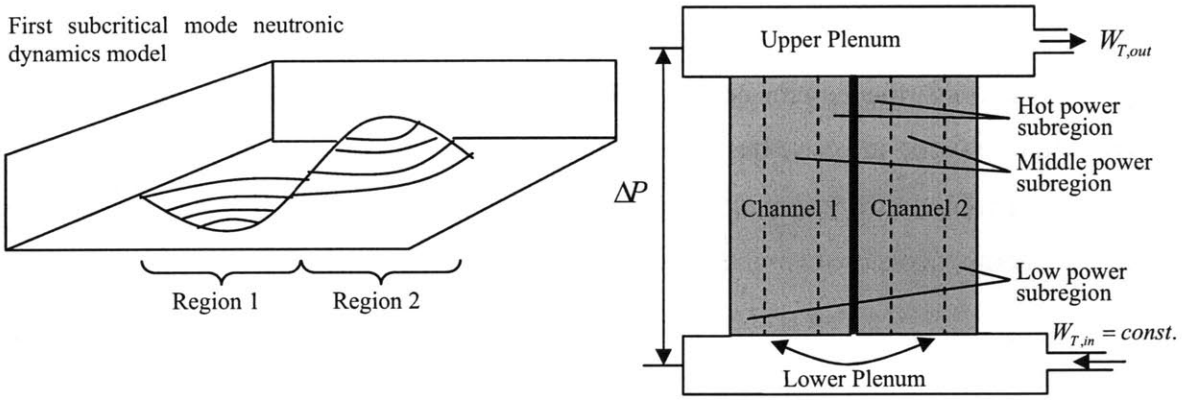

Figure 5.5: Illustration of out-of-phase stability model

5.4.3 Coupled neutronic core-wide in-phase instability

Core-wide in-phase instabilities have been observed in several BWRs under close-to-natural circulation conditions where the stability margin is lowest in the power/flow map. The term "core-wide in-phase" refers to the case when oscillations of the neutron flux and flow in the whole core are in-phase. The boiling two-phase flow in the core may become less stable because of the time lag between accommodating a mass flow change at one location and through adjustments of mass flow due to a different density at another location in a channel, or through adjustments of vapor generation. Furthermore, void reactivity feedback may make the system less stable.

The thermal-hydraulics and neutronic models in core-wide in-phase instability can be illustrated in Figure 5.6. The whole core is assumed to consist of three subregions

representing hot, middle and low power fuel assemblies. Unlike the single channel oscillation mode, in which the pressure drop across the single channel remains constant, the core pressure drop during the core-wide in-phase oscillation will fluctuate, and the magnitude of fluctuation is constrained by out-of-core components. The upper plenum, riser, steam separators, downcomer, jet pumps, lower plenum, and the recirculation loop are modeled in the in-phase stability analysis. Also, unlike the regional out-of-phase oscillation, which adjusts the flow between two halves of the core to maintain an almost constant total inlet flow rate, the core inlet flow rate may oscillate during the in-phase oscillation, and the feedback of the inlet flow rate is transmitted by the flow dynamics in the out-of-core components. Furthermore, the in-phase instability mode affects all components in the flow path, while both the single channel instability and the out-of-phase instability modes can be described focusing on a parallel channel system in the core. In core-wide in-phase oscillations, the reactor core is just one of the components in the flow path, and the entire flow path is involved. Therefore, pressure drops in the out-of-core components are also modeled in this analysis.

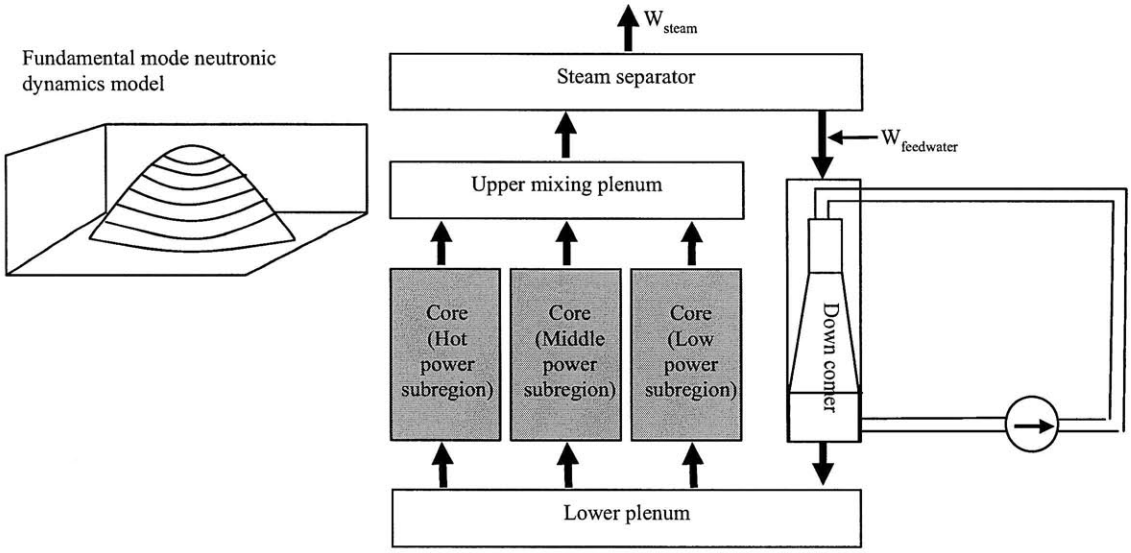

Figure 5.6: Illustration of in-phase stability model

5.5 Stability Analyses of High Power Density BWR Designs

5.5.1 Key Operating Parameters Affecting Stability

The overall design parameters of the LASP and CST designs are described in [Kazimi et al., 2006]. The important thermal-hydraulic/neutronic parameters of the two designs related to stability analyses are listed in Table 5-2, along with those of the reference BWR design in [Kazimi et al., 2006].

Table 5-2: Design Parameters for Stability Analysis under design conditions

Parameters	Ref.	Large Assembly†	CST†
Core thermal power (MW)	3323	3988	3988
Core coolant flow rate (kg/s)	13700	16440	16440
No. of fuel bundles	764	191	764
No. of fuel pins per bundles	74	384	74
Assembly flow area (cm^2)	96	489	88.9
Assembly wetted perimeter (cm)	337	1576	409.8
Assembly hydraulic diameter (cm)	1.14	1.24	0.87
Core average exit quality (%)	13.1		
Hot channel power peaking factor	1.45		
Inlet orifice coefficients	21.1 (central)		
Inlet subcooling	The same		
Axial power distribution	The same		
Grids coefficients	The same		None
Friction factor in the core	Regular		Reduced
Void coefficients ($\Delta k/k/\%void$)	-1.44×10^{-3}	-1.80×10^{-3}	-1.44×10^{-3}
Doppler coefficients ($\Delta k/k/^oC$)	-1.70×10^{-5}	-2.30×10^{-5}	-1.70×10^{-5}

†: The LASP and the CST designs have 20 % higher reactor thermal power and flow rate than the reference core.

The important changes for the large assembly design affecting the stability performance include the fuel geometry and void reactivity coefficients. The detailed neutronic analysis for the CST fuel design has not been done yet, so the void reactivity coefficient is chosen the same as the reference design. This assumption is reasonable because the H/HM ratios for the two designs are similar, and they have the same interassembly gap thickness and number of water rods. Thus, the important changes for CST design affecting the stability

performance include the fuel geometry, the removed spacers, and the changes of friction factor.

The experiments performed at MIT twisted rod bundle facility confirmed that the friction factor of the twisted fuel is for the same Reynolds number smaller than that of the bare rod bundle [Conboy et al., 2007]. This is due to a smaller hydraulic diameter of the twisted rod bundle. The results of pressure drop experiments correlate the reference friction factor with a best fitting factor k_{CST} as:

$$\Delta P = k_{CST} \frac{f_{ref} L}{D_e} \frac{\rho v^2}{2}, \; k_{CST} = 0.9 \qquad \textbf{(5-2)}$$

There are several key parameters affecting the reactor stability. These are the void coefficient, single phase/two phase pressure drop ratio, fuel thermal time constant, power/flow ratio, and core size. The ranges of these parameters are compared between the high power density designs and the reference BWRs to assess the applicability of the experience of the operating BWRs to the high power density design.

Void Coefficient

The void coefficient of the large assembly design is 25% more negative than the reference design, while the value (-180 pcm/%void) is within the range of operating BWR cores.

Single Phase/Two Phase Frictional Pressure Drop

The values of high power density designs are similar to that of the reference design.

Fuel Thermal Time Constant

The large assembly design applied smaller fuel pins, which should have a smaller fuel time constant. However, the fuel pin outer diameter is close to that of the ESBWR. The fuel time constant of the CST design is considered smaller than that of the reference design, as the surface to volume ratio of the CST design is larger. However, the effect of fuel time constant to stability is small, as shown in [Hu and Kazimi, 2007].

Reactor vessel internals

The reactor vessel internals, such as the upper plenum, separator, downcomer of the high power density designs are kept the same as the reference design.

Power/Flow Ratio

In general, the reactor is more stable with lower power/flow ratio. The power-to-flow ratio is kept the same for the high power density designs.

Core Size

The high power density designs are considered to fit in the current BWR reactor vessel, thus the average core sizes are not changed.

5.5.2 Stability Analysis Results for LASP and CST at Uprated conditions

As discussed above, the BWR out-of-phase stability is not sensitive to the degree of channel lumping. A three channel model (high power channel, intermediate power channel, and low power channel) is sufficient to conduct regional and core-wide stability analysis. The detailed lumping parameters for the large assembly design, CST design, and the reference BWR, are listed in Tables 5-3 through Table 5-5. For the candidate designs, the flow of each channel and the orifice coefficient of low power (peripheral) channel are taken from a previous work in [Karahan et al., 2007].

Table 5-3: Parameters in the three lumped channels of the reference core at 100% Power

Assembly Type	# of Assemblies (Reference)	Assembly Power (MW)	Flow per assembly (kg/s)	Orifice Coefficient
Hot	148	5.65	15.79	21.1
Average Power	500	4.37	16.82	21.1
Low Power	116	2.61	8.93	182.0

Table 5-4: Parameters in the three lumped channels of the LASP Core at 120% Power

Assembly Type	# of Assemblies (LASP)	Assembly Power (MW)	Flow per assembly (kg/s)	Orifice Coefficient
Hot	37	27.14	75.99	21.1
Average	125	20.96	81.21	21.1
Low	29	12.53	40.59	214.0

Table 5-5: Parameters in the three lumped channels of the CST Core at 120% Power

Assembly Type	# of Assemblies (CST)	Assembly Power (MW)	Flow per assembly (kg/s)	Orifice Coefficient
Hot	148	6.78	18.94	21.1
Average Power	500	5.24	20.19	21.1
Low Power	116	3.13	10.71	182.0

The calculated decay ratios for the three designs are listed in Table 5-6.

Table 5-6: Results of stability analysis at design conditions

Mode	**Reference**		**LASP**		**CST**	
	Decay Ratio	Frequency (Hz)	Decay Ratio	Frequency (Hz)	Decay Ratio	Frequency (Hz)
Single-Channel	0.12	1.02	0.115	0.90	0.098	1.37
Regional (Out-of-phase)	0.12	0.83	0.25	0.78	0.077	1.10
Core-wide (In-phase)	0.31	0.58	0.42	0.64	0.233	0.92

In single-channel DWO stability analysis under design conditions, it is found that the flow oscillation decay ratio of the CST design is smaller than that of the reference BWR, indicating a bit more robust thermal-hydraulic stability margin, while the decay ratio of the LASP design is almost the same as the reference design.

However, in the coupled regional and core-wide stability analyses, the decay ratio of large assembly design is much larger than that of the reference BWR. It is dominantly affected by the larger void reactivity coefficients. However, it is still below the design limit of $DR=0.8$ for the core-wide instabilities.

In all oscillation modes, the decay ratios of the CST design are a slightly smaller than those of the reference BWR, due to the reduction of the overall friction loss and the reduction of two-phase pressure loss to single-phase pressure loss ratio.

In all cases, the oscillation frequencies of the CST design are the highest among the three designs. This is consistent with the understanding that the higher average flow velocity results in higher oscillation frequency.

5.5.3 The Effects of Power Uprates on Stability in the CST Core

It is shown in Table 5-7 that, in the single-channel modes, the decay ratios at 20% uprated conditions are very close to those at 100% power conditions for the CST design, indicating the stability performance is dependent on the power-to-flow ratio. Power uprates when maintaining the power-to-flow ratio do not have significant impact on single-channel stability performance. However, the increase of core total flow rate slightly increases the stability margin in the coupled regional (out-of-phase) and core-wide (in-phase) mode. It is also seen that, in all cases, the oscillation frequencies under uprated conditions are higher than those under rated conditions due to the increase of flow velocity.

Table 5-7: Results of CST stability analysis at 100% power and uprated conditions

	CST (100% power)		CST (120% power)	
Mode	Decay Ratio	Frequency (Hz)	Decay Ratio	Frequency (Hz)
Single-Channel	0.101	1.15	0.098	1.37
Regional (Out-of-phase)	0.102	0.93	0.077	1.10
Core-wide (In-phase)	0.251	0.77	0.233	0.92

However, if higher enrichment is needed for the CST design to facilitate higher power density at the same fuel cycle length, a harder spectrum is expected. Hence, the void coefficient would be different in the CST design. Therefore, the influence of the void

reactivity coefficients on in-phase oscillations is investigated for the CST design. It is shown in Figure 5.7 that the calculated decay ratios from the assumed void coefficients are all very small, comparing to the design limit of *DR=0.8*.

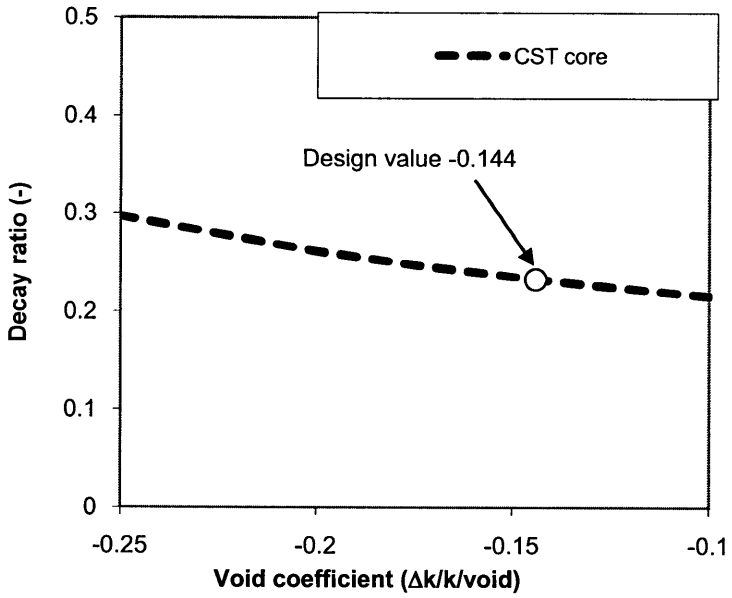

Figure 5.7: Stability sensitivity to void feedback coefficients of CST design, in-phase

It can be concluded that the power uprate for the CST design does not pose stability problems. However, the Critical Power limit should be also checked for the power uprate, since the increase of flow rate and cross flow would decrease the critical heat flux under dryout conditions.

The hot fuel assembly is analyzed as a single channel, ignoring the inter-assembly flow distribution. A VIPRE model for CST was applied in Kazimi et al. [2006], and accounted for the cross flow, but remains subject to uncertainties about the appropriate correlations. A one-dimensional thermal-hydraulic code is developed in the MATLAB platform to calculate the CPR in the hot channel. This was deemed easier than applying the standard code like VIPRE, as long as the appropriate flow in the hot channel was estimated. The flow quality and the critical quality are calculated under the design operating conditions. Then, the CPR can be calculated by progressively increasing the channel (fuel assembly) power until the flow quality exceeds the critical quality at any location. The CISE-4

correlation [Todreas and Kazimi, 1990], also attached in Appendix A, for the conventional BWR fuel bundle is applied in this work as a first attempt. It would be replaced if the specific correlation for the CST fuel assembly is derived from the critical heat flux experiments for CST fuel at MIT.

The CPR analysis results for the reference design and CST fuel under both normal operating and uprated power conditions are listed in Table 5-8.

Table 5-8: Critical power ratio for the reference design and CST fuel

	Reference Design		CST	
	100% power	120% power	100% power	120% power
CPR	1.50	1.35	1.59	1.47

From Table 5-8, the CPR of the CST design under 120% is 1.47, a large margin to the critical heat flux limit. However, it should be noted that the effect of cross flow in the CST fuel is not included in this analysis. Also, the local critical heat flux is more limited if the effects of non-uniform power distributions in the assembly and in the surface on a single fuel rod are considered. A detailed sub-channel analysis is still required.

It is also seen that the CPR of the CST design is larger than that of the reference bundle design for both rated and uprated conditions, due to higher hydraulic diameter to heated diameter ratio D_e / D_h in the CISE-4 correlation. Of course, the effect of the CST twisted geometry on the dryout CHF at rated and uprated power and flow conditions are not known. But at the same flow quality distribution, it is expected that the CHF will be smaller at the uprated conditions due to the higher coolant velocity of the uprated case.

5.6 Stability Analysis of LASP - Design Effects and Parametric Study

To develop guidance for designers to avoid the instabilities during the operation of BWRs, stability sensitivity analyses are conducted for the LASP, including both operating parameter sensitivity and the effects of the design features.

5.6.1. The Effects of Water Rods and Partial Length Rods

The effects of Water Rods (WRs) and Partial Length Rods (PLRs) are first investigated, since the presence of existing water rods and partial length rods was neglected in the initial runs. The fuel assembly parameters of the reference and LASP core are listed in Table 5-9 and 5-10, while the analysis results are summarized in Table 5-11. In the cases without WRs and/or PLRs, these components were replaced by full length fuel rods.

Table 5-9: Comparison of the Fuel Assembly Design for Reference and LASP Cores

Parameters	Ref. core (9x9 fuel)	LASP core
Reactor thermal power (MW)	3323	3988
Core flow rate (kg/s)	13700	16400
Number of fuel assemblies	764	191
Assembly inner dimension (mm)	132.5	289.7
Number of full length fuel pins	66	372
Number of part length rods	8	12
Number of water rods	2	25
Fuel pin outer diameter (mm)	11.2	9.6
Fuel pin pitch (mm)	14.3	13.1
Active fuel pin height (m)	3.71	3.71
Part length rod height (m)	2.44	2.44
Water rod outer diameter (mm)	24.9	27.2

Table 5-10: Comparison of major hydraulics parameters

Items	Reference core			LASP core		
	W/o WRs and PLRs	With WRs, w/o PLRs	Base design†	W/o WRs and PLRs	With WRs, w/o PLRs	Base design†
Flow area in PLR region (m^2)	0.0096	0.0093	0.0093	0.0489	0.0417	0.0417
Flow area above PLR region (m^2)	–	–	0.0101	–	–	0.0425
Wetted perimeter in PLR region (m)	3.37	3.28	3.28	15.76	14.87	14.87
Wetted perimeter above PLR region (m)	–	–	3.00	–	–	14.51
Hydraulics diameter in PLR region (mm)	11.4	11.3	11.3	12.4	11.2	11.2
Hydraulics diameter above PLR region (mm)	–	–	13.4	–	–	11.7
Inlet coolant mass flux ($kg/m^2/s$)	1644	1697	1697	1554	1822	1822
Average heat flux (kW/m^2)	412	451	470	386	486	492

†: Base design includes both the WRs and PLRs.

Table 5-11: Analysis results of decay ratio for three instability modes

Items	**Ref. core at 100% power**	**LASP core at 120% power**
Single channel thermal-hydraulics		
Without WRs and PLRs	0.122	0.115
With WRs, W/O PLRs	0.122	0.120
Base design (with WRs and PLRs)	0.111	0.116
Regional out-of-phase		
Without WRs and PLRs	0.119	0.251
With WRs, W/O PLRs	0.110	0.186
Base design (with WRs and PLRs)	0.084	0.175
Core-wide in-phase		
Without WRs and PLRs	0.307	0.423
With WRs, W/O PLRs	0.315	0.320
Base design (with WRs and PLRs)	0.285	0.314

It is seen in Table 5-11 that for the single channel thermal-hydraulics stability, the LASP core without WRs and PLRs results in somewhat smaller decay ratio than the reference core, because of the larger hydraulic diameter. Since the hydraulic diameter of the LASP core decreases when the WRs are considered, the decay ratio of the LASP core increases. On the other hand, the decay ratio change when WRs were considered for the reference core was very small, because the reference core has few WRs. In the base design cases, both WRs and PLRs were considered. Since the reference core has more PLRs than the LASP core, their effect in the reference case is more pronounced. It is well known that PLRs improve BWR stability, because they reduce the pressure drop in the two-phase region. Thus, the decay ratio of the reference core improved more than that of the LASP core when PLRS were considered. Consequently, the LASP core showed a little higher decay ratio than the reference core. However, the obtained decay ratios of both cores were much smaller than the criterion shown in Table 5-1.

In coupled neutronic regional out-of-phase and core-wide in-phase stability analyses, the inlet coolant mass flux changes had more impact on decay ratios than the hydraulic diameter changes, so the existence of WRs much improved the decay ratios for the LASP core in contrast with the single channel thermal hydraulics stability analysis. However, because the LASP core had larger void coefficient, larger average heat flux and smaller hydraulics diameter in the PLR region, the LASP core showed higher decay ratios than the reference core. Nevertheless, the obtained decay ratios were much lower than the criterion shown in Table 5-1.

Thus, it was found that the stability performance of the LASP core can be maintained within the traditionally applied design conditions.

5.6.2 Sensitivity Analyses for Single Channel Stability

For single channel thermal-hydraulics stability, sensitivities against three parameters were investigated, accounting for both WRs and PLRs. The three parameters are

1) Inlet orifice coefficient (range: 50 – 200 % of design value);

2) Core mass flow rate (range: 70 – 120 % of design value);

3) Core thermal power (range: 80 – 130 % of design value).

Figure 5.8 shows the influence of the inlet orifice coefficient, mass flow rate and thermal power. It is well known that the single phase to two phase pressure drop ratio plays a significant role in the stability. The system is more stable when a higher single phase fraction pressure drop exists. Therefore, the inlet orifice coefficient plays a very important role in the system stability characteristics, because it strongly affects the single phase pressure drop. As shown in Figure 5.8a, the decay ratios decrease with the increase of inlet orifice coefficient, since the pressure drop increases in the single phase region. In Figure 5.8b and Figure 5.8c, it is found that the mass flow changes and the thermal power changes also affect the decay ratios. This result is consistent with the general understanding that the reactor is more stable with smaller power-to-flow ratio. It is because the two-phase pressure drop to single-phase pressure drop ratio increases when the mass flow rate decreases or the thermal power increases. From the obtained results, it can be seen that both cores have almost the same sensitivities against the evaluated three parameters. Furthermore, the obtained decay ratios are still sufficiently lower than the criterion of 0.5 within the considered parameter ranges.

The sensitivities to the analyzed parameters show their effects on the thermal-hydraulic oscillation mechanisms. Varying the inlet orifice coefficients, reactor power, and core flow rate would change the ratio of single-phase to two-phase pressure drop in the system, which is the key parameter affecting pure thermal-hydraulic DWOs. The increase of inlet orifice coefficients would increase the pressure drop in the single-phase region, thus stabilizing the system; the increase of core flow rate and decrease of reactor power would extend the single phase region, and also increase the single-phase to two-phase pressure drop ratio.

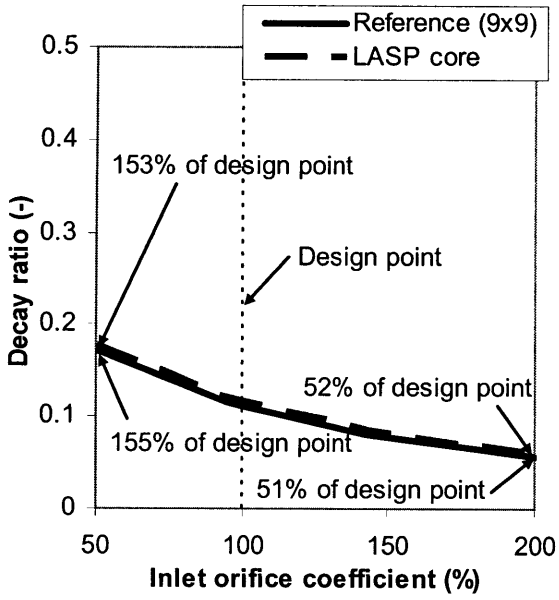

(a) Inlet Orifice Coefficient Effects

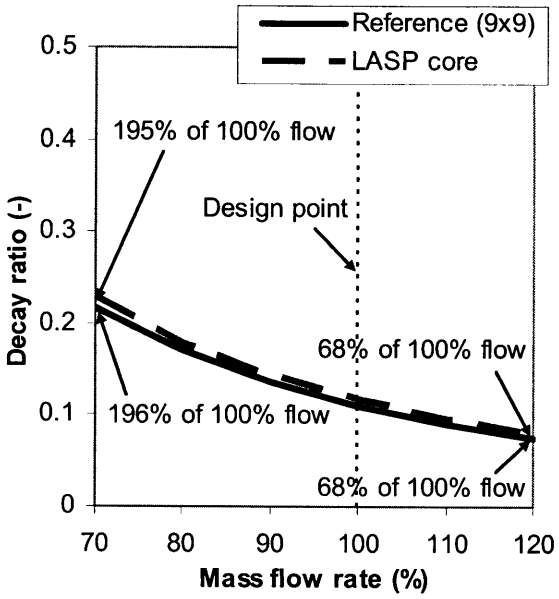

(b) Mass Flow Rate Effects

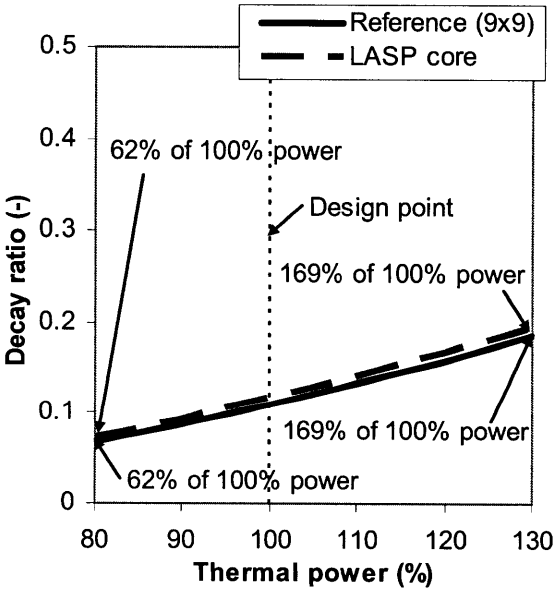

(c) Thermal Power Effects

Figure 5.8: Parametric Sensitivities of LASP Core, single-channel mode

5.6.3 Sensitivity Analyses for Regional Out-of-Phase Stability

For regional out-of-phase stability, sensitivities against five parameters were investigated. In addition to the operating conditions, void and Doppler coefficients were added as sensitivity parameters. The total studied parameters are:

1) Void coefficient (range: -0.100 to -0.250 $\Delta k/k/void$, design values are shown in Table 5-2);
2) Doppler coefficient (range: -1.00 to -3.00×10^{-5} $\Delta k/k/^{o}C$, design values are shown in Table 5-2);
3) Inlet orifice coefficient (range: 50 – 200 % of design value);
4) Core mass flow rate (range: 70 – 120 % of design value);
5) Core thermal power (range: 80 – 130 % of design value).

Figure 5.9a and Figure 5.9b show influences of the void and Doppler reactivity coefficients. In regional out-of-phase sensitivity analyses, the void and Doppler reactivity feedbacks couple the thermal-hydraulics and neutronics behavior. As shown in Table 5-2, the LASP core has a 25 % more negative void coefficient and 35 % more negative Doppler coefficient than those of the reference core. A more negative void reactivity coefficient increases neutronic feedback directly and destabilizes the core. From Figure 5.9a, it can be seen that the decay ratios of both cores increase with the reductions of void coefficient (more negative void coefficient). It was also found that the decay ratio of the LASP core is a little higher than that of the reference core, if the void coefficient of the reference core was the same as that of the LASP core. This may be caused by the differences in the channel geometries. In effect, the Doppler coefficient induces negative reactivity feedback with short delay time. Thus, it is expected to enhance stabilizing of the core. However, because the fuel temperature changes are generally mitigated by the heat capacity of fuel assembly, the influence of Doppler coefficient changes is very small compared to the void coefficient changes. The results shown in Figure 5.9b correspond to the above mentioned trend.

Figure 5.9c, 5.9d and 5.9e show influences of the inlet orifice coefficient, mass flow rate and thermal power. The decay ratio trends against the three parameters correspond to the results for single channel thermal-hydraulics stability. The sensitivities of the LASP core are similar to those of the reference core. Furthermore, the obtained decay ratios were much smaller than the criterion of 0.8 within the considered parameter ranges.

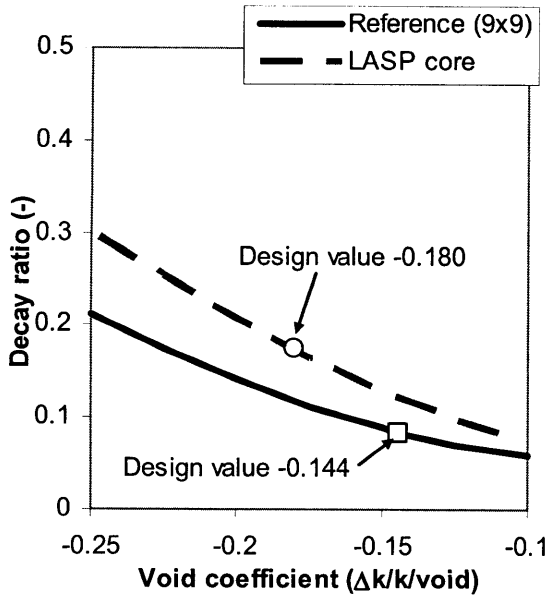

(a) Void Coefficient Sensitivity

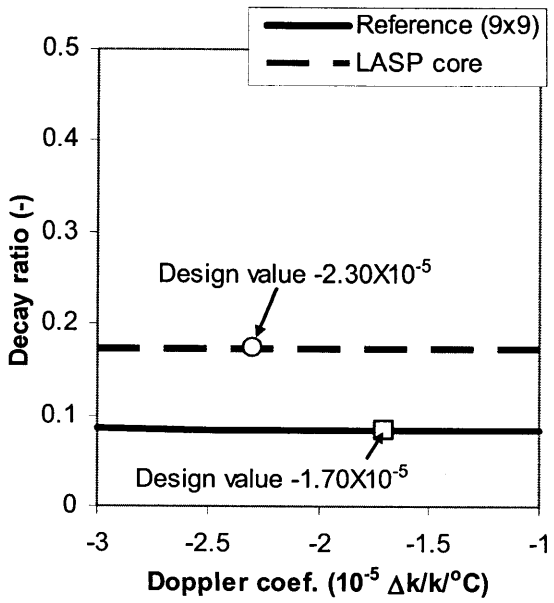

(b) Doppler coefficient Sensitivity

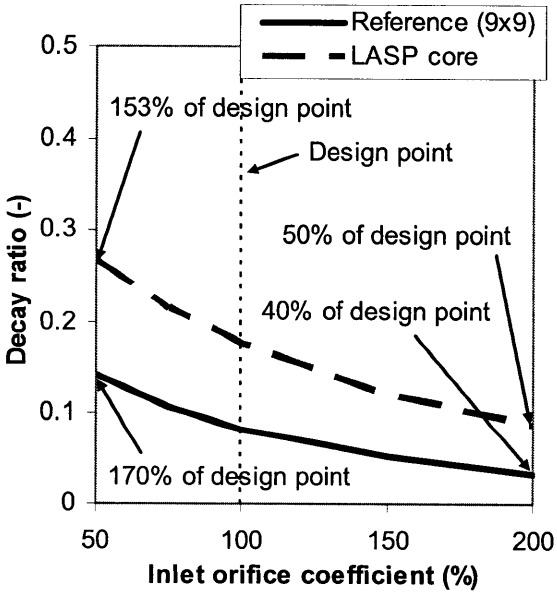

(c) Inlet Orifice Coefficient Sensitivity

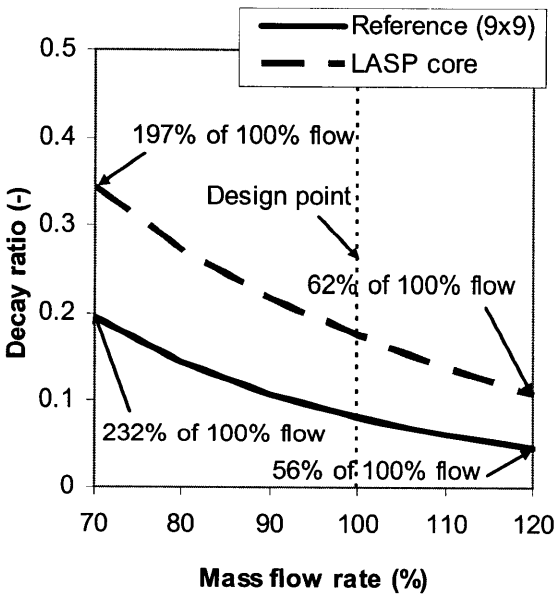

(d) Mass Flow Rate Sensitivity

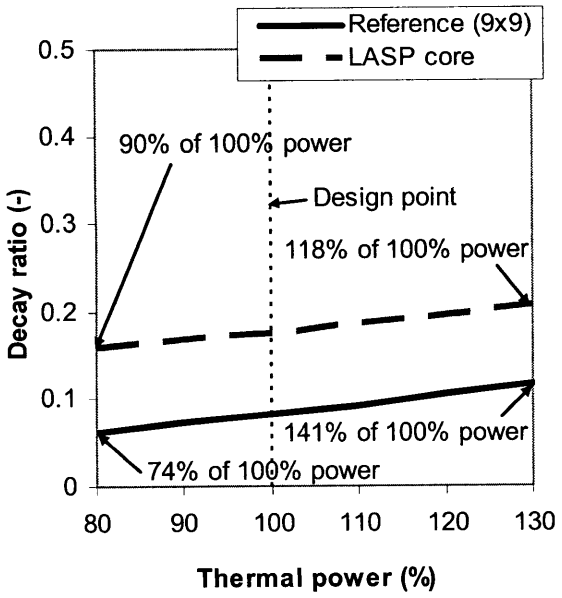

(e) Thermal Power Sensitivity

Figure 5.9: Parametric Sensitivities of LASP Core, out-of-phase mode

5.6.4 Sensitivity Analyses for Core-Wide In-Phase Stability

For core-wide in-phase stability, the sensitivities against five parameters were investigated. The chosen parameters and considered parameter ranges are the same as those for the regional out-of-phase stability:

1) Void coefficient (range: -0.100 to -0.250 $\Delta k/k/void$, design values are shown in Table 5-2);
2) Doppler coefficient (range: -1.00 to -3.00×10^{-5} $\Delta k/k/^{o}C$, design values are shown in Table 5-2);
3) inlet orifice coefficient (range: 50 – 200 % of design value)
4) core mass flow rate (range: 70 – 120 % of design value)
5) core thermal power (range: 80 – 130 % of design value)

Figure 5.10a and Figure 5.10b plot the decay ratio changes against the void and Doppler reactivity coefficients. Similar to the regional out-of-phase sensitivity analyses, the sensitivity to the void coefficient is relatively large while the sensitivity to the Doppler coefficient is very small. However, unlike the regional out-of-phase sensitivity analyses, the decay ratio of the LASP core shows almost the same value as that of the reference

core under the same void coefficient. The stability performance for the core-wide in-phase oscillation is affected by not only core characteristics but also characteristics of the out-of-core components in the flow path as mentioned in section 5.4.3. Since only the LASP core is assumed to be uprated from the reference core, the out-of-core components' characteristics are the same. Thus, the influence of core geometry differences between the two cores is small.

Figure 5.10c, Figure 5.10d and Figure 5.10e show the influence of inlet orifice coefficient, mass flow rate and thermal power. Compared with results of the single channel thermal-hydraulics stability and regional out-of-phase stability, the sensitivities to these three parameters were small, especially for the inlet orifice coefficient. In core-wide in-phase stability, neutronic feedback is dominant. Therefore, the importance of the orifice coefficient is depreciated. In Figure 5.10d, the decay ratio of the LASP core shows smaller values than the reference core below a flow rate of 90 %. In this analysis range, some convergence errors occurred in solving the characteristic equation with the Newton solver. So, there is a possibility that this tendency is an artifact of the calculation. The sensitivities of the LASP core for other parameters are similar to those of the reference core. The obtained decay ratios were much smaller than the criterion of 0.8 within the considered parameter ranges.

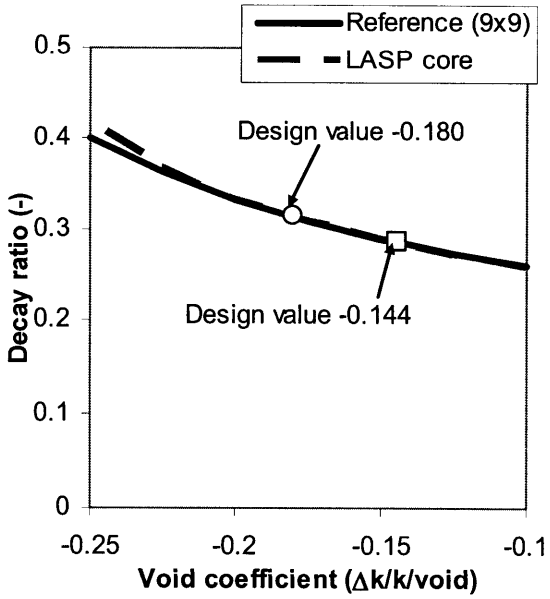

(a) Void Coefficient Sensitivity

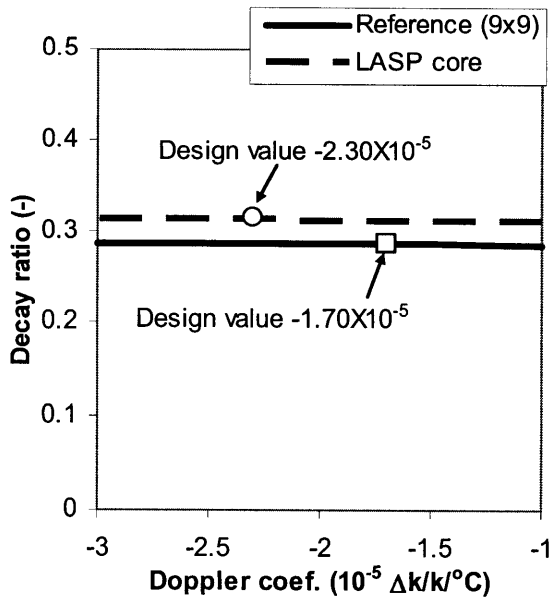

(b) Doppler coefficient Sensitivity

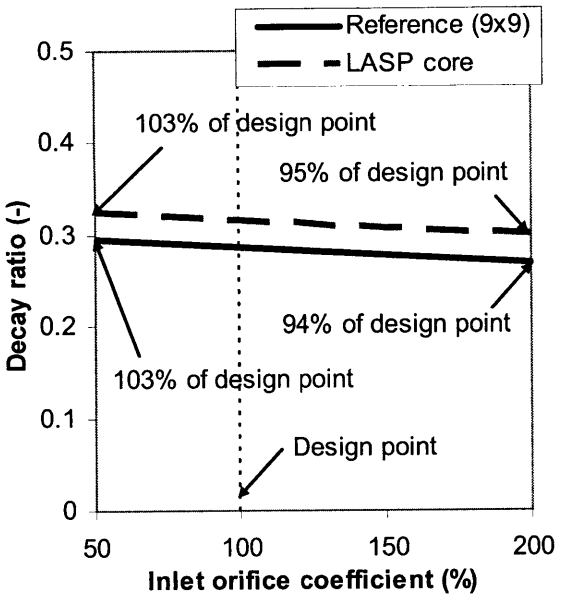

(c) Inlet Orifice Coefficient Sensitivity

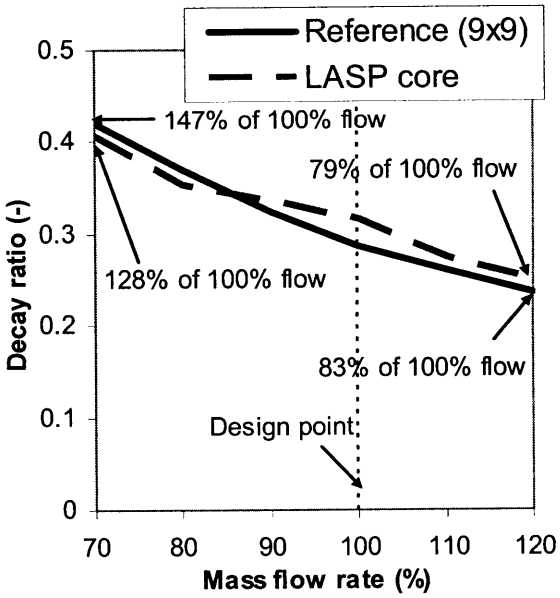

(d) Mass Flow Rate Sensitivity

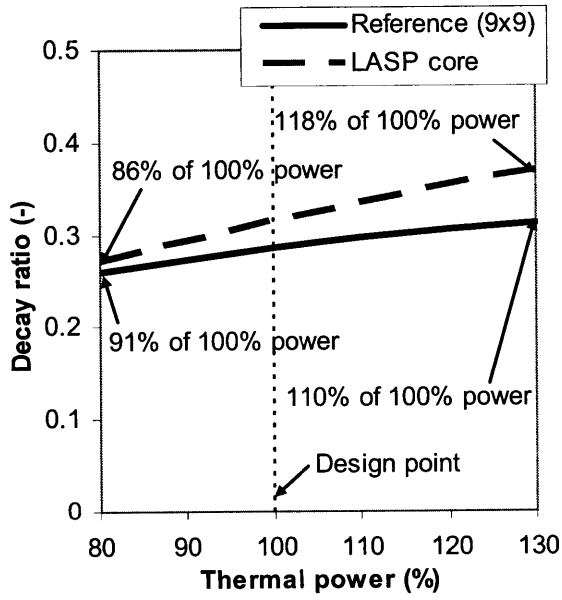

(e) Thermal Power Sensitivity

Figure 5.10: Parametric Sensitivities of LASP Core, in-phase mode

From Figure 5.8 to Figure 5.10, the parametric sensitivities of decay ratio are confirmed with the general understandings in the literature, which also agreed with the results in the previous MIT studies for SCWR and ESBWR [Zhao et al., 2005, Hu and Kazimi, 2007].

5.6.5 Pin Diameter Effects on Stability Performance

Before the change in power can affect the coolant, it has to change the fuel temperature, in order to alter the heat flux from fuel to coolant. Current commercial BWRs use Zircaloy-clad UO_2 fuel pins that have a relatively large thermal time constant in the range of 6 to 8 second [Lahey and Moody, 1993]. Thus, the change in coolant density due to changes in internal heat generation (i.e., reactivity) tends to be strongly damped. It is of interest to address the effect of the smaller pin diameter used in the LASP design on this behavior.

In reality, significant changes in the pin diameter could alter the basic neutronic and thermal-hydraulic characteristics of the reactor (such as: P/D, H/HM, flow area, pin surface heat flux, etc.). Here, it is assumed that the flow conditions (flow rate, flow area, and coolant density distribution) and the total heat generation in the fuel pin are maintained when changing the pin diameter in the sensitivity study.

As seen in Figure 5.11, when the pin diameter is increased, the decay ratio is almost unaffected in the pure thermal-hydraulic instability (i.e. single channel), but is decreased in the coupled regional and core-wide instabilities. With smaller pin diameter, the response time from the heat generation in the fuel to heat transfer to the coolant is reduced, which destabilizes the system. Furthermore, in this study, the total power in the fuel pin is maintained when the pin diameter is changed, thus, the heat flux becomes higher with smaller pin diameter, as does the perturbation of the heat flux during oscillation on the cladding wall which reduces the margin for stability of the core.

In the LASP design when operating at 20% higher core power, the average pin power is only 92.5% of that of the reference core, the average wall heat flux is 5% higher and the average volumetric heat generation rate in the fuel is 20% higher than those of the reference core. Thus, the smaller pin diameter destabilizes the LASP core besides the more negative void coefficient.

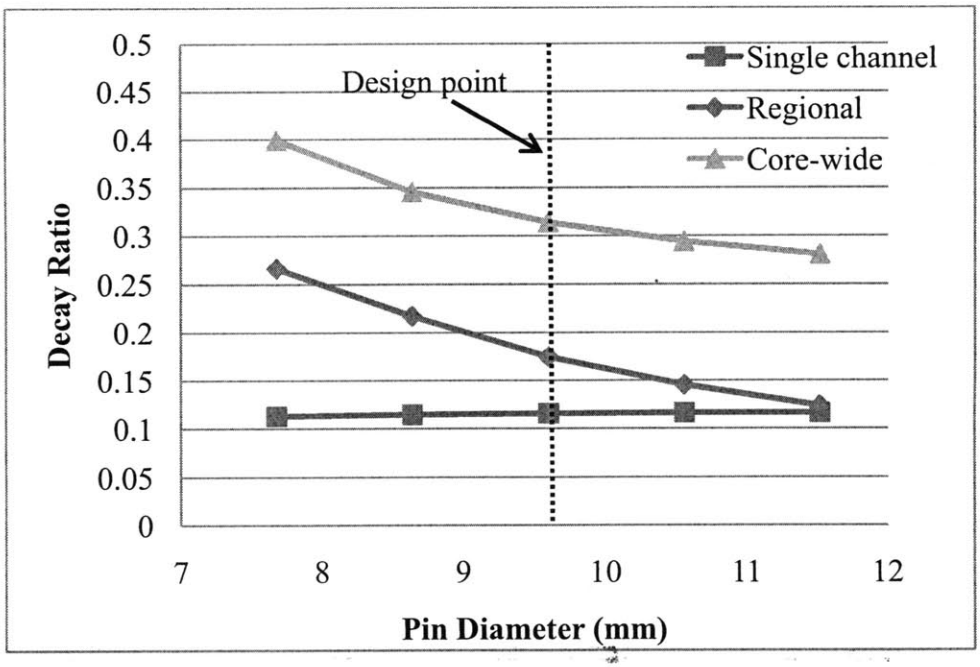

Figure 5.11: Pin diameter effects to stability performance

5.6.6 Stability Exclusion Region

All U.S. BWRs are required to have licensed stability solutions that satisfy General Design Criteria (GDC) 10 and 12 of 10CFR50, Appendix A. Solutions have been developed and implemented that combine two basic elements: a detect and suppress feature and a preventive feature. Detection and suppression of power oscillations is accomplished by specialized hardware/software, e.g., the Oscillation Power Range Monitor utilized in the Option III stability Long Term Solution (LTS). A prevention feature is provided by an Exclusion Region (ER) that is defined in the power-flow map. This was investigated in this work, as shown in Fig. 5.21. The exclusion region boundary is defined as the line of Decay Ratio equal to one, which is calculated by the STAB code. This should be a cycle specific region. However, for simplicity, the neutronic feedback coefficients are assumed the same for various operating points in this work. The exclusion region is determined from core-wide instability mode, since it is the limiting mode in the considered rand of operating conditions.

It is shown in Figure 5.12 that the LASP core is unstable when the operating points shift to low core flow and high core power region, near the transition from natural convection

to forced convection. Thus, the operating instructions for the LASP core should contain rules to avoid entering into the exclusion region. It should be pointed out that the operating power-to-flow map for LASP has not been developed yet. The minimum pump speed line, 100% control rod line, and the rated power line shown in Figure 5.12 are general for BWRs, but the exclusion region boundary is specifically for LASP core. It is also seen in Figure 5.12 that the allowed operation region of the LASP core is smaller than that of the reference core. Further investigation would be required for the reactor startup and the operation procedures in the regions with high power but low flow rate.

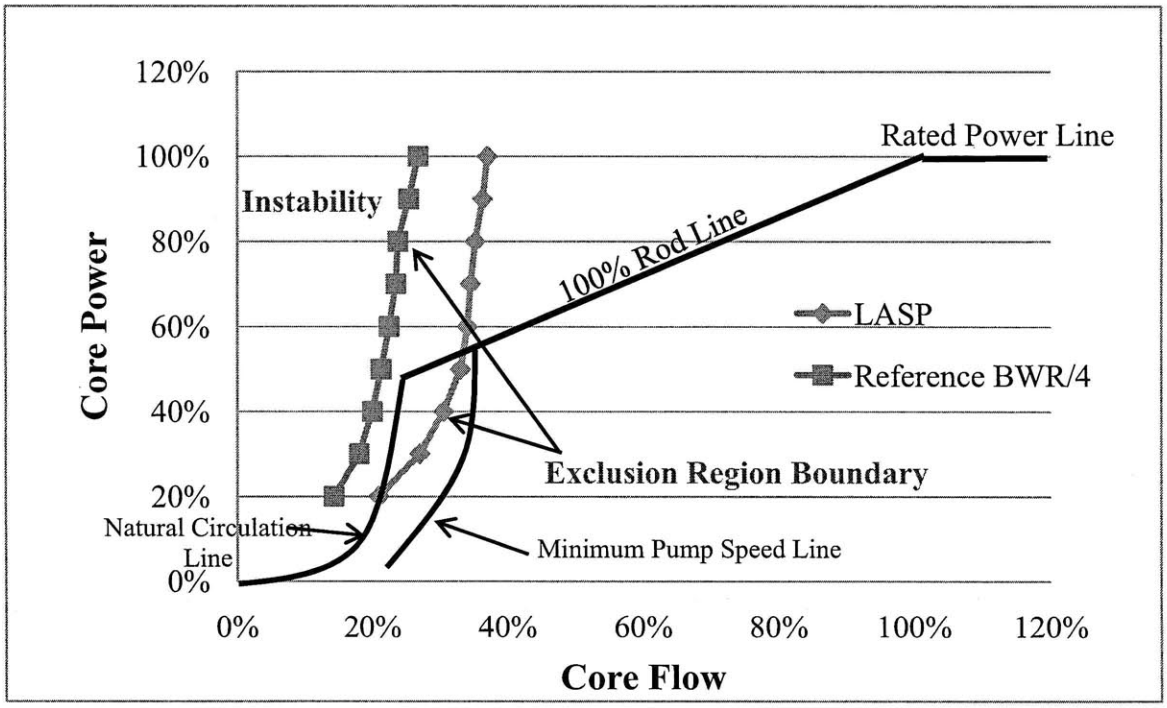

Figure 5.12: Exclusion Region for LASP core in a Typical BWR Power/Flow Map

5.7 Summary

Stability performance of the large assembly with small pins (LASP) concept and of the cross shape twisted fuel rods (CST) have been investigated and compared with the BWR reference core. Single channel thermal-hydraulics oscillation, neutronic regional out-of-phase oscillation and neutronic core-wide in-phase oscillation were considered as instability modes.

It is found that, in the coupled regional and core-wide stability analyses, the decay ratio of the large assembly design is much larger than that of the reference BWR due to its larger void reactivity coefficients. However, it is still below the design limit of *DR=0.8* for the core-wide instabilities. To enhance the stability performance of the large assembly design, the increase of inlet orifice could be considered.

In all oscillation modes, the decay ratios of the CST design are somewhat smaller than those of the reference BWR, due to the reduction of the overall friction loss and the reduction of two-phase pressure loss to single-phase pressure loss ratio, which indicates more robust stability margin.

It is also seen that the decay ratios under uprated conditions are slightly smaller than those under rated conditions, indicating that the stability performance is dependent on the flow rate. However, the changes are small. Power uprates do not have important effects on stability performance when the power-to-flow ratio is maintained.

Furthermore, for the LASP core and the reference core, decay ratio sensitivities were evaluated against void coefficient, Doppler coefficient, inlet orifice coefficient, coolant mass flow rate and reactor thermal power. In evaluated three instability modes, both cores showed similar sensitivities. The decay ratios were much smaller than stability limits within the considered parameter ranges.

It could be concluded that good stability performance of the LASP core and the CST core could be maintained at nominal conditions, even though they have 20 % higher reactor thermal power than the reference core. However, further investigation would be still required for the LASP core startup and the operation procedures in the regions with high power but low flow rate.

6. Stability Analysis of the Reduced Moderation RBWR Designs

6.1 Introduction

An adaptation of the BWR has been conceived at Hitachi that demonstrates yet another aspect of the superiority of the BWR, as an LWR which has the potential to breed and consume TRUs using a multi-recycling process. It is referred to as the Resource-Renewable BWR (RBWR) and can be used as a long-term energy supply, while greatly reducing the negative environmental concerns about long-lived transuraniums in radioactive wastes. [Takeda et al., 1995a]

The RBWRs are composed of three cores with a compatible fuel bundle of an RBWR-T3, -AC and -TB. The rated electric power, core pressure and diameter of the RPV are 1350MWe, 7.2 MPa and 6200 mm, respectively, and are identical to those of the ABWR. The RBWRs could be retrofitted to an ABWR. The RBWR-AC could be characterized as a BWR that operates with mixed (depleted uranium and TRUs) oxide fuel, and that has a breeding ratio of 1.01. However, the RBWR-TB is designed to fission almost all the TRUs, leaving only a critical mass of TRUs, by repeating the recycling and collection process, thus removing the concern that TRUs might pose a threat as long-lived radioactive wastes.

Similar concepts are under investigation at JAEA. The innovative water-cooled reactor concept named FLWR, aims at achieving a sustainable energy supply in the future based on the water reactor technology. The concept consists of two parts in the chronological sequence. The first part realizes a high conversion type core concept, which is basically intended to keep technical continuity from the current LWR technologies without significant gaps to overcome from a technical point of view. The second part represents the RMWR core concept, which realizes a high conversion ratio, more than 1.0. This provides a long-term sustainable energy supply through Pu multiple recycling based on

the well-developed LWR technologies. The key point is that the two core concepts utilize compatible and the same size fuel assemblies. Hence, the former concept can proceed to the latter in the same reactor system based flexibly on future fuel cycle circumstances during the reactor operation period of around 60 years. [Iwamura et al., 2006]

The innovative designs in the RBWRs and RMWRs (or FLWRs) require intensive investigations including the core conceptual design, the core characteristics under Pu multiple recycling, the thermal-hydraulics in the tight-lattice core, fuel rod performance, and so forth. Specially, the RBWR and RMWR both use very short and tight lattice bundle arrangements to achieve a hard neutron spectrum and negative void coefficients. The reactor is designed to operate with a low flow rate, but intend to produce the same total power as an ABWR, resulting in a much higher core average void fraction. This raises the concern about the operational margin to thermal limits and the stability performance.

In this work, the stability performance of the RBWR-AC and RBWR-TB2 (an updated version of RBWR-TB) are examined.

6.2 Overall thermal-hydraulic characteristics of RBWRs

In order to achieve the hard neutron spectrum (for higher conversion ratios) in the RBWR designs, the hexagonal tight-lattice fuel rod arrangement and very high core average void fraction are adopted. To achieve the negative void reactivity coefficients, the core is designed to be short and flat which increases neutron leakage from the core. Axial and internal blankets with depleted uranium are also introduced to increase the conversion ratio and to reduce the void reactivity coefficients. With the upper and lower blankets, the total core region has a five-layer structure with a total height below 1.5m, as schematically shown in Figure 6.1. It should be noted that the latest design information is proprietary data of Hitachi Ltd. The values shown in Figure 6.1 are obtained from [IAEA, 2004], which are from the earlier RBWR designs and are not necessary consistent with the latest values used in the actual analysis in this chapter.

The 223 Y-type control rods with three wings are inserted into gaps among the 720 hexagonal fuel bundles to constitute the nuclear core. Followers consisting of zircaloy are attached to control rods to prevent water from going into spaces after rods are withdrawn. The triangle fuel rod lattice is effective in decreasing the ratio of water to fuel while keeping cooling ability.

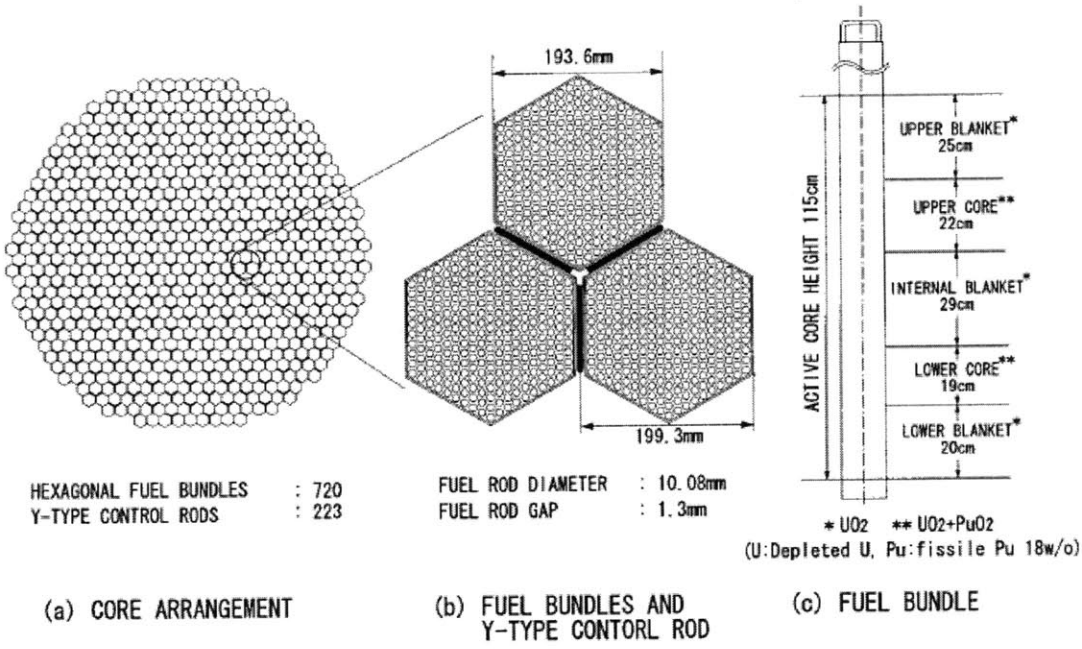

Figure 6.1: Configuration of the RBWR core and fuel assembly (from [IAEA, 2004])

The overall design and thermal-hydraulic parameters of the RBWR-AC and RBWR-TB2 are listed in Table 6-1, along with those of the ABWR design. Some proprietary information of Hitachi Ltd. is removed. The information of the early RBWR designs is listed in Table 6-2.

As shown in Table 6-1, the thermal/electrical power of the RBWRs is nearly the same as that of the ABWR. To compensate for its short reactor core, the RBWR uses many more fuel rods, 2.4-3 times as many as the ABWR. All together, this results in an average and Maximum Linear Heat Generation Rate (MLHGR) of the RBWRs in the same range as the ABWR, therefore within the range of operating BWR cores.

However, the average core power densities are higher than (2.5-3.5 times) the ABWR, since the RBWRs use very short and tight lattice bundle arrangements to produce the same total power. Also, the reactor is designed to operate with a low flow rate, resulting in a much higher core average void fraction. This raises a concern about the RBWRs operational margin to thermal limits. Both the Critical Power limit and the thermal stability should be checked.

Compared to conventional BWRs, important RBWR T/H parameters include:

- High power to flow ratio at rated conditions
- High core average void fraction
- Tight fuel bundle configuration, smaller equivalent hydraulic diameter (De), higher De/Dh (equivalent heated diameter)
- Very short reactor core
- Very high inlet orifice coefficients in the peripheral region
- Small void feedback coefficient
- High axial power peaking

Table 6-1: Overall Design Parameters of RBWRs and ABWR

Item	RBWR-AC [Hitachi, 2009a]	RBWR-TB2 ([Hitachi, 2009b])	ABWR ([GE, 2000])
Thermal Power (MWt)	3926	3926	3926
Electrical Power (MWe)	1356	1356	1350
No. of Fuel Bundles	720	720	872
No. of Fuel Rods per Assembly	-	-	92
Fuel Rod diameter (cm)	-	-	1.026
Core Height (mm)	-	-	4470
Coolant Flow Rate (kt/h)	-	-	52.2
Power to Flow Ratio (MW·h/kt)	-	-	75.2
Average Inlet Velocity (m/s)	-	-	1.96
Core Exit Quality (%)	41	40	14.5
Core Average Void Fraction (%)	56	57	36
Core Pressure Drop (MPa)	0.12	0.06	0.168
Void Coef. ($\Delta k/k/\%void$)	-3×10^{-4}	-7×10^{-4}	-1.2×10^{-3}
Average Heat Flux (kW/m^2)	-	-	440
Peak Heat Flux (kW/m^2)†	1412	2089	1036
Max. LHGR (kW/m)	44.6	47.5	39.4
Average Core Power Density (kW/L)	127	173	49.2

- : Hitachi proprietary information;
†: assumed 1.25, 1.3, and 1.5 for radial power peaking factors, and 2.4, 2.7, and 1.57 for axial power peaking in AC, TB2, and ABWR respectively.

Table 6-2: Specifications and Core Performance of early RBWR Designs (from [Takeda et al., 1995b])

ITEM		RBWR-HO	RBWR-HB	RBWR-HE	RBWR-AC	ABWR
ELECTRIC POWER	MWe	1356	1356	1356	1356	1356
DOME PRESSURE	MPa	7.2	7.2	7.2	7.2	7.2
CORE OUTER RADIUS	m	2.88	2.88	2.88	2.88	2.69
NUMBER OF FUEL BUNDLES		720	720	720	720	872
BURNUP	GWd/t	45	70	45	45	39.5
CORE ACTIVE HEIGHT[a]	m	0.52	0.77	0.65	0.68	3.7
COOLANT FLOW RATE	10^4 t/h	2.6	2.5	3.0	2.9	5.2
CORE EXIT QUALITY	%	34	35	29	31	14.5
AVERAGE VOID FRACTION	%	65	65	61	64	43
CORE PRESSURE DROP	MPa	0.15	0.16	0.16	0.19	0.17
FISSILE Pu ENRICHMENT	%	10.8	10.4	10.5	10.3	3.5[c]
FISSILE Pu INVENTORY[b]	t	4.4	6.0	5.2	5.5	...
BREEDING RATIO		1.01	1.01	1.02	1.01	...
MAX. LINEAR HEAT GENERATION RATE[a]	kW/ft	13.3	12.5	13.3	13.3	13.4
MCPR[d]		1.32	1.32	1.32	1.32	1.22
VOID COEFFICIENT	$10^{-4}\Delta k/k/\%void$	-0.5	-0.5	-1.8	-0.5	-8.0
AXIAL Pu DISTRIBUTION	w/o cm / cm / w/o cm	12 / 17 / 10 / 35	17 / 25 / DU / 29 / 17 / 23	13.5 / 27 / DU / 15 / 13.5 / 23	13.5 / 27 / DU / 18 / 13.5 / 23	

[a]Upper and lower blanket 25, 20 cm.
[b]For 1 GW(electric).
[c]Uranium enrichment.
[d]Hailing.

-HO: Homogeneous core; -HB: High burnup core; -HE: Heterogeneous core.

6.3 Methods Description

In this work, three types of density wave oscillations (DWO): single-channel, regional (also called out-of-phase), and core-wide (or in-phase) oscillations are analyzed. However, the axial power oscillation (the change of axial power distribution during the transient) is not considered in this analysis. Again, the frequency domain stability analysis code STAB, developed at MIT, is used in this work. The STAB code and the three DWOs are briefly discussed in Chapter 5, and the details can be found in reference [Hu and Kazimi, 2007].

To determine the quality and void distribution, either the Homogeneous Equilibrium Model (HEM) or the Non-Homogeneous Equilibrium Model (NHEM) based on the Bestion drift flux correlation can be selected in STAB. HEM is applied in the stability analysis as the HEM predictions are always more conservative in predicting the stability conditions compared to the non-homogeneous models. Also, to be conservative, the two-phase friction multiplier is assumed to be twice the HEM value of ρ_l / ρ_m.

Method to calculate the flow distribution in multi-channels connected only at plena for the RBWR

As discussed in Section 5.4.2., the BWR out-of-phase and in-phase stability are not sensitive to the degree of channel lumping. A three channel model (high power channel, intermediate power channel, and low power channel) is sufficient to conduct out-of-phase and in-phase stability analysis. A one-dimensional thermal-hydraulic code is developed in the MATLAB platform to calculate the lumped channel parameters. This was deemed easier than applying the sub-channel analysis code like VIPRE, as long as the appropriate power and flow distributions among the lumped channels are estimated. They are calculated based on:

(1) The same pressure drop across all of the channels;
(2) Axial and radial power distributions are assigned based on the reference design value (at BOC, MOC, and EOC);
(3) All assemblies within the same orifice group are lumped together;
(4) Keeping constant the total core power and total flow rate.

(1) Governing equations of the two-phase model, NHEM

As discussion in Section 3.1.3, if the water/steam thermodynamics property is independent to local pressure, the conservation equations of the two-phase flow in the Non-Homogeneous Equilibrium Model (NHEM) could be simplified as [Saha, 1974],

$$\frac{\partial j}{\partial z} = \frac{\Gamma \Delta \rho}{\rho_g \rho_f} \tag{3-49}$$

$$\frac{\partial \rho_m}{\partial t} + C_k \frac{\partial \rho_m}{\partial z} + \rho_m \frac{\Gamma \Delta \rho}{\rho_g \rho_f} = 0 \tag{3-50}$$

$$\rho_m\left(\frac{\partial u_m}{\partial t}+u_m\frac{\partial u_m}{\partial z}\right)=-\frac{\partial P_m}{\partial z}-\frac{f_m}{2D_e}\rho_m u_m^2-g\rho_m-\frac{\partial}{\partial z}\left[\frac{\rho_f-\rho_m}{\rho_m-\rho_g}\frac{\rho_f\rho_g}{\rho_m}V_{gj}^2\right] \quad \textbf{(3-51)}$$

$$\rho_m\left(\frac{\partial h_m}{\partial t}+u_m\frac{\partial h_m}{\partial z}\right)=\frac{q_w^{"}P_h}{A_c}+\frac{\partial P_m}{\partial t}-\frac{\partial}{\partial z}\left(\frac{\rho_f-\rho_m}{\rho_m}\frac{\rho_f\rho_g}{\Delta\rho}V_{gj}h_{fg}\right) \quad \textbf{(3-52)}$$

Where, $C_k=j+V_{gj}$; $u_m=j-(\frac{\rho_f}{\rho_m}-1)V_{gj}$; and $\Gamma=\frac{q_w^{"}P_h}{A_c h_{fg}}$.

(2) The Bestion drift flux model

Unlike the Maier and Coddington correlation used in FISTAB, which employs a purely empirical approach to the evaluation of C_0 and V_{gj} of the drift-flux equation by [Zuber and Findlay, 1965], Bestion correlation is used in this analysis. The Bestion correlation was developed for use in the CATHARE code. Despite the simplicity of the correlation, it yields very good results for most of the experimental data analyzed [Coddington and Macian, 2002].

$$C_o=1.0, V_{gj}=0.188\sqrt{\frac{gD_e\rho_{fg}}{\rho_g}} \quad \text{(6-1)}$$

The Bestion correlation is examined by a simple vertical upflow problem, and compared to HEM, the Premoli and Chexal-Lellouche (EPRI) correlations. Consider the two-phase steam-water flow in a 20mm diameter tube and use three values of mass velocity (G1=3000 kg/m^{2}s, G2=1000 kg/m^{2}s, G1=100 kg/m^{2}s), the variation of the void fraction with the flow quality are shown in Figure 6.2.

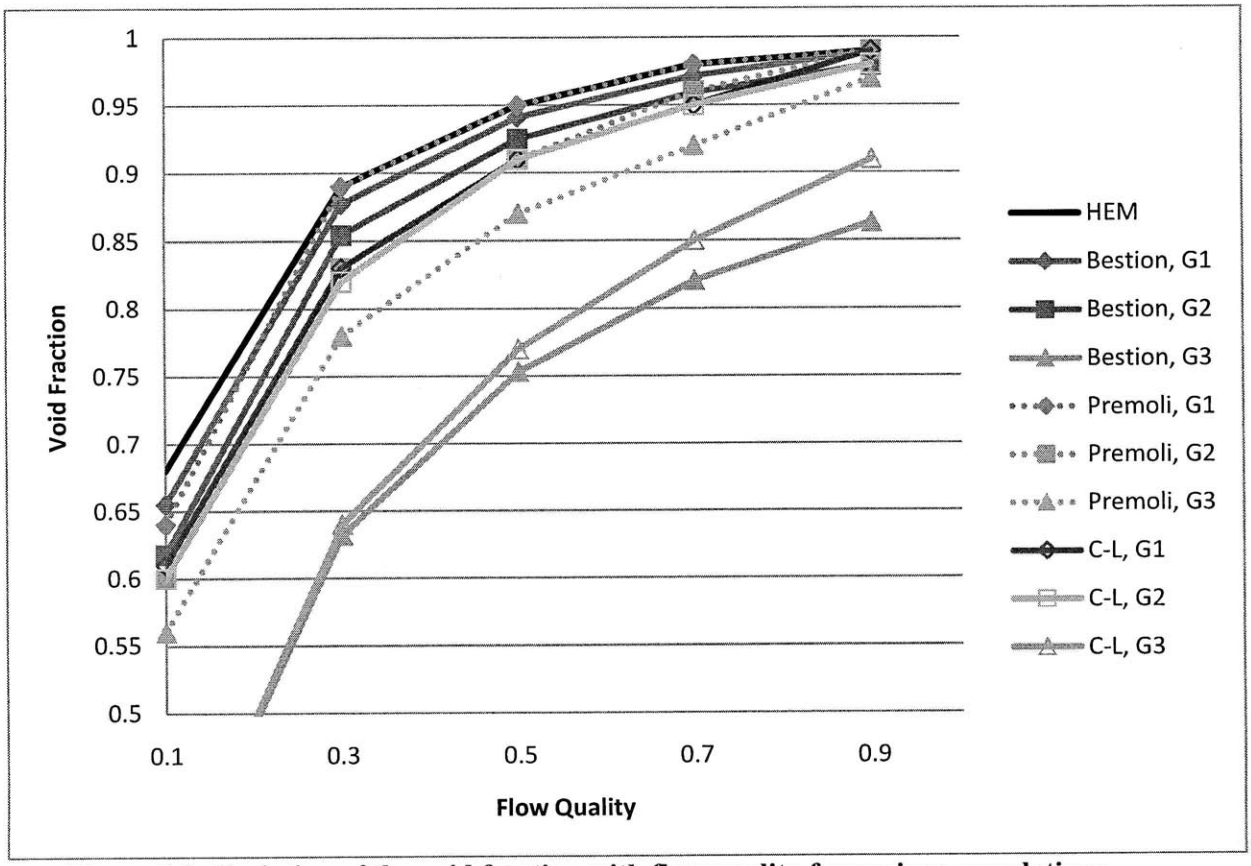

Figure 6.2: Variation of the void fraction with flow quality for various correlations

It is seen in Figure 6.2 that, at very high mass flux condition (G1), Bestion correlation and Premoli correlation approaches the HEM model, while the void fractions predicted by C-L correlation at G1 and G2 are almost the same and difficult to distinguish in the figure. At low mass flux condition (G3), the Bestion correlation gives similar results with C-L correlation, while the void fractions predictioned from Premoli correlation are much higher. At BWR operating conditions (G2), all the three correlations give similar results, while the Bestion correlation gives the highest void fraction for flow quality between 0.1 and 0.5, as shown in the Figure 6.3.

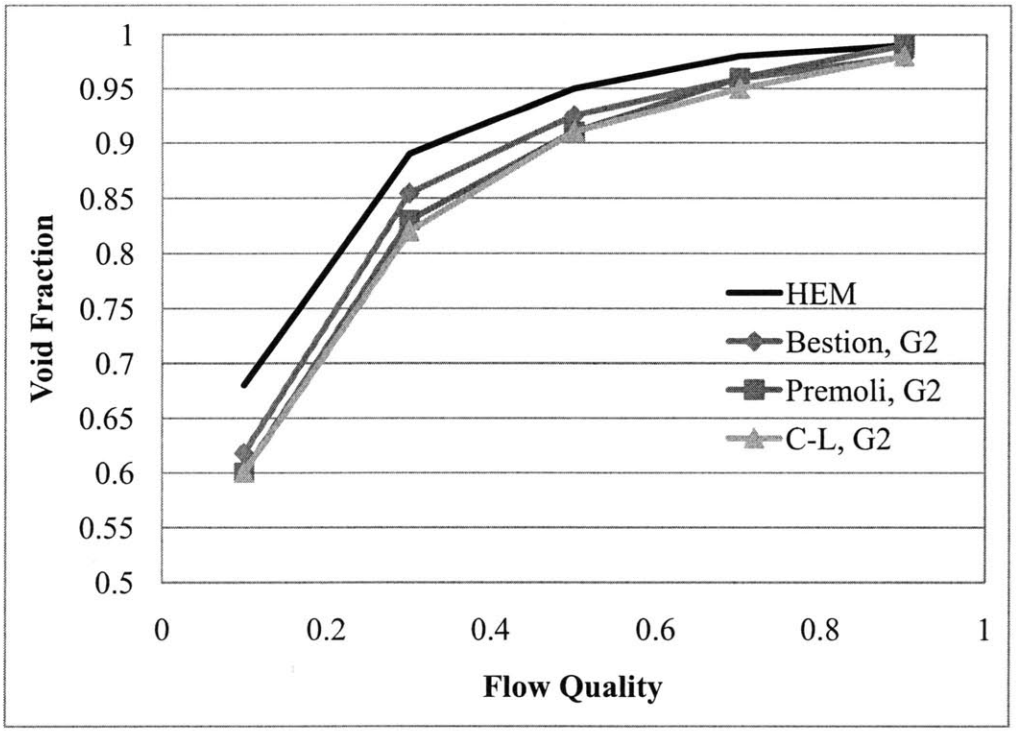

Figure 6.3: Variation of the void fraction with flow quality, G=1000 kg/m^{2}s

(3) Solution schemes for the inlet flow distribution

The total pressure drop is assumed to equal the sum of the friction, gravity, form, and acceleration pressure drops. Thus:

$$\Delta P_{core} = \Delta P_{channel,1} = \Delta P_{channel,2} = \ldots\ldots = \Delta P_{channel,n} \tag{6-2}$$

$$\Delta P_{channel} = \Delta P_{grav} + \Delta P_{acc} + \Delta P_{fric} + \Delta P_{inlet} + \Delta P_{grid} \tag{6-3}$$

For a given inlet flow rate of a channel, the steady state parameter distributions can be easily obtained by dividing the RBWR flow channel into a large number of axial nodes and solving the conservation equations in the NHEM by marching up the nodes. Some flow parameters and the pressure drop at any kth-node of the channel could be calculated as:

$$j_k = j_{k-1} + \Gamma_{k-1} \frac{\rho_{fg}}{\rho_f \rho_g} dz \tag{6-4}$$

$$\rho_{m,k} = \rho_{m,k-1} - \left[\frac{\rho_{m,k-1}\Gamma_{k-1}}{(j_k + V_{gj})} \frac{\rho_{fg}}{\rho_f \rho_g} dz \right] \tag{6-5}$$

$$u_{m,k} = \frac{G_m}{\rho_{m,k}} \tag{6-6}$$

$$\alpha_k = \frac{\rho_f - \rho_m}{\rho_{fg}} \tag{6-7}$$

$$\Delta P_m(k) = \left[G_m \left(u_{m,k} - u_{m,k-1} \right) + \rho_{m,k-1} g dz + \frac{f_{m,k-1}}{2D_e} \frac{G_m^2}{\rho_{m,k-1}} dz \right] + \left[\frac{\alpha_k}{1-\alpha_k} \frac{\rho_f \rho_g}{\rho_{m,k}} V_{gj}^2 - \frac{\alpha_{k-1}}{1-\alpha_{k-1}} \frac{\rho_f \rho_g}{\rho_{m,k-1}} V_{gj}^2 \right] \tag{6-8}$$

$$x_{eq}(k) = x_{eq}(k-1) + \frac{q''_{(k-1)} P_h}{\dot{m} h_{fg}} dz \tag{6-9}$$

Depending on the equalization of the pressure drop across the lumped channels, the inlet flow rates of all lumped channels could be calculated by iteration if the total channel pressure drop is given. If the total mass flow rate is not conserved, the total channel pressure drop would be adjusted and the iteration process would start over again. The iteration scheme for the channel inlet flow rate calculation is illustrated in Figure 6.4.

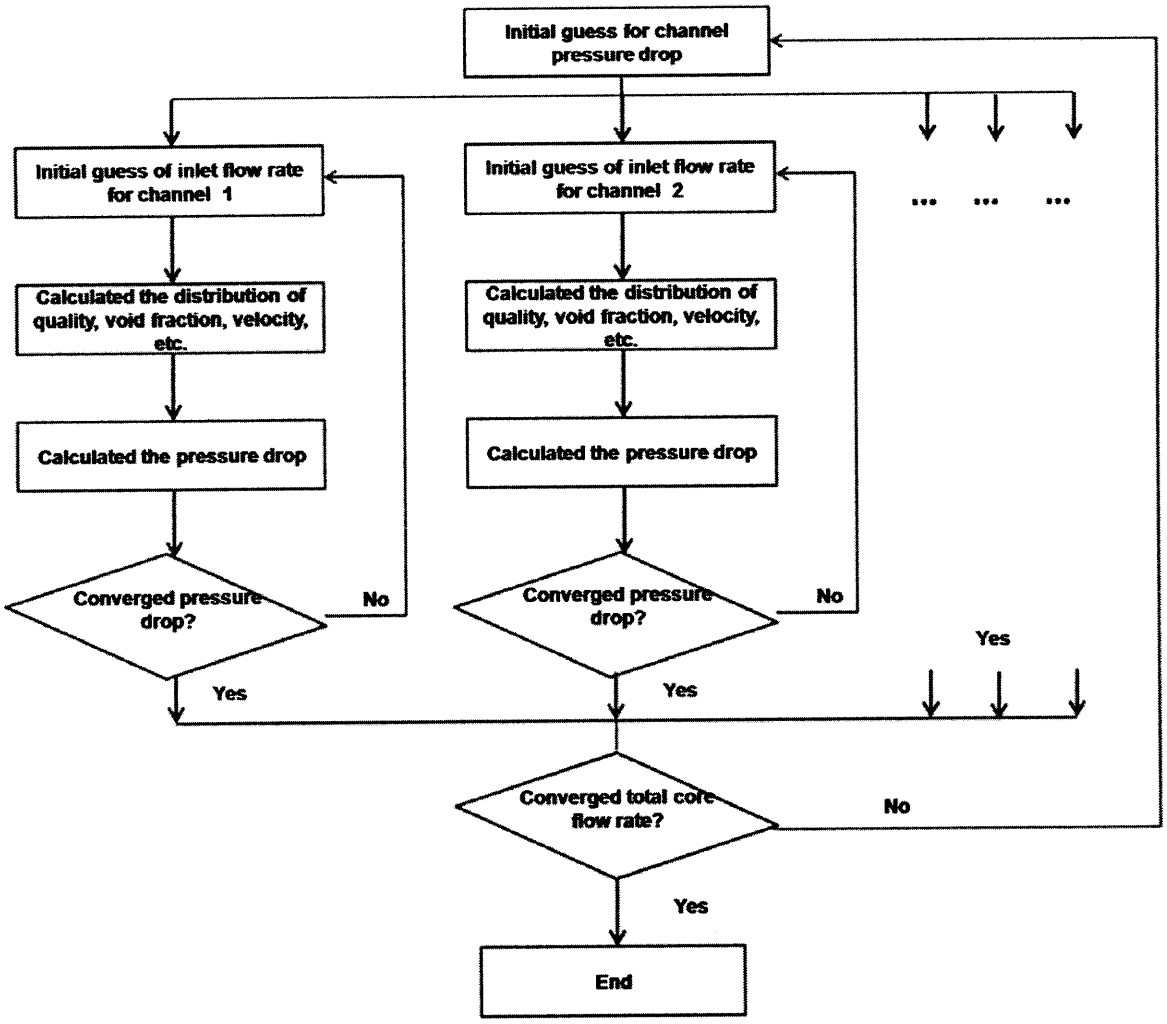

Figure 6.4: Solution scheme for the inlet flow distribution among the lumped channels

(4) Heat conduction model

This flow distribution calculation tool is also developed to calculate the fuel temperature distribution (radially and axially), to fulfill its capability to supply the thermal-hydraulic parameters for a neutronic analysis, which calculates the core power distribution.

A lumped fuel dynamics model with the temperature distribution in the fuel pin developed at Brookheaven National Lab [Wulff, et al, 1984] was applied in the STAB code [Hu and Kazimi, 2007]. The same model is applied here. However, the fuel conductivity model is changed to the FEAST model since the RBWRs utilize the MOX fuel.

Fuel Engineering and Structural analysis Tool (FEAST) is a code developed at MIT to analyze fuel pins in sodium fast reactors [Karahan and Buongirono, 2009]. The model used in FEAST is based on [Inoue et al., 2004], where the conductivity k_{MOX} is

$$k_{MOX} = k_0 * F_1 * F_2 * F_3 * F_4 \tag{6-10}$$

Where k_0 is the as-fabricated thermal conductivity, F_1 is the effect of dissolved solid fission products, F_2 is the effect of precipitated solid fission products, F_3 is the effect of radiation damage, and F_4 is the effect of porosity. The correlation is a recent correlation designed to reduce experimental uncertainty. This conductivity correlation is more complete than the Wulff model.

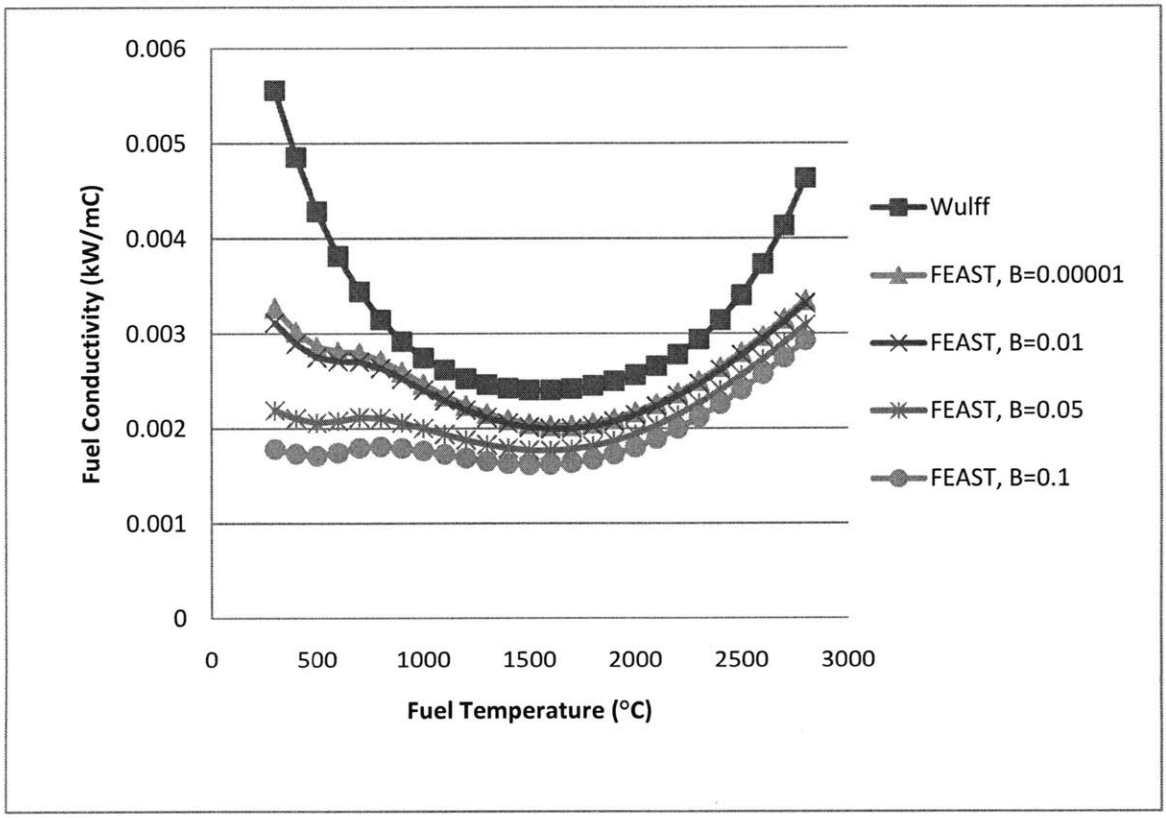

Figure 6.5: Thermal conductivity comparison among different models

The Wulff thermal conductivity model is used for UO_2. It is seen in Figure 6.5 that it overestimates the fuel conductivity comparing the model for MOX fuel used in FEAST (B is the burnup in heavy metal fraction).

6.4 Stability Analysis of RBWR-AC

6.4.1 Single Channel Stability analysis

As discussed above, the RBWR-AC has a relatively high average core void fraction, which makes it potentially more susceptible to density wave oscillations. In this section, the single channel stability is evaluated for the highest power channels by perturbing the inlet flow velocity while maintaining constant channel power and constant pressure drop. Both the BOC and EOC axial power shapes are again considered in the analysis, as the maximum radial power peaking happen at BOC, but the EOC is more bottom power-peaked.

The hot channel parameters used in the channel stability analysis and the calculated decay ratios are listed in Table 6-3 for RBWR-AC and BWR/4. Compared with the BWR/4, the following design parameters will affect the single channel stability of the RBWR-TB:

- Higher power to flow-rate ratio (reduces stability)
- Shorter reactor core (enhances stability)

From Table 6-3, we can see that the RBWR-AC has a similar decay ratio, i.e. similar stability margin compared to a typical BWR. It is stable with a large stability margin. It is seen that although the RBWR-AC has a very high power-to-flow ratio, the shorter core length (faster transient response) improves the overall stability performance. Another reason is that in the very high quality two-phase flow regime, the void fraction is not as sensitive to the perturbation of flow quality as that in the low quality regime. It is also shown that the decay ratio at EOC is larger than that at BOC, which indicates that the effect of a bottom peaked power shape is more prominent.

Table 6-3: Parameters for hot channel stability analysis of RBWR-AC

Parameter	RBWR-AC		BWR/4
Average assembly power (MW)	5.45		4.35
Radial power peaking factor	1.25 (BOC)	1.2 (EOC)	1.45
Hot Assembly flow rate (kg/s)	10.04	9.73	15.3
Inlet enthalpy (kJ/kg)	1250		1228
Inlet flow velocity (m/s)	1.44	1.39	1.85
Inlet orifice coefficient	29.6		21.1
Hydraulic diameter (m)	0.0041		0.0113
Flow area (m^2)	0.0095		0.0094
Heated length (m)	1.347		3.71
Decay Ratio	**0.087**	**0.109**	**0.115**
Frequency (Hz)	2.62	2.63	1.02

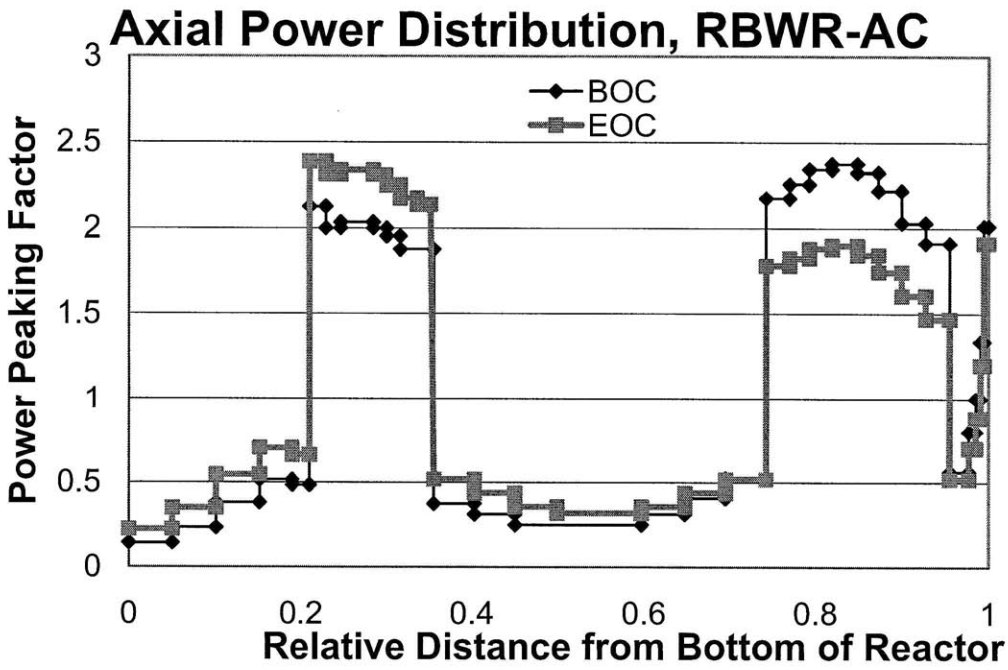

Figure 6.6: Axial power profile of RBWR-AC

A sensitivity study has been performed on the effects of axial power shape. The assembly flow rate is assumed unchanged in this analysis. Also, the power profiles are assumed flat in both the fissile and blanket zone. The assumed power profiles in the analysis are shown in Figure 6.7.

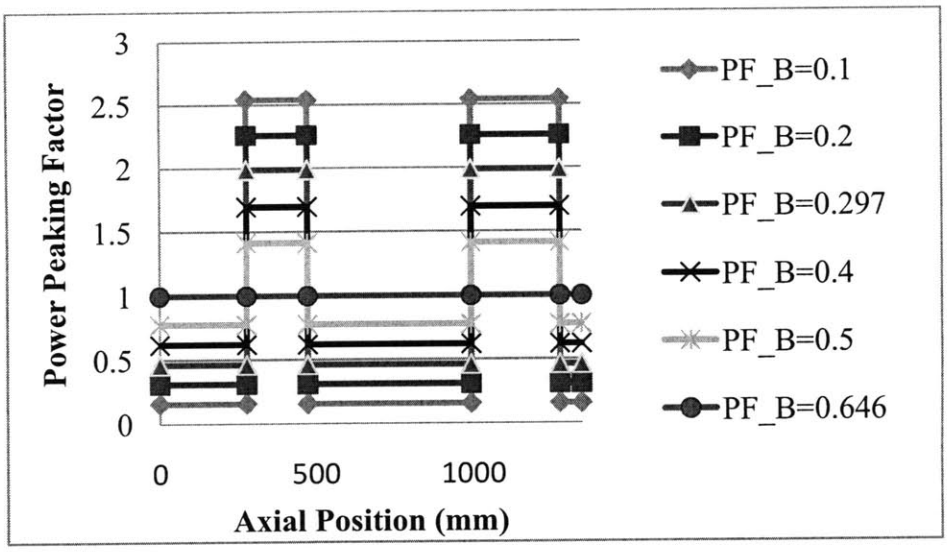

Figure 6.7: Axial power profiles for sensitivity study in single channel stability analysis

The axial power shape plays a very important role in the system stability characteristics. The decay ratios at different axial power shapes (different blanket power fraction) are shown in Figure 6.8.

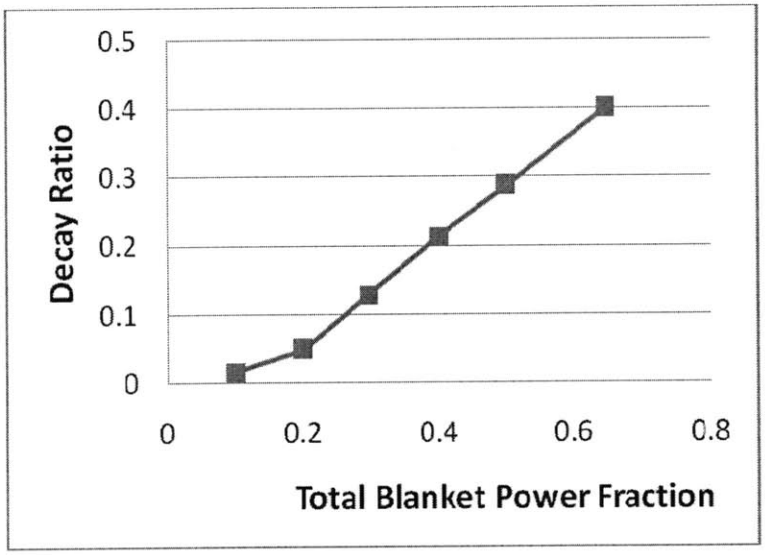

Figure 6.8: Effects of axial power shape in single channel stability analysis

From Figure 6.8, it is seen that the decay ratios of RBWR-AC increases significantly for a larger total blanket power fraction. This is because the upper fissile zone is longer that the lower one. Thus, larger blanket power fraction will shift more power to the bottom of the core, which leads to longer two-phase flow region and higher average channel void

fraction, and then deteriorate the stability performance. Still, in the expected range of power fraction going from 0.1 to 0.4 during the fuel irradiation in the fuel cycle, the decay ratio stays well below the limiting value.

6.4.2 Coupled neutronics stability analysis

When a void fraction oscillation is established in a BWR, the power will also oscillate according to the fuel Doppler reactivity feedback and coolant density reactivity feedback. The reactivity coefficients and the calculated decay ratios of out-of-phase and in-phase modes for both the RBWR-AC and BWR are listed in Tables 6-4 and 6-5. The EOC axial power shape is chosen in the analysis as its thermal-hydraulic stability performance is worse than that at BOC.

Table 6-4: Reactivity coefficients for RBWR-AC and BWR

Reactor	Doppler coefficient	Void coefficient
BWR	-1.7e-5($\frac{\Delta k}{k}/^{o}C$)	-0.144 ($\frac{\Delta k}{k}/void$)
RBWR-AC	-1.7e-5($\frac{\Delta k}{k}/^{o}C$)	-0.014($\frac{\Delta k}{k}/void$)

Table 6-5: Results of stability analysis under design conditions

Mode	**Reference BWR/4**		**RBWR-AC (EOC)**	
	Decay Ratio	Frequency (Hz)	Decay Ratio	Frequency (Hz)
Single-Channel	0.115	1.02	0.109	2.63
Regional (Out-of-phase)	0.117	0.83	0.125	2.49
Core-wide (In-phase)	0.279	0.58	0.227	2.56

Again, in the coupled out-of-phase and in-phase stability analyses, the decay ratios of RBWR-AC are similar to those of BWR/4, well below the criterion of 0.8. This is due to its high thermal-hydraulics stability performance and the small neutronic feedback

coefficients. However, the stability performance during powering up and shutting down are still uncertain, and for which the void coefficients may be very different.

6.4.3 Reflector effects on stability analysis

Long upper and lower reflectors are introduced in the updated RBWR-AC design [Hitachi, 2009a] comparing to the old one [Hitachi, 2008] in order to achieve desired axial power shape and other features of neutronic performance. Assuming that core-wide pressure equalization takes place at the upper plenum above the upper reflectors, the stability analysis is updated to account for the effect of pressure drop oscillations in the reflectors.

Table 6-6: Results of stability analysis under design conditions

Mode	RBWR- AC (EOC) without reflector		RBWR-AC (EOC) with reflector	
	Decay Ratio	Frequency (Hz)	Decay Ratio	Frequency (Hz)
Single-Channel	0.109	2.63	0.125	2.69
Regional (Out-of-phase)	0.125	2.49	0.143	2.54
Core-wide (In-phase)	0.227	2.56	0.237	2.56

It is seen in Table 6-6 that the decay ratios are slightly higher in all three cases if the reflectors are included. It is clear that adding the reflector in the model would affect the pressure drop distribution in the channel, thus affect the stability performance. For the hottest single fuel bundle, the pressure distributions are listed in Table 6-7 for the cases with and without reflector, which shows that the two-phase pressure drop increases around 10 percent while the single-phase pressure drop is nearly unchanged.

Table 6-7: Pressure drop distribution in the single hottest fuel bundle of RBWR-AC

Pressure drop	RBWR- AC (EOC) Without reflector (KPa)	RBWR-AC (EOC) With reflector (KPa)
Channel Total	120	131.3
Single phase region	28.6	29.4
Two phase region	91.3	101.9
Upper reflector region	N/A	10.5

6.4.4 Axial power shape effects on stability analysis

Given the abnormal power peaking (for batch 1 and 2) of RBWR-AC design obtained by the research group at UC Berkeley in a joint study [Downar, Greenspan, Kazimi et al., 2009], sensitivity study for the axial power shape is conducted, assuming:

1) Power shape within the blankets and fissile zones are flat.
2) The power in the blankets is kept the same, but the power peaking factor in the lower and upper fissile zones is customized.

The assumed power profiles in the analysis are shown in Figure 6.9, and the results of the decay ratios and oscillation frequencies are shown in Figure 6.10 and 6.11.

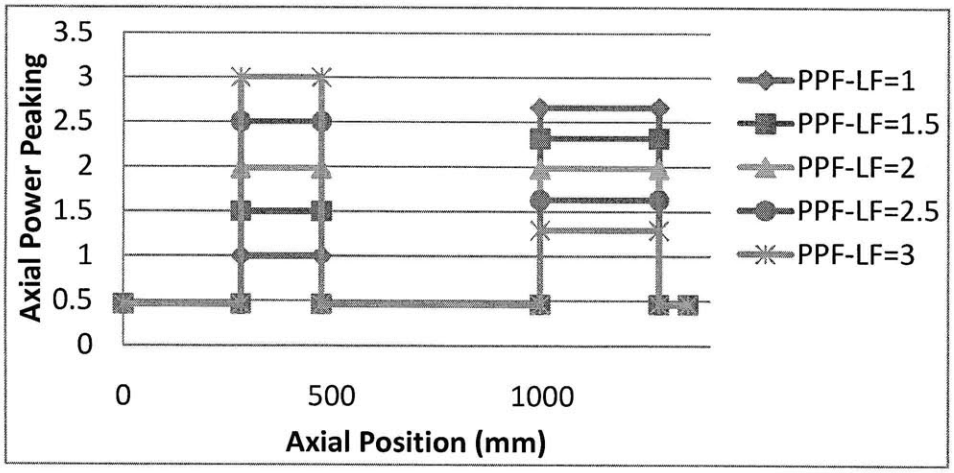

Figure 6.9: Axial power shape for sensitivity study

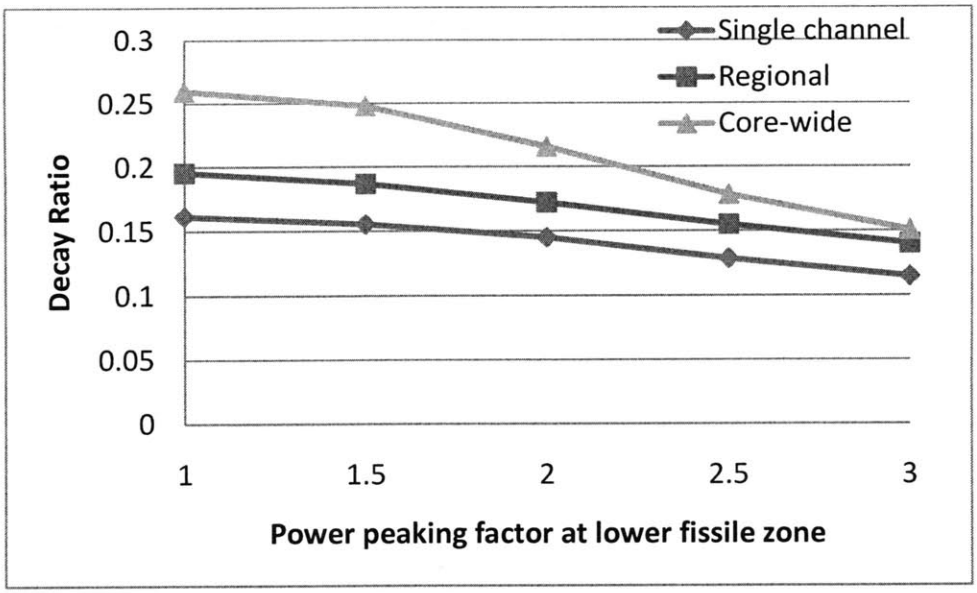

Figure 6.10: Axial power shape effects to decay ratio in stability analysis

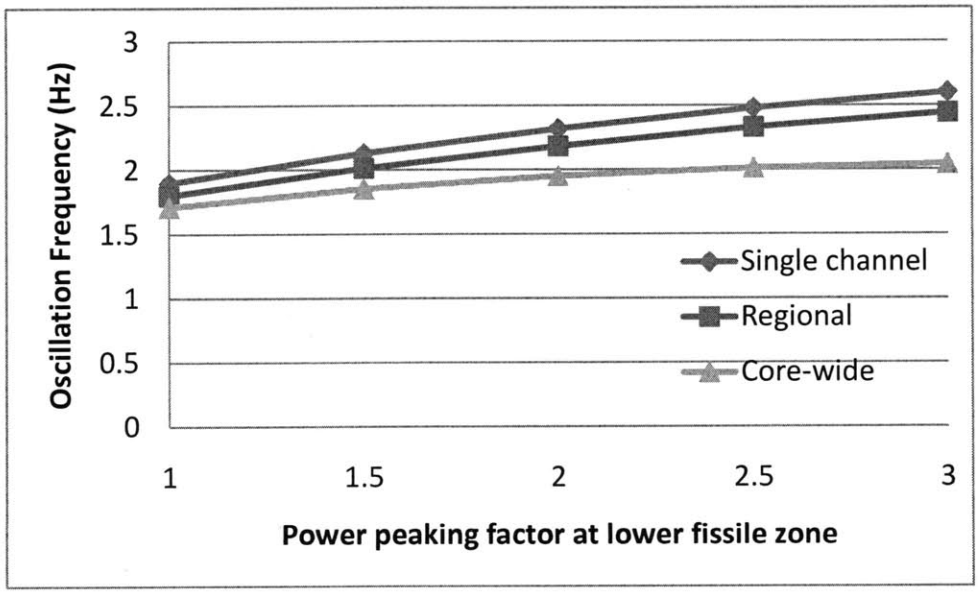

Figure 6.11: Axial power shape effects to oscillation frequencies

It is very interesting to find in Figure 6.10 that the decay ratio deceases when increasing the power in the lower fissile zone in the RBWR-AC. Bottom peaked power shapes are usually less stable because they tend to shift down the boiling boundary; this brings an increase of the axially averaged void fraction and also produces a larger delay in the local pressure drops adjustments. However, in RBWR-AC case, shifting the power to the core bottom showed a stabilizing effect. It could be due to: 1) decrease in the coolant transit

time, thus increase in the resonance frequency; 2) reducing the neutronics feedback in the upper, high void fraction content region of the core; 3) the boiling boundary is the same for all cases since the power in the lower blanket, where boiling starts, is unchanged.

6.4.5 Neutronics modeling effects on stability analysis

As mentioned in Section 5.3, the point kinetics model is used in the STAB code, in which the neutronic feedback is controlled by the whole core average properties. The oscillations of the core average parameters are obtained by adding up the weighted contributions for all reactivity changes of the nodes, radial and axially through out of the core. If the core has N channels and each channel has M nodes axially, the average core coolant density and fuel temperature oscillations can be expressed as [Zhao et al., 2005]:

$$\delta\tilde{\rho}_c = \delta w_{in}\sum_{j=1}^{N}\sum_{i=1}^{M} W_{j,i}U_{den}^{j,i} + \delta q_o'''\sum_{j=1}^{N}\sum_{i=1}^{M} W_{j,i}Q_{den}^{j,i} = U_{den}\delta w_{in} + Q_{den}\delta q_o''' \tag{6-11}$$

$$\delta\tilde{t}_f = \delta w_{in}\sum_{j=1}^{N}\sum_{i=1}^{M} W_{j,i}U_{f}^{j,i} + \delta q_o'''\sum_{j=1}^{N}\sum_{i=1}^{M} W_{j,i}Q_{f}^{j,i} = U_{f}\delta w_{in} + Q_{f}\delta q_o''' \tag{6-12}$$

Therefore, the reactivity feedback oscillation can be obtained as:

$$\begin{aligned}\delta\rho_F &= \delta\rho_{den}^F + \delta\rho_{dop}^F \\ &= C_{den}\delta\tilde{\rho}_c + C_{dop}\delta\tilde{t}_f \\ &= (C_{den}U_{den} + C_{dop}U_f)\delta w_{in} + (C_{den}Q_{den} + C_{dop}Q_f)\delta q_o'''\end{aligned} \tag{6-13}$$

The average density oscillation in the core, $\delta\tilde{\rho}_c$, can be also expressed as

$$\delta\tilde{\rho}_c = \sum_{j=1}^{N}\sum_{i=1}^{M} W_{j,i}\delta\rho_{c,j,i} \tag{6-14}$$

and the average fuel temperature oscillation in the core, $\delta\tilde{t}_{1,f}$, can be expressed as

$$\delta\tilde{t}_f = \sum_{j=1}^{N}\sum_{i=1}^{M} W_{j,i}\delta t_{f,j,i} \tag{6-15}$$

In which, $W_{j,i}$ is the weighting factor at each node, which is usually in the point kinetics model provided in the form of:

$$W_{j,i} = \frac{P_{j,i}^2}{\sum_{j=1}^{N}\sum_{i=1}^{M} W_{j,i} P_{j,i}^2} \tag{6-16}$$

Weighting the local reactivity changes by the square of the local power fraction is a good approximation for a reactor in which the importance function spatial distribution is similar to the power distribution. For the RBWR core, it may not be as good an approximation as for a conventional BWR, since the neutron spectrum of the RBWR core is in the epithermal region, and the fuel compositions are not uniform. A sensitivity study on the weighting function factor is therefore conducted.

The weighting function can be generalized into:

$$W_{j,i} = \frac{P_{j,i}^n}{\sum_{j=1}^{N}\sum_{i=1}^{M} W_{j,i} P_{j,i}^n} \tag{6-17}$$

Using different weighting function factors, the decay ratios of the RBWR-AC in-phase oscillations is calculated. The weighting function factor, n, has been changed from 1 to 2.5 in the sensitivity analysis.

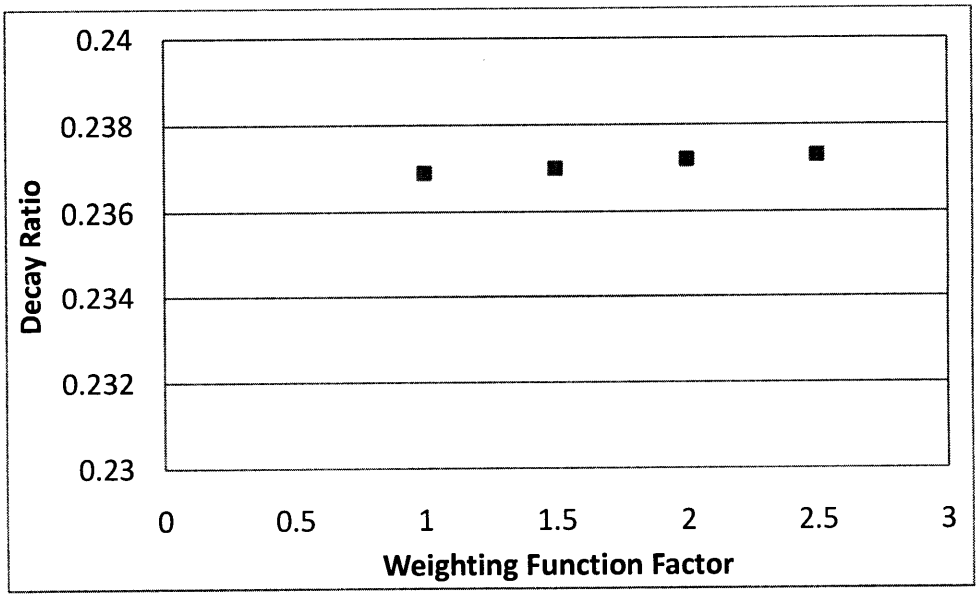

Figure 6.12: Weighting function factor effects to RBWR-AC in-phase stability

It is seen in Figure 6.12 that the calculated decay ratios are not sensitive to the weighting function factor. This may indicate that the point kinetics model is not sufficient for the highly heterogeneous and short RBWR cores. A detailed 3D neutron kinetics model is required in case that the heterogeneity effects are important. This should be checked in the future work.

6.5 Stability Analysis of RBWR-TB2

6.5.1 Single channel stability analysis

In this section, the single channel stability of RBWR-TB2 is evaluated for the highest power channels by perturbing the inlet flow velocity while maintaining constant channel power and constant pressure drop. Both the BOC and EOC axial power shapes are again chosen in the analysis as the maximum radial power peaking occur at BOC, but the power distribution of the EOC is more bottom-peaked.

When the pressure equalization occurs above the axial top reflector, the hot channel parameters used in the channel stability analysis and the calculated decay ratios are listed in Table 6-8 for RBWR-TB2, RBWR-AC, and BWR/4. From Table 6-8, we can see that the RBWR-TB2 has a higher decay ratio, i.e. less stability margin, compared to a typical BWR. However, it is stable with a large stability margin. It is also shown that the decay ratio at EOC is larger than that at BOC, which indicates that the effect of bottom peaked power shape is more prominent. It is seen in the RBWR-AC study that, although the RBWR-AC has a very high power-to-flow ratio, the shorter core length (faster transient response) improves the overall stability performance. However, the shorter core length does not help as much in the TB2 case since it has a larger flow area and much smaller flow velocity.

If the core pressure equalization occurs at the top of the core, below the 1.3m reflector, the single hot channel stability performance is greatly improved; the decay ratio of RBWR-TB2 is 0.24 at BOC and 0.31 at EOC. In RBWR-TB2 design, the second layer upper reflector is very tight (i.e. very small flow area), it greatly increases the two-phase

friction pressure drop and thus destabilizes the system. For the hottest single fuel bundle, the pressure distributions are listed in Table 6-9 for the cases with and without reflector, which shows that the two-phase pressure drop increases more than 30 percent while the single-phase pressure drop is unchanged.

Table 6-8: Parameters for hot channel stability analysis, with the radial core pressure equalization occurring above the upper reflector

Parameter	**RBWR-AC**		**RBWR-TB2**		**BWR/4**
Average assembly power(MW)	5.45		5.45		4.35
Radial power peaking factor	1.25 (BOC)	1.2 (EOC)	1.30 (BOC)	1.25 (EOC)	1.45
Hot Assembly flow rate(kg/s)	10.05	9.73	9.28	8.88	15.3
Inlet enthalpy(kJ/kg)	1250		1230		1228
Inlet flow velocity(m/s)	1.44	1.39	0.87	0.83	1.85
Inlet orifice coefficient	29.6		71.4		21.1
Hydraulic diameter (m)	0.0041		0.0061		0.0113
Flow area(m^2)	0.0095		0.0148		0.0094
Heated length(m)	1.347		1.015		3.71
Decay Ratio	**0.101**	**0.125**	**0.39**[†]	**0.50**[†]	**0.115**
Frequency(Hz)	2.67	2.69	1.64	2.03	1.02

[†]: If the core pressure equalization occurs at the top of the core, below the 1.3m reflector, the single hot channel stability performance is greatly improved; the decay ratio is 0.24 at BOC and 0.31 at EOC.

Table 6-9: Pressure drop distribution in the single hottest fuel bundle

Pressure drop	**RBWR- TB2 (EOC) Without reflector (KPa)**	**RBWR-TB2 (EOC) With reflector (KPa)**
Channel Total	59.8	72.3
Single phase region	19.9	19.9
Two phase region	39.9	52.4
Upper reflector region	N/A	12.5

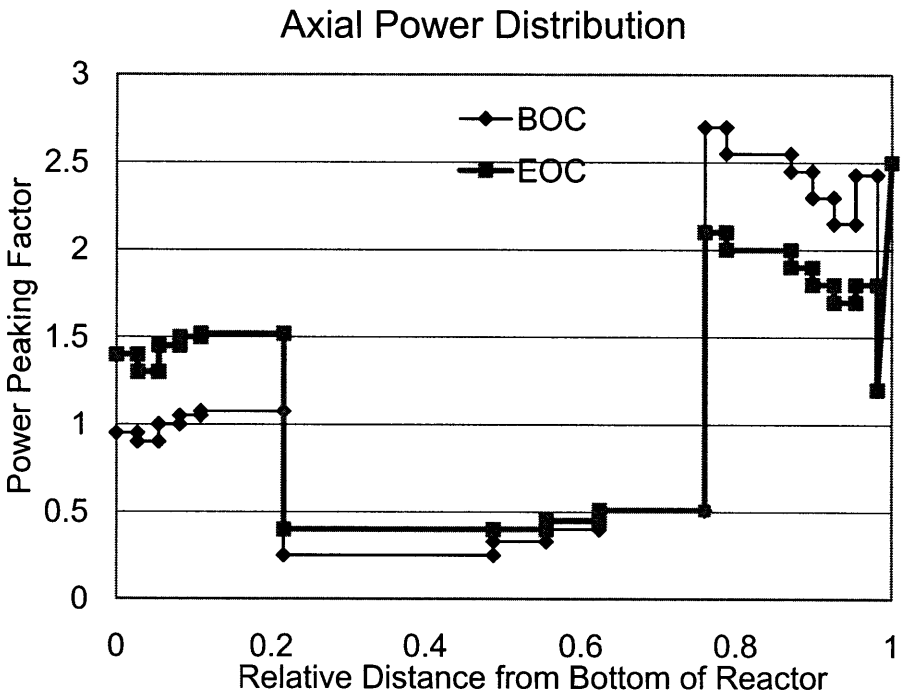

Figure 6.13: Axial power profile of RBWR-TB2

The axial power shape plays a very important role in the system stability characteristics. At EOC, more power will be shifted to the bottom of the core, which leads to larger two-phase flow region and higher average core void fraction, and thus deteriorates the stability performance.

Inlet orifice coefficient effects

It is shown that the single hot channel stability performance is poor for RBWR-TB2 if the coolant mixing between various bundles could only occur above the long narrow reflector. However, the stability performance could be improved with a better inlet orifice scheme. The increase of inlet orifice coefficients would increase the pressure drop in the single-phase region, thus would stabilize the system.

It is shown in Figure 6.14 that the decay ratio could be reduced to 0.2 if the inlet orifice coefficient of the hot channel is increased to 150. Since the core pressure drop of RBWR-TB2 design is very small, only 0.06 MPa, the increase of inlet orifice coefficient is feasible.

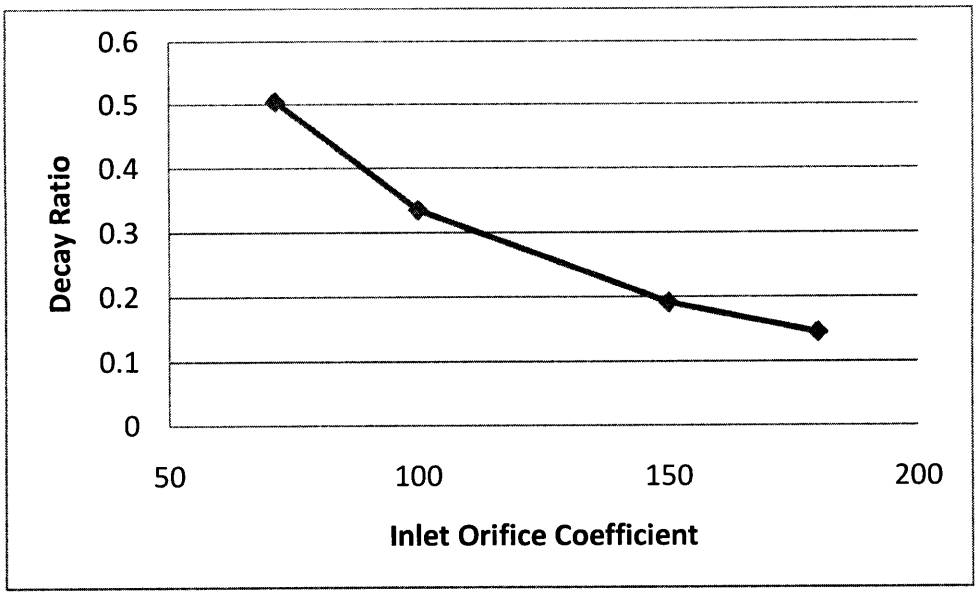

Figure 6.14: Stability sensitivity to inlet orifice coefficients of RBWR-TB2, single-channel mode

6.5.2 Coupled neutronics stability analysis

For out-of-phase and in-phase stability modes, the reactivity coefficients and the calculated decay ratios for both the RBWRs and BWR are listed in Table 6-10 and 6-11. The EOC axial power shape is chosen in the analysis as its thermal-hydraulic stability performance is worse than that at BOC. The pressure equalization is assumed to occur above the axial top reflector.

Table 6-10: Reactivity coefficients for RBWR-TB2 and BWR

Reactor	Doppler coefficient $(\frac{\Delta k}{k}/^{o}C)$	Void coefficient $(\frac{\Delta k}{k}/\%void)$
BWR	-1.7e-5	-0.144
RBWR-AC	-1.7e-5	-0.014
RBWR-TB2	-1.7e-5	-0.070

Table 6-11: Results of stability analysis under design conditions

Mode	Reference BWR/4		RBWR-AC		RBWR-TB2	
	Decay Ratio	Frequency (Hz)	Decay Ratio	Frequency (Hz)	Decay Ratio	Frequency (Hz)
Single-Channel	0.115	1.02	0.109	2.63	0.50	2.03
Regional (Out-of-phase)	0.117	0.83	0.125	2.49	0.236	1.84
Core-wide (In-phase)	0.279	0.58	0.227	2.56	0.62	1.59

In coupled neutronics out-of-phase and in-phase stability analyses, the decay ratios of RBWR-TB2 are both higher than those of BWR/4 and RBWR-AC. In the in-phase mode, it is very close to the criterion of 0.8. This is due to its lower thermal-hydraulics stability performance and a relative large void feedback coefficient (comparing to RBWR-AC).

The influence of the void reactivity coefficients on in-phase oscillations has been also investigated for RBWR-TB2. As shown in Table 6-10, the RBWR-TB2 has a comparable void coefficient to that of the reference BWR/4, but much more negative than that of the RBWR-AC design. A more negative void reactivity coefficient increases neutronic feedback directly and destabilizes the core. From Figure 6.15, it can be seen that the decay ratios of RBWR-TB2 increase with the reductions of void coefficient (more negative void coefficient). The stability performance could be greatly enhanced if the void coefficient could be designed to be less negative.

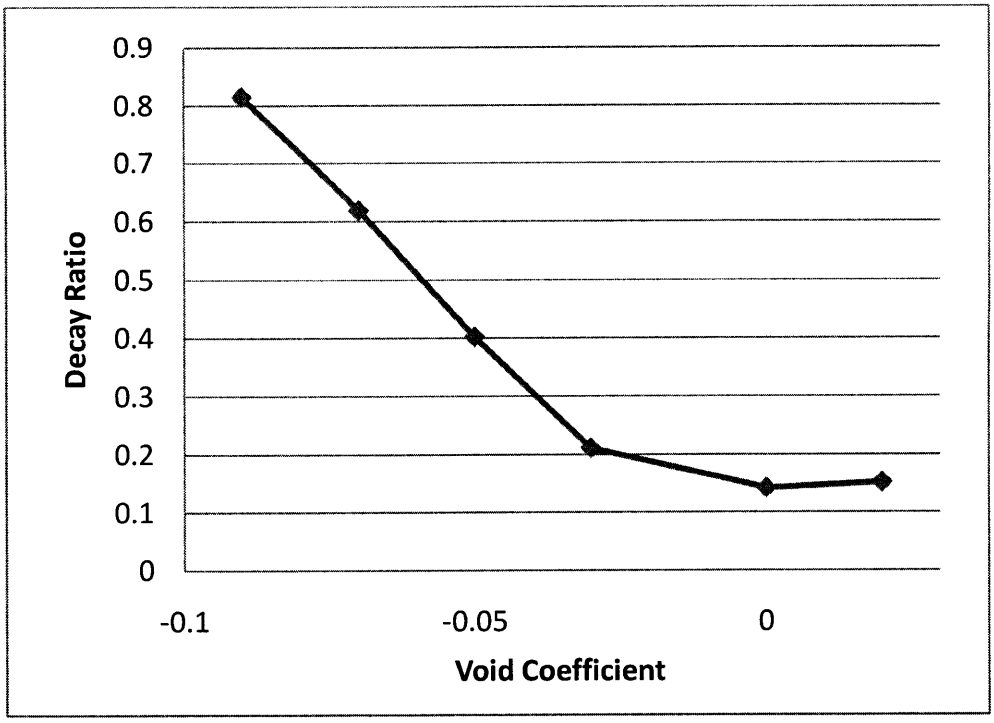

Figure 6.15: Stability sensitivity to void feedback coefficients, in-phase mode

6.6 Summary

Three types of density wave oscillations: single-channel, out-of-phase, and in-phase oscillations have been examined for both the RBWR-AC and RBWR-TB2.

It is found in the single-channel stability analysis that the shorter core length speeds up the transient response, thus improving the overall stability performance of the RBWR-AC. It could also be concluded that the coupled neutronic stability performance is not an issue for the RBWR-AC because of its small neutronic feedback coefficients. However, the values of the coefficients under powering-up or -down need to be ascertained to ensure satisfactory performance during such operations.

RBWR-TB2 has a smaller stability margin to single-channel type instability compared to a typical BWR due to its higher power-to-flow ratio and the tight second layer upper reflector. Although the shorter core length helps speed up the transient response, the smaller flow velocity reduces its effects. Coupled neutronic stability performance should

be further addressed for RBWR-TB2 since it has a comparable void feedback coefficient to regular BWR and worse thermal-hydraulic stability performance. The stability performance could be greatly enhanced if the inlet orifice coefficient is increased and the void coefficient could be designed to be less negative.

It could be concluded that both the RBWR-AC and RBWR-TB2 designs are viable from stability performance point of view, even their exit qualities are around 3 times of a regular BWR. The RBWRs shift more flow to the high power region by, better orifice design, narrow inter-assembly gap, and more flat radial power distribution, which all improve the stability performance. The active coolant flow rates in the hottest assemblies of RBWRs are shown in Table 6-12, with the comparison to the reference BWR.

Table 6-12: Parameters in the hottest assembly of RBWR-AC, RBWR-TB2 and BWR/4

Parameter	RBWR-AC	RBWR-TB2	BWR/4
Average assembly power(MW)	5.45	5.45	4.35
Radial power peaking factor	**1.25**	**1.30**	**1.45**
Bypass flow fraction (%)	**2**	**2**	**14**
Average channel flow rate (kg/s)	8.32	8.32	15.4
Inlet orifice coefficient in the hot channel	29.6	71.4	21.1
Maximum inlet orifice coefficient	1416	1837	182
$k_{in,max}/k_{in,hot}$	**47.8**	**25.7**	**8.63**
Hot channel flow rate(kg/s)	10.05	9.28	15.3
$\dot{m}_{hot}/\dot{m}_{avg}$	**1.20**	**1.12**	**0.99**

However, there are uncertainties in the models used in this analysis since we have less knowledge about the thermal-hydraulics of the tight triangular lattice, and the neutronics behavior in these highly heterogeneous cores. Also, detailed thermal-hydraulics (more lumped channels) and neutronics (3D feedback on axial/radial power distribution) modeling may be required for stability analysis in which the axial oscillation can be considered.

Part III: Stability Analysis Approach, time domain vs. frequency domain

Contents

Part III: Stability Analysis Approach, time domain vs. frequency domain 143

7. Overview of BWR Stability Analysis Methods 145
   7.1 Methods Used to Analyze BWR Instability 145
   7.2 Present Capabilities of Stability Analysis Codes 149
      7.2.1 Applicability to real plant conditions 149
      7.2.2 Considerations on code capabilities 150
   7.3 Applications of Coupled Three-Dimensional Analysis 152
   7.4 Scope of Part III of This Work 154
8. Analysis of Ringhals Stability Test in the Time Domain – Model Descriptions 157
   8.1 Ringhals 1 Stability Test 157
   8.2 Adopted Computational Codes - TRACE/PARCS 161
      8.2.1 TRACE 161
      8.2.2. PARCS 162
   8.3 The Decay Ratio Analysis Tool – DRACO 164
   8.4 The Coupling Process 169
   8.5 Thermal-Hydraulics Model 173
   8.6 Neutronics Model 175
9. Analysis of Ringhals Stability Test in the Time Domain - Analyses and Results 178
   9.1 Steady State Results 178
   9.2 Simulation of Oscillation Transients, In-Phase 180
      9.2.1 P01 Case study, transient response 181
      9.2.2 P01 Case study, time window effects 184
      9.2.3 Ringhals Benchmark for all test points in Cycle 14 186
   9.3 Simulation of Oscillation Transients, Out-of-Phase 189
      9.3.1 Simulation of asymmetric initial neutronic perturbation, using half-core symmetry TRACE model 189
      9.3.2 Simulation of Parallel Channel Type of Instabilities 194
      9.3.3 Out-of-phase Instability Simulation with the full-core 648-channel model 196
   9.4 Numerical Scheme Effects: SI and SETS 200
   9.5 Lumped channel Effects 205
      9.5.1 Core channel lumping/mapping schemes 205
      9.5.2 Transient responses 207
   9.6 Neutronics Modeling Effects: 3D vs. 0D 211
      9.6.1 Reactivity Feedback model in TRACE 211
      9.6.2 Void coefficient calculation from PARCS simulation, C14P01 213
      9.6.3 Transient responses under the point kinetics model 215
   9.7 Control System Effects 218
      9.7.1 BWR stability and control system 218

9.7.2 Transient responses after small perturbations 219
9.7.3 Transient responses after recirculation pump trip 221
9.8 Summary 225
10. Ringhals 1 Stability Test Benchmark – Frequency Domain vs. Time Domain 228
10.1 Ringhals Stability Benchmark with STAB 228
10.1.1 Model description and assumptions 228
10.1.2 Evaluation Results 230
10.2 Comparison between the Frequency Domain Approach and the Time Domain Approach 234
10.3 Summary 237

7. Overview of BWR Stability Analysis Methods

A wide variety of codes and models may be used to address the stability issues, ranging from sophisticate system codes, able to calculate an overall plant behavior, to very simple models for a single heated channel. All of them have the capability to quantify stability, although their reliability may be different [D'Auria, 1997]. In fact, the objectives of qualification and the level of approximation, thus the reliability of results, are different for the various models. Multipurpose codes solving multi-dimensional equations both for neutronics and thermal-hydraulics have become available recently. On the other hand, simplified codes based on one-dimension Homogeneous Equilibrium Model (HEM) for the two-phase flow are still used in the same frame.

In this chapter, after a brief introduction and literature review of the methods used for BWR stability analysis, the current capabilities of the codes, latest development and research trends are introduced. Then, the scope of work for this part of the thesis is described.

7.1 Methods Used to Analyze BWR Instability

Instabilities that may occur during the BWR operation constitute a widely known issue in the scientific community for more than thirty years. A vast volume of literature is available, including data and models. Many computer programs have been developed or adopted to evaluate stability of BWRs and other boiling channel systems. In general, there have been three approaches to analyze the nuclear coupled thermal-hydraulics in BWRs:

1) **Frequency Domain Analyses**. In the frequency domain approach, the linear equations rather than the full set of differential equations are considered. Perturbing and Laplace transforming the neutron kinetics equations allow easy inclusion of the fission power dynamics into the linear model for BWR stability.

2) **Time Domain Analyses**, which include analysis tools specifically developed to simulate the transient behavior of plant systems. These codes numerically integrate the differential equations that describe the physical behavior of the system in time. They have the capability to deal with the non-linear features of BWRs.

3) **Bifurcation Analyses**, which usually carried out with low-dimensional models that are obtained after reducing the set of governing partial differential equations (PDE) to a set of ordinary differential equations (ODE) [Tsuji et al., 1993; Muñoz-Cobo and Verdú, 1991; March-Leuba et al., 1986a, 1986b]. The mathematical model is treated as a dynamical system; both supercritical and subcritical Hopf bifurcations can be identified.

The drawback of Bifurcation Analysis is that the algebraic complexity increases rapidly with the number of equations (related to the unknown state parameters), which limits its application to small regions in the parameter space. Thus, this type of methods will not be discussed further in this work.

The first two approaches are more widely used, and examples of codes based on both were shown in Table 1-2, noted that the details of modeling are different. A more detailed comparison for various common frequency domain codes is shown in Table 7-1, including modeling of the thermal-hydraulics, neutronics, fuel dynamics and heat transfer in the core, the modeling of ex-core systems, and code qualification studies relevant to BWR stability. A more detailed list and description of the frequency domain and time domain codes used for BWR stability analysis can be found in [D'auria et al., 2005].

Table 7-1: Comparison of some frequency domain codes

Code	LAPUR-5 [Otaduy and March-Leuba, 1989]	NUFREQ-NP [Peng et al., 1984]	MATSTAB [Hanggi, 2001]	STAB [Hu and Kazimi, 2007]
Property/Developer	NRC/ORNL	RPI	Forsmark AB, Sweden	MIT
Capabilities	• Core-wide, out-of-phase, and channel decay ratios from transfer functions • 1D parallel channel (max. 7) T/H simulation of the core with dynamic flow redistribution	• 1D parallel channel T/H simulation • Coupling with point 1D, 2D, or 3D neutronics • Ex-core recirculation dynamics	• All channels T/H simulation • 3D neutronics model • Eigenvalue and eigenvector analysis	• Core-wide, out-of-phase, and channel decay ratios from transfer functions • 1D parallel channels (currently 3) T/H simulation
Thermal-hydraulics	• Two-phase slip model in the core • Non-equilibrium (subcooled boiling model) • Intergral formulation of ex-core vessel components • Core pressure/flow boundary conditions are automatically selected to estimate the core-wide or out-of-phase oscillation modes	• Three balance equations in the liquid region of the channel • Four equations drift-flux model with thermal non-equilibrium in the subcooled boiling region • Thermal-equilibrium drift-flux model in the bulk boiling region	• Four equations drift-flux model with thermal non-equilibrium between phases	• Three equations HEM model, or four equations drift-flux model with thermal equilibrium. • Pressure dependent thermodynamic property is modeled in FISTAB
Neutronics	• Point kinetics for core-wide neutronics • Out-of-phase mode neutronics modeled using the point kinetics equivalent equations for the first subcritical mode • Reactivity feedback calculated as power-square average of	• Coupling with models for point, 1D, 2D, 3D kinetics	• Based on a $1\frac{1}{2}$ energy group approach with 6 delayed neutron groups. The power generation is calculated with full	• Point kinetics • λ modal expansion method for out-of-phase analysis • Constant Doppler feedback coefficient • Quadratic form for density coefficient.

	local reactivity contributions • Density reactivity coefficient may be input as a polynomial of local density or it may be calculated by LAPUR-5 based on 2-group cross sections and control-rod positions		3D kinetics	• Reactivity feedback calculated as power-square average of local reactivity contributions
Fuel dynamics and heat transfer	• Discrete parameter model for 1D radial heat conduction in fuel rods • Explicit model for pellet-clad gap • Up to five different fuel types	• Radial heat conduction in the fuel gap and cladding • Heat transfer coefficients from Dittus-Boelter, Jens-Lottes and Thom for single-phase and boiling	• 1D heat conduction in the fuel, gap and cladding • Temperature dependent gap conductance	• A lumped fuel dynamics model with an assumed temperature shape in the fuel pin, gap, and clad.
Ex-core systems	None. Recirculation loop integral momentum dynamics are user input	Simulation of separation and recirculation	The complete model is divided into 8 regions (downcomer 1&2, lower plena 1&2, core, bypass, riser, steam dome), each of which has an individual and variable number of nodes.	Integral momentum dynamics in the riser, separator, downcomer, and the recirculation loop.
Assessment/Qualification relevant to BWR Stability	Documented Benchmarks against: Peach Bottom, Vermont Yankee, Dresden Browns Ferry, Susquehanna-2, Grand Gulf and Oskarshamn	Application to: Peach Bottom-2, FRIGG tests	Application to: Forsmark, Oskarshamn, leibstadt	Application to: Peach Bottom-2, Ringhals 1, ESBWR

7.2 Present Capabilities of Stability Analysis Codes

The available literature on codes adopted for BWR stability reports many successful applications to out-of-pile and in-pile experiments, showing good agreement between observations and predictions. This supports the conclusion that presently available codes are capable of providing a quantitative explanation of the most significant phenomena.

However, some considerations can be made, indicating that the issue of BWR stability prediction is not completely closed. D'Auria et al. [1997, 2005, 2008] summarized the capabilities of the stability analysis tools and concluded that:

1) Most of reported code applications refer to analyses of tests or inadvertent occurrences performed as "open" comparisons of calculations and experimental data. This does not help very much in assessing the actual predictive capabilities of codes, due to the large number of uncertain or undefined parameters, required as input, which can depend on the user's skill and experience in seeking a known solution.
2) The above is particularly true in simulation of out-of-phase oscillations. In fact, knowledge of the observed oscillation pattern is often used as guidance for the particular grouping to be adopted for thermal-hydraulic channels in order to obtain the expected result.
3) Analyses involving a certain degree of uncertainty about the boundary conditions or system parameters often point out that slightly different modeling assumptions may lead to strongly different calculated results. Thus, the considered phenomena are very sensitive to the user's or code options. This is indeed a peculiarity of this kind of coupled phenomena, asking for a higher level of knowledge of a reactor system than required in other safety analyses.

7.2.1 Applicability to real plant conditions

The BWR stability issue is a multi-disciplinary subject, including core thermal-hydraulics, neutronics, fuel dynamics and heat transfer, ex-core systems, and plant control, etc. Detailed description of some phenomena but poor description of others, would not

capture realy plant behavior. Such models would be mainly useful for phenomenological or sensitivity studies.

Generally, full applicability to real plant conditions requires that allowance be made for at least the following capabilities:

1) Parallel channel thermal-hydraulics, with sufficient axial and radial detail (e.g., many nodes per channel, many parallel channels);
2) Neutron kinetics model consistent with the purpose of the intended application; in particular, point kinetics should be used only if changes in power distribution during oscillations and other space dependent effects can be neglected;
3) Fuel and heat transfer models capable of adequately describing the filtering and delaying effect due to the presence of fuel rods and to assess the margin to boiling transition;
4) Ex-core models capable of providing an adequate representation of recirculation gain and core boundary conditions; BOP models are an additional capability which further enlarges the range of application of the code.

7.2.2 Considerations on code capabilities

More considerations of code capabilities for BWR stability analysis are summarized based on [D'Auria, 1997].

1. Formulation of thermal-hydraulic balance equations

The available models adopted for describing the behaviour of the two-phase flow mixture range from a simple 1D homogeneous equilibrium model to 1D or 3D complete non-homogeneous non-equilibrium formulations. In principle, the more detailed the description of the two-phase filed, the better the prediction. A warning must be stated against the use of complex models requiring a large amount of information to explicitly describe relevant physical processes. In fact, such information may be difficult to provide because of limitation of knowledge. Thus, the detailed modeling would introduce a different level uncertainty, which is claimed to be avoided. In this respect, the adoption of

complete non-homogeneous non-equilibrium models for analyzing channel thermal-hydraulics in place of the mixture formulations during instabilities should be assessed in view of the possible improvements in fidelity of the predictions.

2. Constitutive (Closure) laws

As previously mentioned, the greater the model complexity, the larger the number of constitutive laws to be provided to close the balance equations. A larger number of constitutive laws, in turn, raise additional problems about the definition and the qualification of the related correlations. In some cases, uncertainty can be introduced at this level if appropriate detail in knowledge of physical processes is lacking. In this light, setting up a model for channel thermal-hydraulics is a trade-off between detail and simplicity, either extreme is associated with approximate knowledge of the system behavior.

A further problem concerning closure laws is related to the adequacy of correlations developed and assessed for steady-state phenomena in representing transient behavior. This difficulty, which is met also in the case of codes for LOCA analyses, is even more limiting under oscillating flow conditions, which cannot be thought of as quasi-steady processes. In particular, the critical heat flux and wall friction laws (two examples of phenomena which are particularly sensitive to the fully developed or transient character of the flow) must be assessed in conditions typical of density waves to be reliably validated.

3. Numerics

When dealing with partial differential equations, the adopted numerical schemes may have a strong effect on the predicted dynamic behavior. Truncation error effects must be carefully assessed to make sure that they are relatively unimportant in the addressed conditions. Explicit methods are generally preferred to implicit ones, since they are characterized by a lower degree of artificial damping with similar mesh and time step size. A good rule is anyway to directly assess, whenever possible, the effect of adopted

nodalizations in the considered application, in order to have a precise idea of the contribution given to stability by artificial damping.

4. Multidimensional analysis

The use of 3D equations is mandatory in neutronics if precise knowledge of the regional character of core oscillations is sought for. It must be added that 3D kinetics can provide a reliable description of the neutron flux oscillation pattern only if the required detail is used in describing fuel and channel conditions. Due to scattered fuel loading and diversify of burn-up, composition, enrichment, control rod pattern and flow rate, a multi-nodal channel-by-channel description of the core appears in many cases as the only predictive means for discriminating between regional and core-wide oscillations. Even if such a complex description is available, due to the great sensitivity of the phenomena, detailed information must be included on pressure drops, flow distribution and other relevant local parameters to adequately describe core behaviour. On the other hand, thermal-hydraulic channel grouping and fuel region collapsing, though convenient from a computational point of view, are likely to influence the expected oscillation pattern, mostly providing only an a posteriori explanation of the observed behavior. Nevertheless, reduced complexity representations may be useful when the regional pattern of oscillation is not the main goal of the simulation.

On the side of thermal-hydraulics, a 3D description of some critical vessel regions (e.g., the upper and lower plenum) is helpful in providing more realistic boundary conditions for the core channels. Few codes presently have this capability, and the amount of information to be included in two-phase flow closure laws is even higher than in the corresponding 1D models, requiring a greater effort in the assessment of adopted correlations.

7.3 Applications of Coupled Three-Dimensional Analysis

Nowadays, the coupled codes method, which consists of incorporating three-dimensional (3D) neutron kinetics modeling of the reactor core into thermal-hydraulic system codes,

is extensively used. It is particularly suited for simulating transients that involve core spatial asymmetric phenomena and strong feedback effects between the neutronics and the reactor thermal-hydraulics. For most events, the three-dimensional nature of in-core coupled neutronic-thermal-hydraulic processes will not play an important role in macroscopic plant behavior. However, events exist in which the 3-D power distribution is strongly dependent on the plant dynamic performance, such as out-of-phase oscillations in BWRs.

The coupled code RELAP5/PARCS was used in [Costa, 2007] and [Bousbia-Salah and D'Auria, 2006], to characterize the unstable behaviour of the BWR NPP Peach Bottom unit 2 during the "Low-Flow Stability Test" conditions [Carmichael and Niemi, 1978]. Steady state coupled calculations were compared with available reference data, showing good agreement. For the perturbation analysis, the outlet reactor pressure was perturbed by a twin-peak signal having an amplitude equal to 0.055 MPa. After the perturbation, the pressure oscillation turned to a stable trend in few seconds. The core power exhibited damped oscillations, with typical frequency values ranging between 0.3 and 0.4 Hz. However, large discrepancies exist between the evaluated decay ratios and the reference value based on experimental results.

Miró et al. [2002] proposed a modal method to integrate the neutron kinetics diffusion equations in a code called MODKIN. The behaviour of two operational points of the NPP Leibstadt (cycles 10 – in phase oscillation – and 7 – out-of-phase oscillation) was discussed. The MODKIN and the RAMONA codes were coupled to obtain detailed information regarding the state of the reactor for each integration time step.

Hotta et al. [2001a] studied the applicability of TRAC/BF1-ENTRÉE to the regional instability. The fidelity of the numerical model was studied with regard to the thermal-hydraulic mechanism (density-wave oscillation) based on the FRIGG-4 loop test results.The fidelity of the code was demonstrated in predicting the stability limit power level and the limit-cycle amplitude for a wide range of system pressures based on the FRIGG-4 loop test. Then, Hotta et al. [2001b] applied the system to the coupled neutron

kinetics - thermal hydraulic instability analysis for the Ringhals NPP stability test, and demonstrated that the system can predict the regional decay ratio under a wide range of operating conditions.

Xu, et al. [2009] applied TRACE/PARCS to the stability test points from Cycle 14 of the Ringhals benchmark and investigated the TRACE numerical performance during stability analysis. The work focused on the in-phase (i.e., core-wide) oscillation and used a half-core symmetric, 325 channel TRACE model. A detailed numerical study was performed on the SI and SETS numerical integration methods. Parametric study on the axial nodalization and time step size were performed using test point 10 of Cycle 14. When the SI method was applied with a variable axial mesh and the Courant time step size (the largest time step size under the Courant limit), the numerical damping was minimized and the predicted Decay Ratio (DR) agreed well with the measured values.

Some applications of coupled NK/TH code to BWR stability analysis are listed in Table 7-2, with brief description of the modeling methods.

7.4 Scope of Part III of This Work

It can be concluded that BWR stability analyses are arguably among the most complex numerical simulations that are performed for a nuclear reactor design, especially for time-domain calculations. For most other reactor simulations, the initiating event is a boundary condition (e.g., a pipe break), and as long as the simulation code conserves mass and energy, it will track the evolution of the event at least in an approximate way. Instability simulations, however, develop by themselves without having the benefit of a boundary condition that forces them. Small modeling errors, in both the physical processes and numerical schemes, can result in extremely large errors in the final predictions.

Prediction of the stability boundary and the simulation of a stability transient in a real BWR core and plant present a very challenging application of the coupled codes. The 1D thermal-hydraulic solvers of two-fluid model are known for significant numerical

diffusion. It has been argued that such numerical diffusion errors are detrimental to stability-related predictions. However, examples exist for successful applications of the 1D thermal-hydraulics codes for stability problems. For example, Ambrosini and Ferreri [2006] showed that the RELAP5 code can reproduce density wave oscillations; and Xu et al. [2009] demonstrated in the Ringhals-1 stability benchmark that decay ratio can be predicted reasonably well by TRACE/PARCS code. Apparently, the codes are able to capture instability and produce physically sound oscillations induced by a sufficiently strong disturbance. In all these exercises, careful control of time-space discretization to minimize numerical diffusion error is reported to be central to a successful outcome.

Thus, one part of the present work is to examine the code capability to capture key aspects of the physics in a full-core 3D TH/NK model, its effectiveness and accuracy in prediction of different stability scenarios, and the interference of numerical oscillations and physical instability. The proposed scope of work includes:

1) Ringhals 1 stability test benchmark at cycle 14, by using the time domain code, TRACE/PARCS, and the frequency domain code, STAB.
2) Modeling effects of TRACE stability analysis, including time-spatial discretization and numerical schemes, channel grouping (TH/NK mapping), neutronics modeling (point kinetics vs. 3D), etc.
3) Simulation of a large transient scenario and associated oscillation developments.

However, the open question of the applicability of static flow regime maps and constitutive laws obtained for fully developed and quasi-steady flow to oscillatory flows in stability transients, will not be addressed in this work.

Table 7-2: Various applications of coupled NK/TH code to BWR stability analysis

Research Group	References	Code	Oscillation Mode	Numerical schemes in T/H Modeling	Time step and Spatial Nodalization	Channel lumping	Application
TSI & TIT, Japan	[Hotta et al., 2001a 2001b]	TRAC/BF1-ENTRÉE	Regional (out-of-phase)	SI	The limiting CFL = 0.9999	Various number of lumped channels	FRIGG, Ringhals 1
University of Pisa, Italy	[Costa, 2007; Bousbia-Salah and D'Auria, 2006]	RELAP5/ PARCS	Global (In-phase)	Not Mentioned†	Not discussed	77 heated channels	Peach Bottom 2 LFST
KTH(RIT), Sweden	[Kozlowski et al., 2007]	RELAP5/ PARCS	Global	Not Mentioned†	Sensitivity study for space-time convergence	Various number	Peach Bottom 2 pump trip
Purdue/UMich, USA	[Xu et al., 2009]	TRACE/ PARCS	Global	SI	Adjustable axial mesh size to allow CFL =1 in most cells	325 (half core symmetry)	Ringhals 1
MIT	/	TRACE/ PARCS	Global & Regional	SI	Adjustable axial mesh size & sensitivity study	325 for global mode, 648 for regional model, and sensitivity study	Ringhals 1

†: RELAP5 use Semi- Implicit or Nearly-Implicit (a variant of SETS in TRACE) method to solve T/H equations.

8. Analysis of Ringhals Stability Test in the Time Domain – Model Descriptions

Coupled 3D thermal-hydraulics and neutron kinetics system codes are now available, adopting detailed 3D kinetics, one thermal-hydraulic channel per fuel assembly and detailed descriptions of the vessel and the balance of the plant (BOP). Such a very detailed description can in principle provide an adequate capability for predicting the oscillation behavior (core-wide and region-wide) of a given core when operating under prescribed conditions. However, some considerations, as discussed in Chapter 7, indicate large uncertainties still exist in the application of the 3D coupled system codes for BWR stability analysis. Therefore, the TRACE/PARCS code is applied to simulate the Ringhals 1 stability test in this part of the present work.

In this chapter, the Ringhals 1 stability test, and the adopted computation tools, the thermal-hydraulics and neutronics models for the Ringhals tests, are described.

8.1 Ringhals 1 Stability Test

The Ringhals unit 1 was designed and constructed by ABB-ATOM (ASEA-ATOM) and started its commercial operation in 1976. A brief plant description is given in Table 8-1 to 8-3. A series of stability measurements were performed from the 14^{th} to the 17^{th} cycles. The Nuclear Energy Agency/Nuclear Science Committee (NEA/NSC) proposed a BWR stability benchmark based on this test series and supplied participants with the plant data necessary for numerical simulations [Lefvert, 1994, 1996].

The Ringhals 1 core was well instrumented and the benchmark contains a comprehensive and well-defined set of time series data from measurements at beginning of the cycles (BOC) 14, 15, 16 and 17, as well as in the middle of the cycle 16. In this work, we focus on the instability of test points in BOC 14. The reactor core consists of 648 fuel assemblies. Three types of assemblies (8x8 assembly with 63 fuel rods, SVEA assembly

with 63 or 64 fuel rods), are loaded in Cycle 14 to 17. The number of assemblies for each type loaded in cycle 14 were 145 8x8 assemblies, 183 SVEA(63) assemblies and 320 SVEA(64) assemblies. The nominal core power was 2270 MW.

The Local Power Range Monitor (LPRM) and Average Power Range Monitor (APRM) detector signals were sampled for 660 seconds with 80msec interval which yielded 8250 data points for each channel at each test condition. The reference decay ratio and frequency were abstracted from measured APRM noise signals using the ARMA process [Lefvert, 1996]. The power and flow history of the test points in Ringhals-1 stability benchmark at cycle 14 are shown in Figure 8.1, while the test conditions and results are listed in Table 8-4. More details of the description of the Ringhals stability benchmark can be found in [Lefvert, 1994] and [Lefvert, 1996].

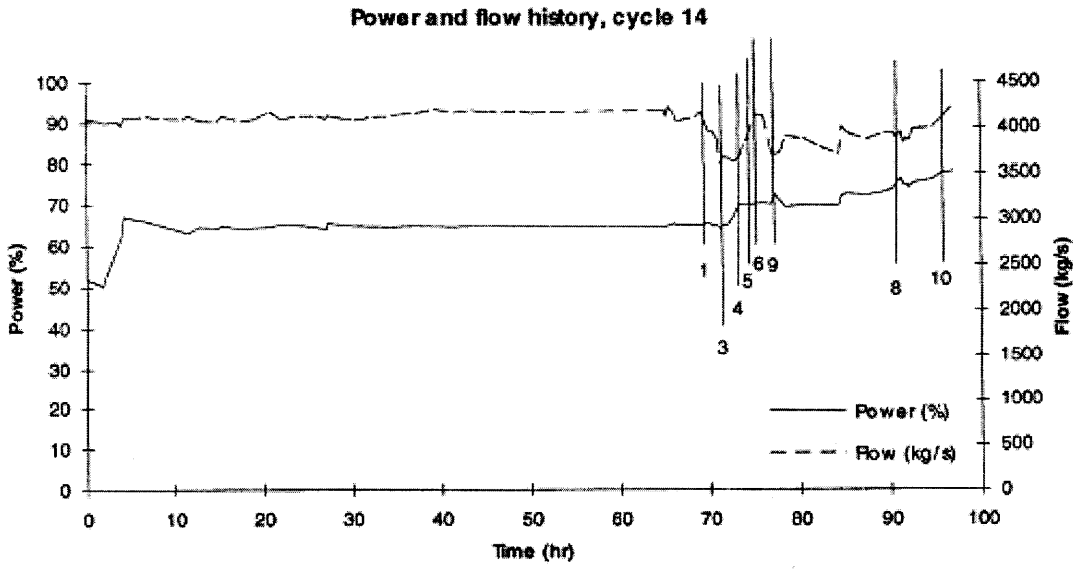

Figure 8.1: Power and flow history of the test points in cycle 14 (from [Lefvert, 1994])

Table 8-1: Ringhals 1 core T/H parameters

Core		
Nominal thermal power (MWt)	2270	
Nominal coolant flow rate (kg/s)	7000	
Nominal steam flow rate (kg/s)	1121	
Fuel assembly		
Assembly number	648	
Assembly Type	SVEA	8*8
Number of fuel pins per assembly	64 (63)	63
Overall length (m)	4.17	4.17
Active fuel pin length (m)	3.68	3.68
Length of non-uranium inlet section (m)	0.23	0.23
Length of non-uranium outlet section (m)	0.26	0.26
Assembly flow area (m^2)	0.0097	0.0104
Hydraulic diameter (m)	0.011	0.014
Fuel pin OD (mm)	12.5	12.5
Cladding thickness (mm)	0.8	0.8
Pellet diameter (mm)	10.44	10.44
Grids pressure loss coefficient		
Lower tieplate coefficient	5.2	0.8
Upper tieplate coefficient	1.0	0.7
Spacer coefficient	0.65	0.60
Spacer axial location from bottom of active core (m)	[0.55, 1.12, 1.69, 2.26, 2.82, 3.39]	
Inlet Orifice coefficient	Central 40.0; Semi-peripheral 63.4; Peripheral 92.9	Central 60.0; Semi-peripheral 100; Peripheral 140

Table 8-2: Fuel property and heat transfer data

Pellet-clad gap heat transfer coefficient ($kW/m^2 \cdot °C$)	Interpolation curve ($\bar{T}_{pellet}$ *vs.* h_{gap}) $\bar{T}_{pellet}$ = [400 500 600 700 800 900]; h_{gap} = [3.8 4.0 4.3 4.8 5.4 6.0];
Pellet thermal conductivity ($W/m \cdot °C$)	$e_1/(1+e_2T)$ $e_1 = 10.0507, e_2 = 0.0021196$, T=average fuel temperature, °C
Cladding thermal conductivity ($W/m \cdot °C$)	16.0
Cladding heat capacity ($J/kg \cdot °C$)	287.0

Table 8-3: Recirculation loop geometry information

Mixing upper plenum	Height: 1.21m Flow area: $17.61m^2$
Riser	Height: 1.88m Flow area: $3.93m^2$ †
Steam separator	Height: 1.92m Flow area: $8.55m^2$ Pressure loss coefficient: 28.0
Downcomer Part 1	Height:6.79m Equivalent diameter: 0.574m Volume: $50.58m^3$
Downcomer Part 2	Height:6.89m Equivalent diameter: 0.51m Volume: $13.63m^3$
Lower plenum	Equivalent diameter: 0.332m Volume: 77.77 m^3

†: Unknown, BWR/4 vlaue used instead.

Table 8-4: Ringhals-1 stability test conditions and results in cycle 14 (from [Lefvert, 1994])

Tests Case	Steam dome Pressure (MPa)	Power (% rated)	CoreFlow rate (kg/s)	Core inlet temperature (°C)	Experimental oscillations			
					Global DR	Freq. (*HZ*)	Regional DR	Freq. (*HZ*)
1	7.00	65.0	4105	265.7	0.3	0.43	_	_
3	7.00	65.0	3666	262.6	0.69	0.43	0.57	0.43
4	7.01	70.0	3657	261.1	0.79	0.55	0.75	0.52
5	7.01	70.0	3868	262.7	0.67	0.51	0.6	0.5
6	7.01	70.2	4126	263.9	0.64	0.52	0.59	0.5
8	6.99	75.1	3884	260.9	0.78	0.52	0.79	0.5
9	7.01	72.6	3694	260.4	0.8	0.56	0.99	0.54
10	69.9	77.7	4104	261.9	0.71	0.5	0.63	0.49

8.2 Adopted Computational Codes - TRACE/PARCS

8.2.1 TRACE

The TRAC/RELAP Advanced Computational Engine (TRACE, formerly called TRAC-M) is the latest in a series of advanced, best-estimate reactor systems codes developed by the U.S. Nuclear Regulatory Commission (NRC) for analyzing transient and steady-state neutronic-thermal-hydraulic behavior in light water reactors. It is the product of a long term effort to combine the capabilities of the NRC's four main systems codes (TRAC-P, TRAC-B, RELAP5 and RAMONA) into one modernized computational tool [NRC, 2008]. TRACE has been designed to perform best-estimate analyses of loss-of-coolant accidents (LOCAs), operational transients, and other accident scenarios in both PWRs and BWRs. It can also model phenomena occurring in experimental facilities designed to simulate transients in reactor systems. The development of the code began in about 1990 and continues at present time. The version used in this work is the TRACE-V5.170 (a special version from V5.0Patch1 to fix a "bug" with large number of components).

The code is based on a non-homogeneous and non-equilibrium two-fluid model for the two-phase flow conservation equations, coupled with a 2D heat conduction equation for the fuel. A flow-regime dependent constitutive-equation package has been incorporated

into the code. The heat-transfer equations are evaluated using a semi-implicit time-differencing technique. The fluid-dynamics equations in the spatial one-dimensional (1D) and three-dimensional (3D) components use, by default, a multi-step time-differencing procedure that allows the material Courant-limit condition to be exceeded. A more straightforward semi-implicit (SI) time-differencing method is also available, as a user option.

TRACE takes a component-based approach to modeling a reactor system. Each physical piece of equipment in a flow loop can be represented as some type of component, and each component can be further nodalized into some number of physical volumes (also called cells) over which the fluid, conduction, and kinetics equations are averaged.

In TRACE, neutronics are evaluated on a core-wide basis by a point-reactor kinetics model with reactivity feedback. One-dimensional or three-dimensional reactor kinetics capabilities are possible through coupling with the Purdue Advanced Reactor Core Simulator (PARCS) program.

8.2.2. PARCS

PARCS is a three-dimensional (3D) neutronic reactor core simulator code developed for the NRC by the Purdue University [Downar et al., 2004]. The version used in this work is the latest released at the present time (PARCS version 3.0).

PARCS solves the steady state and time-dependent neutron diffusion equations to predict the eigenvalue and the dynamic response of the reactor to reactivity perturbations such as control rod movements or changes in the temperature/fluid conditions in the reactor core. The code is applicable to both PWR and BWR cores, loaded with either rectangular or hexagonal fuel assemblies. The major features in PARCS include the ability to perform *eigenvalue* calculations, *transient (kinetics)* calculations, *Xenon transient* calculations, *decay heat* calculations, *pin power* calculations, and *adjoint* calculations.

The neutron diffusion equation is solved with two energy groups for the rectangular geometry option, whereas any number of energy groups can be used for the hexagonal geometry option. PARCS is coupled directly to the thermal-hydraulics system codes TRACE, which provide the temperature and flow field information to PARCS during the transient. The thermal-hydraulic solution is incorporated into PARCS as a feedback into the few group cross-sections. The coarse mesh finite difference (CMFD) formulation is employed in PARCS to solve for the neutron fluxes in the homogenized nodes.

PARCS can operate either with an internal limited TH model or coupled with other codes (TRACE or RELAP) that provide the TH model (external TH). The time step size used in the system TH calculation is often selected to be very small because of numerical stability considerations; sometimes, it is so small that no considerable changes occur in the core TH condition, and performing a neutronic calculation with such a small change would be unnecessary since the flux variation would also be small. As a consequence, in order to improve code efficiency, a skip factor can be used in the coupled calculation such that the TH code calls PARCS based on this user defined frequency.

PARCS uses macroscopic cross-sections which can be viewed as input in either the two-group or multi-group form using the same input cards. The macroscopic nodal cross-sections (Σ) are assigned as a function of boron concentration (B, in ppm), the square root of fuel temperature (T_f), moderator temperature (T_m) and fluid densities (D_m), void fraction (α) and the effective rodded fractions (ξ). Only a linear dependence of cross-sections is considered with respect to these state variables except for the moderator density and void fractions for which the quadratic variation is provided. Symbolically, the cross sections are functionalized as:

$$\begin{aligned}\Sigma(B, T_f, T_m, D_m, \alpha, \xi) = \Sigma_0 &+ a_1 (B - B_0) + a_2 (T_f^{1/2} - T_{fo}^{1/2}) + a_3 (T_m - T_{m0}) \\ &+ a_4 (D_m - D_{m0}) + a_5 (D_m - D_{m0})^2 + a_6 \alpha + a_7 \alpha^2 + \xi \Delta\Sigma_{CR}\end{aligned} \quad (8\text{-}1)$$

8.3 The Decay Ratio Analysis Tool – DRACO

The Decay Ratio Analysis COde (DRACO) is a program developed in this work to calculate the decay ratio (DR) and natural frequency (NF) from BWR transient signals (simulated by TRACE/PARCS in this work). It is a program written in MATLAB scripts and utilizes the Optimization Toolbox and System Identification Toolbox in MATLAB. The procedure to drive the DR and NF from the transient signals in DRACO is:

1) The direct current (DC) component from the time series was removed. (The best fit linear trend was removed.)
2) The time series data was fitted using an auto-regressive (AR) model. The order of the model was determined by the Akaike Information Criteria (AIC). For the fitting, the Yule-Walker approach was adopted.
3) The impulse response of the identified AR model was calculated.
4) The impulse response was then fitted by the function:

$$y(t) = \lambda_1 e^{-\lambda_2 t} \cos(\lambda_3 t + \lambda_4) \tag{8-2}$$

   Where $y(t)$ is the impulse response at time t; λ_i are fitting parameters. The trust-region reflective Newton method of the non-linear curve fitting technique was used. The fitting region of impulse response was around 10 second from the beginning, but the first several seconds of the time series were discarded to avoid the initial disturbance.
5) The decay ratio (DR) and the oscillation frequency (f) are evaluated by:

$$DR = e^{-2\pi\lambda_2/\lambda_3}, \quad f = \lambda_3 / 2\pi \tag{8-3}$$

The DRACO code has an option to direct fit the raw signals from the transient simulation, rather than its impulse response function. With the direct fit of the raw signals, the steps 2 and 3 of the above procedure are neglected. The details of the curve fitting methods, the auto regressive model, and the impulse response function could be found in [The MathWorks, 2004] and [Chatfield, 2003]. More detailed description of the definitions of decay ratio and the time series analysis methods is given in Appendix E.

Validation of the time series analysis code, DRACO

The DRACO code is validated against the Ringhals 1 stability experimental signal and the benchmark results.

Digital recordings of data in about 90 channels were taken in all measurements. The sample interval was 0.08 s and the number of samples per channel 8250. Thus, each recording lasted about 11 minutes in real time. The various APRMs were combined from different LPRM strings. The LPRMs are given for detectors on levels 2 and 4, respectively in all 36 locations. The locations of LPRM are shown in the Figure 8.2 below.

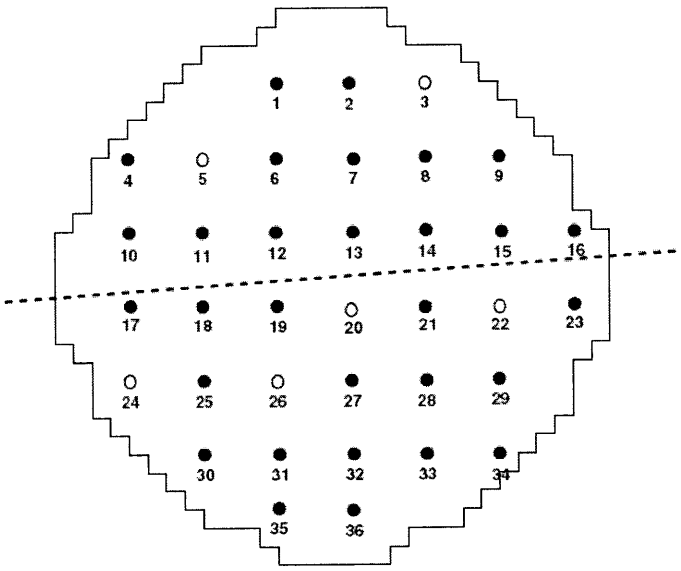

Figure 8.2: Positions of LPRMs and the axis of regional power oscillation (from [Hotta et al., 2001b])

A typical experimental signal in the Ringhals 1 stability test, such as the APRM-M signal of test point 1 at cycle 14, is shown in Figure 8.3.

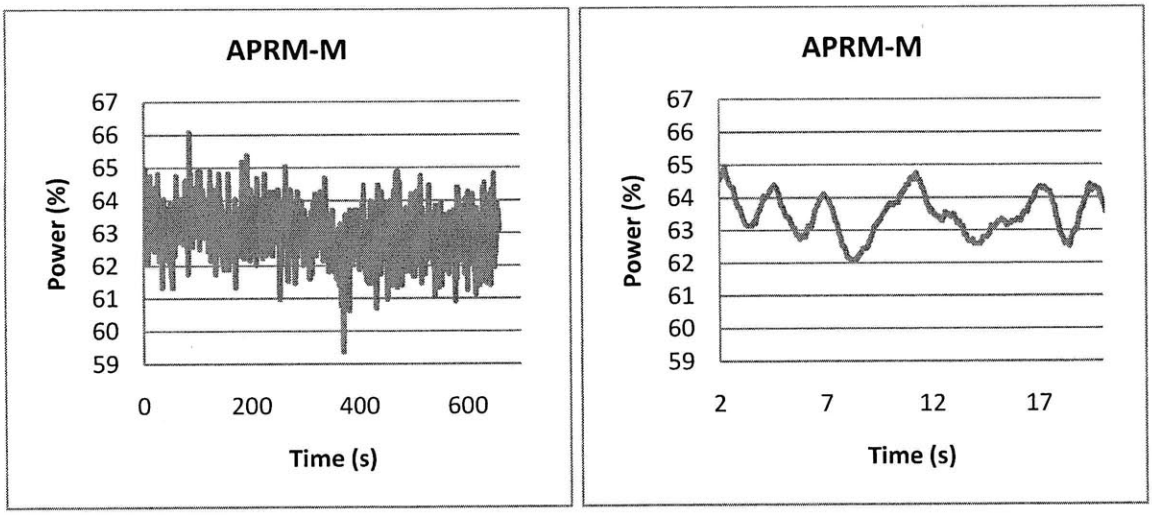

(a) Sample experimental power signal (b) Power signal, time window of 2s-20s

Figure 8.3: Experimental signal of APRM-M at test point C14P01

The decay ratios and frequencies of all measured state points were evaluated from the given signals using DRACO. Results are evaluated for the average APRM-M signal, taken over all APRMs defined in Ringhals 1 and including all four levels of the respective detector strings, and four selected LPRM strings.

Table 8-5: Comparison of decay ratios for all test points at Cycle 14 of Ringhals-1

Test Point	Decay ratios						
	Ref. Global	**Ref. Regional**	APRM-M	LPRM2:2	LPRM11:2	LPRM15:2	LPRM27:2
P01	0.30	-	0.38	-	0.28	-	-
P03	0.69	0.57	0.65	0.42	0.48	0.46	0.52
P04	0.79	0.75	0.79	0.50	0.53	0.56	0.67
P05	0.67	0.6	0.71	-	0.58	-	0.57
P06	0.64	0.59	0.64	0.37	0.59	0.56	0.62
P08	0.78	0.79	0.77	0.73	0.70	0.69	0.77
P09	0.80	0.99	0.77	1	1	1	1
P10	0.71	0.63	0.74	0.66	0.70	0.66	0.74

Table 8-6: Comparison of oscillation frequencies for all test points at Cycle 14 of Ringhals-1

Test Point	Frequency						
	Ref. Global	**Ref. Regional**	APRM-M	LPRM2:2	LPRM11:2	LPRM15:2	LPRM27:2
P01	0.43	-	0.42	-	0.45	-	-
P03	0.43	0.43	0.45	0.48	0.39	0.39	0.38
P04	0.55	0.52	0.54	0.45	0.50	0.47	0.53
P05	0.51	0.5	0.50	-	0.45	-	0.50
P06	0.52	0.5	0.52	0.55	0.52	0.52	0.52
P08	0.52	0.5	0.52	0.51	0.51	0.51	0.51
P09	0.56	0.54	0.57	0.52	0.53	0.53	0.52
P10	0.50	0.49	0.50	0.50	0.50	0.50	0.50

The calculated decay ratios and oscillation frequencies are compared with the reference values, as listed in Table 8-5 and 8-6. The results from APRM-M signal are used to compare the reference value in the global mode, while the maximum decay ratios from LPRMs (LPRM27:2) are compared with the reference value in the regional mode. The biases and the standard deviations for the decay ratios and frequencies are shown in Table 8-7.

The Definitions of the biases and the standard deviations for the decay ratios and frequencies are given by:

$$\widetilde{E}_{DR} = \frac{\sum_{n=1}^{n_{\exp.}} (DR_{pre.} - DR_{ref.})_n}{n_{\exp.}}, \quad \widetilde{E}_{Frq.} = \frac{\sum_{n=1}^{n_{\exp.}} (F_{pre.} - F_{ref.})_n}{n_{\exp.}} \tag{8-4}$$

$$\sigma_{DR} = \sqrt{\frac{\sum_{n=1}^{n_{\exp.}} (DR_{pre.} - DR_{ref.})_n^2}{n_{\exp.}}}, \quad \sigma_{Frq.} = \sqrt{\frac{\sum_{n=1}^{n_{\exp.}} (F_{pre.} - F_{ref.})_n^2}{n_{\exp.}}} \tag{8-5}$$

Table 8-7: Difference between DRACO predictions and the reference values

Mode	Decay ratio		Frequency	
	Bias	Standard deviation	Bias	Standard deviation
Global	0.01	0.04	0	0.01
Regional	-0.004	0.06	-0.003	0.02

Note that there are some uncertainties in the decay ratio evaluation method (does not include the measurement error) for the reference value [Lefvert, 1996]. Error estimates according to Table 8-8 are given for the evaluation of the stability parameters of the global mode based on an optimal choice of model order in the analysis of sampled data.

Table 8-8: Uncertainty in estimating the DR due to model order selection (from [Lefvert, 1996])

Decay Ratio	Uncertainty
0.2	±0.15
0.4	±0.09
0.6	±0.07
0.8	±0.05

It is seen in Table 8-7 and Table 8-8 that the biases of the decay ratios calculated from DRACO are much less than the uncertainities of the time serial analysis method in the reference. Thus, the vadility of the DRACO code is demostrated.

Application to limit cycle oscillation at test point 9

At the test point 9, operating at 73% reactor power and 32% core flow rate, the evaluated decay ratio of the regional mode is 1, which means that the reactor power oscillated in a limit cycle in the out-of-phase mode. The raw LPRM11:2 signal and its related IRF (Impulse Response Function) signal are shown in Figure 8.4 and 8.5. The sustainable undamped oscillation is shown in the IRF signal derived by the DRACO code.

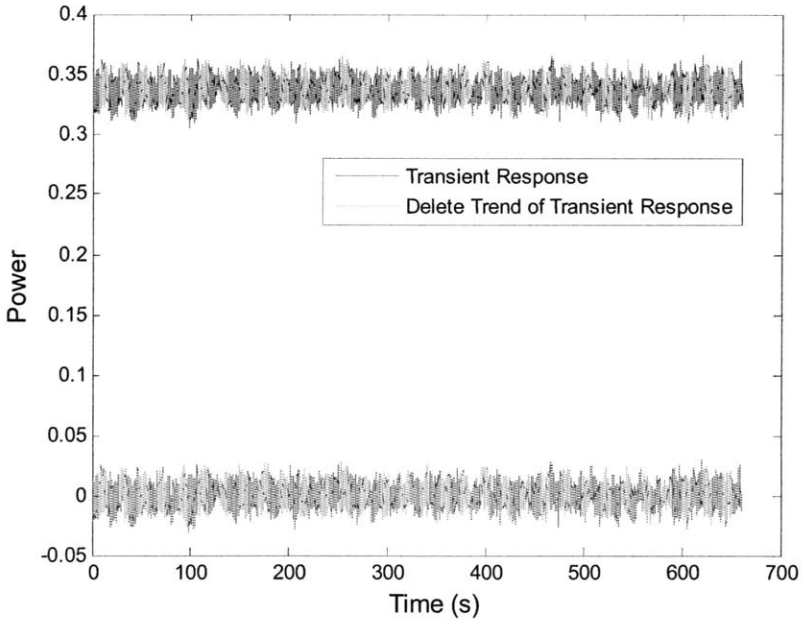

Figure 8.4: LPRM11:2 Signal at Point 9

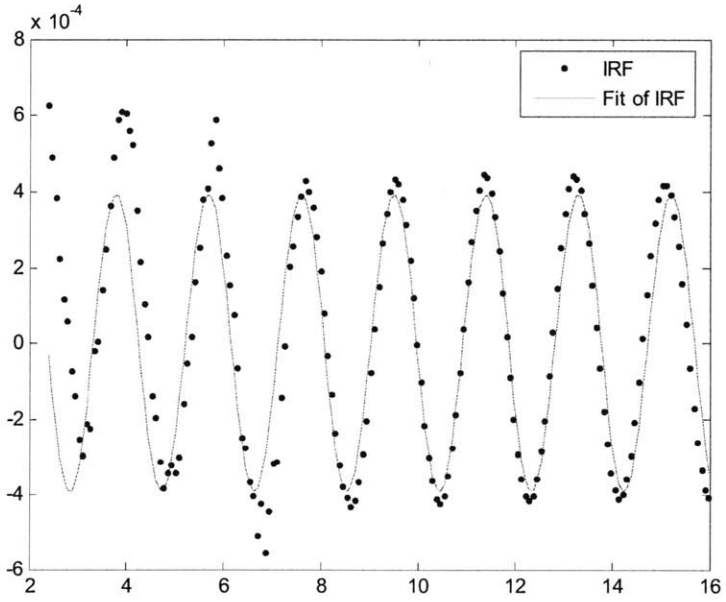

Figure 8.5: IRF of LPRM11:2 Signal and its fitting curve at Point 9

8.4 The Coupling Process

The typical coupled TH/NK code system is shown in Figure 8.6 [Downar et al., 2009], in which three types of codes are included: (1) a code for deriving suitable neutron kinetics

cross-sections, (2) a neutron kinetics code, and (3) a thermal-hydraulic system code. The consistent application of these three code is required to perform a full 3D coupled TH/NK calculation. However, the cross-section generation code can be used independently and the TH and NK codes must be coupled and interacting at each time step.

In this work, the benchmark cross-section library specified for Cycle 14 of RH1 was based on the CASMO-3/SIMULATE-3 codes and it was reformatted by GENPMAXS to comply with the cross section format required in PARCS. The node-wise burnup and history values for all test points from the core simulator, SIMULATE-3, were used in the PARCS model.

The coupled TRACE/PARCS code uses a General Interface which manages the mapping of property data and solution variables between the thermal-hydraulics and neutronics codes, as seen in Figure 8.7 [Downar et al., 2009].

Previously, TRACE and PARCS are executed as separate processes and communicate with each other through the use of message-passing protocols in the Parallel Virtual Machine (PVM) package. Starting with version 2.60, PARCS can be compiled into a static library which is linked into TRACE executable. Only the static library option now remains in the coupled TRACE/PARCS calculation. For a coupled calculation, a merged TRACE will call *parcs* subroutine which is available from the static library, instead of calling PVM library subroutines to communicate with a separate PARCS process. [Downar et al., 2004]

In general, the neutronic node structure is different from the T-H node structure. The difference is to be mitigated by a proper mapping scheme. This mapping used to be explicit in that the fractions of different T-H nodes belonging to a neutronic node had to be specified in a file called MAPTAB for all the neutronic nodes, and vice versa.

The coupled TRACE /PARCS codes utilize an internal integration scheme in which the solution of the system and core thermal-hydraulics is obtained by TRACE and only the

spatial kinetics solution is obtained by PARCS. In this scheme, PARCS utilizes the thermal-hydraulics solution data (e.g., moderator temperatures/densities and fuel temperatures) calculated by TRACE to incorporate appropriate feedback effects into the cross-sections. Likewise, TRACE takes the space-dependent powers calculated in PARCS and solves for the heat conduction in the core heat structures.

The temporal coupling of TRACE and PARCS is explicit in nature, and the two codes are locked at the same time step. For this implementation, the TRACE solution lags the PARCS solution by one time step. Specifically, the advancement of the time step begins with TRACE, obtaining the solution of the hydrodynamic field equations using the power from the previous time step. The necessary data obtained from this solution is then sent to PARCS and the power at the current time step is computed.

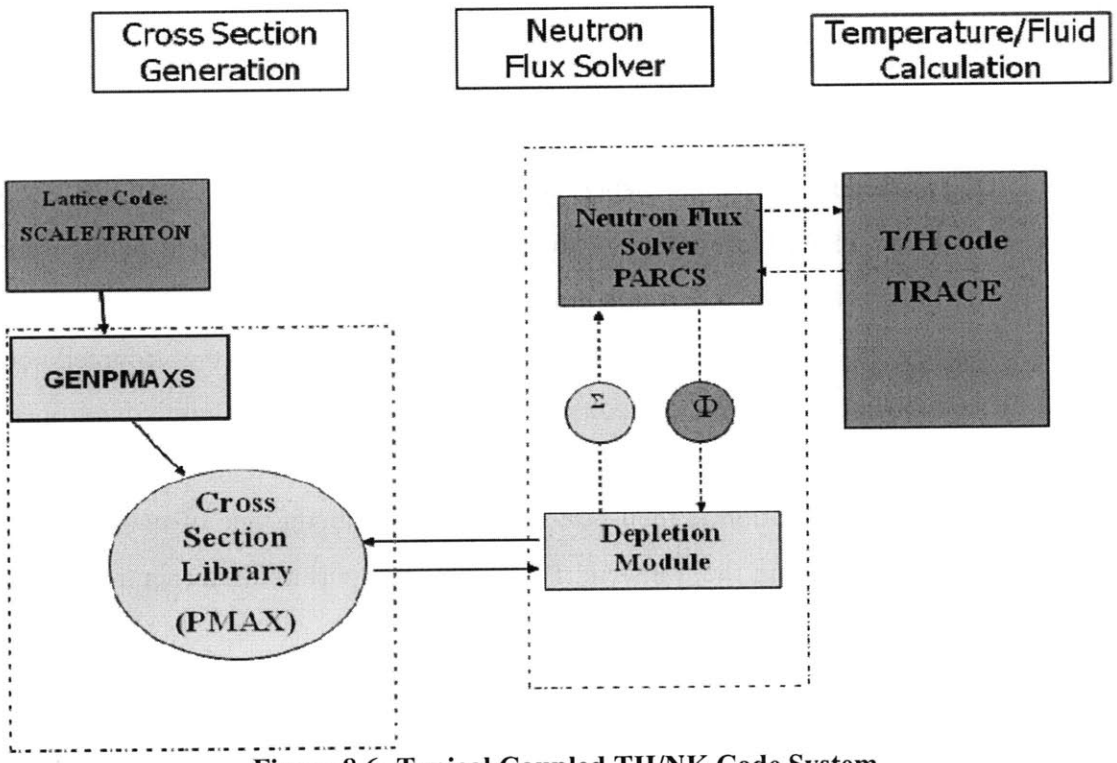

Figure 8.6: Typical Coupled TH/NK Code System (from [Downar, 2009])

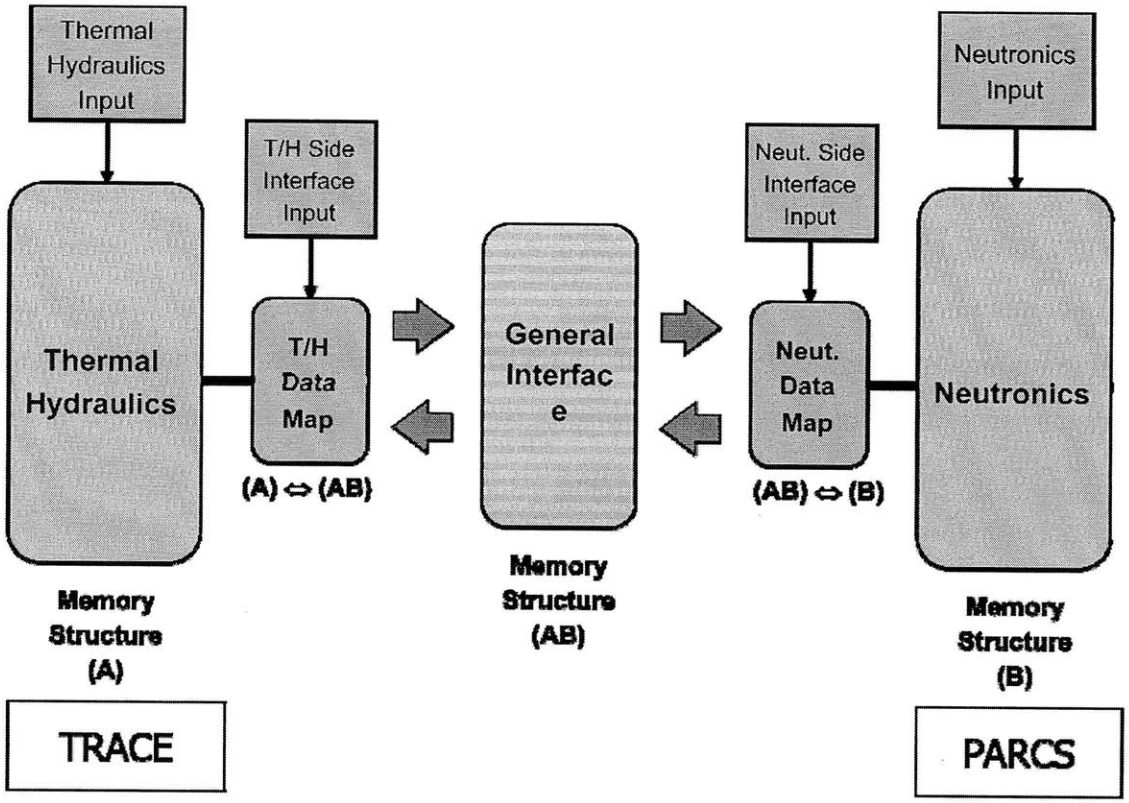

Figure 8.7: Coupling between TRACE and PARCS (from [Downar, 2009])

The following procedure is applied during the stability simulation with TRACE/PARCS:

1) Stand-alone TRACE initialization of the thermal-hydraulics field using a fixed power distribution and a constant power.
2) A steady state re-calculation is then performed with the coupled code TRACE/PARCS to achieve a converged coupled thermal-hydraulic/neutron flux solution.
3) The stability simulation is then performed by introducing one of two excitations to the core to initiate the transient: i) Control Rod perturbation (neutronics), and ii) Pressure Perturbation (thermal-hydraulic).
4) Time-series analysis is performed to evaluate the decay ratio and oscillation frequency from the transient results.

8.5 Thermal-Hydraulics Model

The TRACE thermal-hydraulics model for Ringhals 1 stability test is shown in Figure 8.8, including the reactor pressure vessel and recirculation loops. The boundaries are at the turbine inlet and feed water pipes. The separator and down comers are modelled within the vessel. One of the most important issues for coupled code analysis is the use of sufficient parallel thermal-hydraulics channels such that the respective field equations can be solved with sufficient accuracy for the particular application. As depicted in Figure 8.9, a 325 channel model with half-core symmetry model was used in the work for the in-phase stability analysis. Each T-H channel also had a leakage path from the channel to the vessel along the bypass region. This leakage simulates the external core flow bypass, which typically is about 10% of the total core coolant flow. A one to one, full core model (648 channel) is used for out-of-phase oscillations, and the lumped channel effects are investigated in Chapter 9.

All the material properties, such as thermal conductivities, heat capacities, densities of the fuel pellets and claddings from the specifications [Lefvert, 1994] were used directly in the TRACE model. The hydraulic parameters in the specifications were also used in the TRACE model, such as the channel and fuel rod dimensions, flow areas, hydraulic diameters, pressure loss coefficients for channel orifices, lower and upper core tie plates.

Table 8-9 shows the main components in the TRACE input deck. The core active zone was axially divided non-uniformly into 25 cells within the CHAN model, to allow the Courant numbers in most cells to approach unity simultaneously and therefore to minimize the numerical dissipation. The details of the effects of time-spatial discretization schemes will be discussed in Chapter 9.

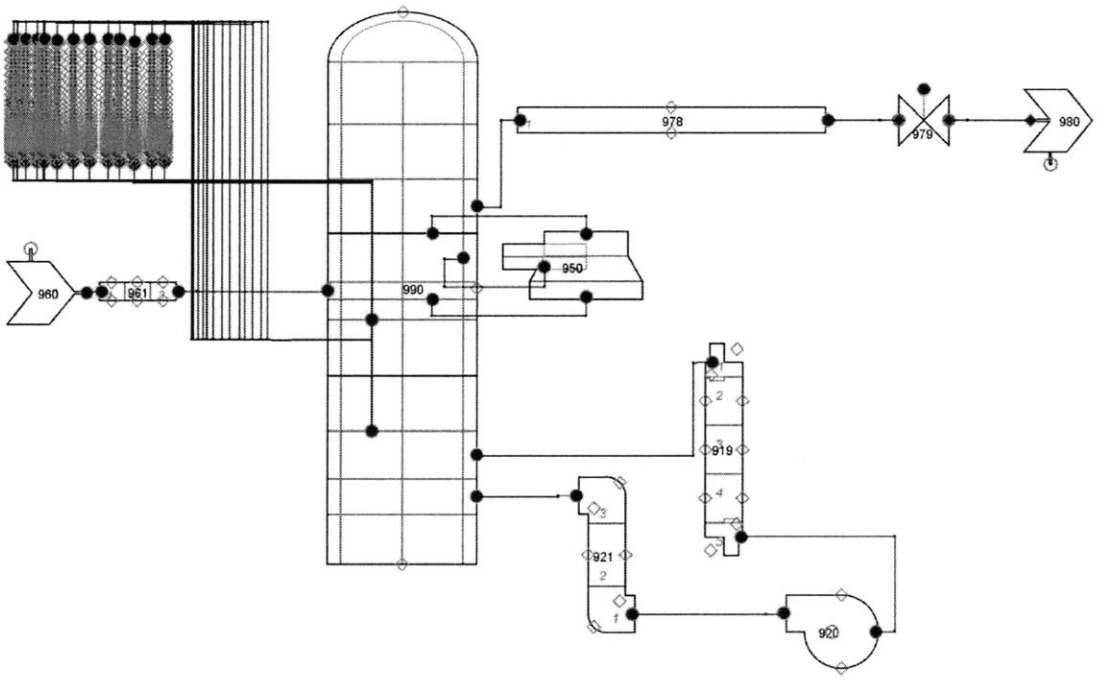

Figure 8.8: TRACE Model for Ringhals 1 power plant

												342	329	315	215	229	242													
											353	341	328	314	214	228	241	253												
								377	370	362	352	340	327	313	213	227	240	252	262	270	277									
							382	376	369	361	351	339	326	312	212	226	239	251	261	269	276	282								
						385	381	375	368	360	350	338	325	311	211	225	238	250	260	268	275	281	285								
					086	384	380	374	367	359	349	337	324	310	210	224	237	249	259	267	274	280	284	186							
				085	084	083	379	373	366	358	348	336	323	309	209	223	236	248	258	266	273	279	183	184	185						
			082	081	080	079	078	372	365	357	347	335	322	308	208	222	235	247	257	265	272	178	179	180	181	182					
		077	076	075	074	073	072	071	364	356	346	334	321	307	207	221	234	246	256	264	171	172	173	174	175	176	177			
		070	069	068	067	066	065	064	063	355	345	333	320	306	206	220	233	245	255	163	164	165	166	167	168	169	170			
		062	061	060	059	058	057	056	055	054	344	332	319	305	205	219	232	244	154	155	156	157	158	159	160	161	162			
	053	052	051	050	049	048	047	046	045	044	043	331	318	304	204	218	231	143	144	145	146	147	148	149	150	151	152	153		
042	041	040	039	038	037	036	035	034	033	032	031	030	317	303	203	217	130	131	132	133	134	135	136	137	138	139	140	141	142	
029	028	027	026	025	024	023	022	021	020	019	018	017	016	302	202	116	117	118	119	120	121	122	123	124	125	126	127	128	129	
015	014	013	012	011	010	009	008	007	006	005	004	003	002	001	101	102	103	104	105	106	107	108	109	110	111	112	113	114	115	
115	114	113	112	111	110	109	108	107	106	105	104	103	102	101	001	002	003	004	005	006	007	008	009	010	011	012	013	014	015	
129	128	127	126	125	124	123	122	121	120	119	118	117	116	202	302	016	017	018	019	020	021	022	023	024	025	026	027	028	029	
142	141	140	139	138	137	136	135	134	133	132	131	130	217	203	303	317	030	031	032	033	034	035	036	037	038	039	040	041	042	
	153	152	151	150	149	148	147	146	145	144	143	231	218	204	304	318	331	043	044	045	046	047	048	049	050	051	052	053		
		162	161	160	159	158	157	156	155	154	244	232	219	205	305	319	332	344	054	055	056	057	058	059	060	061	062			
		170	169	168	167	166	165	164	163	255	245	233	220	206	306	320	333	345	355	063	064	065	066	067	068	069	070			
		177	176	175	174	173	172	171	264	256	246	234	221	207	307	321	334	346	356	364	071	072	073	074	075	076	077			
			182	181	180	179	178	272	265	257	247	235	222	208	308	322	335	347	357	365	372	078	079	080	081	082					
				185	184	183	279	273	266	258	248	236	223	209	309	323	336	348	358	366	373	379	083	084	085						
					186	284	280	274	267	259	249	237	224	210	310	324	337	349	359	367	374	380	384	086							
						285	281	275	268	260	250	238	225	211	311	325	338	350	360	368	375	381	385							
							282	276	269	261	251	239	226	212	312	326	339	351	361	369	376	382								
								277	270	662	252	240	227	213	313	327	340	352	362	370	377									
											253	241	228	214	314	328	341	353												
												242	229	215	315	329	342													

Figure 8.9: Planar representation of the 325 TH channels in TRACE

Table 8-9: Main components in the TRACE input deck

Plant Component	TRACE component type	Component number
Fuel Bundels	chan	1, 2,3, ... 86,101, ...662 (total 325 chans)
Recirculation Piping from Vessel to Rec. Pump	pipe	919
Recirculation Pump	pump	920
Recirculation Piping from Rec. Pump to Vessel	pipe	921
Separators and Dryers	sepd	950
Feedwater Supply System Boundary	fill	960
Feedwater Piping	pipe	961
Main Steam Lines	pipe	978
Turbine Inlet Boundary	break	980
Turbine Control Valve	valve	979
Reactor Vessel	vessel	990
Reactor Core Power	power	999

8.6 Neutronics Model

The PARCS core neutronics model was developed using the neutronics data provided in the benchmark specifications. The core nodalization is based on one node per assembly in the radial plane (32x32 planar nodes) and 27 axial nodes. The nodalization includes explicit modelling of both the radial and axial reflectors. The PARCS neutronics solutions for both steady-state and transient conditions were based on the two-group nodal diffusion option.

The benchmark cross-section library specified for Cycle 14 of RH1 was based on the CASMO-3/SIMULATE-3 codes, and was reformatted by GENPMAXS to comply with the cross section format required in PARCS. The cross section lookup table is read through two independent thermal-hydraulic parameters: fuel temperature and moderator density (T_f, ρ_m). A complete set of diffusion coefficients, macroscopic cross-sections for

scattering, absorption, and fission, assembly discontinuity factors, as a function of the moderator density and fuel temperature is defined for each composition.

The axial compositions in the fuel assemblies and reflector are assigned in the *planar_reg* card of the PARCS input file, in a 2D array for the radial configuration, as shown in Figure 8.10. Each number in the array represents one type of composition. The control rod banks and the neutron detectors are also explicitly modeled in PARCS, as shown in Figure 8.11 and 8.12.

```
                                    26 26 26 26 26 26 26 26
                                 26 26 23  6  4  1  4  1 26 26
                              26 26 26 26  1  1  1  4  1  4  4  1 26 26 26 26
                           26 26 23  1 23  1  4  4  9  9  9  4  1 23  1  4 26 26
                        26 26  4  1  1  4  9  9  9  9 15  9  9  9  4  4  1  1 26 26
                     26 26  1  4  4  9 12  1 15  9 12  4 12  4 12  1  9  9  1  1 26 26
                  26 26  1  1  9  9  9  4 12  4 15  1 12  9 15  9 12  9 15  9  1  1 26 26
               26 26  1  1  9  9 12  4  9  1 12  9  9  1 12  4 12  4 12  1 12  9  1  4 26 26
            26 26  1  4  9  9 15  1 12  9  9  1 12  1  9  1 12  9  9  9 12  4 15  4  4  1 26 26
            26  1  4  9  9 12  1 15  4 12  4  9  1  9  4  9  9  1  4 12  1 12  1 12  9  1  4 26
            26  1  4  9  9  1 12  9 12  1 12  1  9  1 12  4 15  1  1  9 15  1 12  9  9  4 23 26
         26 26 23  4  9  4 15  9  1  1 15  4 12  1 15  1  9  9  9  4 12  4  9  1 12  1  4  4 26 26
      26 26  1  1  9  1 12  4 15  4  1  9  9  9  9  4  9  4 12  1 15  1 12  9 15  4 12  9  1  1 26 26
      26  4  1  4  9 12  4 12  9  9  9  9  4 15  1 12  4 15  4 12  9  9  1 12  9 15  4  9  9  1  1 26
      26  1  1  9 12  9 15  4 12  1 15  1 12  1  9  1 12  1  9  1  9  1  9  4 12  9 12  4  9  1  4 26
      26  1  4  9  9  1  1 12  9 12  1  9  9  1  4 12  9  1  1 12  4 12  4  9  4  1  4 12  4  1  1 26
      26  1  1  4 12  4  1  4  9  4 12  4 12  1  1  9 12  4  1  9  9  1 12  9 12  1  1  9  9  4  1 26
      26 23  1  9  4 12  9 12  4  9  1  9  1  9  1 12  1  9  1 12  1 15  1 12  4 15  9 12  9  1  1 26
      26  1  1  9  9  4 15  9 12  1  9  9 12  4 15  4 12  1 15  4  9  9  9  9 12  4 12  9  4  1  4 26
      26 26  1  1  9 12  4 15  9 12  1 15  1 12  4  9  4  9  9  9  9  1  4 15  4 12  1  9  1  1 26 26
         26 26  4  4  1 12  1  9  4 12  4  9  9  9  1 15  1 12  4 15  1  1  9 15  4  9  4 23 26 26
            26 23  4  9  9 12  1 15  9  1  1 15  4 12  1  9  1 12  1 12  9 12  1  9  9 23  1 26
            26  4  1  9 12  1 12  1 12  4  1  9  9  4  9  1  9  4 12  4 15  1 12  9  9  4  1 26
            26 26  1  4  4 15  4 12  9  9  9 12  1  9  1 12  1  9  9 12  1 15  9  9  4  1 26 26
               26 26  4  1  9 12  1 12  4 12  4 12  1  9  9 12  1  9  4 12  9  9  1  1 26 26
                  26 26  1  1  9 15  9 12  9 15  9 12  1 15  4 12  4  9  9  9  1  1 26 26
                     26 26  1  1  9  9  1 12  4 12  4 12  9 15  1 12  9  4  4  1 26 26
                        26 26  1  1  4  4  9  9  9 15  9  9  9  4  1  1  4 26 26
                           26 26  4  1  1  1  4  9  9  9  4  4  1 23  1 23 26 26
                              26 26 26 26  1  4  4  1  4  1  1  1 26 26 26 26
                                 26 26  1  4  1  4  6 23 26 26
                                    26 26 26 26 26 26 26 26
```

Each number represents one type of fuel or moderator property.

Figure 8.10: Radial composition in the PARCS input, at one axial plane

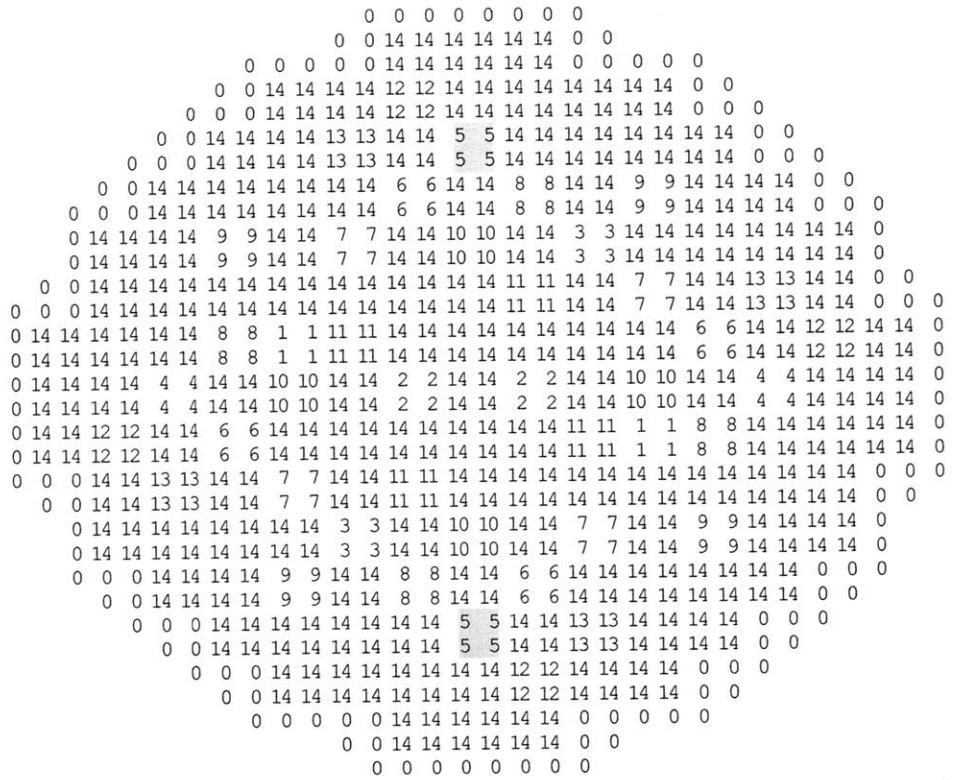

Each number represents one control rod bank; the same 4 numer in a 2×2 array represent one control rod.

Figure 8.11: Control rod bank configurations of Ringhals 1 at cycle 14

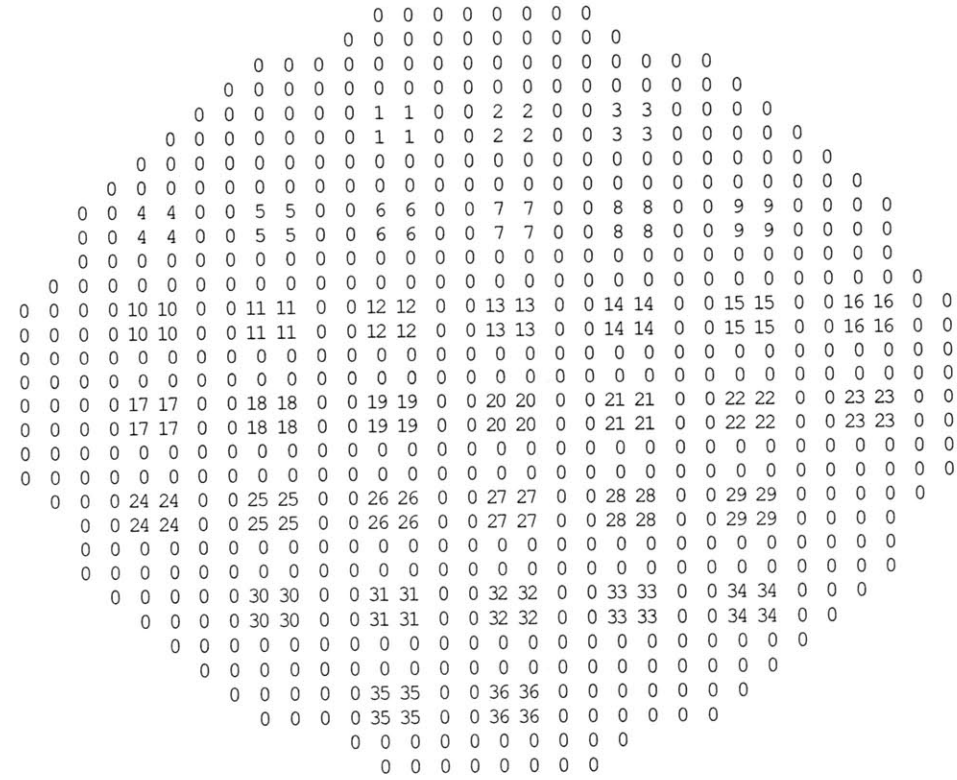

The center of 4 same numer in a 2×2 array represents one dectector.

Figure 8.12: Detector configurations of Ringhals 1 at cycle 14

9. Analysis of Ringhals Stability Test in the Time Domain - Analyses and Results

The TRACE/PARCS code is applied to simulate the Ringhals 1 stability test in this chapter. The goal is to examine the code capability to capture key aspects of the physics in a full-core 3D TH/NK model. Various modeling effects to the stability predictions are also investigated.

9.1 Steady State Results

For all eight test points, the steady states simulations were first performed using the TRACE stand-alone calculation under the assumption of fixed and uniform axial power distribution. Thus, the initial thermal-hydraulic operating conditions were obtained and used to perform the coupled calculation.

The main steady-state results from the coupled TRACE/PARCS calculation are listed in Table 9-1, along with the reference value in the benchmark specificaitons. Good agreements of the steady-states are confirmed. Note that the differences of the core power and flow rate are very small, below 0.04%, as shown in Table Table 9-1.

The axial power distribution is shown in Figure 9.1 for all test points. The axial and radial power shape at one test point, P09, are compared with the experimental results, as shown in Figure 9.2 and Figure 9.3. The results are in reasonably good agreements with the benchmark specifications.

Table 9-1: Steady state parameters from coupled calculation

Test Case	TRACE/PARCS calculations				Experimental Results			
	Steam dome Pressure (MPa)	Power (% rated)	Core Flow rate (kg/s)	Core inlet temperature (°C)	Steam dome Pressure (MPa)	Power (% rated)	Core Flow rate (kg/s)	Core inlet temperature (°C)
1	7.00	65.0	4105	265.7	7.00	65.0	4105	265.7
3	7.00	65.0	3666	262.6	7.00	65.0	3666	262.6
4	7.01	70.0	3657	262.5	7.01	70.0	3657	261.1
5	7.01	70.0	3868	262.7	7.01	70.0	3868	262.7
6	7.01	70.2	4126	263.9	7.01	70.2	4126	263.9
8	6.99	75.1	3884	260.9	6.99	75.1	3884	260.9
9	7.01	72.6	3694	260.4	7.01	72.6	3694	260.4
10	69.9	77.7	4104	261.9	69.9	77.7	4104	261.9

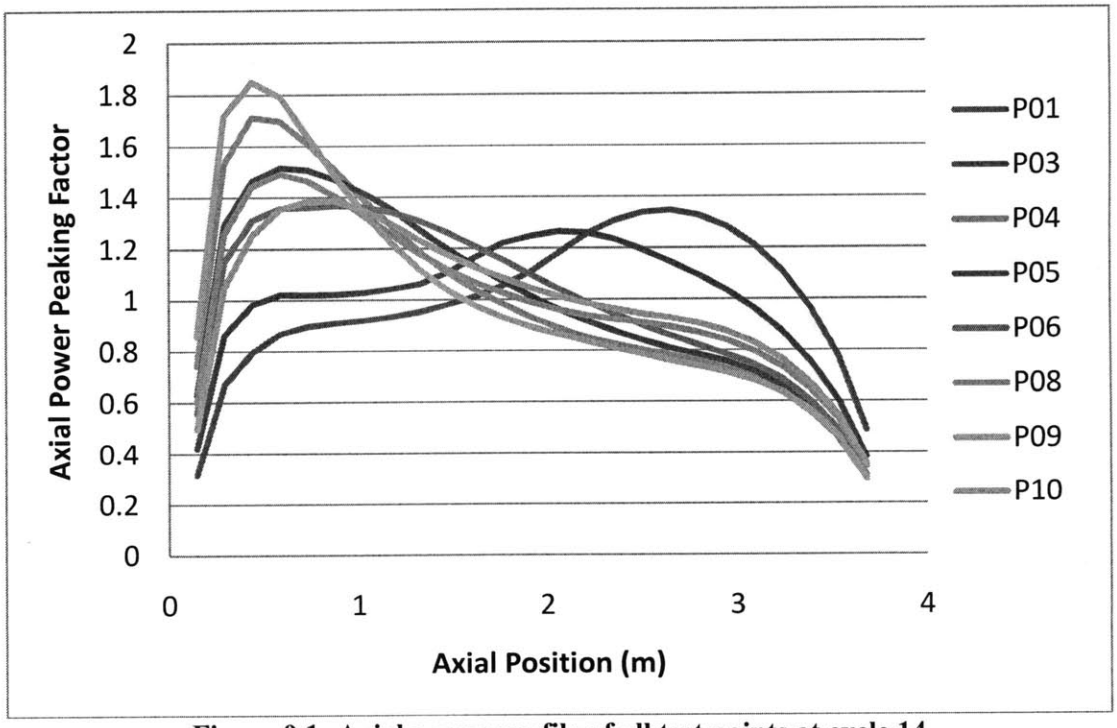

Figure 9.1: Axial power profile of all test points at cycle 14

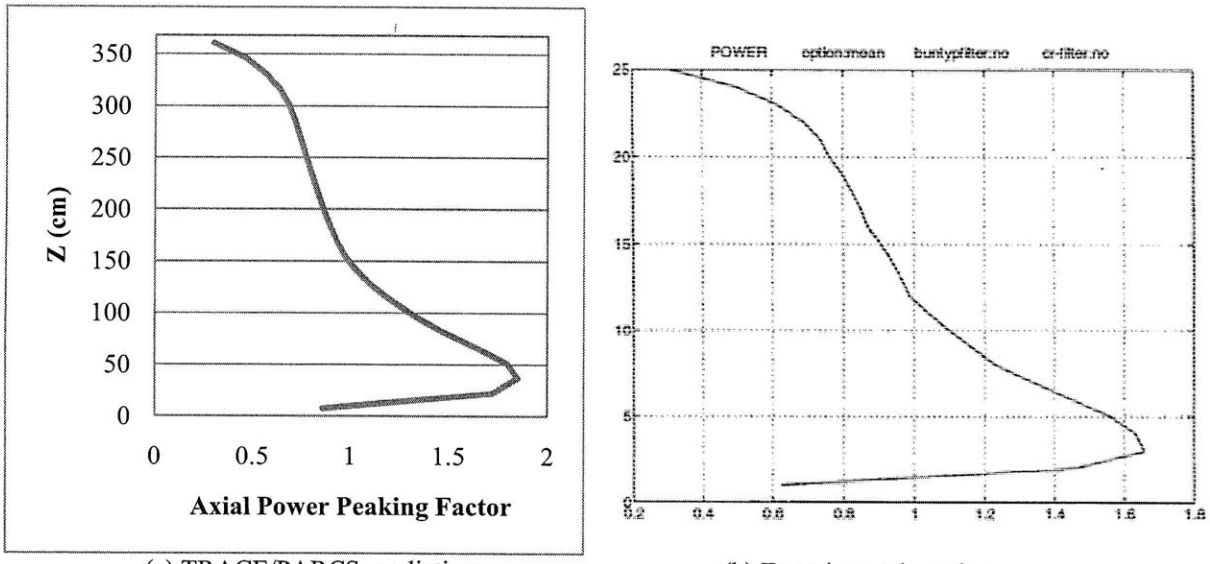

(a) TRACE/PARCS predictions (b) Experimental results

Figure 9.2: Axial power profile of C14P09

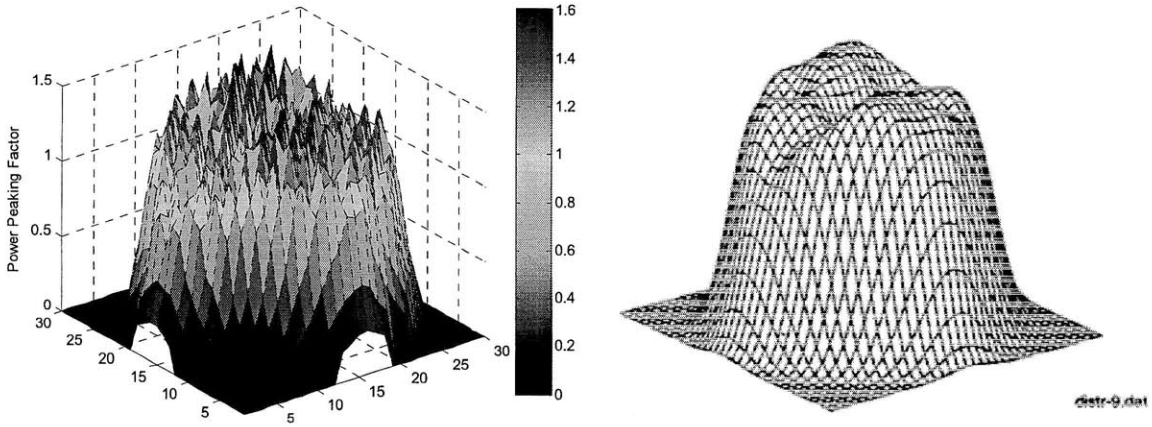

(a) TRACE/PARCS predictions (b) Experimental results

Figure 9.3: Radial Power distribution of C14P09

9.2 Simulation of Oscillation Transients, In-Phase

The stability simulation is performed using the semi-implicit scheme in TRACE by introducing initial excitations to initiate the transient. These perturbations are:

(1) Control rod (neutronics) perturbation: one or more control rods is temporarily moved and then restored to its original position in the PARCS model.

- T=1s, start moving the control rod bank 5 (as shown in Figure 8.11) at step 50;
- T=1.5s, the control rod is at its maximum position, step=51;

- T=2s, the control rod is moved back to the original position, step=50.

(2) Pressure (thermal-hydraulic) perturbation: a short perturbation is applied to the turbine inlet pressure of the TRACE model.

- T=1s, pressure step increase 20 kPa;
- T=1.1s, pressure step decrease 20 kPa.

9.2.1 P01 Case study, transient response

The power and core flow responses of the CR case for point P01 are presented in Figure 9.4 and Figure 9.5. As can be observed in Figure 9.4, the power oscillated due to the initial control rod perturbation, which disturbed the core flow in Figure Figure 9.5. The power oscillated around 10 second (5 cycles) until the steady state conditions are re-established. It is also interesting to point out that the initial oscillation amplitude of the power is about 1.6%, while the oscillation amplitude of the core flow is around 0.13%. The variation in the mass flow rate is more than 10 times smaller than that of the power.

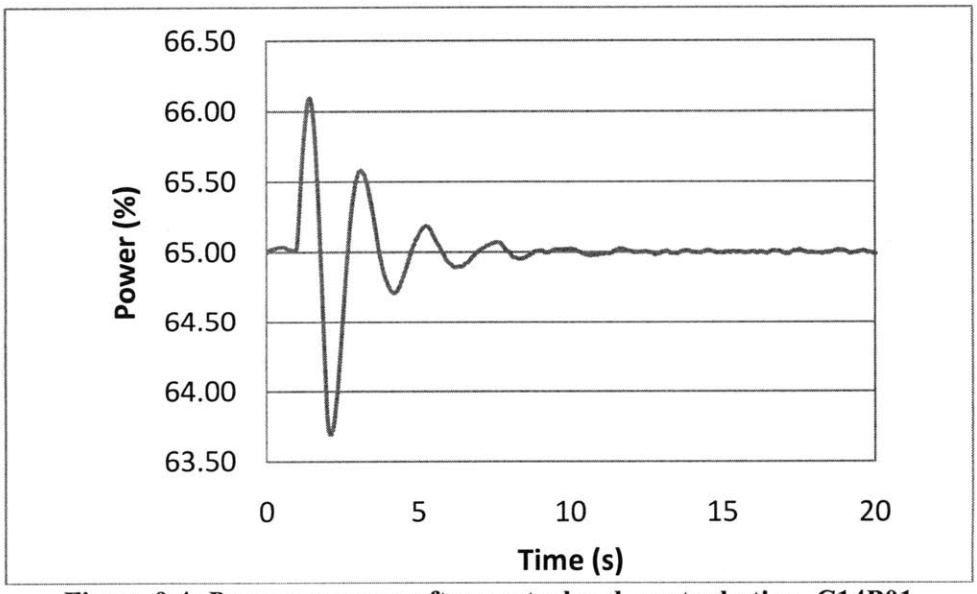

Figure 9.4: Power response after control rod perturbation, C14P01

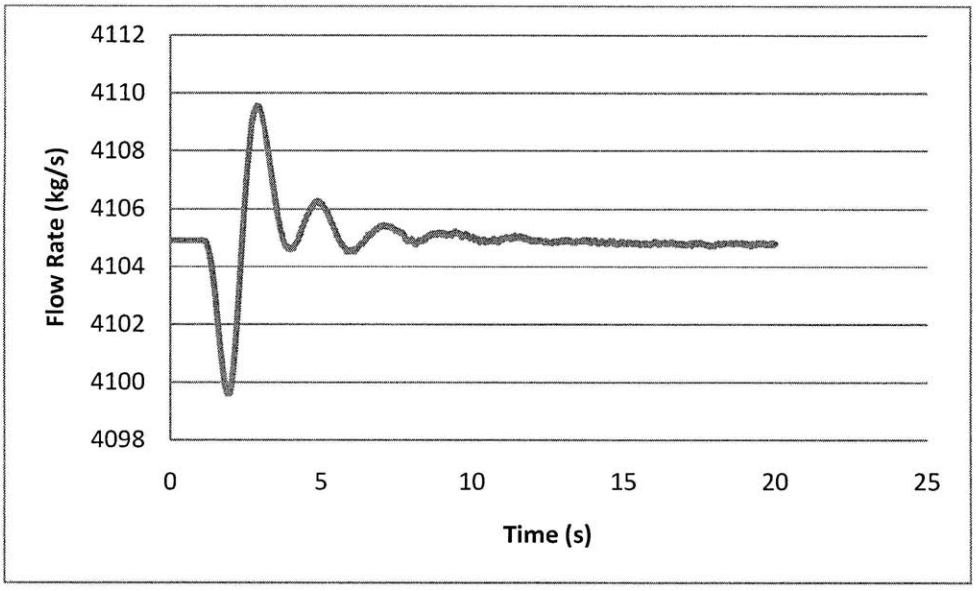

Figure 9.5: Core flow response after control rod perturbation, C14P01

Semilar results are obtained from the pressure perturbation, as shown in Figure 9.6 to Figure 9.8. During the pressure perturbation, a small pressure wave is created and it propagates along the steam line reaching the core zone through two different paths: the steam separator filled with water and steam, and the downcomer and lower plenum filled with water. The pressure perturbation disturbs the mass flow rate in a increasing or decreasing way, depending on whether the pressure wave reaches the upper or the lower plenum first. As shown in Figure 9.7, the core mass flow rate increases as an effect of the pressure wave being in the bottom-up direction. The core void fraction correspondingly decreases; then a positive reactivity is introduced into the core due to void fraction decrease, bringing an increase in power. When the perturbation terminates, the value of the void fraction increases again; consequently, the negative reactivity feedback causes power to decrease. This process lasts several cycles with some damping in the power oscillation and, after approximately 10 seconds, the oscillations are terminated.

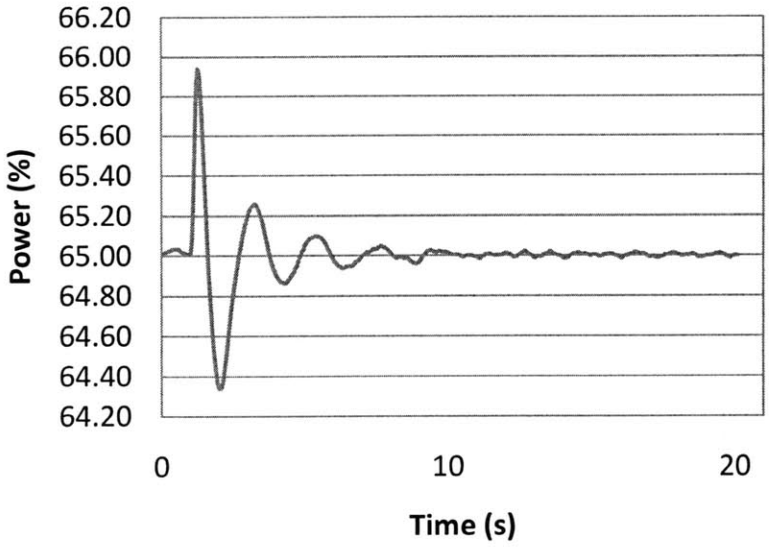

Figure 9.6: Power response after pressure perturbation, C14P01

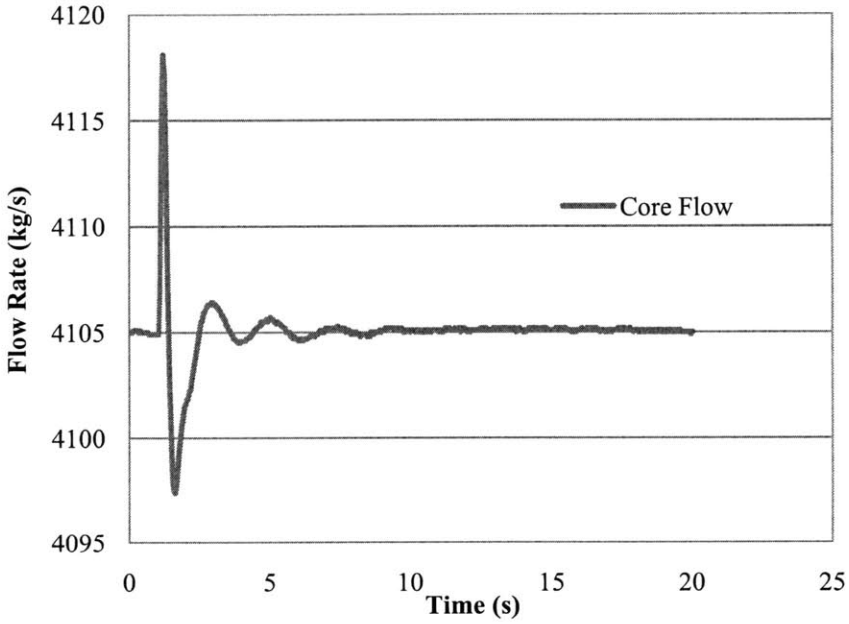

Figure 9.7: Core flow response after pressure perturbation, C14P01

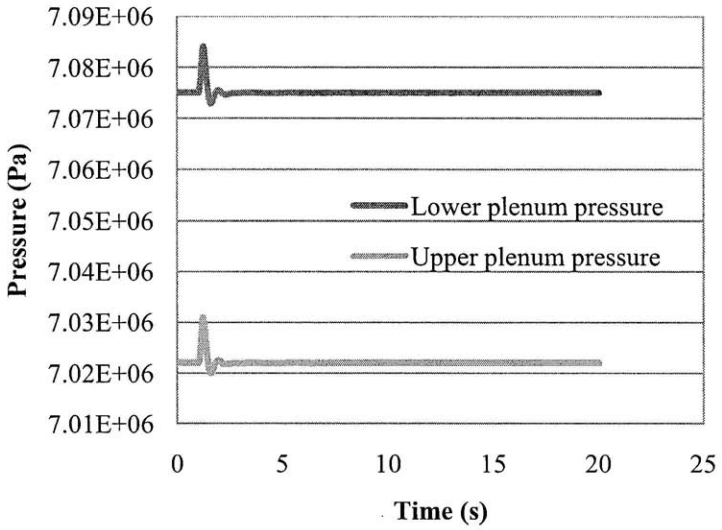

Figure 9.8: Pressure response at lower and upper pelnum after pressure perturbation, C14P01

9.2.2 P01 Case study, time window effects

The decay ratios (DR) and natural frequencies (NF) from the power signal have been calculated using the DRACO code described in Section 8.3. The direct fitting method is used here to investigate the effects of considered signals, as shown in Figure 9.9. It can be observed in Table 9-2 that the DR and NF can vary significantly depending on the time window considered in the calculation.

The DR is calculated from the direct fitting of the power signal to a damped sinusoidal form:

$$x(t) = c_0 + ce^{-\alpha t}\cos(\omega t + \varphi) \tag{9-1}$$

If the least square fitting is successful, the DR and NF of the system are given as:

$$DR = e^{-2\pi\alpha/\omega}, \quad NF = \omega/(2\pi) \tag{9-2}$$

This definition of DR and NF is appropriate for transients with small and short perturbations, as the CR and PP cases used in this work. The first several seconds of the calculated time trace are usually not good for the fit because they have contamination from higher-order modes and the particular shape of the perturbation used. As shown in

Table 9-2, the three good fits (*R-square* close to one and *DR* close to the reference value) are derived from the data points 50-200, 50-300, and 50-448. The first cycle signals are all neglected in these cases.

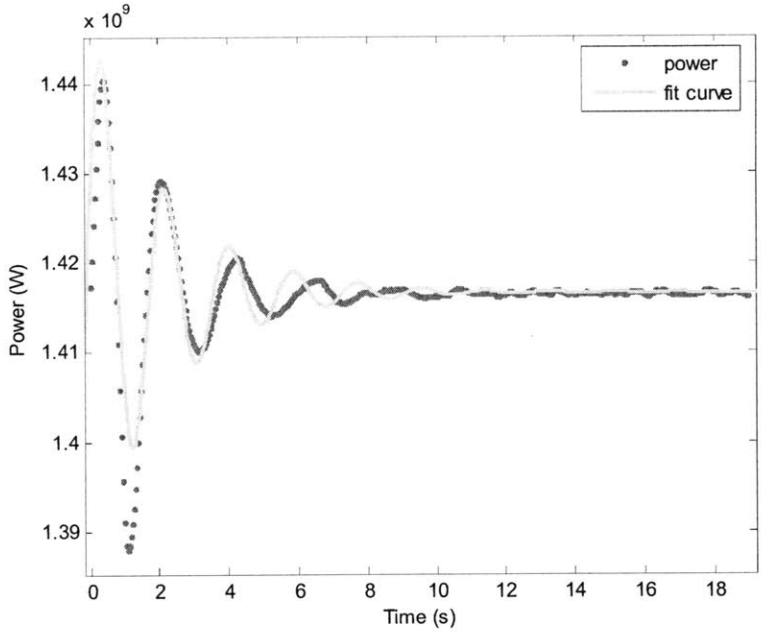

Figure 9.9: Power response and its fitting curve after control rod perturbation, C14P01

Table 9-2: Decay ratio evaluation from power signal during CR, C14P01

Case (data points)	α	*c*	*w*	ϕ	*SSE*	*R-square*	*DR*	*Freq.*
Reference Value	-						0.30	0.43
All data point (0-448)	0.4326	2.97E+07	3.394	5.123	2.97E+15	0.8125	0.449	0.540
0-100	0.3915	2.93E+07	3.495	5.027	2.46E+15	0.8386	0.495	0.557
0-200	0.4225	2.93E+07	3.379	5.142	2.92E+15	0.8136	0.456	0.538
26-200	0.7068	6.23E+07	3.026	5.944	7.13E+13	0.9921	0.231	0.482
26-400	0.7059	6.23E+07	3.024	5.948	8.96E+13	0.9903	0.231	0.482
51-200	*0.5355*	*3.75E+07*	*2.963*	*6.149*	*2.15E+13*	*0.9878*	*0.321*	*0.472*
51-300	*0.5317*	*3.72E+07*	*2.956*	*6.17*	*3.09E+13*	*0.9826*	*0.323*	*0.471*
51-448	*0.5319*	*3.72E+07*	*2.956*	*6.169*	*4.15E+13*	*0.9768*	*0.323*	*0.471*
100-200 (no fit)	0.8106	1.00E+08	6.29	4.205	1.16E+14	0.436	0.445	1.002
100-300 (no fit)	0.8061	1.00E+08	4.223	6.29	1.34E+14	0.4217	0.302	0.672
100-448(no fit)	0.8061	1.00E+08	4.223	6.29	1.44E+14	0.3865	0.302	0.672

SSE: Sum of Square due to Error;
SST: Sum of Squares about the mean;
R-Square: 1-SSE/SST

9.2.3 Ringhals Benchmark for all test points in Cycle 14

The transient instability tests (control rod perturbation and pressure perturbation) were performed for each of the 8 test points in Cycle 14. The results of the DR and NF are shown in Table 9-3 and graphically in Figure 9.12 and Figure 9.13. The decay ratios are derived from the raw signals and IRFs in both the CR and PP simulations. The examples of the curve fitting of the original power and the fitting of the IRF signal are shown respectively in Figure 9.10 and Figure 9.11 for test point 10.

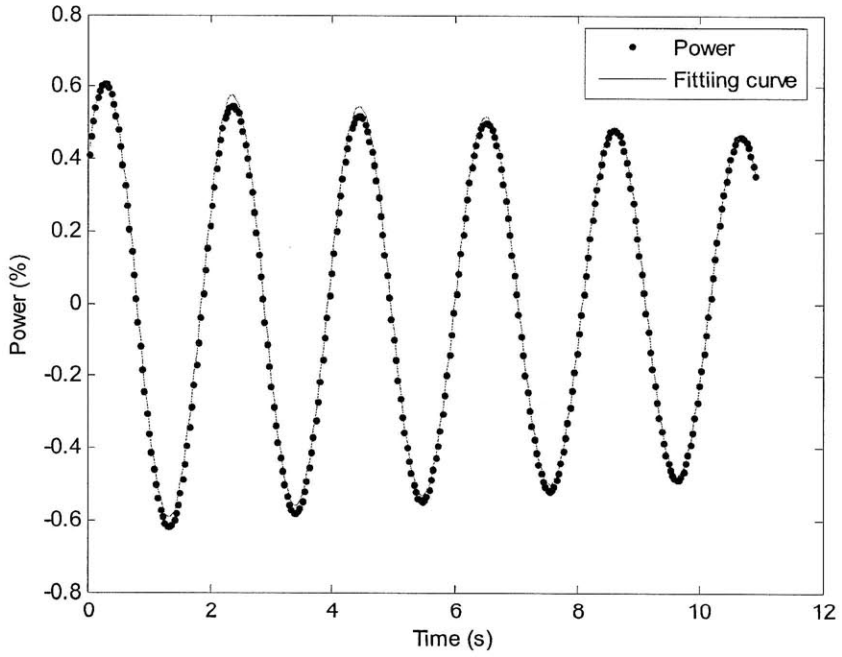

Figure 9.10: Power signal and its fitting curve under pressure perturbation, C14P10

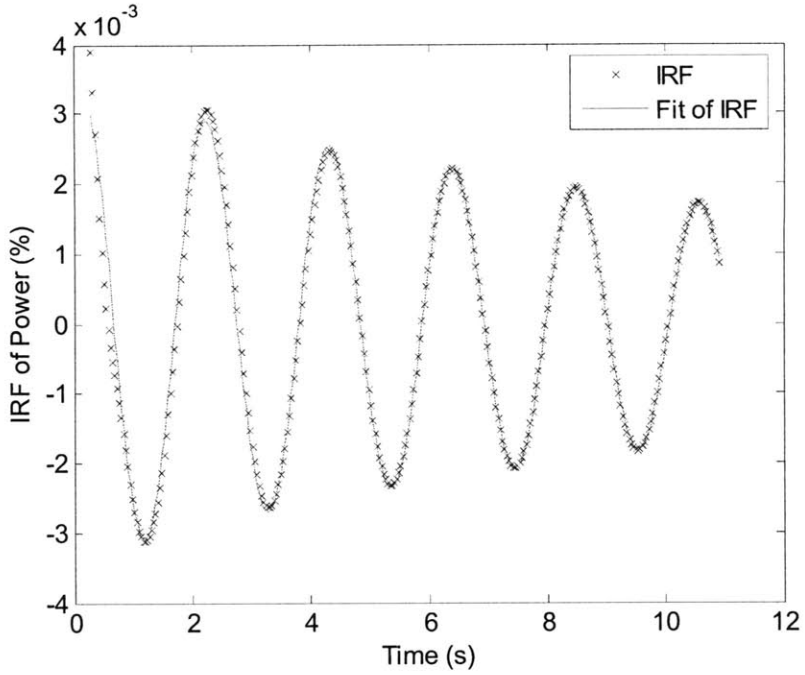

Figure 9.11: IRF of Power signal and its fitting curve under pressure perturbation, C14P10

Table 9-3: Summary of Ringhals 1 Stability Test Results in Cycle 14, In-phase

Test Cases	DR					Frequency (Hz)				
	Ref.	CR-RAW	PP-RAW	CR-IRF	PP-IRF	Ref.	CR-RAW	PP-RAW	CR-IRF	PP-IRF
P01	0.3	0.33	0.42	0.31	0.39	0.43	0.48	0.47	0.47	0.46
P03	0.69	0.58	0.61	0.56	0.61	0.43	0.44	0.43	0.45	0.45
P04	0.79	0.88	0.87	0.85	0.84	0.55	0.53	0.53	0.53	0.53
P05	0.67	0.93	0.94	0.87	0.87	0.51	0.51	0.51	0.51	0.51
P06	0.64	0.82	0.84	0.81	0.82	0.52	0.50	0.50	0.50	0.50
P08	0.78	1	1	0.69	0.84	0.52	0.49	0.49	0.49	0.49
P09	0.8	0.84	0.85	0.85	0.83	0.56	0.55	0.55	0.55	0.55
P10	0.71	0.93	0.95	0.86	0.87	0.5	0.48	0.48	0.48	0.48

RAW: raw power signal from the transients

IRF: impulse response function of the power signal

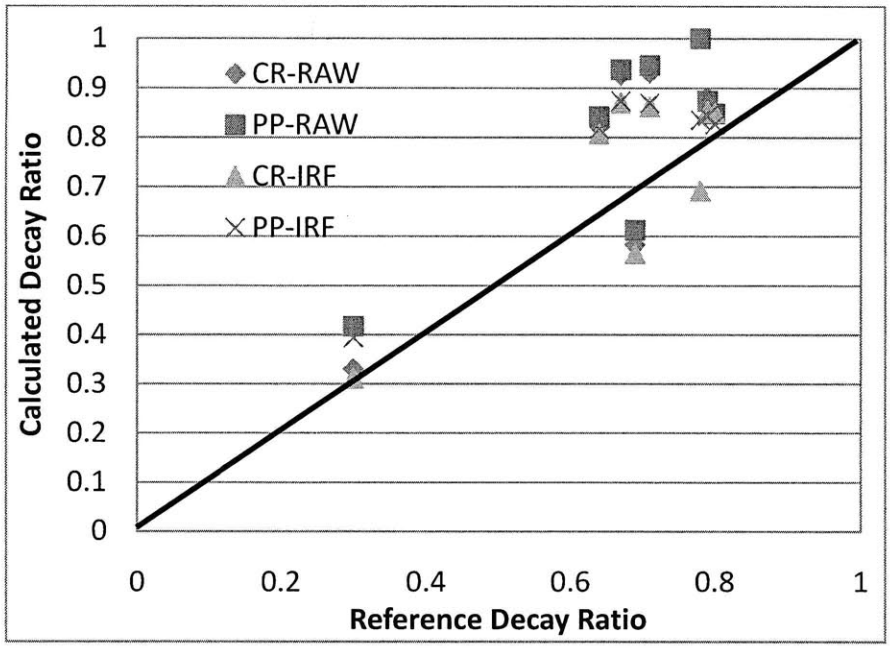

Figure 9.12: Calculated decay ratios in Cycle 14

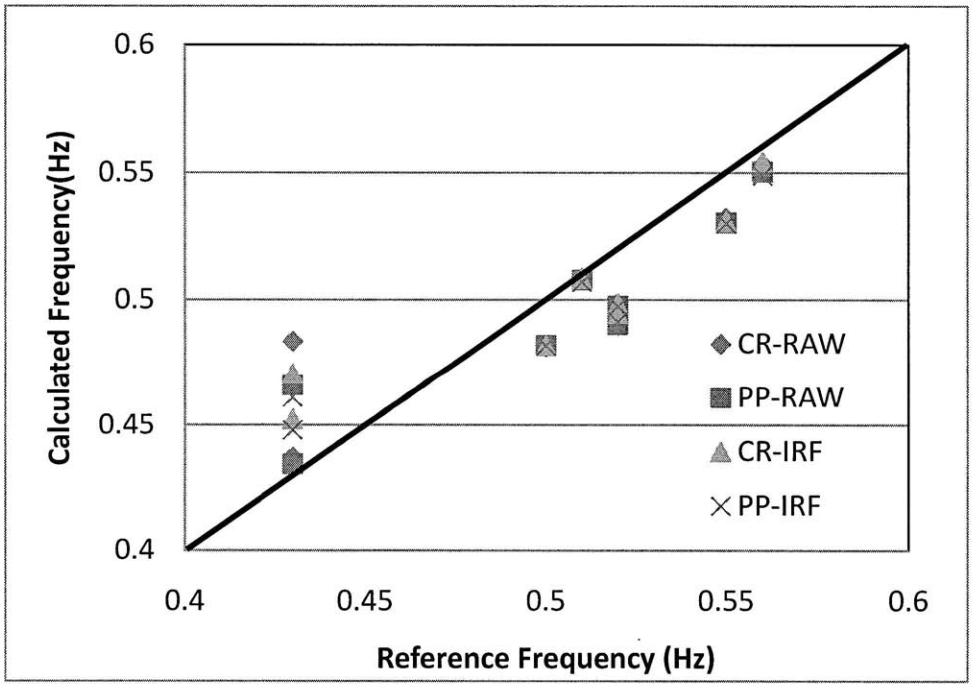

Figure 9.13: Calculated oscillation frequencies in Cycle 14

Using the formula in Eq. (8-4) and (8-5), the biases and standard deviations of the difference between the calculated and reference decay ratios and oscillation frequencies are shown in Table 9-4.

Table 9-4: Bias and standard deviation of the difference between calculated and reference decay ratios and oscillation frequency

Mode	Decay ratio		Frequency	
	Bias	Standard deviation	Bias	Standard deviation
CR-RAW	0.12	0.12	-0.004	0.026
PP-RAW	0.14	0.12	-0.008	0.021
CR-IRF	0.05	0.12	-0.004	0.024
PP- IRF	0.087	0.09	-0.007	0.021

It is seen that the biases of the predicted decay ratio are between 0.05 and 0.14 respectively for the different signals used. However, the evaluated frequencies are in very good agreement with the reference values, all the biases are less than 0.01 and the standard deviations are less than 0.03. It can be concluded that the TRACE/PARCS analysis results are in reasonably good agreement with the experimental results, at least of the same level of accuracy as the benchmark work in [Lefvert, 1996].

9.3 Simulation of Oscillation Transients, Out-of-Phase

9.3.1 Simulation of asymmetric initial neutronic perturbation, using half-core symmetry TRACE model

The simulation of out-of-phase oscillation starts with the half-core symmetric 325 channel model, but is initiated with an asymmetric initial control rod perturbation. Test point 9 is chosen in this analysis since it experienced a limit cycle out-of-phase oscillation during the test.

To model the asymmetric control rod perturbation, the control rod bank configuration in Figure 8.11 is modified, as shown in Figure 9.14. The control rod bank 5 (with 2 control rods) is divided into 2 banks, bank 5 and bank 15. Only the new bank 5 will be moved in the asymmetric control rod perturbation.

Various initial perturbations were introduced:

0) Symmetric initial perturbation, as described in Section 9.2, moving both the bank 5 and bank 15 in 1 second: step 50->51->50
   - T=1s, start to moving the control rod bank 5 and 15 from step 50,
   - T=1.5s, the control rod banks are at its maximum position, step=51
   - T=2s, the control rod banks are moved back to the original position, step=50.

1) Change the control rod bank position in 1 s: step 50->52->50
   - T=1s, start to moving the control rod bank 5 from step 50,
   - T=1.5s, the control rod is at its maximum position, step=52
   - T=2s, the control rod bank is moved back to the original position, step=50.

2) Change the control rod bank position in 1 s: step 50->54->50
3) Change the control rod bank position in 0.5 s: step 50->54->50
4) Change the control rod bank position in 0.5 s: step 50->54->54
   - T=1s, start to moving the control rod bank 5 from step 50,
   - T=1.5s, the control rod at its maximum position (step=54) and remain there.

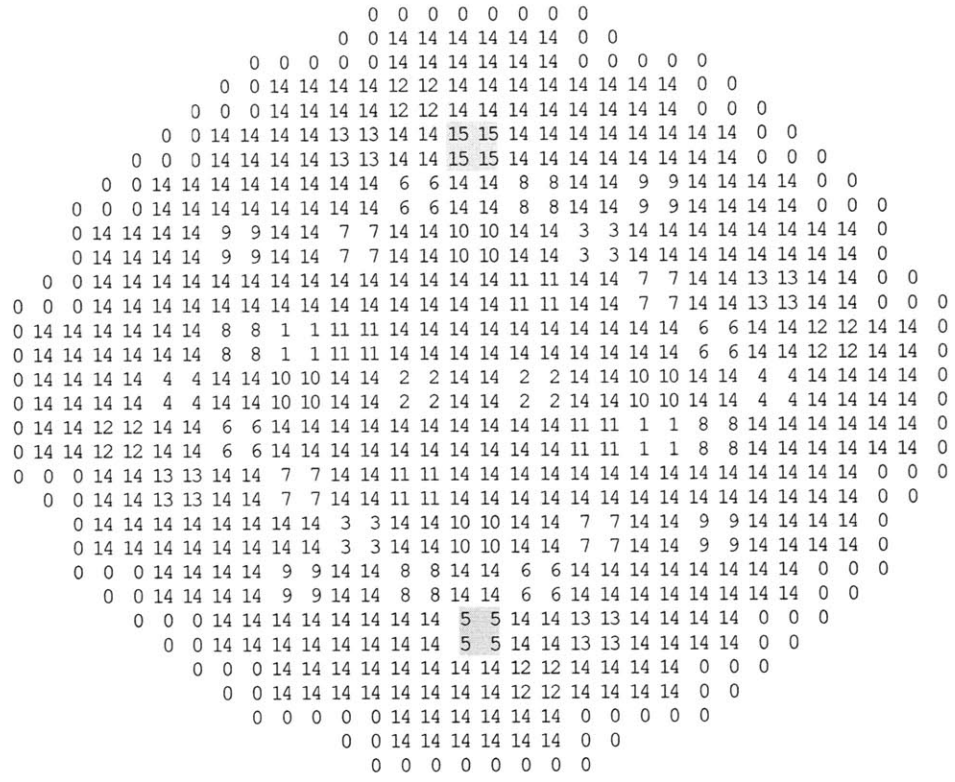

Figure 9.14: Control rod bank configurations of Ringhals 1 at cycle 14

To investigate the out-of-phase oscillation, several local assembly power signals are required. The interesting assemblies are highlighted in Figure 9.15. The transient power response signals of the APRM and LPRMs are shown in Figure 9.16 and Figure 9.17. Note that LPRM1 to LPRM4 in Figure 9.17 are the channel power signal of the interesting assemblies F1 to F4 in Figure 9.15, which are not the same as the LPRM signals from the neutron detectors in the experiments.

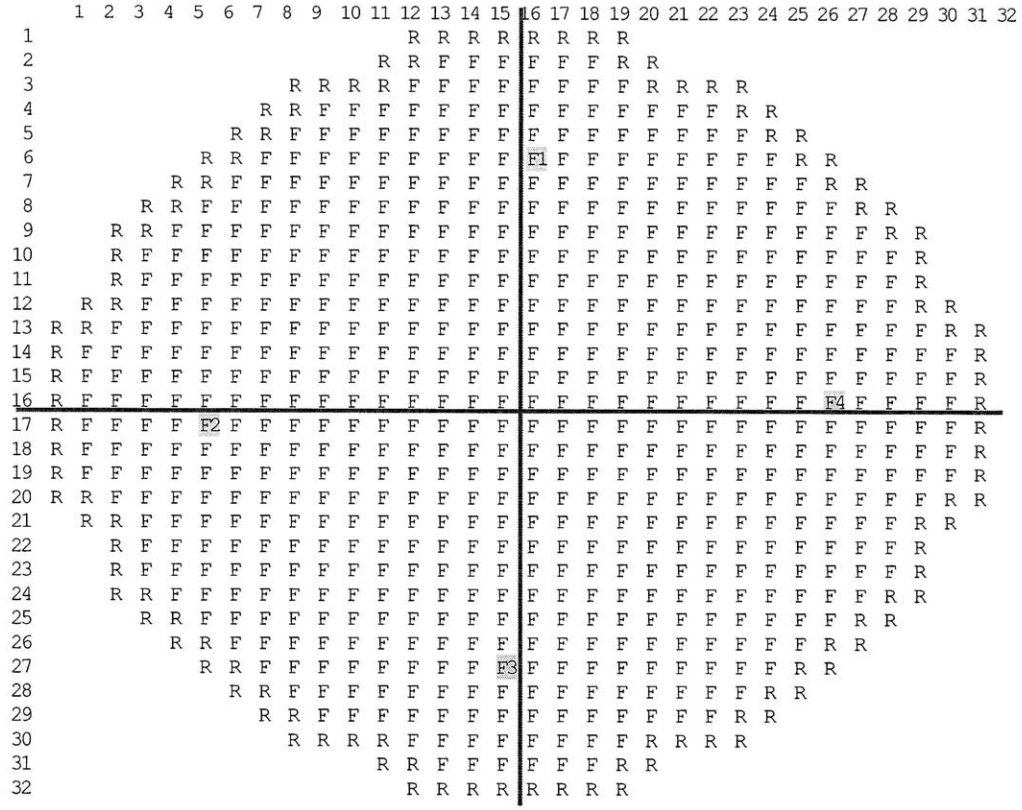

R: Reflector, F: Fuel

Figure 9.15: Planar representation of the PARCS model

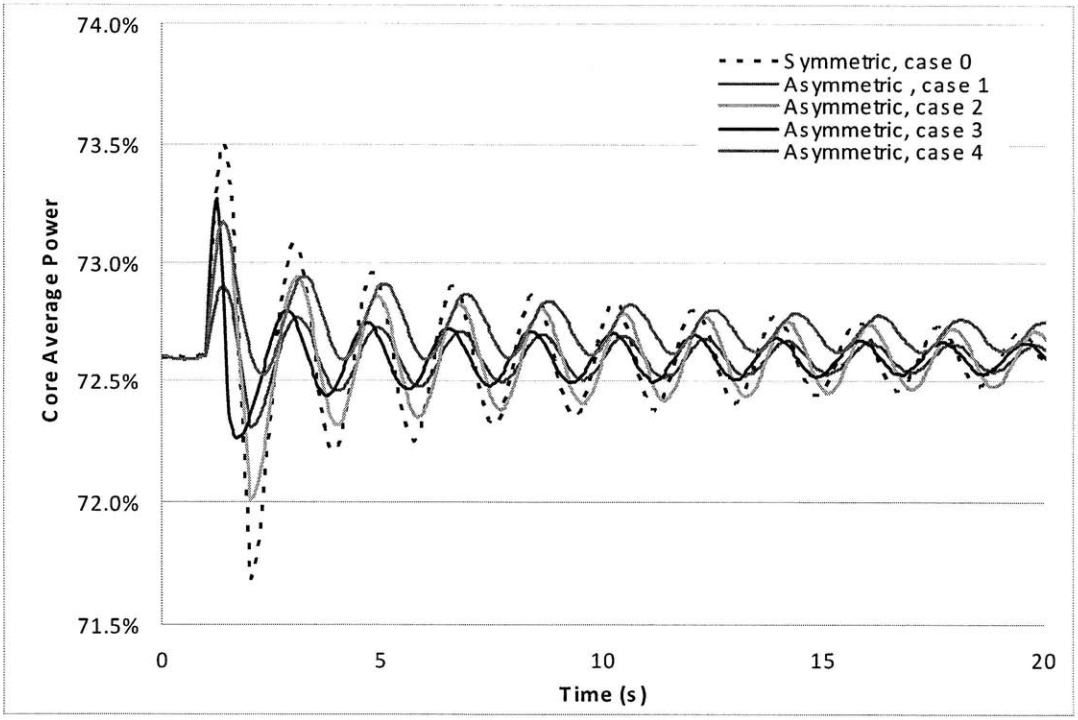

Figure 9.16: Core average power responses after initial perturbations

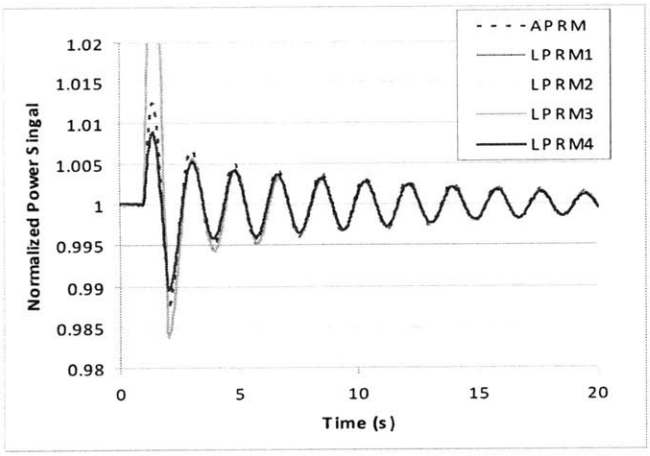

(a) Symmetric initial perturbation, Case 0

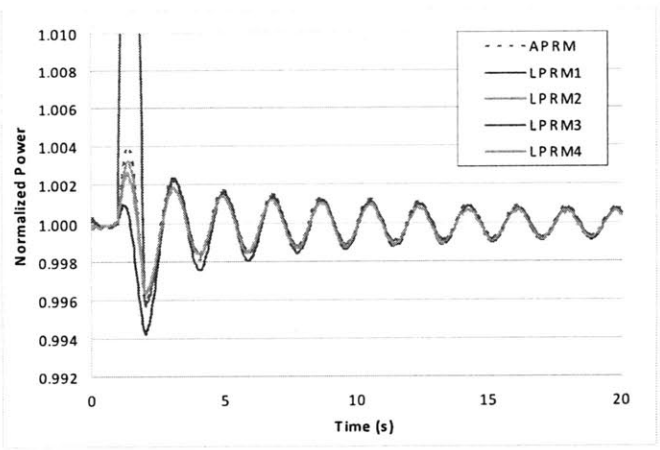

(b) Asymmetric initial perturbation, Case 1

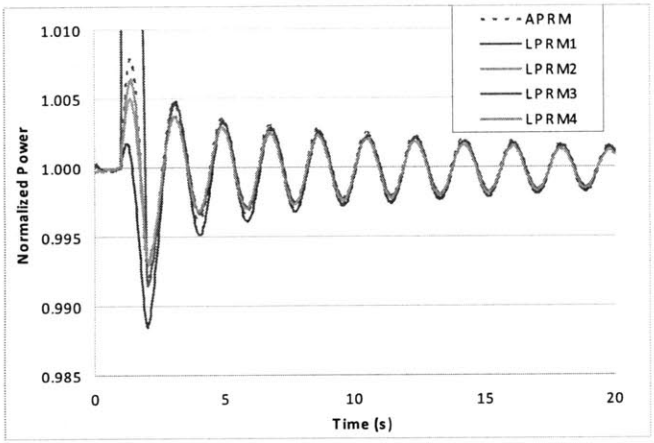

(c) Asymmetric initial perturbation, Case 2

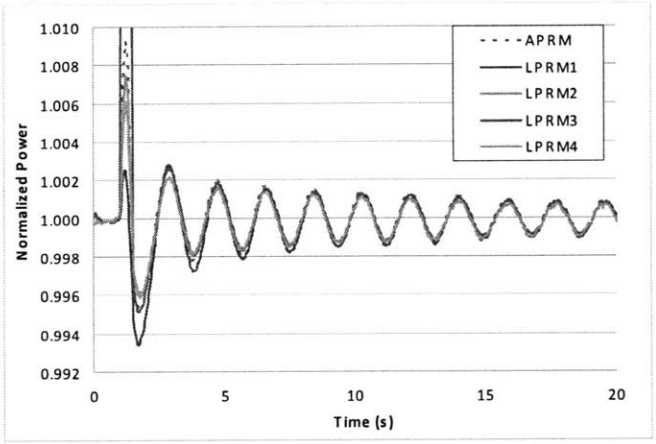

(d) Asymmetric initial perturbation, Case 3

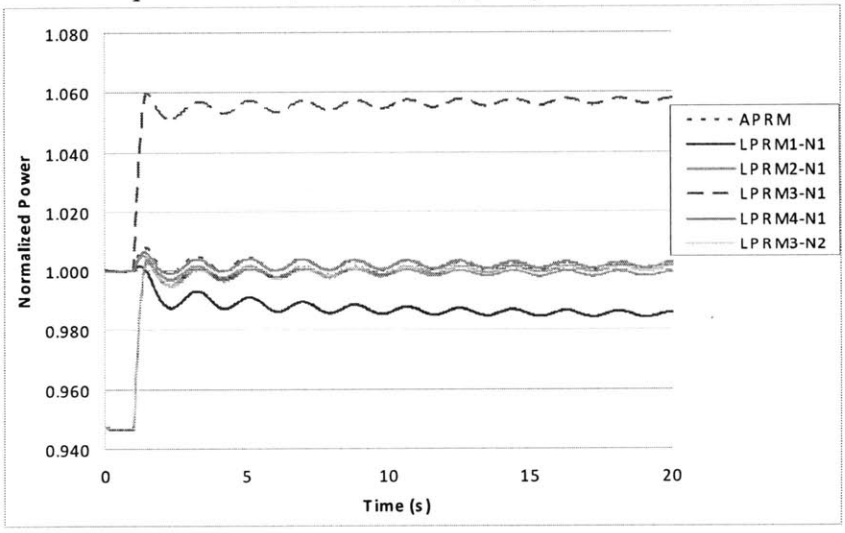

(e) Asymmetric initial perturbation, Case 4;

N1: normalized to its initial steady-state value; N2: normalized to the average value of its final state.

Figure 9.17: Normalized (to its own steady state value) power signal during power oscillation for various initiation cases

It is seen in Figure 9.17 that no phase lag between the LPRM and APRM signals is observed during both the symmetric and asymmetric initial perturbations; all interesting LPRM (channel power) signals are in-phase with the APRM (core average power). Thus, it is confirmed that the out-of-phase oscillation can not be simulated with a symmetric thermal-hydraulics model, even with asymmetric initial perturbations. Other notable results include:

1) The control rod worth of moving the control rod banks is higher in the symmetric case (case 0) than those in the asymmetric cases (case 1, 2 3), although the total changes of the control rod steps are the same.
2) Despite the differences in initial perturbations, the normalized LPRM signals stand together with the APRM signal right after the end of the initially introduced perturbation.
3) In case 4, the core power does not return to its initial steady-state value, but is stabilized at a higher power condition.

9.3.2 Simulation of Parallel Channel Type of Instabilities

It is concluded in Section 9.3.1 that the out-of-phase oscillation could not be simulated with a symmetric thermal-hydraulcs model even it initiated asymmetric neutronics perturbations. On the contrary, a simple 2-channel thermal-hydraulcs model with constant power (no neutronics feedback) is used in this section to investigate the mechanisms of the out-of-phase oscillations.

The 2-channel model is illustrated in Figure 9.18. The feedwater is injected from Component 100 with constant flow rate, flowing through two channels (320 and 420), which are connected at the top (104) and bottom (103) of the two channels, and finally entered into 535. Each channel is connected with a special injection flow path, which is used to initiate channel inlet flow perturbation.

An arbitrary initial flow perturbation is applied by changing the time-dependent extra injection flow through junction 201 and 401 to channel 320 (later referred to as channel 1) and 420 (later referred to as channel 2), as shown in Figure 9.19.

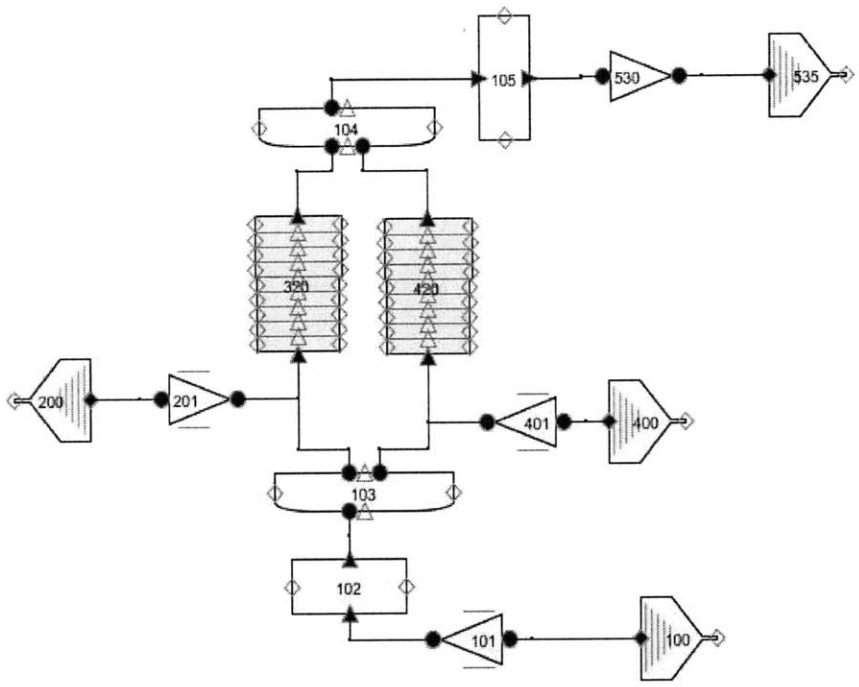

Figure 9.18: 2-channel model for parallel channel instability

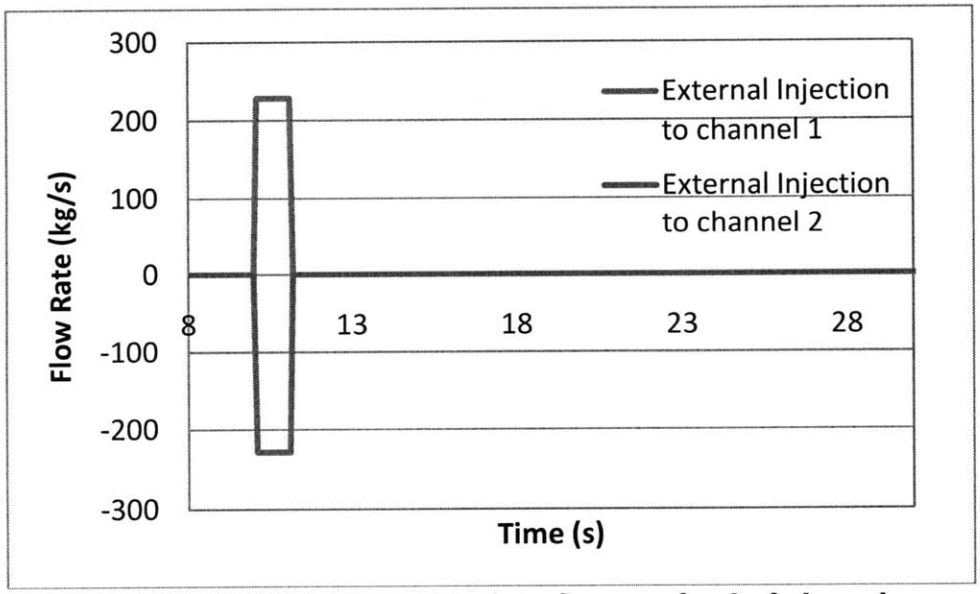

Figure 9.19: Perturbation of the inlet flow rate for the 2 channels

The transient flow rate responses of the two channels are shown in Figure 9.20. It is seen that the inter-channel phase difference between the two parallel channels matches the ideal out-of-phase relation, i.e. 180 degree. Also, an out-of-phase relation (180 degree phase delay) is observed between the inlet and outlet mass flow rate for two channels.

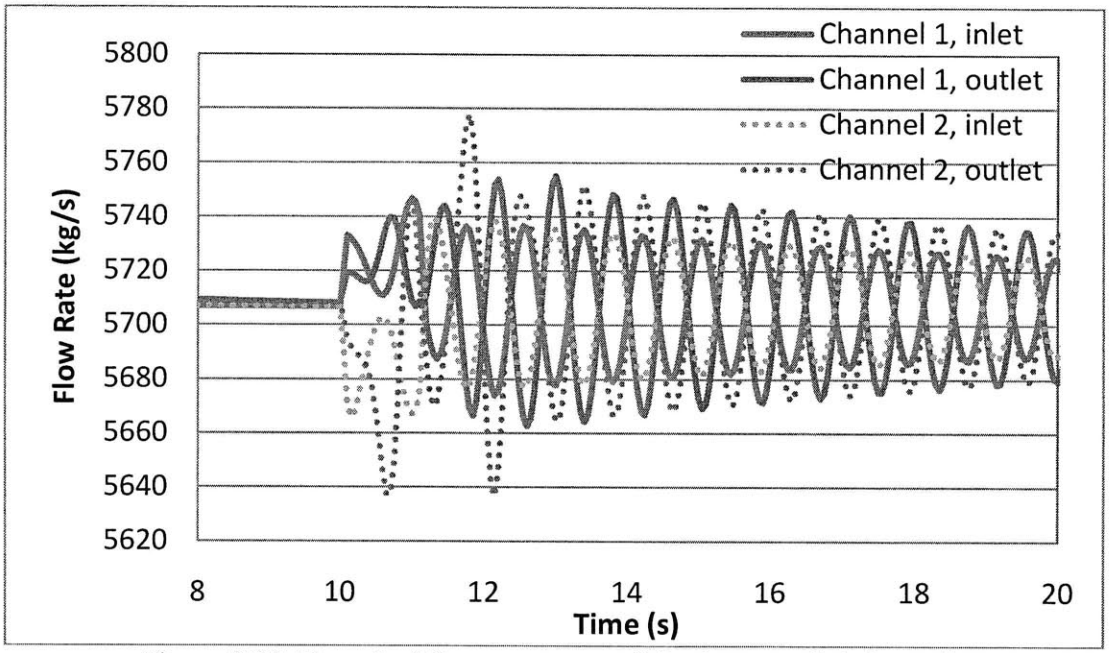

Figure 9.20: Transient flow responses of the two parallel channels

It is thus confirmed that out-of-phase type of DWO is initiated by the thermal-hydraulics dominated by thermal-hydraulic characteristics.

9.3.3 Out-of-phase Instability Simulation with the full-core 648-channel model

As shown in Section 9.3.1, the asymmetric neutronic excitation (initial control rod perturbation) cannot introduce asymmetric hydraulic disturbances, and the regional (out-of-phase) oscillation was not observed in the TRACE simulations. Thus, the half-core symmetric 325 channel model is modified to a one-to-one channel modelling, i.e. 648 channel model, for out-of-phase instability simulation, as depicted in Figure 9.21.

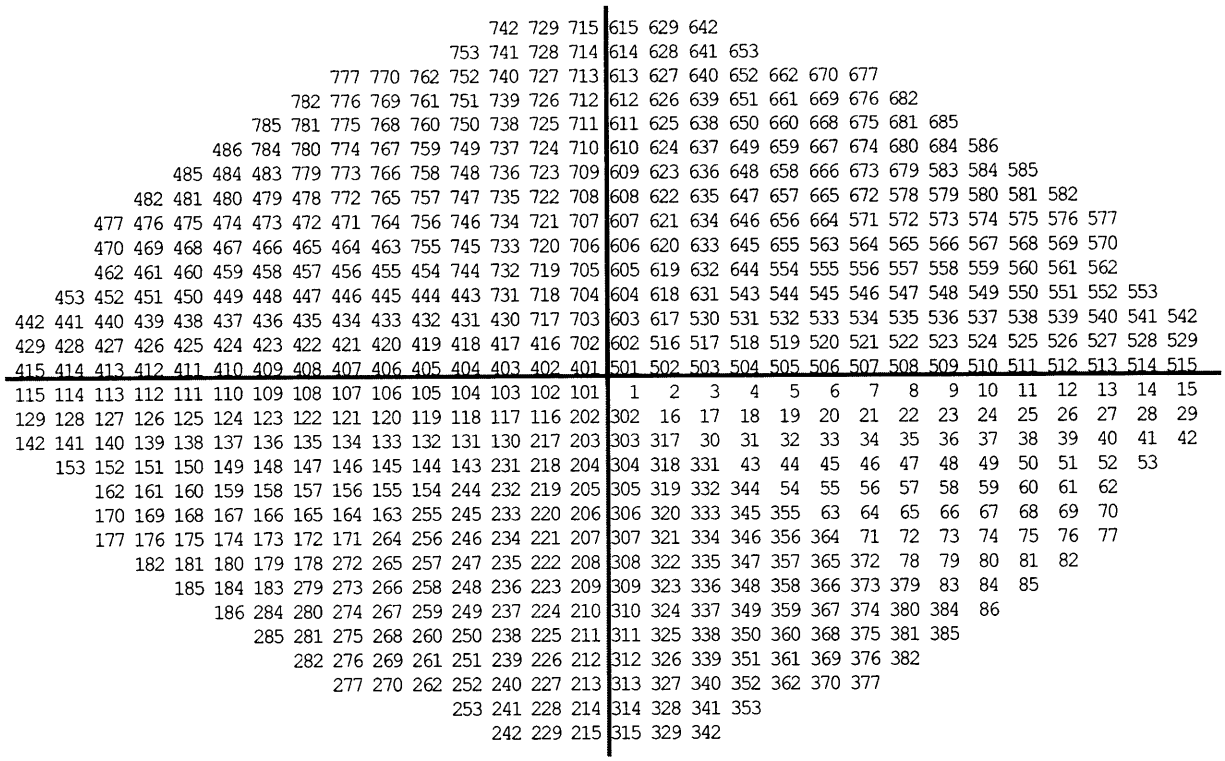

Figure 9.21: TRACE 648 Channel Model for Out-of-Phase Stability Analysis

A coupled null transient step is added in the simulation procedure to smooth the transition from steady-state calculation to transient calculation in TRACE/PARCS coupled simulations. The following procedure is applied during the out-of-phase stability simulation:

1) Stand-alone TRACE initialization of the thermal-hydraulics field using a fixed power distribution and a constant power.
2) A steady state calculation is then performed with the coupled code TRACE/PARCS to achieve a converged coupled thermal-hydraulic/neutron flux solution.
3) A coupled TRACE/PARCS null transient is performed.
4) The stability simulation is then performed by introducing the asymmetric control rod perturbation, moves both the bank 5 and bank 15 (as shown in Figure 8.26) in 1 second:
   - T=51s, start to moving the control rod bank 5 and 15 from step 50;
   - T=51.5s, the control rod bank 5 is at its maximum position, step=54; and control rod bank 15 is at its minimum position, step=46.

- T=52s, the control rod banks are both moved back to the original position, step=50.

5) Time-series analysis is performed to evaluate the decay ratio and oscillation frequency from the transient results.

Test point 9 is again chosen in this analysis since it experienced a limit cycle out-of-phase oscillation during the stability test. *However*, a *convergence problem was encountered in the TRACE simulation with the 648 channel model.* It is shown in Figure 9.22 that the average core power signal did not achieve steady-state before the transients was initiated at T=51s, and it continued oscillating during the transients. The initial movement of the control rods should have very small impact on APRM, since the two control rod banks have the same control rod worth and they were moved in reverse directions.

The transient power signals of the four interesting local assemblies, highlighted in Figure 9.15, are shown in Figure 9.23. It is seen that the channel power signal LPRM1 and LPRM3, respond simultaneously to the control rod bank movements; but the oscillation amplitudes are very small compared to the initial perturbation. The limit cycle out-of-phase oscillation in the experiment is not observed and the oscillation amplitude is damped during the transient. However, a 180° phase lag between the LPRM1 and LPRM3 signals is observed; also some phase lag between LPRM2 and LPRM4 signals is noted.

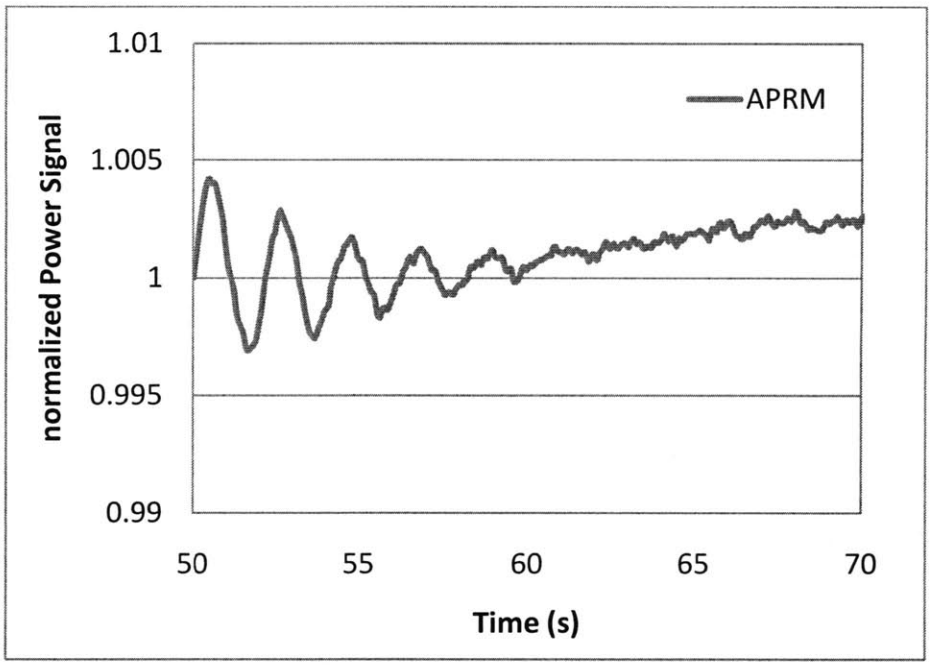

Figure 9.22: Normalized (to its initial value) core power signal during asymmetric control rod perturbation, 648 channel model at C14P09

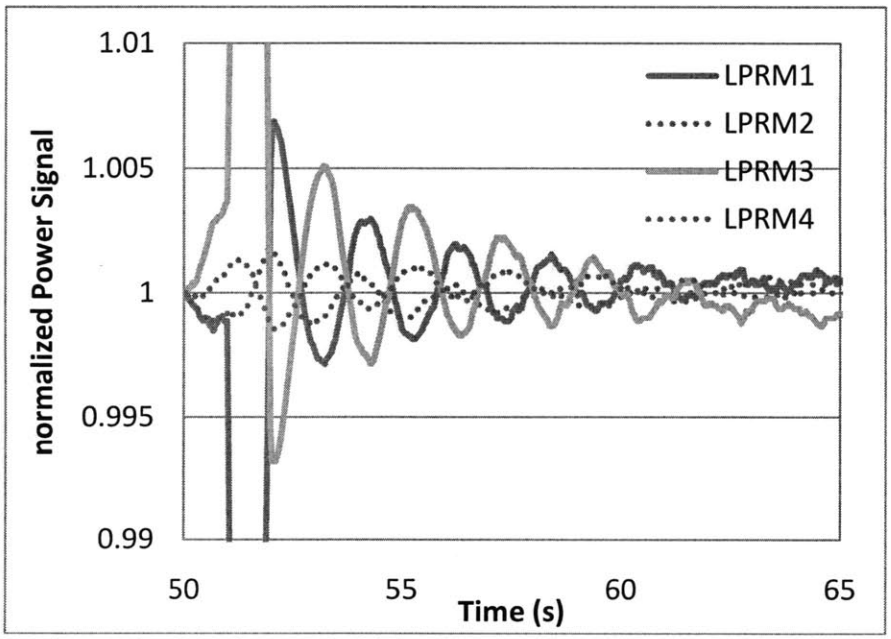

Figure 9.23: Normalized (to its own initial value) channel power signal during asymmetric perturbation, 648 channel model at C14P09

A time-series analysis is used to evaluate the decay ratio from the transient results. To calculate the out-of-phase decay ratios, the differences between APRM and LPRM signals (each normalized to its own steady-state value) are used instead. The evaluated

decay ratios are much smaller than the reference value. This is expected since the limit cycle out-of-phase oscillation was not observed in the TRACE simulation. The TRACE modeling is not successful for this analysis since the 648 channel model failed to achieve good initial steady-state and the local power oscillation signals are in the noise of the average core power signal. Thus, the results in this section only have limited value, such as an attempt to use TRACE to simulate BWR out-of-phase instability.

Table 9-5: Calculated Decay ratios for C14P09, out-of-phase

Model	Decay ratios					
	Ref.	APRM	LPRM1	LPRM2	LPRM3	LPRM4
Regional	0.99	-	0.81	0.75	0.82	0.75

9.4 Numerical Scheme Effects: SI and SETS

The type of time discretization adopted for the thermal-hydraulic balance equations contributes to determining the effect of truncation errors on the calculated results. In particular, diffusion is responsible for smoothing out sharp propagation fronts in the calculated results, and for damping of free oscillations as a consequence of spurious energy dissipation. The latter phenomenon is particularly relevant for the simulation of thermal-hydraulic instabilities, and may lead to prediction at stable conditions, whereas unstable ones would be expected on the basis of the physical conditions.

According to the TRACE manual [NRC, 2008], there are two numerical schemes in TRACE: the semi-implicit (SI) method and the Stability Enhanced Two-Step (SETS) method. In the SI method, the pressure equation is solved implicitly, and the density, velocity and energy equations are solved explicitly. Therefore, the numerical dissipation in SI is similar to the explicit method and the time step size can exceed the acoustic (pressure velocity propagation) Courant limit, but not the material Courant number. The SETS method has more implicit treatment of Convection Terms. It is in essence a prediction-correction method. It first uses the SI scheme as a predictor; then, a set of stabilizer equations are used to calculate the state parameters in the actual new time step. The time-step size is NOT limited by the material Courant number.

Previous studies [Mahaffy, 1993] have suggested the potential for numerical damping in the SETS method, which is the primary numerical solution method in TRACE. Because of these concerns, the semi-implicit method option in TRACE was used for stability analysis in this work. However, when the semi-implicit method is used for stability analysis, it is important to achieve a material Courant limit (CFL) near unity in order to minimize numerical dissipation:

$$CFL: c = v\Delta t / \Delta x; \tag{9-3}$$

where v is coolant velocity, Δx is mesh size and Δt is time step size.

A discussion of the numerical dissipation and the SI scheme can be found in [Xu et al., 2009], and is also given in Appendix F.

Because the velocities in the various cells of the TRACE model are generally different due to differences in the cell void fraction, an adjustable axial mesh size was introduced for stability modelling to allow the material courant numbers in most cells to approach unity simultaneously and therefore to minimize the numerical dissipation. However, it is very difficult to allow the courant number to approach unity for all the nodes due to the nonuniform power and flow distributions. For simplicity, all the channels are assigned the same nodalizaiton scheme (the first two and the last one are non-heated nodes), as shown in Figure 9.24. The cell size increases axially since the vapor velocities increase due to the boiling. The liquid and vapor velocities from three typicl channels (high power channel 63, middle power channel 1, and the peripherial low power channel 385) are shown in Figure 9.25; and the resulted Courant number for the axial cells are shown in Figure 9.26. It is seen that the Courant number distribution along the axial cells is more uniform under the new nodalization schemes.

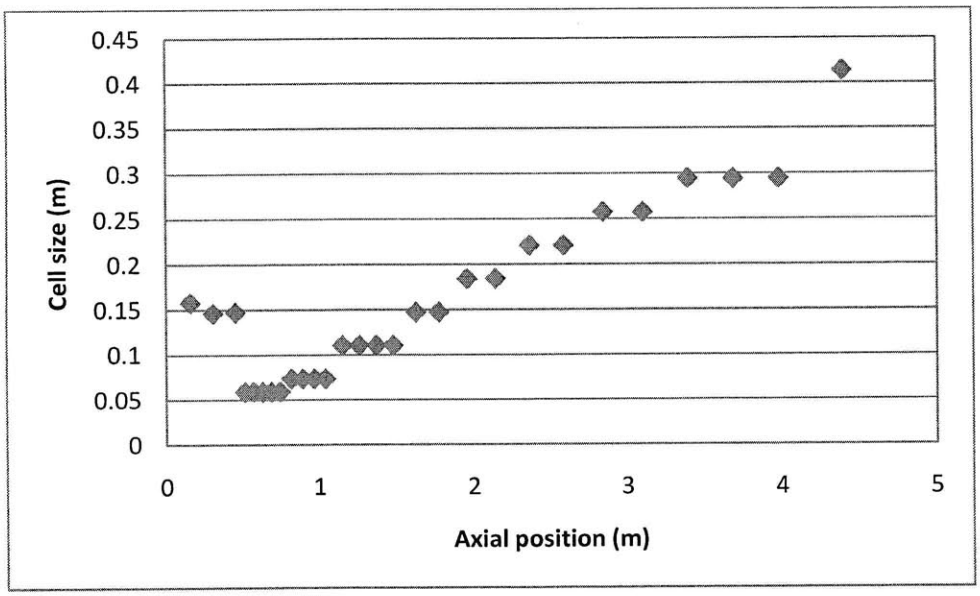

Figure 9.24: Axial cell size in the fuel channels

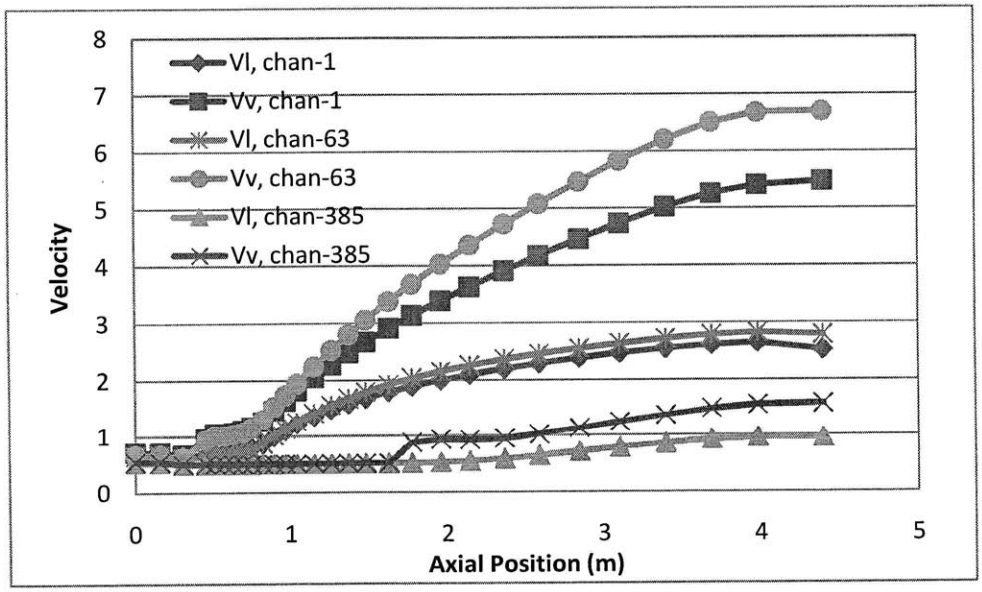

Figure 9.25: Axial vecolity in three typical channels, C14P04

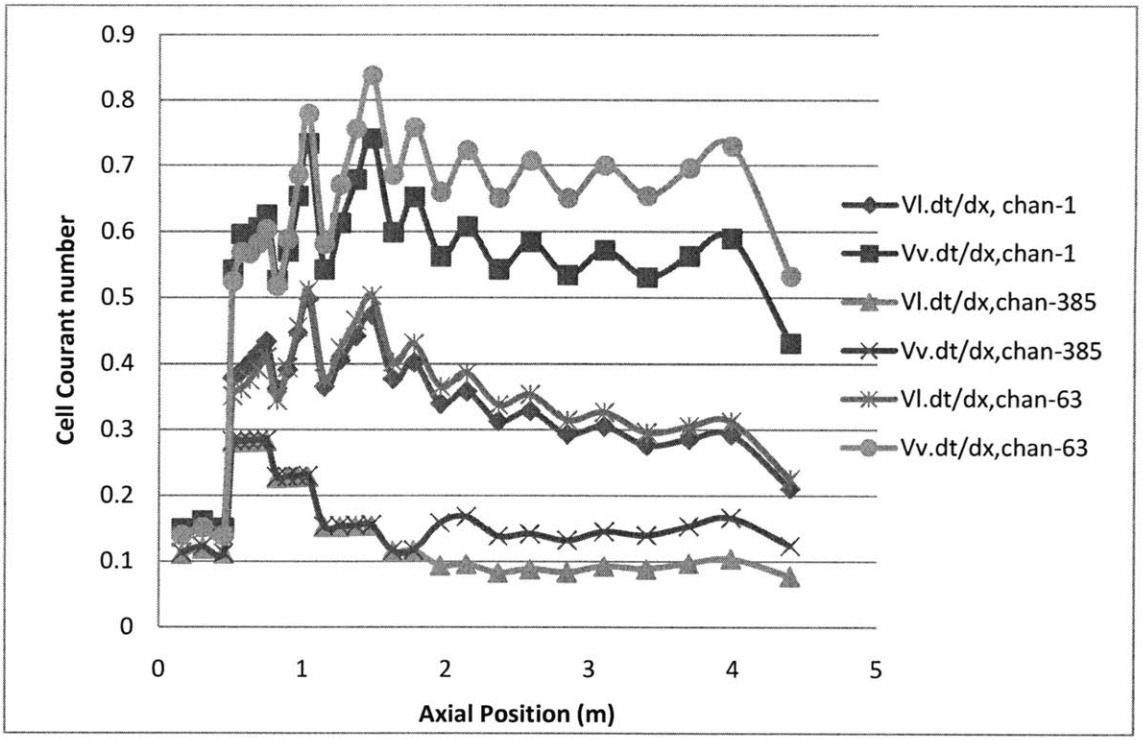

Figure 9.26: Courant number along axial cells in three typical channels, C14P04

The core power response and decay ratios from the transient simulation of test point 4 of Ringhals-1 cycle 14 for the SI and SETS methods are shown in Figure 9.27 and Figure 9.28, respectively. Three different time step sizes from, 10 ms to 33 ms, are used in the simulations. For comparison, the reference decay ratio for this test point of 0.79 is also shown in Figure 9.28.

The results in Figure 9.27 and Figure 9.28 indicate that for the SI method with adjusted axial mesh size, the numerical damping decreases when the time step size is increased. The numerical damping for SI is minimized when the step size reaches the material courant limits (about 33 msec). Conversely, the SETS method is not very sensitive to the time step size; the numerical damping slightly decreases when the step size is decreased. The results from the SETS and the semi-implicit method become closer when the time step size is small.

The findings in the sensitivity study of the time-space descretization schemes are consistent with [Xu et al., 2009]. It can be concluded that the stability analysis using

TRACE (and other similar 1D thermal-hydraulics system codes) is sensitive to the time-space discretization scheme, and the numerical diffusion should be carefully controlled. The SI method with adjustable meshsize is successful in minimizing the numerical diffusion and produces reasonable agreements with the Ringhals stability test, as seen in Section 9.2. However, its fidelity in a large transient, during which the flow velocities will change, is still in question. It would be impossible to allow the Courant number to approach unity all the time for all the cells in all channels.

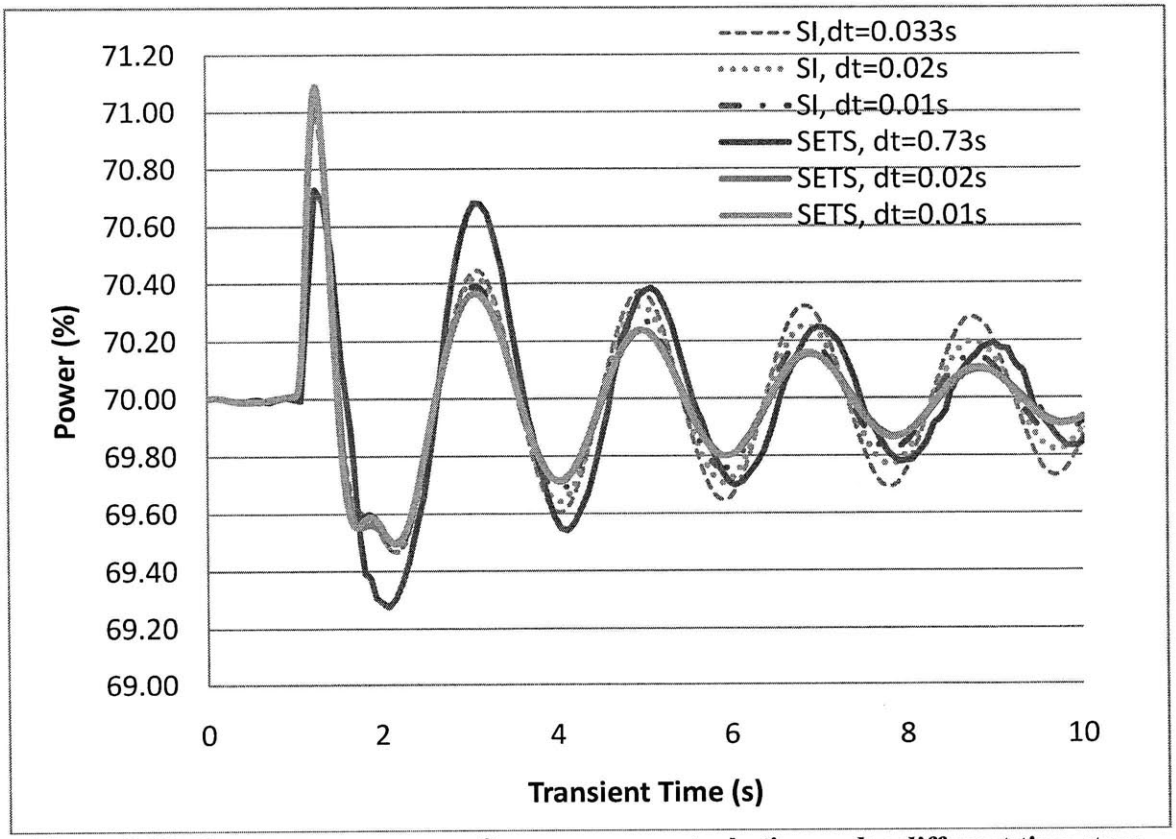

Figure 9.27: Core power response after pressure perturbation under different time steps and numerical methods, C14P04

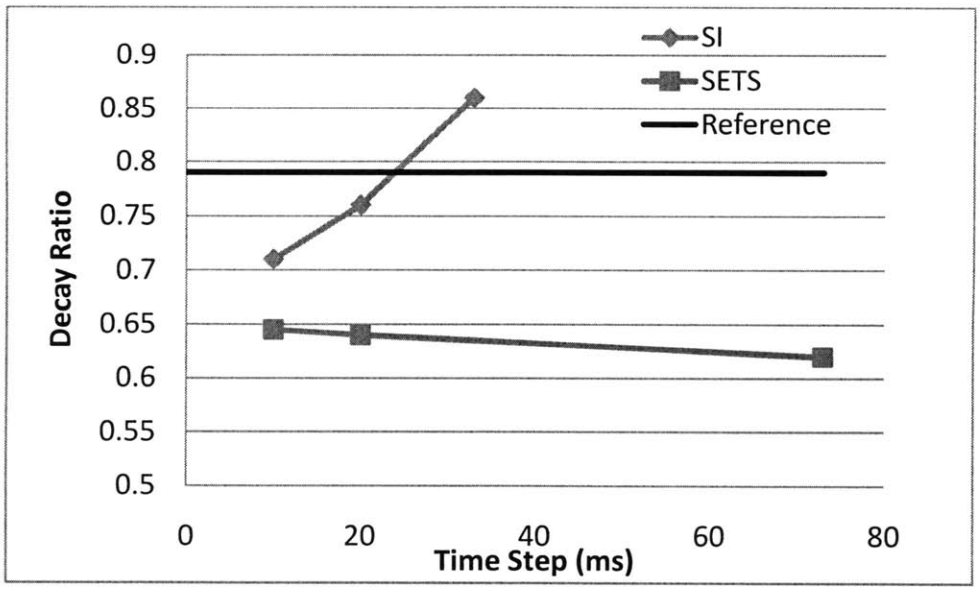

Figure 9.28: Decay Ratios for Various Time Step Sizes at C14P04

9.5 Lumped channel Effects

Although it is possible to allow one-to-one channel modelling (full-core model) in TRACE now, it is time-consuming to execute TRACE models with large number of components. Also, the lumped channel approach (a large number of flow channels are represented by a small number of channels), is still widely used. It is of interest to investigate the effects of the lumped channel scheme on stability predictions in TRACE.

9.5.1 Core channel lumping/mapping schemes

Four patterns of region maps, 6-, 10-, 20-, and 50-CHANs (CHAN is the thermal-hydraulic component used in TRACE to model the flow dynamics and fuel heat conduction in a fuel bundle) were constructed for modeling C14P09 of Ringhals 1 stability test. The basic mapping strategy includes:

- Flat power distribution inside the lumped channels
- The same fuel bundle types
- The same inlet orifice types
- The lumped fuel bundles are physically beside each other.

With the considerations of:

- The mapping from neutronic nodes to fewer thermal-hydraulic nodes would smooth the distribution of core state variables, and smear the resultant reactivity feedback.
- Spatial coupling effect induced by the void feedback is important in the regional instability.

The radial power distribution from the 648 channel (one-to-one channel modeling) TRACE/PARCS simulation, as shown in Figure 9.29, is used in these mapping schemes. The resulting core channel mapping patterns are shown in Figure 9.30. The 6-channel model consists of channels representing the peripheral, centeral higher power, and centeral middle power region for one half of the core. The 10-channel model is modified from the the 6-channel model, by adding one channel to the centeral middle power region to capture the lower power region around the control rods; and adding another channel to the centeral high power region. Then, the 20-channel and 50-channel models are generated by assigning more channels to the centeral low power and centeral high power regions. The neutronics model in PARCS is kept the same, as described in Chapter 8, for all these T-H models.

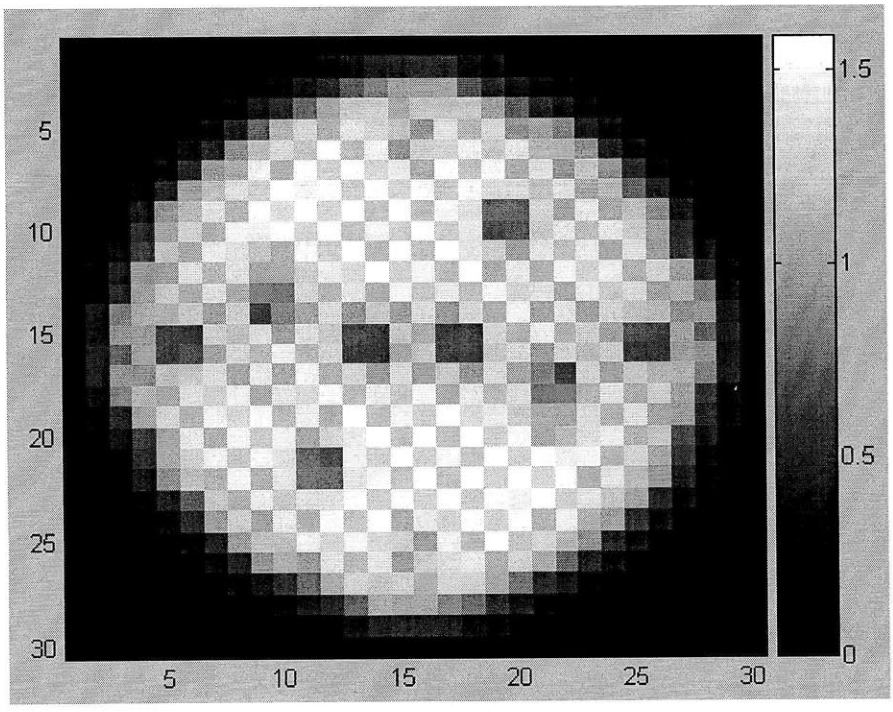

Figure 9.29: Radial power distribution from TRACE/PARCS simulation, 648-chan model for C14P09

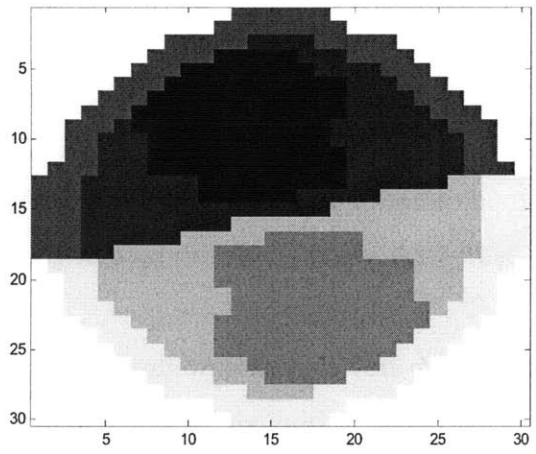

(1) 6-chan model

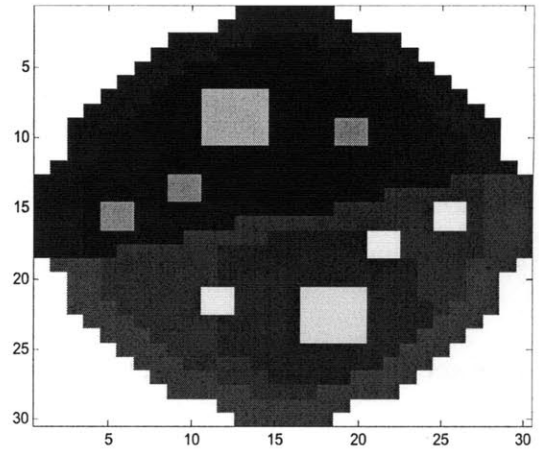

(2) 10-chan model

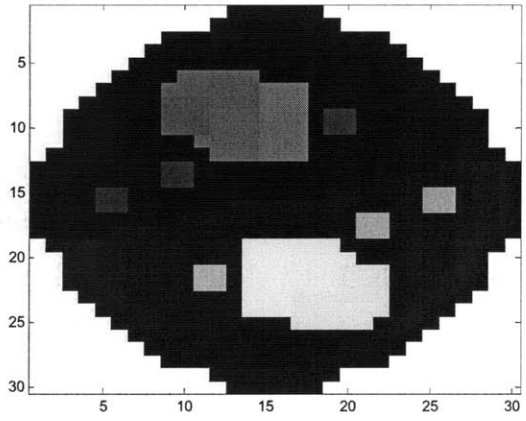

(3) 20-chan model

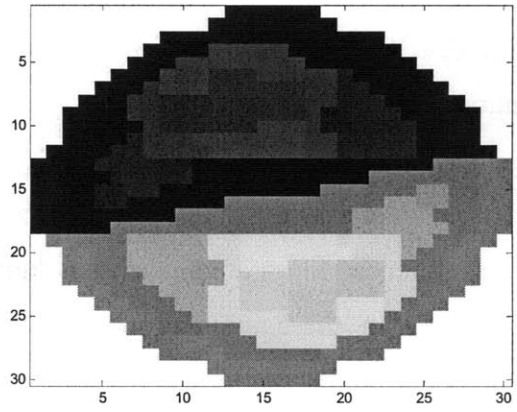

(4) 50-chan model

Figure 9.30: Channel mapping schemes for C14P09 in Ringhals 1

9.5.2 Transient responses

The standard procedure described in Section 8.3, is applied to simulate the transient responses of different lumped channel models. The stability simulation is performed using the semi-implicit scheme in TRACE by introducing initial symmetric control rod perturbation:

- T=1s, start to moving the control rod bank 5 (as shown in Figure 8.11) at step 50;
- T=1.5s, the control rod is at its maximum position, step=52;
- T=2s, the control rod is moved back to the original position, step=50.

The transient power responses from the control rod perturbation are shown in Figure 9.31, and the cacluated DRs and NFs are listed in Table 9-6.

It is seen in Table 9-6 that the initial steady states (core power and flow rate) among different channel mapping schemes are somewhat different, although several control systems are used in the steady state simulation to adjust the core flow rate, core inlet temperature, steam dome pressure, and downcomer water level. The power levels and distributions would change once the neutronic feedback is activated in coupled TRACE/PARCS simulation. It is very difficult to achieve the same state for all different lumped channel schemes.

The calculated DRs from the power response signals are somewhat different (±0.06 from the reference value) among various lumped channel models. But a clear tendency is not observed in these simulations. In principle, the neutron spatial coupling facilitates spreading the oscillation of the hottest region to the entire core and therefore lowers the core-wide threshold power for instability to that of the hottest channel. On the one hand, the models with less number of channels force more spatial coupling and thus destabilize the core. On the other hand, the thermal-hydraulic oscillation parameters in the hottest region are attenuated in the small number channel model, which reduce the neutronics feedback and helps the stability.

It can be concluded that the transient response is not overly sensitive to the lumped channel scheme in the coupled TRACE/PARCS simulation. A clear tendency for a larger magnitude of oscillation with increasing or decreasing the channel number is not observed in these simulations, and the differences in the calculated decay ratios are within the model uncertainties.

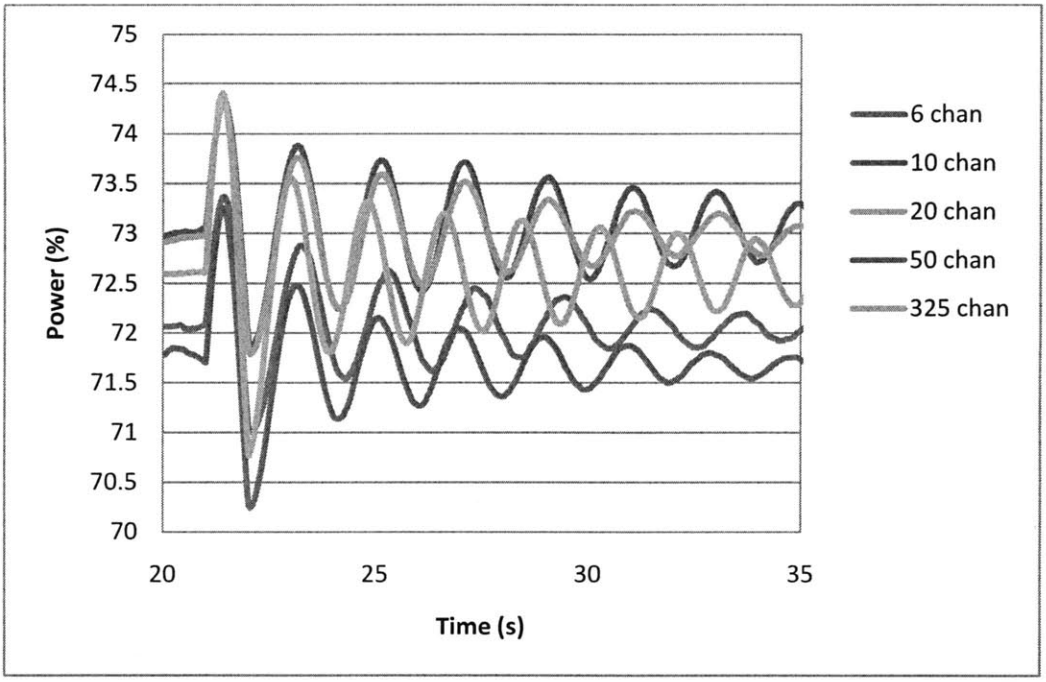

Figure 9.31: Power responses from different lumped channel models, control rod perturbation

Table 9-6: Steady-state and oscillation parameters among different mapping schemes

Channel number	Control Rod Perturbation Transient			
	Core Power (%)	Core Flow (kg/s)	DR	Frequency (Hz)
6	72.1%	3689	0.75	0.49
10	73.0%	3691	0.84	0.51
20	72.9%	3689	0.74	0.51
50	71.8%	3699	0.75	0.51
325 (half core symmetry)	72.6%	3694	0.84	0.55
Reference	72.6%	3694	0.80	0.56

The differences in the radial and axial power distributions among different lumped channel shemes are shown in Figure 9.32 and Figure 9.33. Large differences exist in the radial power distributions among different lumped channel shemes, while the axial power shapes are almost the same.

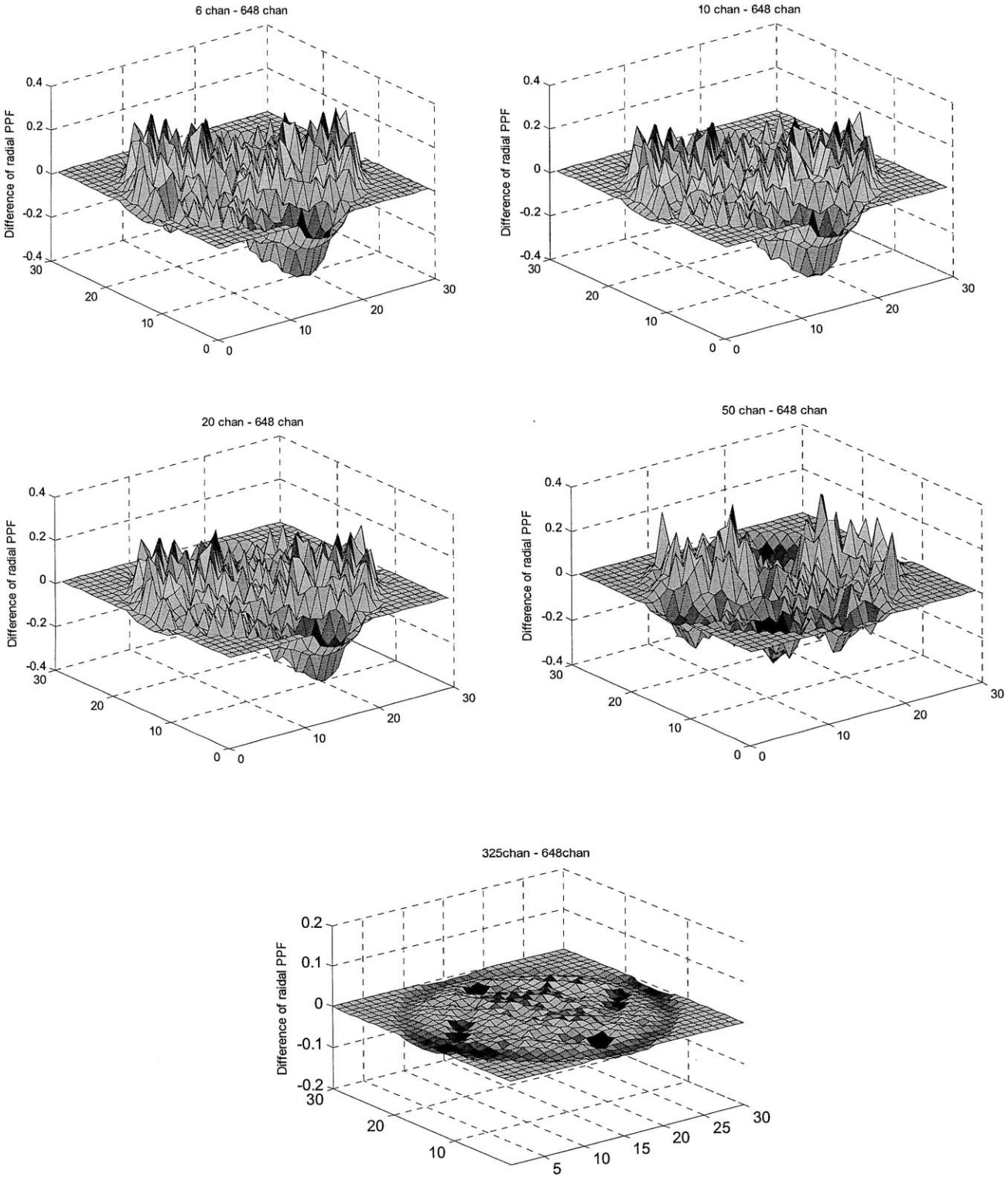

Figure 9.32: Differences in radial power peaking among different channel mapping models

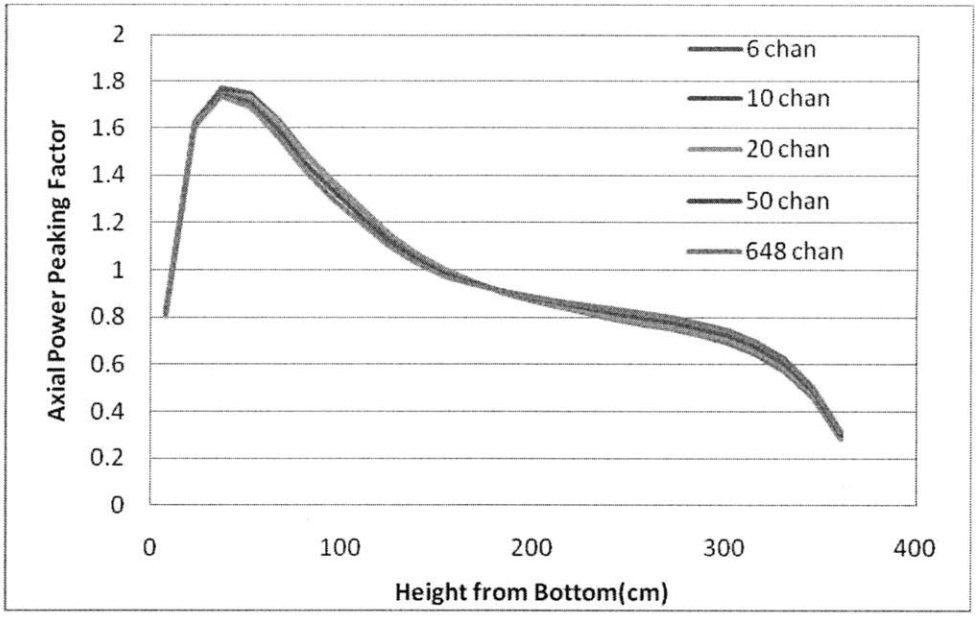

Figure 9.33: Axial power distribution differences among different channel mapping models

9.6 Neutronics Modeling Effects: 3D vs. 0D

There are two options in TRACE for modeling neutronics:

1) Stand-alone TRACE calculation, embedded with several choices: constant power, power specified from a table, point-reactor kinetics with reactivity feedback, user specified reactivity table, etc.
2) Coupled TRACE with PARCS, for 3D neutronics capability.

Since the point kinetics model is still widely used for reactor transient simulations and other stability analysis tools, it is of interest to investigate the effects of the 3D modeling versus the point kinetics model in TRACE.

9.6.1 Reactivity Feedback model in TRACE

There are three reactivity-feedback models available in TRACE, the TRAC-P, reactivity feedback model, the TRAC-B reactivity-feedback model, and the RELAP5 reactivity feedback model. The TRAC-B reactivity feedback model is used in this work since the TRACE input files for the Ringhals 1 benchmark test are in the TRAC-B free format.

As stated in TRACE manual [NRC, 2008], the TRAC-B reactivity feedback model is based on the assumption that for BWR applications accurate reactivity feedback cannot be obtained based on the change in core average parameters (i.e., core average void fraction, core average moderator temperature, core average fuel temperature, and core average boron concentration). A more accurate approximation is to sum the reactivity change for each node (i.e., fluid node for void fraction, moderator temperature and boron concentration and fuel rod node for fuel temperature reactivity-feedback). The total change in reactivity is given by Eq. (9-4).

$$R^n = \sum_{i=1}^{NFluid} C_{\alpha i} \times (\alpha_i^n - \alpha_i^{n-1}) \times WF_{ci} + \sum_{i=1}^{NFluid} C_{tmi} \times (T_{li}^n - T_{li}^{n-1}) \times WF_{ci} \times (1 - \alpha_i^n) + \sum_{i=1}^{NFluid} C_{bi} \times (B_i^n - B_i^{n-1}) \times WF_{ci} + \sum_{i=1}^{NFuel} C_{tfi} \times ((T_{fi}^n)^{0.5} - (T_{fi}^{n-1})^{0.5}) \times WF_{fi} \quad (9\text{-}4)$$

Where,

NFluid = Total number of fluid cells in the core, include fluid cells inside the BWR fuel assemblies, water rods, and core bypass.

NFuel = Total number of fuel nodes in the core, include all average rod groups associated with each CHAN component in the model.

$C_{\alpha i}$ = Reactivity feedback coefficient for changes in the void fraction for fluid cell i.

C_{tmi} = Reactivity feedback coefficient for changes in the moderator temperature for fluid cell i.

C_{bi} = Reactivity feedback coefficient for changes in the boron concentration for fluid cell i.

C_{tfi} = Reactivity feedback coefficient for changes in the fuel temperature for fuel node i.

WF_{ci} = Weighting factor for fluid cell i, depends on the square of local power fraction in this work.

WF_{fi} = Weighting factor for fuel node i, depends on the square of local power fraction in this work.

α_i^n = Void fraction in fluid cell i at time step n.

T_{li}^{n} = Liquid temperature in fluid cell i at time step n.

B_{i}^{n} = Boron concentration in fluid cell i at time step n.

T_{fi}^{n} = Fuel temperature in fuel node i at time step n.

9.6.2 Void coefficient calculation from PARCS simulation, C14P01

The void coefficient in the TRACE point kinetics model is crucial to the transient response. It was evaluated from the PARCS simulations of the operating condition at C14P01 and an assumed 95% flow conditions. The void coefficient was calculated from:

$$C_{\alpha} = \frac{\Delta R_{\alpha}}{\Delta \alpha} = \frac{\Delta R_{tot} - \Delta R_{tf}}{\Delta \alpha} = \frac{\Delta R_{tot} - C_{tf} \cdot \Delta T_{tf}}{\Delta \alpha} \tag{9-5}$$

In which, the reactivity feedbacks due to the coolant temperature change and the boron concentration change are neglected from Eq. (9-5).

The operating condition at C14P01 and the assumed 95% flow conditions were simulated by TRACE/PARCS with the 325-channel model, and the results of moderator density and fuel temperature distributions are shown in Table 9-7 and Table 9-8. Since BWR stability is not sensitive to the Doppler feedback (see Section 5.6.4), a reference value of fuel temperature coefficient, $-2.30\times10^{-5}\Delta k/k/°C$ for BWR/4, was used in this analysis. Then, the calculated void coefficient for Ringhals C14P01 was found to be -1.30×10^{-3} $\Delta k/k/\%void$. A calculation of the void fraction was also undertaken by considering a smaller flow reduction (99%). The resulting void coefficient yielded the same value.

Table 9-7: Moderator density and Fuel temperature distributions at C14P01, 325-chan model

Axial position	Average Axial Moderator Temperature (°C)	Average Axial Fuel Temperature (°C)	Average Axial Moderator Density (kg/m^3)
7.36	267.02	611.252	778.873
22.08	268.927	693.107	774.66
36.8	271.614	712.31	766.167
51.52	274.675	724.974	751.162
66.24	277.268	724.885	731.155
80.96	279.695	720.209	699.384
95.68	281.185	718.494	671.057
110.4	282.364	717.653	641.152
125.12	283.526	717.233	602.976
139.84	284.307	718.461	571.583
154.56	285.057	720.793	532.368
169.28	285.466	725.753	503.283
184	285.824	732.949	470.466
198.72	286.046	738.492	447.357
213.44	286.32	753.489	403.772
228.16	286.408	758.83	381.759
242.88	286.497	764.171	359.754
257.6	286.564	767.48	332.761
272.32	286.587	768.582	323.766
287.04	286.603	758.333	291.815
301.76	286.603	758.333	291.815
316.48	286.561	730.096	268.987
331.2	286.561	730.096	268.987
345.92	286.45	664.049	256.219
360.64	286.45	664.049	256.219
Average	282.58	723.76	495.10
k_{eff}	0.991597		

Table 9-8: Moderator density and Fuel temperature distribution at C14P01 with 95% flow condition, 325-chan model

Axial position	Average Axial Moderator Temperature (°C)	Average Axial Fuel Temperature (°C)	Average Axial Moderator Density (kg/m^3)
7.36	267.163	616.554	778.609
22.08	269.26	701.47	773.659
36.8	272.182	720.558	763.527
51.52	275.439	730.982	745.799
66.24	278.075	728.306	722.131
80.96	280.436	720.955	686.602
95.68	281.829	718.04	656.002
110.4	282.907	716.319	624.807
125.12	283.975	714.645	586.274
139.84	284.679	715.489	554.83
154.56	285.337	717.661	515.616
169.28	285.688	722.794	486.873
184	285.989	730.209	454.479
198.72	286.172	735.914	431.674
213.44	286.395	751.524	389.245
228.16	286.466	757.239	367.872
242.88	286.536	762.955	346.506
257.6	286.587	766.833	320.29
272.32	286.604	768.125	311.553
287.04	286.601	758.486	280.54
301.76	286.601	758.486	280.54
316.48	286.549	730.443	258.524
331.2	286.549	730.443	258.524
345.92	286.437	664.779	246.314
360.64	286.437	664.779	246.314
Average	282.84	724.16	483.48
k_{eff}	0.989436		

9.6.3 Transient responses under the point kinetics model

The transient response under the TRACE point kinetics model is simulated by introducing a pressure perturbation at the turbine inlet, as described in Section 8.2. Several void coefficients (i.e. reference value calculated in Section 9.6.2, twice and three times reference value) are used in the simulation, and the transient responses are

compared with the coupled TRACE/PARCS 3D neutronics analysis results in Figure 9.34 to Figure 9.36.

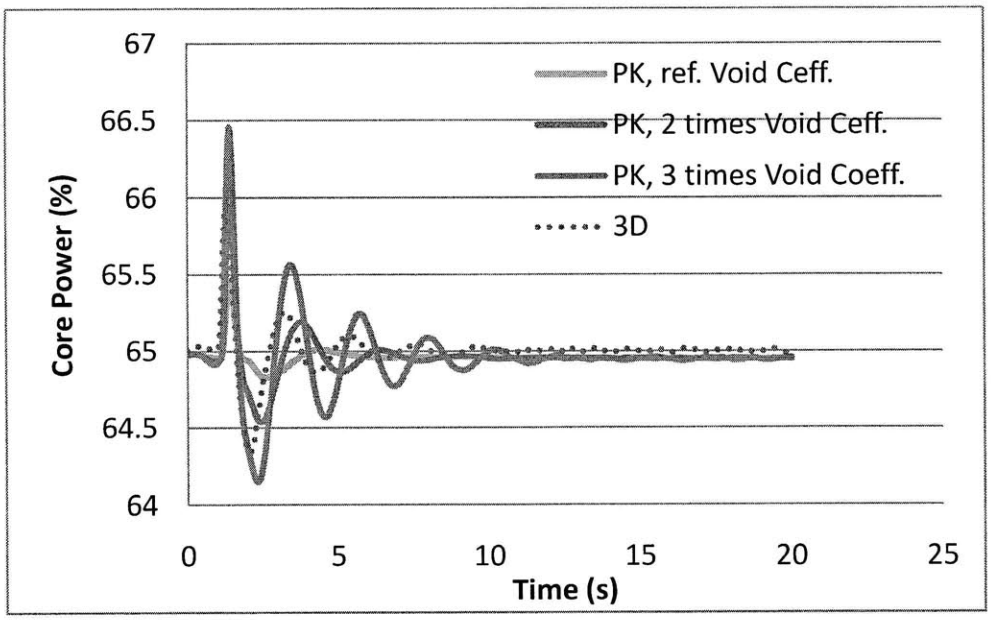

Figure 9.34:Transient core power responses under pressure perturbation, C14P01

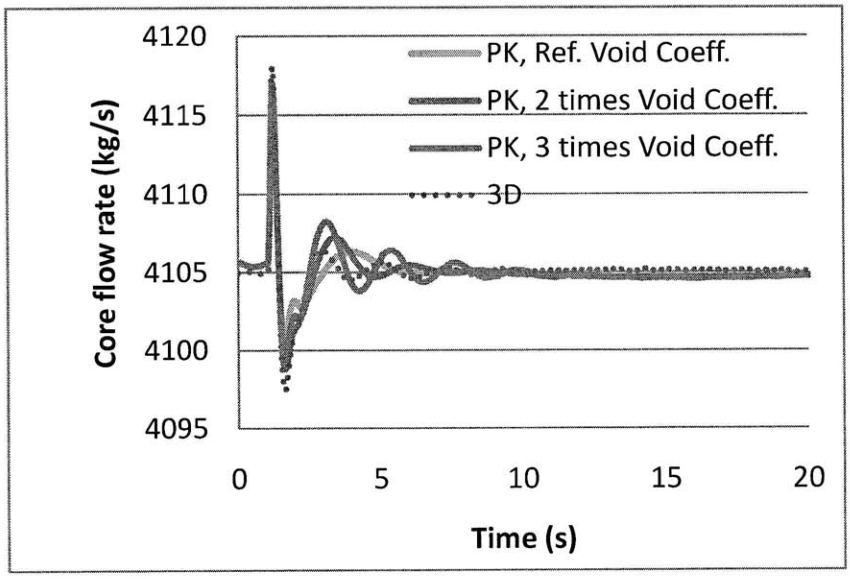

Figure 9.35: Core flow rate responses under pressure perturbation, C14P01

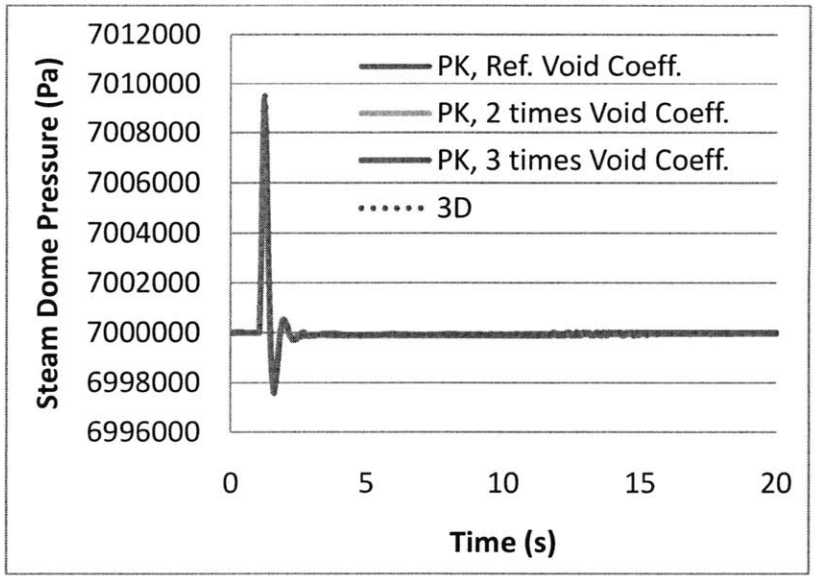

Figure 9.36: Steam dome pressure response under pressure perturbation, C14P01

It is seen in Figure 9.35 and Figure 9.36 that the steam dome pressure responses are the same for the various neutron kinetics models, also the initial peak core flow response following the steam dome pressure spike. However, the power responses shown in Figure 9.34 are very different, both the amplitude and oscillation frequencies. It is seen as expected that the power oscillation amplitude is higher when the void coefficient is larger in the point kinetics model, so is the oscillation frequency.

It is interesting to find that the power responses between the 3D PARCS model and the reference point kinetics model are very different, although the void coefficient in the reference point kinetics model is calculated based on the PARCS 3D neutronics model. Both the oscillation amplitude and frequency in the 3D model are higher than those in the reference point kinetics model, which indicates that the neutronics feedback is attenuated by the the point kinetics model in TRACE.

The oscillation DRs and NFs are calculated from the transient power signals, as shown in Table 9-9. It is shown that the decay ratio from the 3D model lies between those of the PK-2 (twice reference value for the void coefficients) and PK-3 (three times reference value for the void coefficients) model, similar to the power responses in Figure 9.34.

Table 9-9: Decay ratios and oscillation frequencies at C14P01

NK	Power (%)	Flow (%)	Decay ratio	Natural frequency (Hz)
Reference	65.0	58.64	0.30	0.43
3D	65.0	58.64	0.39	0.46
PK-1	65.0	58.64	<0.1	<0.1
PK-2	65.0	58.64	0.21	0.38
PK-3	65.0	58.64	0.46	0.44

9.7 Control System Effects

9.7.1 BWR stability and control system

BWR stability performance is also affected by the control systems, which attempt to regulate some reactor variables through some actuators for pump, turbine, and feedwater operation. Similarly, some proportional–integral–derivative (PID) controllers are used in our TRACE model to achieve satisfying initial steady states. They are very close to the the actual plant control systems, including the control function and logic. It is of interest to use these controllers in the TRACE model to investigate the control system effects on BWR stability performance.

There are four controllers in the TRACE (325 channel) model, which would adjust the recirculation pump speed, turbine pressure, feedwater flow rate and temperature during the simulation. The general form of these controllers is:

$$MV = c + K_p E(t) + K_i \int_0^t E(t')dt' + K_d \frac{dE(t)}{dt} \tag{9-6}$$

In which,

E: Error = *SP* − *PV*

PV: Process Variable, measurement of the process value

SP: Set Point, the desired value

Kp: Proportional Gain,

Ki: Integral Gain,

Kd: Derivative Gain,

MV: Manipulated Variable.

9.7.2 Transient responses after small perturbations

These controllers are designed to obtain satisfying initial steady states for TRACE simulations. And in general, they would be removed in a transient simulation. In this work, the transient responses with and without these control systems are both simulated and compared. If the control systems are removed in the transient simulation, fixed boundary conditions for the controlled variables are used. The results of the standard control rod perturbation and pressure perturbation, as described in Section 9.2, are shown in Figure 9.37 and Figure 9.38 for test poin 1.

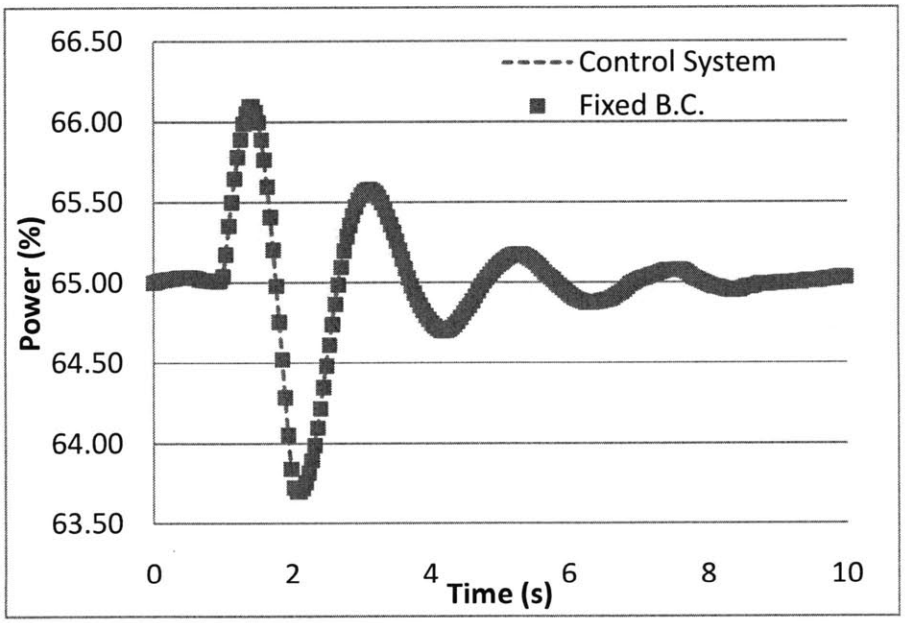

Figure 9.37: Transient core power response under control rod perturbation, C14P01

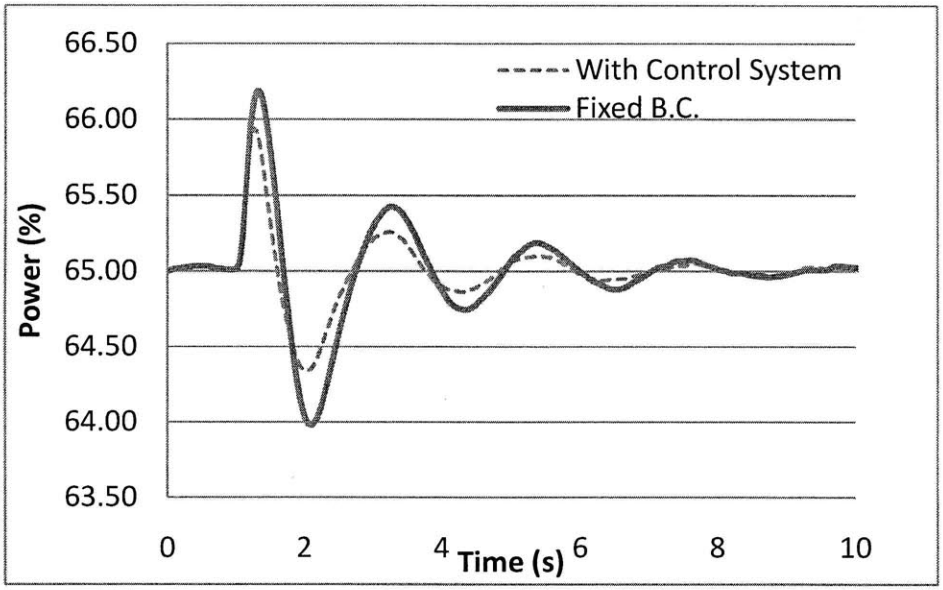

Figure 9.38: Transient core power response under pressure perturbation, C14P01

It is shown in Figure 9.37 and Figure 9.38 that the transient power responses under control rod perturbations are almost the same for the models with and without control systems, while slight differences exist between them for the cases of pressure perturbations. Then, the simulations of pressure perturbation are conducted for all 8 test points at Ringhals 1 cycle 14, and the derived DRs and NFs from transient power signals are listed in Table 9-10.

Table 9-10: Decay ratios and oscillation frequencies under pressure perturbation, control system effects

Test Point	Decay Ratio			Natural Frequency (Hz)		
	Fixed B.C.	Control System	Difference	Fixed B.C.	Control System	Difference
P01	0.43	0.42	-0.01	0.47	0.46	-0.003
P03	0.60	0.61	0.01	0.43	0.43	0.001
P04	0.88	0.87	-0.01	0.53	0.53	0.0015
P05	0.94	0.94	-0.002	0.50	0.51	0.002
P06	0.86	0.84	-0.01	0.50	0.50	0.002
P08	>1	>1	-	0.49	0.49	0.002
P09	0.85	0.85	-0.006	0.55	0.55	0.002
P10	0.95	0.95	-0.004	0.48	0.48	0.003
Bias	-0.004			0.001		
Standard deviation	0.007			0.002		

It is shown in Table 9-10 that the bias and standard deviation of the decay ratios from the fixed B.C. model and the model with control systems are very small. It can be concluded that the effects of control system are very small in small perturbation initiated oscillations (control rod perturbation and pressure perturbation in this work). Thus, it is acceptable to neglect the control systems for investigating the static stability performance of the plant. However, these statements are not necessary true under large transients.

9.7.3 Transient responses after recirculation pump trip

An analysis of the stability performance during a large transient is then performed using point 9 (this point was the least stable one in the experiments). One of the two recirculation pumps was tripped under the assumed transient. This accident causes a drop of the core coolant flow, then a decrease in the reactor thermal power level due to the void reactivity feedback. In general, a scram is not initiated during this event.

In this work, the transient responses after the recirculation pump trip with and without these control systems are simulated and compared. This calculation can be also used as a

further examination of the feasibility of TRACE application for BWR stability analysis for large transients.

Case 1: Control systems remain active.

To simulate the event, the recirculation pump speed is brought to half its value at time = 1s. After that, the recirculation pump speed is adjusted by the control system to match the core flow rate to the setpoint value. The total recirculation pump speed during the transient is shown in Figure 9.39a. It is seen that the total speed returns to its original steady state value in a very shot time and then starts oscillating. The same tendencies are found in the core power and flow rate signals, as shown in Figure 9.40a and Figure 9.41a, but with some delay from the total pump speed signal. The observed oscillations can be identified as the control system overshoot, since the oscillation frequency is very low, around 0.02 Hz, due to the controller characteristics. However, small high-frequency oscillations are also observed in the transient, as shown in Figure 9.40b. This oscillation with small amplitude but high-frequency is recongnized as DWO since the oscillation frequency is around 0.5 Hz.

Case 2: Control systems are removed.

In this case, all the control systems are removed in the transient analysis. The recirculation pump speed is brought to half its value at time =1s, and remained the same value during the transient, as shown in Figure 9.39b. Then, the core flow rate and core power slowly decrease after the pump trip. After a certain time, the core power and core flow rate reach their minmum and start increasing. However, unexpected oscillations are observed for both the core power and core flow rate, as shown in Figure 9.40c and Figure 9.41b after 150 seconds, and the oscillation frequency is around 0.1 Hz. This oscillation can not be explained physically, and could be a numerical instability due to the deficiency of the SI scheme in TRACE.

Comparing the transient responses in the above two cases, it can be concluded that the control systems are significant to the transient behavior and stability performance of BWR in large transients, and could not be neglected in these simulations.

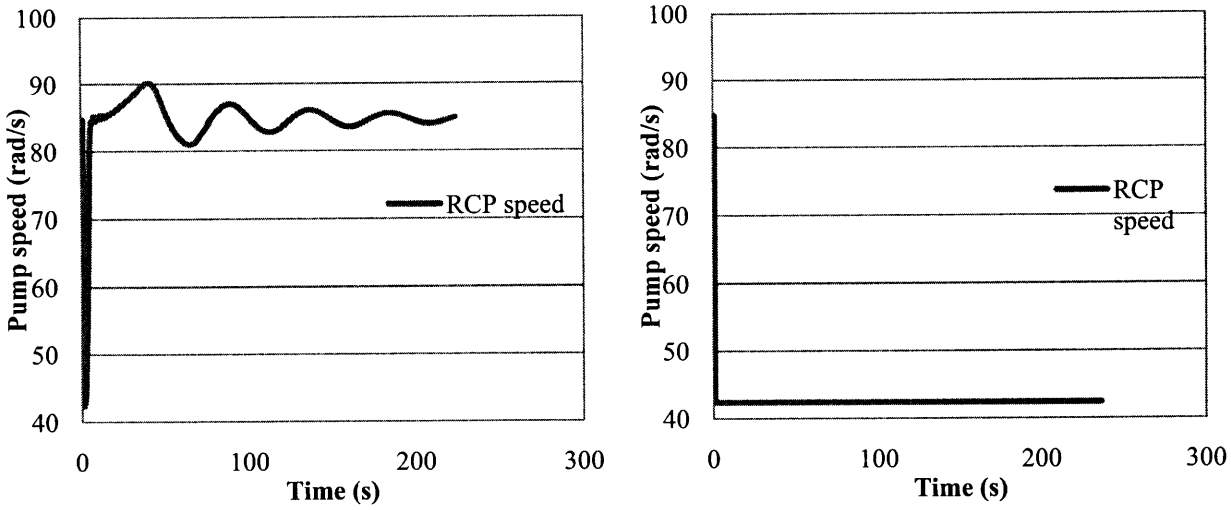

(a) with control system (b) without control system

Figure 9.39: Total Recirculation Pump Speed after One Recirculation Pump Trip, w and w/o Control System

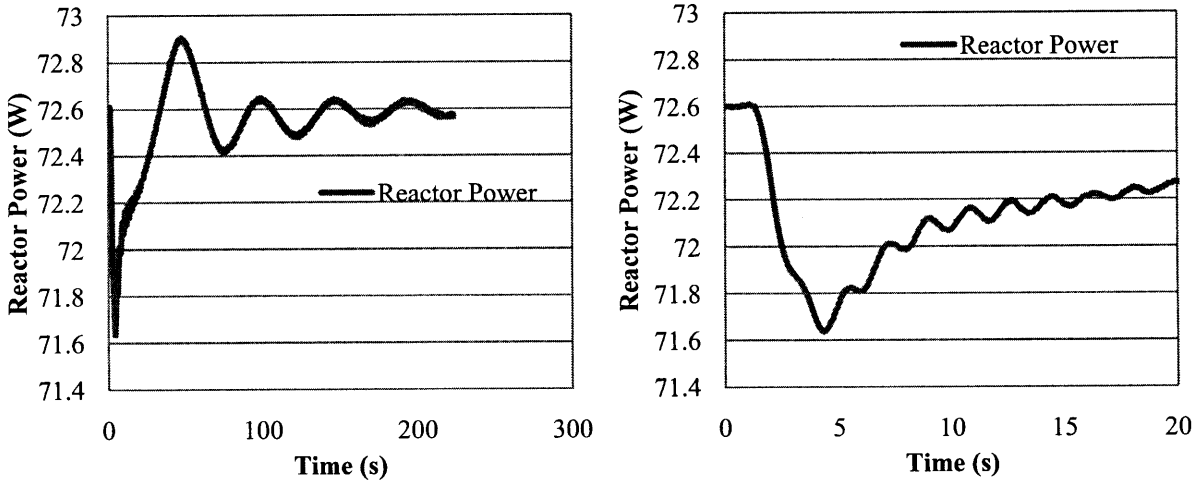

(a) with control system (b) with control system, 0-20s time window

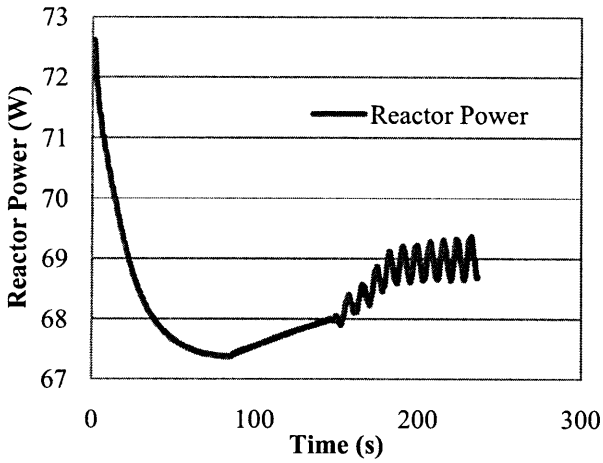

(c) without control system

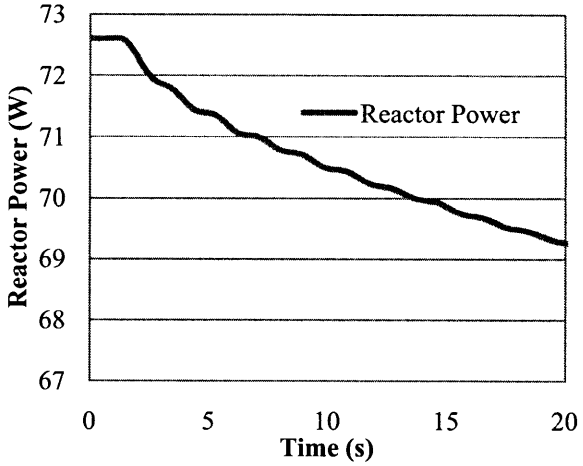

(d) without control system, 0-20s time window

Figure 9.40: Core Power Response after Recirculation Pump Trip, with and without Control System

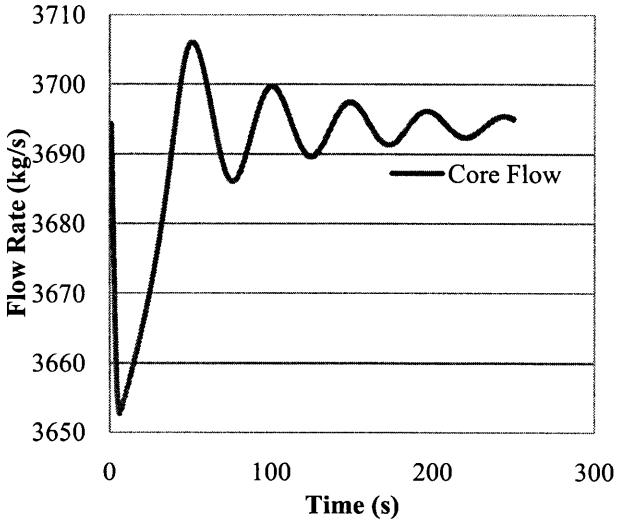

(a) with control system

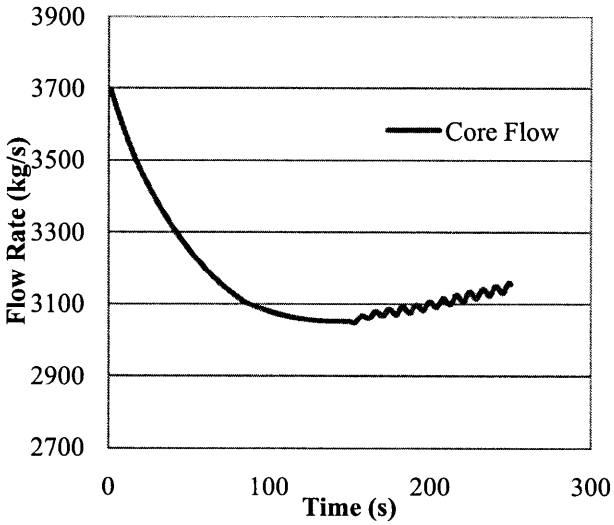

(b) without control system

Figure 9.41: Core Mass Flow Response after Recirculation Pump Trip, w and w/o Control System

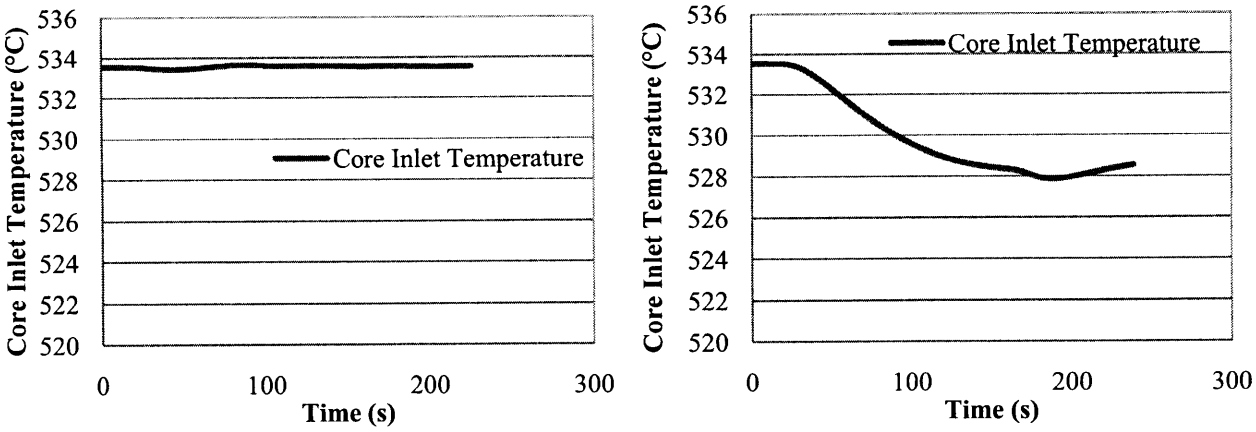

(a) with control system (b) without control system

Figure 9.42: Core Inlet Temperature Response after Recirculation Pump Trip, w and w/o Control System

9.8 Summary

The NRC's latest coupled thermal-hydraulics and neutron kinetics code, TRACE/PARCS, is applied in this work to simulate the Ringhals 1 stability test. Two types of initial perturbation are chosen: control rod perturbation and pressure perturbation. By using the Semi-Implicit scheme and the appropriate nodalization scheme to minimize numerical diffusion, the TRACE/PARCS analysis results are in reasonably good agreement with the experimental results, considering that there are some uncertainties in deriving the oscillation decay ratios from the transient signals of the plant due to the selected time window and the time series analysis methods. The biases of the predicted decay ratios from the reference values are between 0.05 and 0.14 for different used signals; and the evaluated frequencies are in very good agreement with the reference values, all the biases are less than 0.01.

Then, various modeling effects on TRACE stability analysis are assessed, including time-spatial discretization, numerical schemes, channel grouping, neutronics modeling, and control system modeling, as shown in Table 9-11.

Table 9-11: Investigations on modeling effects of coupled NK/TH code in BWR stability analysis

References	Code	Investigation on Modeling Effect
[Hotta et al., 2001a 2001b]	TRAC/BF1-ENTRÉE	▪ Channel grouping ▪ Neutronic modeling: w and w/o
[Costa, 2007]	RELAP5/ PARCS	▪ Time window effects in decay ratio derivation
[Kozlowski et al., 2007]	RELAP5/ PARCS	▪ Time-spatial discretizaiton effect
[Xu et al., 2009]	TRACE/ PARCS	▪ Time-spatial discretizaiton and numerical scheme effect
This work	TRACE/ PARCS	▪ Time-spatial discretizaiton and numerical scheme effect ▪ Lumping channel effect ▪ Neutronic modeling: PK vs. 3D ▪ Control system effect

It is found that numerical damping when using the SI method with adjusted axial mesh size, decreases when the time step size is increased; and the numerical damping for SI is minimized when the step size reaches the material courant limits. Conversely, the SETS method is not very sensitive to the time step size; and the numerical damping slightly decreases when the step size is decreased. The results from the SETS and the SI method become closer when the time step size is small. It can be concluded that the stability analysis by using TRACE (and other similar 1D thermal-hydraulics system codes) is sensitive to the time-space discretization schemes, and that numerical diffusion should be carefully controlled. The SI method with adjustable meshsize was successful in minimizing the numerical diffusion in this work and produced reasonable good agreements with the Ringhals stability test. However, its fidelity in a large transient is still in question. It would be impossible to allow the Courant number to approach unity all the time for all the cells in all channels in TRACE simulations.

Five patterns of region maps, 6-, 10-, 20-, 50- and 325-CHANs are used to investigate the channel grouping effects. Some differences are observed in the coupled steady state results and the radial power distributions among different lumped channel schemes. The calculated DRs from the power response signals after control rod perturbations are somewhat different (±0.06 from the reference value, within the model uncertainties). It can be concluded that the transient response is somewhat sensitive to the lumped channel scheme in the coupled TRACE/PARCS simulation. But a clear tendency for the damping ratio with the channel number is not observed.

The coupled TRACE/PARCS 3D simulation is compared with TRACE stand alone point kinetics models in pressure perturbation transients. It was found that the power responses between the 3D PARCS model and the reference point kinetics model were very different, although the void coefficient in the point kinetics model was calculated based on the PARCS 3D neutronics model. Both the oscillation amplitude and frequency in the 3D model are higher than those in the reference point kinetics model, which indicated that the neutronics feedback is attenuated by the point kinetics model in TRACE.

Although the control systems would regulate some reactor variables (such as the recirculation pump speed, turbine pressure, feedwater flow rate and temperature), their effects on stability performance and transient responses are negligible in small perturbation initiated oscillations (control rod perturbation and pressure perturbation in this work). Thus, it is acceptable to neglect the control systems to investigate the static stability performance of the plant. However, significant differences are found in the simulated recirculation pump trip events for the cases with and without control systems. Very low-frequency oscillations due to control system instability are observed. So, the control systems are significant to the transient behavior and stability performance of BWR in large transients, and cannot be neglected in these simulations.

10. Ringhals 1 Stability Test Benchmark – Frequency Domain vs. Time Domain

Many computer programs have been developed or adopted to evaluate stability of BWRs and other boiling channel systems, and they are generally categorized into two groups: frequency domain codes and time domain codes. Both approaches have been widely used, although the details of modeling (including thermal-hydraulics, neutronics, fuel dynamics and heat transfer, and ex-core systems) are different. Following the qualitative discussion of the two approaches in Chapter 7, and the benchmark of Ringhals 1 stability test with TRACE/PARCS in Chapter 9, the Ringhals 1 stability test is evaluated by the frequency domain code, STAB, in this chapter. Then, a detailed comparison between the results of the frequency domain approach (e.g. STAB) and the time domain approach (e.g. TRACE) is presented.

10.1 Ringhals Stability Benchmark with STAB

10.1.1 Model description and assumptions

The STAB code is described in Chapter 5. It incorporates a linearized model of the reactor core and recirculation loop. The individual model components of STAB, as applied in the Ringhals test analysis, are briefly characterized below:

- ***Channel thermal hydraulics:*** Multiple, parallel channels with independent geometry; Homogeneous Equilibrium Model is used in this benchmark work for the two-phase flow conservation equations;
- ***Neutron kinetics:*** a point kinetics model with void and Doppler feed-back, accounting for six groups of delayed neutrons; λ modal expansion method is used to obtain the first subcritical neutronic mode for out-of-phase instability;
- ***Fuel heat transfer:*** Detailed fuel heat transfer for an average rod per channel using axially variable temperature-dependent properties;

- ***Recirculation loop:*** Detailed representation of all recirculation loop components such as the upper plenum, riser, separators, down-comer region, recirculation pumps and lower plenum.

  The above mentioned out-of-core components are considered for the calculation of the in-phase (i.e. global) mode. For the out-of-phase (i.e. regional) mode, the recirculation loop feed-back is cut off to maintain a constant total core flow, and a variable but the same pressure drop across all channels.

The details of STAB code could be found in [Hu and Kazimi, 2007].

Input preparation

A base STAB input file was generated that contained all the non-case specific input data, and the case specific data. The case (i.e. test point) is selected in the input file. The major modeling/assumptions are:

1) The grouping of bundles per radial peaking factor and fuel type into thermal hydraulic regions is the same for all cases in cycle 14. Three thermal hydraulic regions are used for all cases for the in-phase stability analysis; for out-of-phase instability, three regions are taken to represent each half of the core.
2) Channel grouping is based on the radial power distribution and the fuel assembly type. The geometrical characteristics of the respective fuel assembly including spacer and tie plate loss coefficients are taken from the stability benchmark specifications [Lefvert, 1994]. The inlet orifice loss coefficients are also taken into account.
3) The lumped channels included the active fuel length plus the unheated inlet and outlet section.
4) The geometric data of the various recirculation loop components mentioned above are also taken from benchmark specifications and are used in STAB to calculate the momentum balance for the entire loop.
5) The built-in friction factor model of STAB is used; to be conservative, the two-phase friction multiplier is assumed to be twice the HEM value of ρ_l / ρ_m.
6) Simultaneous mixing is assumed at the core exit among different lumped channels.

7) The gap conductance is based on the core average fuel temperature;
8) A constant Doppler coefficient is used for all the cases. The void coefficient is calculated based on a quadratic form [Munoz-Cobo et al., 2002]: $C_v = C_1 + C_2\overline{\alpha} + C_3\overline{\alpha}^2$, Where $\overline{\alpha}$ is the core average void fraction: $\overline{\alpha} = \frac{\rho_f - \overline{\rho}_m}{\rho_{fg}}$ and $\overline{\rho}_m$ is the core average water density.
9) The six-group delayed neutron parameters and the neutron life time are taken from typical BWR values.

10.1.2 Evaluation Results

The results of the STAB benchmark calculations are shown in Tables 10-1 and 10-2. The calculated decay ratios and oscillation frequencies are compared with measured data in Figures 10.1 and 10.2 (global mode) and Figures 10.3 and 10.4 (regional mode).

Table 10-1: Results of the Ringhals stability benchmark, global mode

Test Case	Power (% rated)	Core Flow rate (kg/s)	Reference		TRACE†		STAB	
			DR	Frequency (Hz)	DR	Frequency (Hz)	DR	Frequency (Hz)
P01	65.0	4105	0.3	0.43	0.35	0.465	0.53	0.42
P03	65.0	3666	0.69	0.43	0.585	0.45	0.65	0.45
P04	70.0	3657	0.79	0.55	0.845	0.53	0.67	0.55
P05	70.0	3868	0.67	0.51	0.87	0.51	0.63	0.58
P06	70.2	4126	0.64	0.52	0.815	0.5	0.6	0.53
P08	75.1	3884	0.78	0.52	0.765	0.49	0.65	0.58
P09	72.6	3694	0.8	0.56	0.84	0.55	0.68	0.56
P10	77.7	4104	0.71	0.5	0.865	0.48	0.64	0.57

†: Average of results from CR-IRF and PP-IRF in Table 9-3.

Table 10-2: Results of the Ringhals stability benchmark, regional mode

Test Case	Power (% rated)	Core Flow rate (kg/s)	Reference		STAB	
			DR	Frequency (Hz)	DR	Frequency (Hz)
P01	65.0	4105	-	-	-	-
P03	65.0	3666	0.57	0.43	0.6	0.43
P04	70.0	3657	0.75	0.52	0.62	0.44
P05	70.0	3868	0.6	0.5	0.6	0.48
P06	70.2	4126	0.59	0.5	0.57	0.46
P08	75.1	3884	0.79	0.5	0.65	0.44
P09	72.6	3694	0.99	0.54	0.83	0.46
P10	77.7	4104	0.63	0.49	0.61	0.49

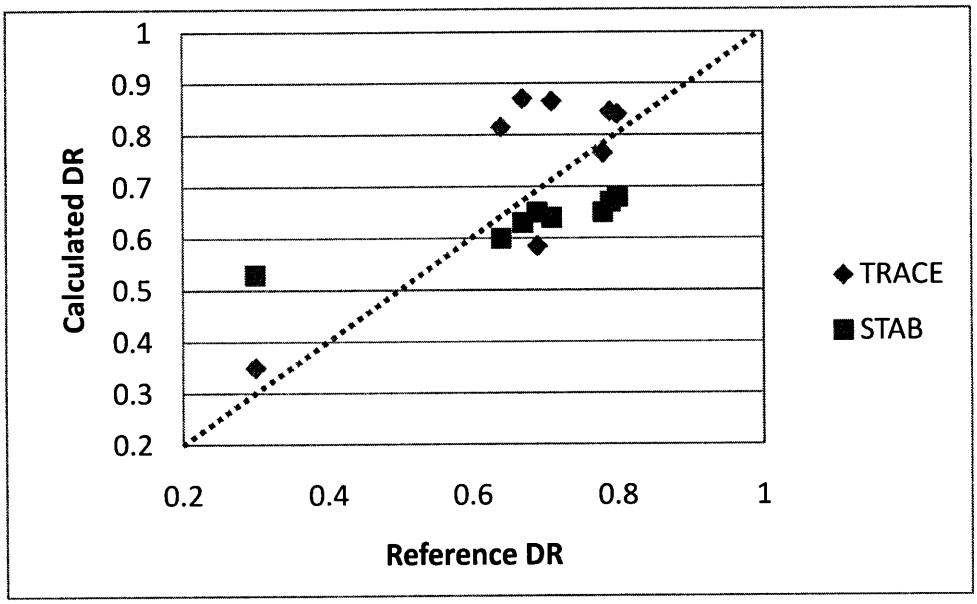

Figure 10.1: Calculated decay ratios of Ringhals-1 cycle 14, Global mode

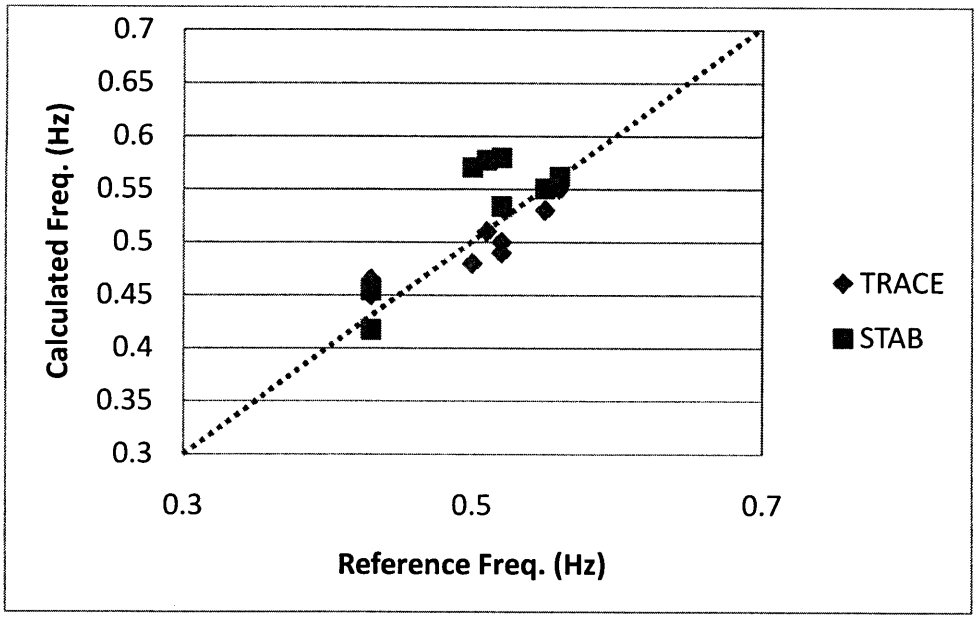

Figure 10.2: Calculated oscillation frequencies of Ringhals-1 cycle 14, Global mode

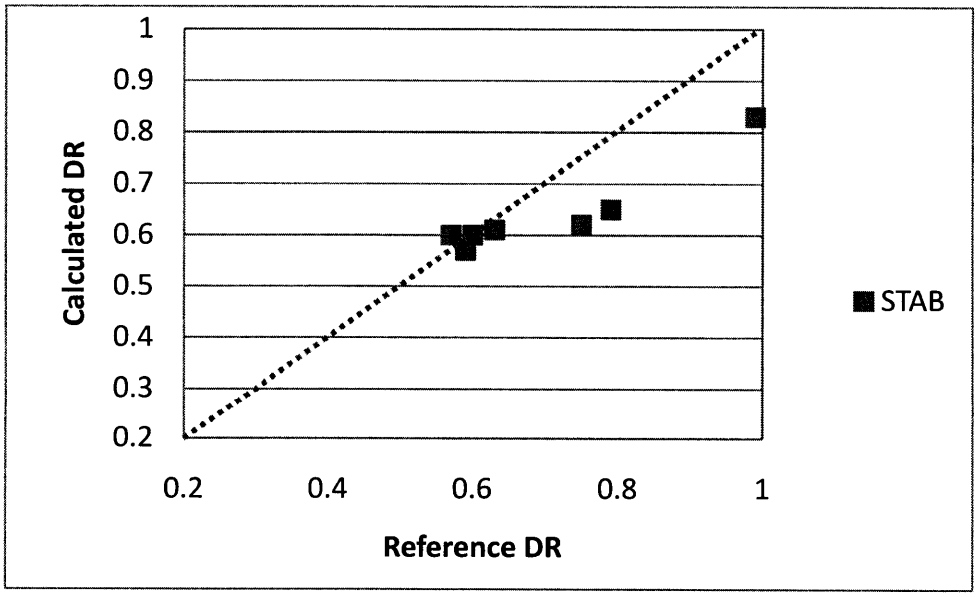

Figure 10.3: Calculated decay ratios of Ringhals-1 cycle 14, regional mode

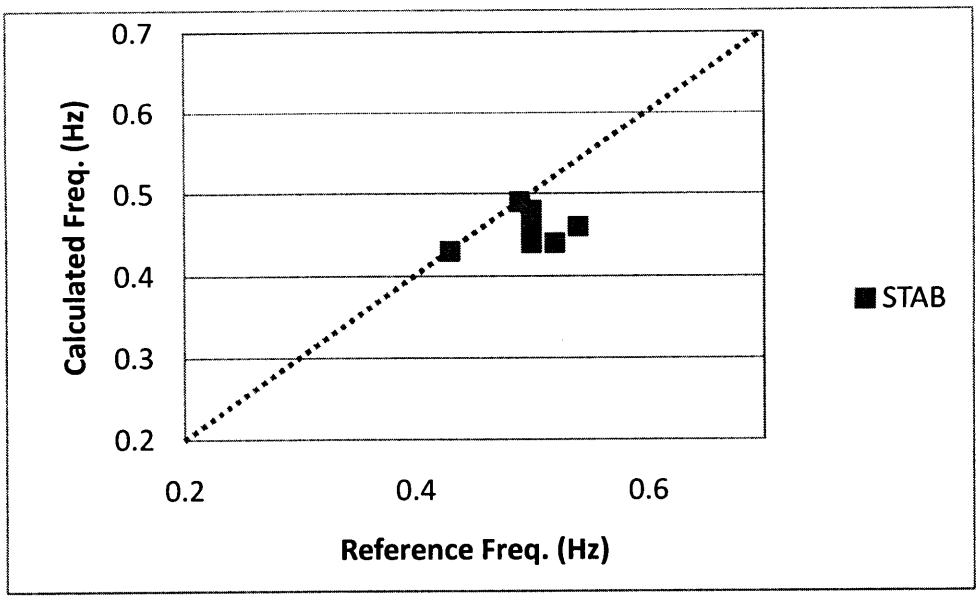

Figure 10.4: Calculated oscillation frequencies of Ringhals-1 cycle 14, regional mode

It is observed from Table 10-3 that both code predictions are close to the experimental results. The biases for the predicted decay ratio are about 0.07 in TRACE results, but -0.04 in STAB results. The biases are close, but with the different signs. The standard deviations of decay ratios are both large, around 0.1, indicating large uncertainties in both analyses. Nonetheless, the results are of the same level of accuracy as many other Ringhals stability benchmark studies, as shown in Table 10-4. The predictions of oscillation frequencies agree better with the reference value in both cases.

For regional instability, the STAB code predictions agree reasonably well with the reference values. The biases and standard deviations of the decay ratio are -0.06 and 0.07 respectively. It is interesting to note in Table 10-4 and 10-5 that both the bias and the standard deviation in the regional mode are higher than in the global oscillation mode, indicating that the understanding of regional stability characteristics is less clear.

It should be also mentioned that the true values of the observed stability parameters (decay ratio and oscillation frequency) are not known in the experiments. There is an error due to the evaluation procedure of a given time series signals in order to get the stability parameters. This error, which can be characterized as a maximum deviation, has been reported in [Lefvert, 1996] and was given in Table 8-8 for the noise analysis method.

It is based on an optimal choice of model order in the analysis of sampled data. Note that this is the uncertainty due to the evaluation method only, and does not include the measurement error.

Table 10-3: Bias and standard deviation between the calculated and reference global decay ratio and oscillation frequency

Code	Decay ratio		Frequency	
	Bias	Standard deviation	Bias	Standard deviation
TRACE-global	0.07	0.10	-0.01	0.02
STAB-global	-0.04	0.11	0.03	0.03
STAB-regional	-0.06	0.07	-0.04	0.03

Table 10-4: Benchmark results of Ringhals 1 stability test from participants, global decay ratio (from [Lefvert, 1996])

Cycle 14 (8 points)	Participant							
	CSN/ UPV	NET-CORP	NFI	PSI	SCP/ ABB	SIE-MENS	TSI des	TSI be
bias	0.01	0.03	0.04	-0.03	-0.05	0.02	0.12	-0.1
std.dev.	0.05	0.16	0.1	0.05	0.05	0.08	0.13	0.1

Table 10-5: Benchmark results of Ringhals 1 stability test from participants, regional decay ratio (from [Lefvert, 1996])

Cycle 14 (8 points)	Participant					
	CSN/ UPV AR-Lyap.	CSN/ UPV LAPUR	NET-CORP	PSI	TSI des	TSI be
bias	0.03	0.08	0.3	0.06	0.15	0.04
std.dev.	0.08	0.14	0.14	0.1	0.11	0.1

10.2 Comparison between the Frequency Domain Approach and the Time Domain Approach

A comparison for the models used in the Ringhals stability benchmark with the frequency domain code, STAB, and the time domain code, TRACE, is shown in Table 10-7. It is

seen that the modeling details in the two codes are quite different. The STAB code is very simple compare to the TRACE code, in thermal-hydraulics, neutronics, fuel heat dynamics, and recirculation loop modeling. However, the STAB code captures all the key components to the reactor stability characteristics; and the benchmark results for Ringhals stability test from the STAB code are in the same level of accuracy as that from the TRACE code, as discussed in Section 10.1.2.

Table 10-6: Models for Ringhals stability benchmark, STAB and TRACE

Model	STAB	TRACE
Thermal-Hydraulics		
Two-phase flow model	HEM	Two-fluid model, six equation
Constitutive equations, friction	Conservative, such as twice HEM value for 2Φ friction multiplier	Flow regime dependent correlations
Lumped channels	3	325
Fuel heat transfer	Lumped fuel dynamics model (analytical model)	2D heat conduction equation
Neutronics	Point kinetics	3D neutron kinetics
Out-of-core components	Integral momentum dynamics	Detailed modeling, two-fluid model

To compare the uncertainties in the stability analyses with the two codes, it is necessary to review the procedures of the two approaches for stability analysis.

The procedure of stability analysis in the frequency domain using STAB is as follows:

1) Determine the steady-state conditions by a suitable method;
2) Solve the set of oscillation equations in the frequency domain, which is obtained from the linearization of the perturbation equations around steady state condition and subsequent Laplace transformation of linearized equations;
3) Construct the system characteristic equation based on the boundary conditions for each type of oscillations (i.e. single-channel, out-of-phase, in-phase);
4) Search the dominant root ($\lambda = \sigma + \omega i$) of system characteristic equation based on a Global Newton method, decay ratio $= \exp(2\pi\sigma / \omega)$.

The following procedure is applied during the stability simulation with TRACE:

1) Stand-alone TRACE initialization of the thermal-hydraulics field using a constant power and fixed power distribution;
2) A steady-state re-calculation is then performed with the coupled code TRACE/PARCS to achieve a converged coupled thermal-hydraulic/neutron flux solution;
3) The stability simulation is then performed by introducing one of two excitations to the core to initiate the transient: Control Rod perturbation (neutronics) and Pressure Perturbation (thermal-hydraulic);
4) Use time-series analysis method to evaluate the decay ratio and oscillation frequency from the transient results, both raw data and its IRF could be used in the signal process code, DRACO.

The major modeling uncertainties in stability analysis with the STAB code and TRACE code are summarized in Table 9-8. It is seen that although TRACE uses more sophisticated models, the uncertainties remain there, and could possibly grow with the details of modeling if we don't have enough knowledge or information about the required details. Furthermore, the numerical diffusion problem and the uncertainty in the time series analysis method are intrinsic in the time domain stability analysis approach.

Both the STAB and TRACE code have certain modeling uncertainties for BWR stability analysis, but the uncertainties listed in Table 9-8 are very difficult to quantify, and are not further investigated in this work. However, the benchmark results for Ringhals stability test are in the same level of accuracy from both codes.

Table 10-7 Major modeling uncertainties in stability analysis with STAB and TRACE

Uncertainties	STAB	TRACE
Details of modeling	▪ The effectiveness of core channel lumping scheme. ▪ Friction, void fraction and wall heat transfer model ▪ Neutronic feedback coefficients ▪ Simple outer-loop model	▪ Constitutive correlations in the two-fluid model, especially the interfacial models ▪ Axial and radial power and flow distribution among large number of channels ▪ Pre-generation of macroscopic cross-sections, detailed neutronic modeling, such as fuel burnup, control rod, etc.
Numerics	Small	Numerical instability and numerical damping
Transient Initiation	None (built-in assumption)	Initial perturbation amplitude[1]
Decay ratio derivation	▪ Dominant root assumption ▪ Solution scheme for the system characteristics equation[2]	Time series analysis method

[1]: Perturbation should be small to avoid large deviation from the initial steady state, but large enough to initiate visible variation from the steady state;
[2]: The system characteristics equation is a very high order algebraic equation in the complex domain.

In general, the frequency domain approach is fast and could be efficiently applied to conduct parametric sensitivity study; the time domain approach has the capability to incorporate the non-linear features and transient behavior of BWRs and could be potentially more accurate, but it is time-consuming and has the concern about numerical diffusion. They are both required for BWR stability analysis, and need further development since both approach have large uncertainties in the stability predictions.

10.3 Summary

Stability calculations are arguably the most complex numerical simulations that are performed for a nuclear reactor design, especially for time-domain calculations. For most

other reactor simulations, the event is controlled by a boundary condition (e.g., a pipe break), and as long as the simulation code conserves mass and energy, it will track the evolution of the event at least in an approximate way. Instability simulations, however, develop by themselves without having the benefit of a boundary condition that forces them. Small modeling errors on both physical processes and numerical schemes can result in extremely large errors in the final results.

Both the frequency domain code STAB and the time domain system code TRACE have been applied in this work to simulate the Ringhals 1 stability test. The code predictions of the stability parameters agree reasonably well with the experimental results. The biases for the predicted global decay ratio are about 0.07 in TRACE results, and -0.04 in STAB results. The standard deviations of decay ratios are both large, around 0.1, indicating large uncertainties in both analyses. The predictions of oscillation frequencies agree better with the reference values in all cases.

The major modeling uncertainties in stability analysis with the STAB code and TRACE code have been summarized. Although TRACE code uses more sophisticated models, the modeling uncertainty is not less than that of the STAB code. The benchmark results for Ringhals stability test are in the same level of accuracy from both codes.

Since the frequency domain approach is generally fast and could be applied efficiently to conduct parametric sensitivity study; while the time domain approach has the capability to capture the non-linear features and transient behavior of BWRs, they are both required for BWR stability analysis. Given the current tendency to multi-dimension multi-physics multi-resolution simulation in nuclear engineering, coupled 3D analysis should be favored for future development. Therefore, the frequency domain code should incorporate the 3D modeling capability in thermal-hydraulics and neutronics; while the time domain approach with 3D capability should focus on minimizing the numerical diffusion for stability prediction, and better ways to interpret the transient signals to stability characteristics.

Part IV Clad performance under power oscillations

Contents

Part IV Clad performance under power oscillations: 239
11. Cladding Performance under Power Oscillations in BWRs 240
11.1 Introduction 240
11.1.1 BWR Stability and Its Effect to Safety 240
11.1.2 Fuel Failure Modes 241
11.1.3 Literature Review of Fuel Performance under Power Oscillations in BWRs 242
11.1.4 Objectives of this Work 243
11.2 Description of FRAPTRAN Code 244
11.2.1 Objectives and Capability of the FRAPTRAN Code 244
11.2.2 Cladding Deformation Model 245
11.2.3 Fuel Rod Internal Gas Pressure Response Model 246
11.3 Simulation of the Power Oscillation Test, FK11 247
11.3.1 FK11 Test Description 247
11.3.2 FRAPTRAN simulation of FK-11 Power Oscillations 252
11.4 Power Oscillations under Normal BWR Operating Conditions 256
11.4.1 BWR Conditions under Normal Operation and Power Oscillations 256
11.4.2 Results of FRAPTRAN Simulation 258
11.4.3 Cladding Stress and Strain Analysis 263
11.5 Cladding Fatigue Analysis 265
11.6 Summary 267

11. Cladding Performance under Power Oscillations in BWRs

11.1 Introduction

11.1.1 BWR Stability and Its Effect to Safety

Stability has been a main concern during the development of BWR technology. Although stability studies of BWRs have a long history and there is extensive literature available, the literature on fuel performance under power and flow oscillations is very limited. It is important to investigate the fuel behavior, and to assure its integrity, in BWR oscillating conditions.

Thermal-hydraulic flow instability may cause large fluctuations in the global or local neutron flux in BWR cores. The resulting power oscillations, at a frequency of 0.4 - 0.5 Hz, in the fuel rods will induce fuel temperature and heat rate changes which are considerably damped and delayed (due to the thermal inertia), typically by a factor >10 and 85-90° out-of-phase relative to the imposed heat generation rate [D'Auria et al., 2008].

Today, the BWR stability is not a major safety problem from a technical point of view. Given appropriate instrumentation, power oscillations are easy to detect and there exist simple, as well as effective, counter measures. A power scram will normally solve the problem. However, the concerns of out-of-phase oscillation and the unavailability of reactor shutdown system (the case of ATWS originated oscillations) keep the stability issue a safety concern. The concerned variables in an instability occurrence with high oscillation amplitudes are the neutron flux and the fuel rod surface temperature. Additional problems might arise due to thermal cycling that may affect the fuel rod integrity, making pellet-cladding interaction more probable; or inducing greater than normal fission product release from the pellets [D'Auria et al., 1997].

In a recent review of BWR stability [D'Auria et al., 2008], an extensive data base was collected in relation to fuel rod behaviour following cyclic thermal loads at the Halden research reactor in Norway. As a main conclusion, it was found that there are large margins against cladding fatigue failure, partly due to the thermal damping by the fuel time constants. In addition, there is a large margin to dryout as long as reverse flow is avoided following excessive amplitude oscillations; short dryout periods (cyclically followed by rewetting) do not endanger the cladding integrity. The situation may be different under RIA (Reactivity Initiated Accident) conditions. Furthermore, recent experience shows that high burnup fuel may fail at energy releases as low as 30 Cal/g, as opposed to the 250 Cal/g that is tolerated by low burnup fuel. This might have implications concerning the behaviour of high burnup fuel subjected to large amplitude oscillations.

11.1.2 Fuel Failure Modes

An LWR fuel rod typically consists of UO_2 fuel pellets enclosed in Zircaloy cladding. The primary function of the cladding is to contain the fuel column and the radioactive fission products. If the cladding does not crack, rupture, or melt during a reactor transient, the radioactive fission products remain contained within the fuel rod. During some reactor transients and hypothetical accidents, however, the cladding may be weakened by a temperature increase, embrittled by oxidation, or over stressed by mechanical interaction with the fuel. These events alone or in combination can cause cracking or rupture of the cladding and release of some radioactive products to the coolant. Furthermore, the rupture or melting of the cladding of one fuel rod can alter the flow of reactor coolant and reduce the cooling of neighboring fuel rods. This event can lead to the loss of a "coolable" fuel assembly geometry.

The primary means of cladding failure result from mechanical loading of the internal clad surface by fuel-clad interactions or from the buildup fission product gasses in the plenum to critical values [Olander, 1976]. Failure in both cases is due to rupture from plastic deformation and creep. Analysis of the mechanical behavior of the fuel is a very

complicated task due to the relationships which exist between the mechanical, thermal, chemical, and structural properties. Additionally, not all of the individual mechanisms involved are completely understood.

The most prevalent failure mode for fuel rods is due to the failure of cladding from Pellet-Cladding Mechanical Interactions (PCMI). PCMI failures are the result of mechanical interaction between the fuel and cladding in a corrosive environment. Thermal expansion mismatches between the fuel pellets and cladding material result in pellet expansion exceeding that of the clad [Frost, 1982]. Fuel element failure may also occur due to the process of embrittlement due to hydriding of the zircaloy cladding, and by wear at contact points between the cladding and the spacer grid caused by flow induced vibrations.

However, in case of power oscillation, the major effect is the cyclic thermal load and its consequence. Thus, our major concern is the thermal oscillation effects on pellet-cladding mechanical interaction, fission gas release, and thermal fatigue of the cladding during long time oscillations.

11.1.3 Literature Review of Fuel Performance under Power Oscillations in BWRs

Although instability studies of BWRs have a long history and there is extensive literature available, the literature on fuel performance under sustained power oscillations is very limited.

In order to examine high burnup fuel performance under power oscillation conditions, two sets of irradiated fuels under simulated power oscillation conditions were conducted in the Nuclear Safety Research Reactor (NSRR) in Japan [Nakamura et al., 2003]. Impacts of cyclic loads on the fuel performance under hypothetical unstable power oscillations arising during an anticipated transient without scram (ATWS) in BWRs were examined in the tests. Deformation of the fuel cladding of the rest rods was comparable

to those observed in shorter transient tests, which simulated reactivity-initiated accidents (RIAs), at the same fuel enthalpy level. It was concluded that the fuel deformation was mainly caused by PCMI and was roughly proportional to the fuel enthalpy. Enhanced cladding deformation due to ratcheting by the cyclic load was not observed. Fission gas release, on the other hand, was considerably smaller than in the RIA tests, suggest different release mechanisms in the two types of transients.

Fukahori et al. [2005] developed an analysis system code, TRUST, for fuel integrity during hypothetical core instability events in BWR cores. This system can estimate the thermal-hydraulic and mechanical properties such as fuel cladding temperature, MCPR, rod internal pressure. Based on their systematic analysis, it was shown that fuel integrity could be maintained even if the neutron flux oscillation would be large enough to exceed the scram level. However, according to their analytical results, pellet-cladding mechanical interaction was not predicted during core-wide oscillation. As a result of the boiling transition during core-wide oscillation, the cladding temperature was up to about 780K, but the cladding oxidation was negligible. At the peripheral region of the pellet, the temperature exceeded the temperature under the rated operation by boiling transition, but fission gas release was not significant.

The limited available literature encouraged a further investigation of the fuel integrity under BWR power oscillations.

11.1.4 Objectives of this Work

This goal of this work is to examine the fuel integrity under power oscillations for high burnup fuels. The calculations of fuel deformation were first conducted by using the FRAPTRAN code [USNRC, 2001]. Then, based on the results of FRAPTRAN, a cladding fatigue analysis was conducted. The work includes:

(1) Simulating the power oscillation tests at the NSRR (FK11) by using FRAPTRAN code, and making a comparison with experiment results.

(2) Simulating the power oscillations without scram for normal BWR operating conditions.

(3) Analyzing the influence on cladding fatigue during power oscillations.

11.2 Description of FRAPTRAN Code

11.2.1 Objectives and Capability of the FRAPTRAN Code

FRAPTRAN (Fuel Rod Analysis Program Transient) is a FORTRAN language computer code developed for the U.S. Nuclear Regulatory Commission to calculate the transient thermal and mechanical behavior of light-water reactor fuel rods. FRAPTRAN is applied for the evaluation of fuel behavior during reactor power and coolant transients such as reactivity accidents, boiling-water reactor power oscillations without scram, and loss-of-coolant-accidents up to burnup levels of 65 GWd/MTU. The FRAPTRAN code is the successor to the FRAP-T (Fuel Rod Analysis Program-Transient) code series developed in the 1970s and 1980s. FRAPTRAN is a companion code to the FRAPCON-3 code developed to calculate the steady-state high burnup response of a single fuel rod [USNRC, 2001].

FRAPTRAN is an analytical tool that calculates LWR fuel rod behavior when power and/or coolant boundary conditions are rapidly changing. This is in contrast to the FRAPCON-3 code that calculates the time (burnup) dependent behavior when power and coolant boundary condition changes are sufficiently slow for the term "steady-state" to apply. FRAPTRAN calculates the variation with time, power, and coolant conditions of fuel rod variables such as fuel and cladding temperatures, cladding elastic and plastic stress and strain, and fuel rod gas pressure. Variables that are slowly varying with time (burnup) such as fuel rod densification and swelling, cladding creep and irradiation growth, and fission gas release, are not calculated by FRAPTRAN. However, the state of the fuel rod at the time of a transient, which is dependent on those variables not calculated by FRAPTRAN, may be read from a file generated by FRAPCON-3 or manually entered by the user [USNRC, 2001].

The FRAPTRAN code has the capability of modeling the phenomena which influence the performance of fuel rods in general and the temperature, embrittlement, and stress of the cladding in particular. The code has a heat conduction model to calculate the transfer of heat from the fuel to the cladding, and a cooling model to calculate the transfer of heat from the cladding to the coolant. The code has an oxidation model to calculate the extent of cladding embrittlement and the amount of heat generated by cladding oxidation. A mechanical response model is included to calculate the stress applied to the cladding by the mechanical interaction of the fuel and cladding, by the pressure of the gases inside the rod, and by the pressure of the external coolant.

11.2.2 Cladding Deformation Model

The detailed description of cladding deformation model used in FRAPTRAN code could be found in [USNRC, 2001]. Here only the models in the strain-stress calculation are discussed for both cases of the cladding-fuel gap being open or closed, which results in different mechanisms of deformation.

Calculations for the closed gap regime are made using a model which assumes that the cladding is a thin cylindrical shell with prescribed external pressure and a prescribed radial displacement of its inside surface. The prescribed displacement is obtained from the fuel thermal expansion model. Furthermore, because no slippage is assumed to take place when the fuel and cladding are in contact, the axial expansion of the fuel is transmitted directly to the cladding. Hence, the change in axial strain in the shell is also prescribed.

The decision as to whether or not the fuel is in contact with the cladding is made by comparing the radial displacement of the fuel with the radial displacement that would occur in the cladding due to the prescribed external (coolant) pressure and the prescribed internal (fission and fill gas) pressure. The decision is expressed by the equation:

$$u_r^{fuel} \geq u_r^{clad} + \ddot{a} \tag{11-1}$$

where: $\ddot{a}$ = as-fabricated fuel-cladding gap size (m)

u_r = radial displacement (m)

If the above equation is satisfied, the fuel is determined to be in contact with the cladding. The loading history enters into this decision by virtue of the permanent plastic cladding strains imposed on the cladding by the cladding loads.

If the fuel and cladding displacements are such that Eq. (11-1) is not satisfied, the fuel-cladding gap is assumed not closed during the current loading step and an open gap solution is used. If Eq. (11-1) is satisfied, however, the fuel and cladding have come into contact during the current loading increment. At the contact interface, radial continuity requires that:

$$u_r^{clad} = u_r^{fuel} - \ddot{a} \tag{11-2}$$

while in the axial direction the assumption is made that no slippage occurs between the fuel and cladding. This state is referred to as PCMI.

Note that only the additional strain, which occurs in the fuel after PCMI is initiated, is transferred to the cladding. Thus, if $\varepsilon_{z,o}^{clad}$ is the axial strain in the cladding just prior to contact and $\varepsilon_{z,o}^{fuel}$ is the corresponding axial strain in the fuel, then the no-slippage condition in the axial direction becomes:

$$\varepsilon_z^{clad} - \varepsilon_{z,o}^{clad} = \varepsilon_z^{fuel} - \varepsilon_{z,o}^{fuel} \tag{11-3}$$

After u_r^{clad} and ε_r^{clad} have been calculated, a solution is made of the stresses and strains in a thin cylindrical shell with prescribed axial strain, external pressure, and prescribed radial displacement of the inside surface. The solution also gives the interface pressure between the fuel and cladding.

11.2.3 Fuel Rod Internal Gas Pressure Response Model

The pressure of the gas in the fuel rod must be known in order to calculate the deformation of the cladding and the transfer of heat across the fuel-cladding gap. The

pressure is a function of the temperature, volume, and quantity of gas. It should be noted that FRAPTRAN does not have a model to calculate the transient release of fission gases as a function of temperature. The fill gas composition and pressure at the time of the transient, which is dependent on fission gas release prior to the transient, is either manually entered by the user or read from a FRAPCON-3 burnup initialization file.

The released fission gas affects the gas pressure and composition, which in turn impacts the transient thermal and mechanical calculations. It has also been proven that some amount of fission gas was released during power oscillation transients. Therefore, a user input option (MODEL data block in the FRAPTRAN input file) is used to specify the fission gas release to the fuel-cladding gap and rod plenum during power oscillation transients.

Although the rod-average fractional fission gas release could be specified as a function of time during the transient, the detailed information about fission gas release is still unknown in a power oscillation event. For simplicity, the internal gas pressure, rather than fission gas release fraction, was specified as a function of time.

It should be noted that Liu and Kazimi [2007] developed a mechanistic model for transient fission gas release and swelling, and implemented them in the FRAPTRAN code to simulate the performance of high burnup fuel during Reactivity Initiated Accident (RIA). However, the NRC version of FRAPTRAN1.3 is used in this work; and the analysis results did not reflect the modification of FRAPTRAN code in their work [Liu and Kazimi, 2007].

11.3 Simulation of the Power Oscillation Test, FK11

11.3.1 FK11 Test Description

In order to examine high burnup fuel performance under power oscillation conditions arising during an anticipated transient without scram (ATWS) in boiling water reactors,

fuel irradiation tests were conducted with irradiated fuels under the simulated power transient conditions in the Nuclear Safety Research Reactor (NSRR), Japan.

The NSRR is a pool type annular core reactor (TRIGA-ACPR) as shown in Figure 11.1. An experimental cavity of about 20cm in diameter is located at the core center, where an experimental capsule containing test fuel rods is placed and irradiated. The power oscillation tests for BWR fuel rods in NSRR is also called test FK-11. The test rod contained 10 pellets, which made a 108 mm long fuel stack. A flat axial power distribution during the transient irradiation in the NSRR was realized over the stack by inserting hafnium disks at each end. In FK-11 test, irradiated fuels at burnups of 56 GWd/tU were subjected to four power oscillations, which peaked at 50 at intervals of 2 s. Peak fuel enthalpies were estimated to be 256 J/g (61 cal/g) in the test. The power oscillation was simulated by quick withdrawal and insertion of six regulating rods of the NSRR. The detailed fuel design and pre-test conditions are shown in Table 11-1.

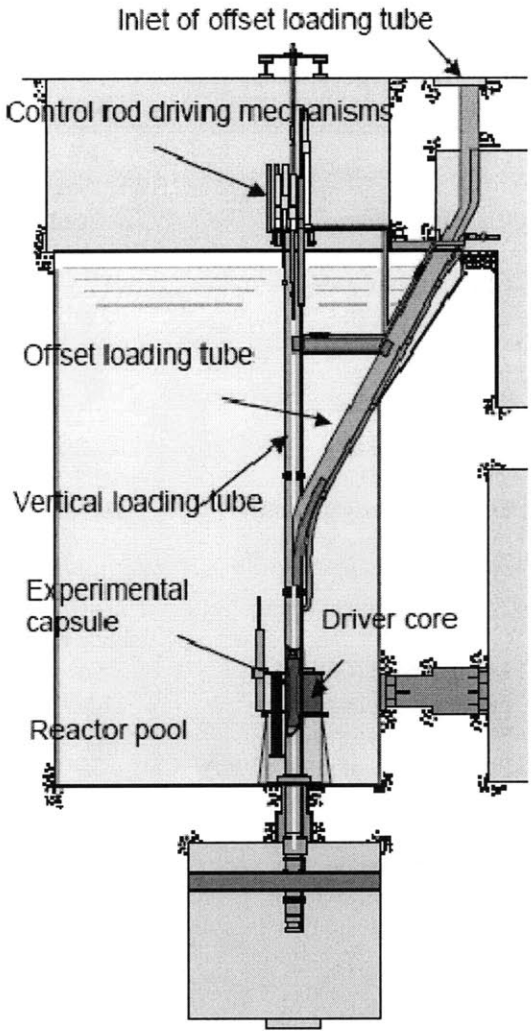

Figure 11.1: Configuration of the NSRR ([Nakamura et al., 2002])

Table 11-1: Fuel design and pre-test conditions of FK-11
(Table 2 in [Nakamura et al., 2003])

Test No.	FK-11
Fuel type	8×8 BWR (Step II)
Cladding type	Zr lined Zircaloy-2
Cladding diameter[a)] (mm)	12.3
Cladding thickness[a)] (mm)	0.86 (Zr liner: 0.09)
Fuel density[a)] (%TD)	97
^{235}U enrichment[a)] (wt%)	4.5
Fill gas[a)] (MPa)	He:0.5
Diameter gap[a)] (mm)	0.2
EOL diameter gap (mm)	<0.085
(pellet-cladding bonding)	(yes)
Oxide thickness (μm)	5 (sibling rod)
Hydrogen content (ppm)	72–107 (sibling rod)
Local burnup (GWd/tU)	56
Fission gas release (%)	12.5
EOL gas pressure (MPa)	1.4
Peak linear heat rate (kW/m)	35
Fast neutron fluence ($E>1$ MeV), (n/m^2)	1.2×10^{26}
Irradiation period	4 cycles

[a)]: Nominal value as fabricated.

Power history in test FK-11 is illustrated in Fig. 11.2. At the beginning of the test, rod power was kept at 27 kW/m for about 5 s to develop a center peaked temperature profile before initiating the power oscillation transient. Then, the test rod was subjected to four power oscillations to the peaks at 38, 43, 47, 50 kW/m at intervals of 2 s. Fuel enthalpy during the test relative to room temperature was estimated with FRAP-T6 and is illustrated in Fig. 11.2.

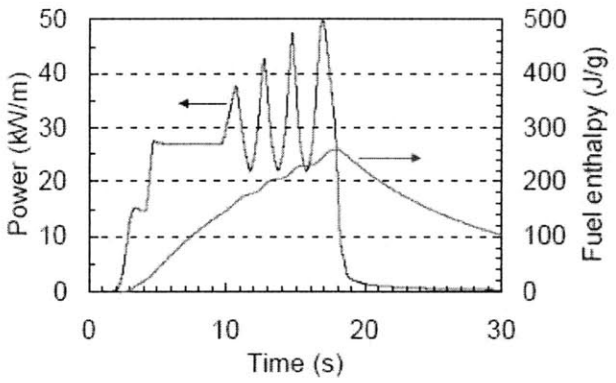

Figure 11.2: Histories of power and calculated fuel enthalpy in test FK-11 (Fig. 4 in [Nakamura et al., 2003])

In FK-11 test, synchronized axial elongation of fuel stack and cladding was observed as shown in Fig. 11.3. This deformation behavior suggests that strong PCMI controlled the cladding deformation during the test. Post-test diameter measurement showed that both radial and axial deformation was elastic. The cladding surface temperature remained about 100°C throughout the power transient. Rod internal pressure increased gradually from 1.4 to 2.2 MPa during the power transient, a result of heat up of the gap/plenum gas and fission gas release from the pellets. Post-test gas analysis indicated that fission gas release during the test was 0.4% of the total produced in the pellets. Test results are summarized in Table 11-3.

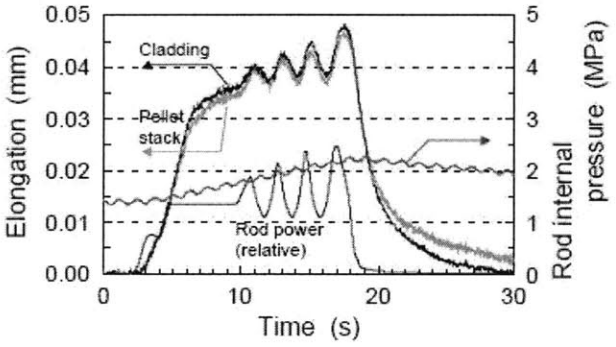

Figure 11.3: Histories of elongation of pellet stack and cladding, rod internal pressure and reactor power in test FK-11 (Fig. 8 in [Nakamura et al., 2003])

Table 11-2: Summary of conditions and results of the power oscillation test, FK-11 (Table 3 in [Nakamura et al., 2003])

Test No.	FK-11
Fuel burnup (GWd/tU)	56
Number of power oscillation	4
Peak linear heat rate during the test (kW/m)	50
Calculated peak fuel enthalpy (J/g)	256
(cal/g)	(61)
Cladding surface temperature (°C)	100
Pellet stack elongation (%)	0.05
Cladding axial strain (%)	0.05
[residual]	[0]
Cladding hoop strain (%)	—
[residual]	[0]
Rod internal pressure (MPa)	2.2
(initial)	(1.4[a)])
Fission gas release (%)	0.4
(base irradiation)	(12.5)
Failure	No

[a)]: He/Ar mixture gas was charged at re-fabrication of the test rod.

11.3.2 FRAPTRAN simulation of FK-11 Power Oscillations

For FRAPTRAN calculation, the initial conditions (including the power history) of fuel rods are supplied by the FRAPCON simulation results. However, the FRAPCON steady-state outputs were originally prepared for the irradiation test FK1, whose test rods were irradiated at Fukushima Daiichi #3 reactor, but the test rods in FK11 were pre-irradiated in Fukushima Daini #2 reactor. There are some differences between FK1 and FK11 pre-test conditions, which are shown in Table 11-3.

The major differences between the pre-test condition and the FRAPCON simulation results may be the power history, burnup and the internal gas pressure. As in our FRAPTRAN input file, the internal gas pressure was specified as a user input, we could changed the initial gas pressure to 1.4 MPa, the same as FK-11 pre-test condition. The difference of burnup may affect the results in some degree, so our comparison between

the test and simulation could only be qualitative. It should be also mentioned that the FK-11 test operated under cold zero conditions before the power oscillation starts. Thus, we need to further conduct some analysis in normal BWR operating conditions to investigate if the fuel integrity could be maintained under the power oscillations at hot conditions.

Table 11-3: Difference between FK-11 pre-test and FRAPTRAN input condition

Parameter	Unit	FK-11 pre-test	FRAPTRAN input (FK-1 pre-test)
Design			
Fill Gas Pressure	MPa	0.5	0.3
Fuel Density	%	97	95
Fuel Enrichment	%	4.5	3.9
Irradiation			
Irradiation Time	-	4 cycles	2500 days
Burnup	MWd/kg	56	65
EOL Gas Pressure	MPa	1.4	0.6†

†: Modified to 1.4 MPa in the FRAPTRAN calculation.

After changing the FRAPTRAN input file to satisfy the FK-11 test conditions, FRAPTRAN-1.3 was used to simulate the FK-11 power oscillation test. The results are shown in Figures 11.4 and 11.5.

From FRAPTRAN simulation results, we can find that the axial elongation of fuel stack and cladding are similar in Figures 11.4c and 11.4d; the structural radial gap is zero during the power oscillation periods (Figures 11.5a); and the gap interface pressure (due to clad-pellet interaction, Figures 11.5d) are very large during the power oscillation periods. These indicate strong PCMI controlled the cladding deformation in the oscillations, which is consistent with the test results.

However, the test results showed that very small plastic cladding deformation was left after the power oscillation; while the FRAPTRAN simulation results indicated fairly large plastic cladding deformation remained after the oscillations. Also the amplitude of the peak clad axial elongations of the test and the simulation are different. These

differences may arise from the difference in pre-test power history and initial burnups (56 MWd/kg in test, 65 MWd/kg in the simulation).

Furthermore, from Figures 11.5e and 11.5f, the cladding deformation was not accumulated through the power cycling, indicating that ratcheting deformation (a progressive incremental inelastic deformation or strain by a nearly equal amount for each cycle) of the cladding by the pellets did not occur, which agree with the test results. It could also be shown that the fuel axial elongation is proportional to the fuel enthalpy increase from Figures 11.4c and 11.5c., which also is consistent with the test results.

Although some differences exist in the initial conditions between FK-11 test and FRAPTRAN simulation, the general tendencies of the results are in good agreement. This gives us some confidence in using the FRAPTRAN code to simulate power oscillations under normal BWR condition, rather than cold zero condition in the FK-11 test. It can be concluded that the clad deformation in power oscillations is mainly caused by PCMI, and is roughly proportional to the fuel enthalpy, and enhanced cladding deformation due to ratcheting by the cyclic load was not observed (also due to the assumption of non axial slippage at fuel-cladding interface in the model).

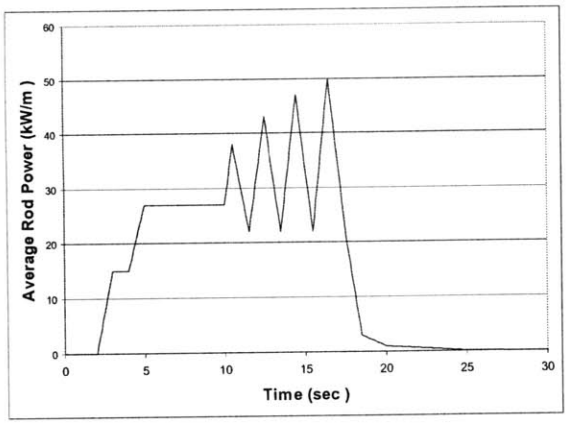

(a) Average Rod Power History

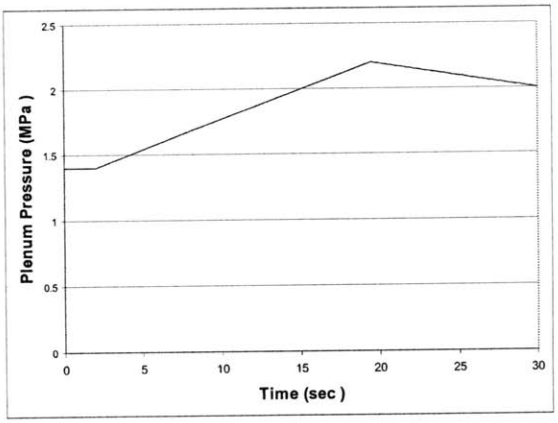

(b) Internal Gas Pressure Histroy

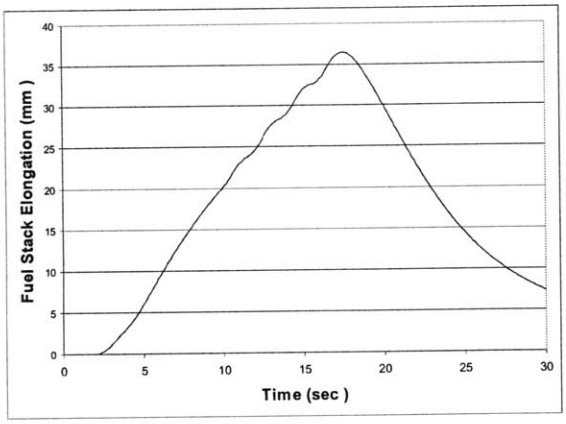

(c) Fuel Stack Axial Elongation

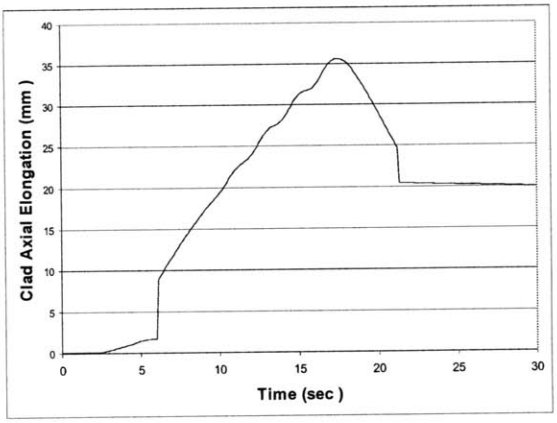

(d) Clad Axial Elongation

Figure 11.4: Results of elongation of pellet stack and cladding, rod internal pressure and reactor power of FRAPTRAN simulation for test FK-11

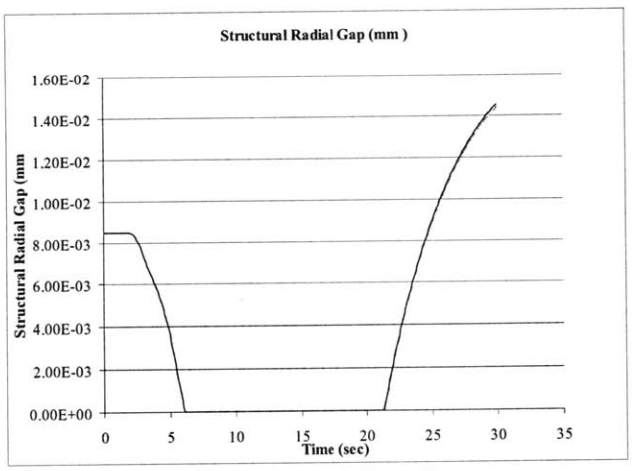

(a) Fuel-Cladding Gap

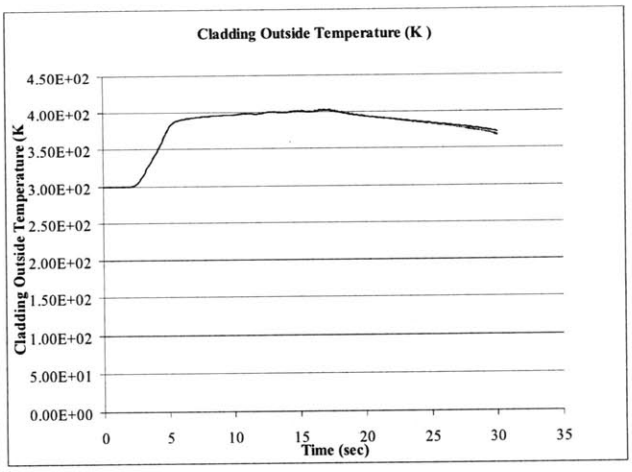

(b) Cladding Outside Temperature

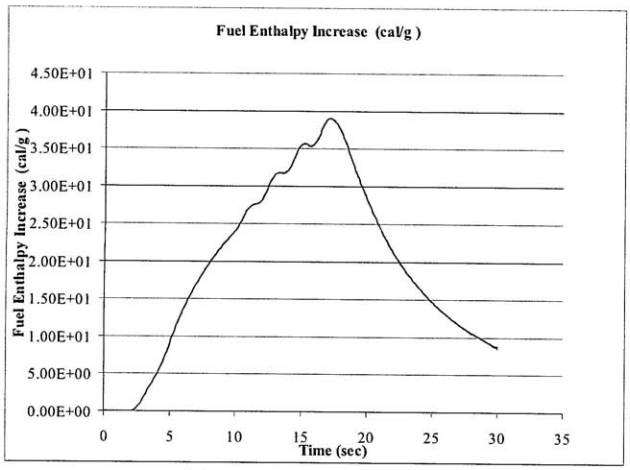

(c) Fuel Enthalpy Increase

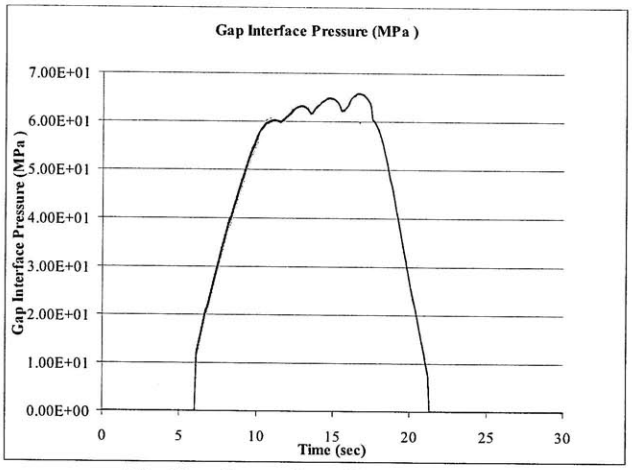

(d) Gap Interface Pressure

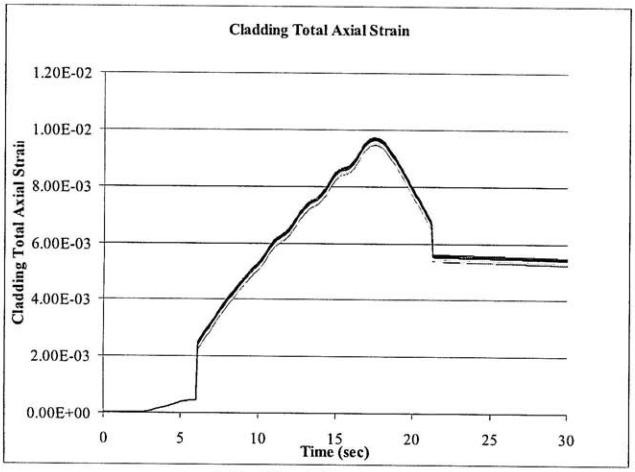

(e) Cladding Axial Strain

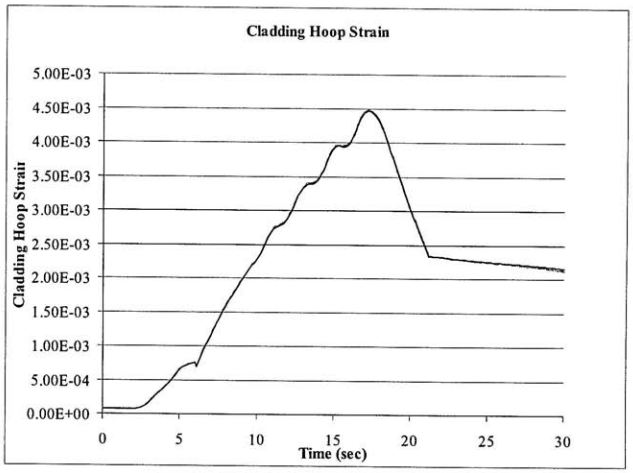

(f) Cladding Hoop Strain

Figure 11.5: Results of other parameters of FRAPTRAN simulation for test FK-11

11.4 Power Oscillations under Normal BWR Operating Conditions

11.4.1 BWR Conditions under Normal Operation and Power Oscillations

As the FK-11 test was operating under cold zero conditions before the power oscillations, the cladding outside pressure and temperature were considerably lower than normal BWR operating conditions, which could make its deformation of cladding different from that under normal BWR oscillations. Therefore, analysis of the cladding deformation under normal undamped BWR power oscillations is needed.

During the out-of-phase instability, half of the core rises in power while the power in the other half decrease to maintain an approximately constant total core power. In the tests described in [Gialdi et al., 1985], local power oscillations amplitude was as large as 70% while the average reactor power oscillated by only 12%. Since the automatic safety systems in BWRs rely on total power measurements to scram the reactor, large amplitude out-of-phase oscillations can occur without reactor scram. Also, the system adjusts flow from one half of the core to the other half while keeping the total flow rate almost constant. Therefore, it is necessary to design the reactors to avoid the out-of-phase instability problem. However, the recent trend of larger reactor core for economic concerns makes reactors more favorable to out-of-phase oscillation mode.

Based on the above discussion, the linear heat generation rates of fuel rods, which are undergoing the power oscillations, are taken to oscillate between 30% and 170% of normal linear heat generation rate. The oscillating coolant mass flow rates were decided by satisfying the constant pressure drop across the reactor core (constant pressure drop boundary condition). The coolant pressure was considered constant across the core as the pressure drop is considerably small comparing to the operating pressure, 7.2 MPa.

The FRAPCON output file prepared for the Fukushima Daiichi #3 reactor, which is a BWR/4 type, is used again to conduct FRAPTRAN transient analysis. The linear heat generation rate and flow rate are calculated based on typical BWR/4 data. All needed information is collected in Table 11-4; the input power history and coolant flow rate are shown in Figure 11.6.

Table 11-4: Needed BWR/4 information for Power and flow rate calculation

Parameter	Typical BWR/4
Core	
Thermal power	3293 MWt
Core flow rate	12915 kg/s
Power density	51 kW/L
Equivalent core diameter	4.75 m
Vessel inner diameter	6.375 m
Operating pressure	7.2 MPa
Core pressure drop	0.15 MPa
Reactor inlet temperature	275 °C
Radial power peaking factor	1.4
Fuel assembly	
Assembly number	764
Fuel pin lattice	Square 8x8
Number of fuel pins per assembly	63

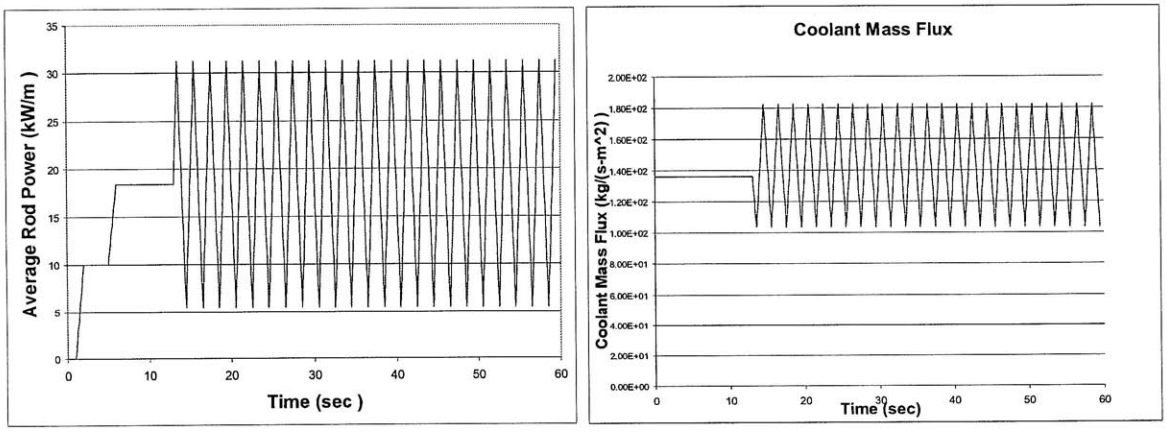

Figure 11.6: Assumed history of linear heat generation rate and flow rate during BWR power oscillations

11.4.2 Results of FRAPTRAN Simulation

The major results of deformation of fuel and cladding under oscillations is shown in the Figures 11.7, 11.8, and 11.9. It should be mentioned here that the fission gas release is not considered in FRAPTRAN code. Thus, as discussed in Section 11.2.3, the internal gas pressure was specified as a function of time in our analysis. The internal gas pressure history could be found in Figure 11.7a.

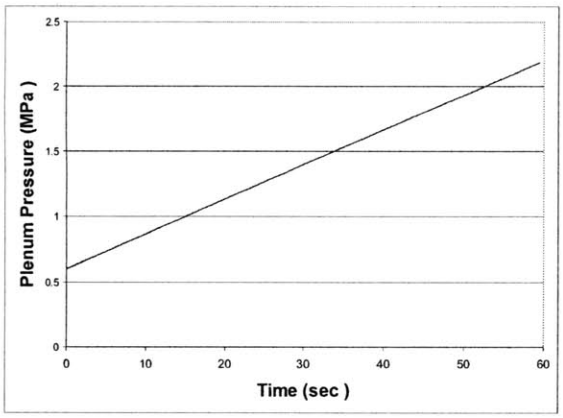

(a) Internal Gas Pressure Histroy

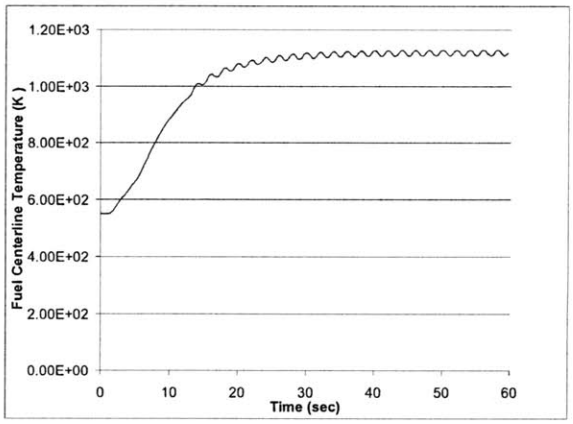

(b) Fuel Centerline Temperature

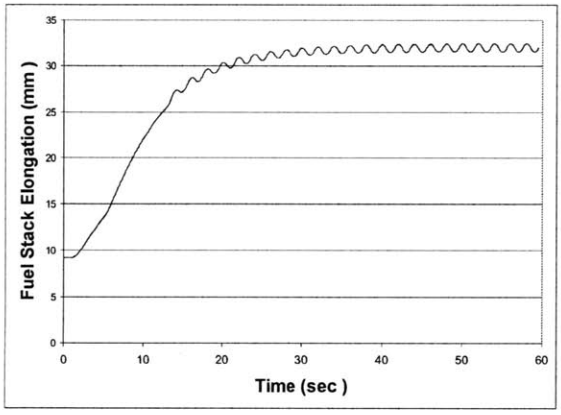

(c) Fuel Stack Axial Elongation

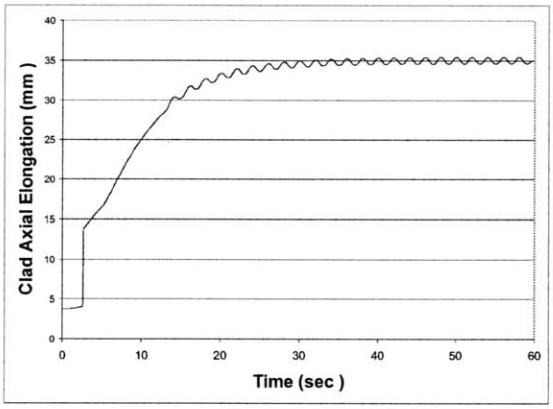

(d) Clad Axial Elongation

Figure 11.7: Results of FRAPTRAN simulation for BWR power oscillation (1)

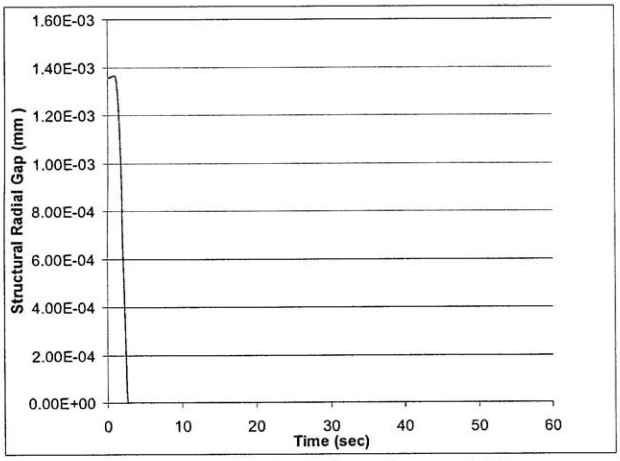

(a) Fuel-Cladding Gap width

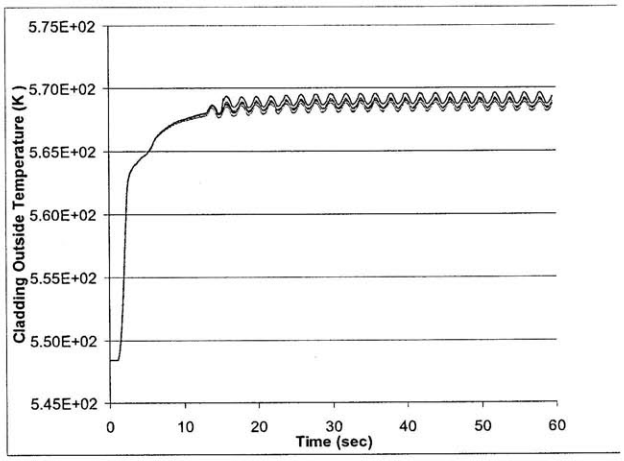

(b) Cladding Outside Temperature

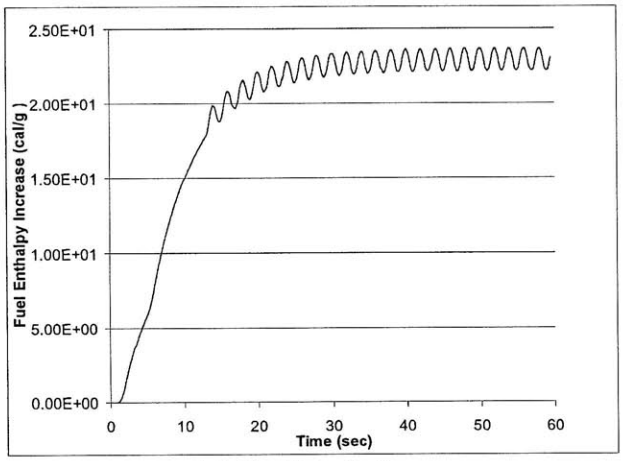

(c) Fuel Enthalpy Increase

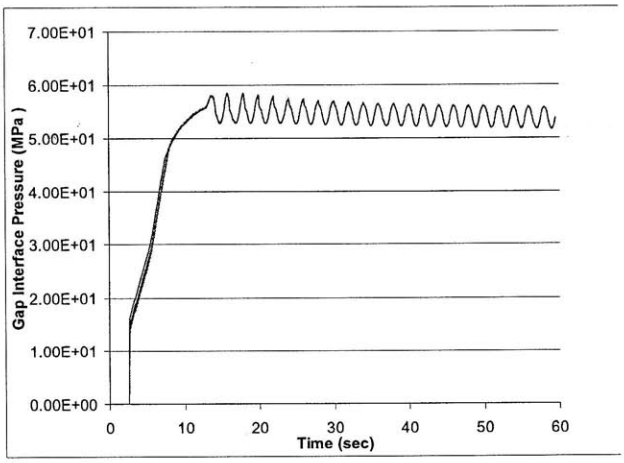

(d) Gap Interface Pressure

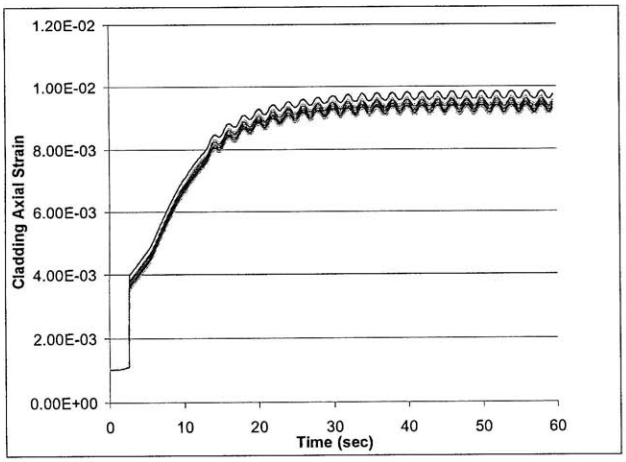

(e) Cladding Axial Strain

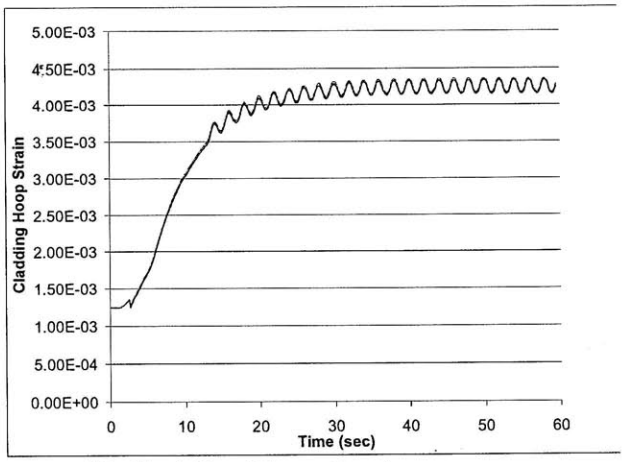

(f) Cladding Hoop Strain

Figure 11.8: Results of FRAPTRAN simulation for BWR power oscillation (2)

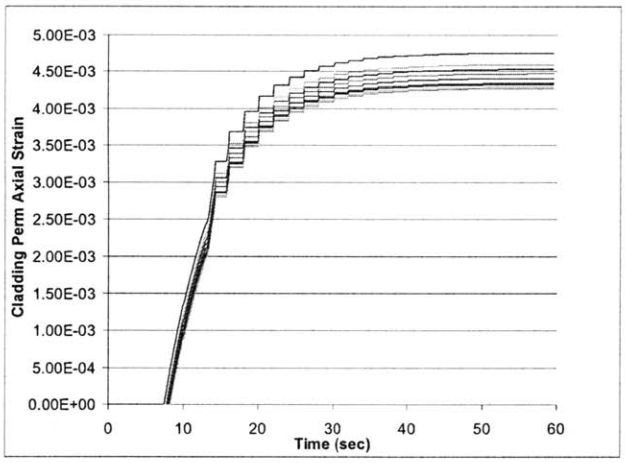

(a) Cladding Permanent Axial Strain

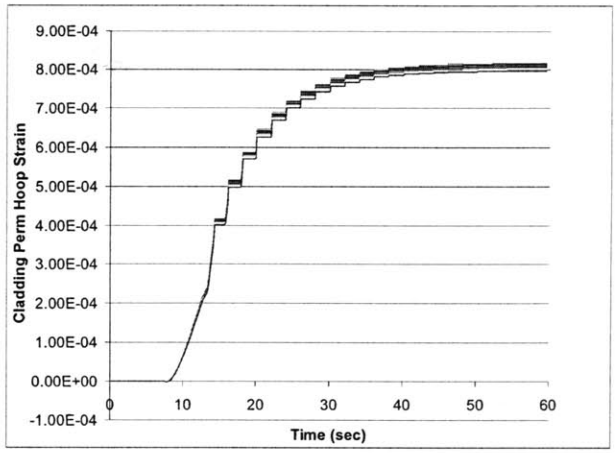

(b) Cladding Permanent Hoop Strain

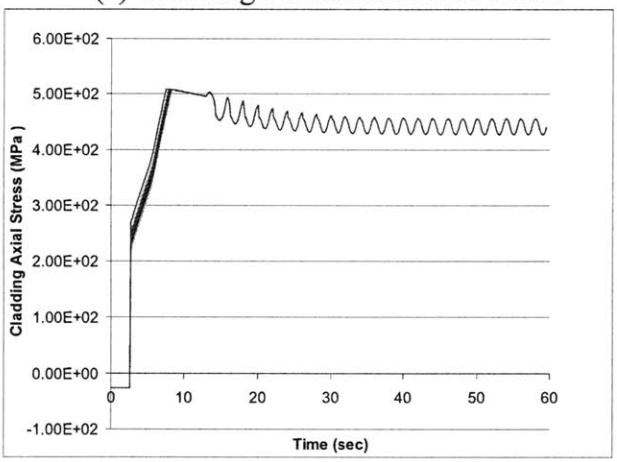

(c) Cladding Axial Stress

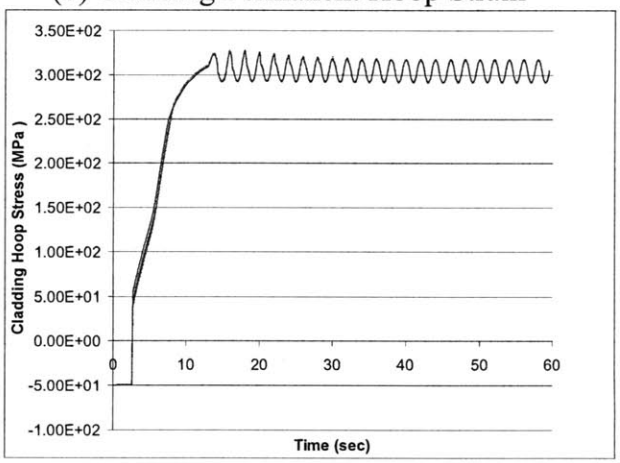

(d) Cladding Hoop Stress

Figure 11.9: Results of FRAPTRAN simulation for BWR power oscillation (3)

From Figures 11.7c and Fig. 11.7d, cladding axial elongation follows quite well with the fuel pellet axial elongation; also Figures 11.8a and Fig. 11.8d indicate that the gap is closed during power oscillations. These facts suggest strong PCMI, which controlled cladding deformation during the oscillations.

Internal gas pressure effects

It should be noted that the internal gas pressure in the above analyses are set as an input, which is still unkown for the real case. Thus, we discard the input for the internal gas pressure history and conducted the analysis again, allowing FRAPTRAN to calculate the internal gas pressure. The results are shown in the Figure 11.10. The curve shape of each parameter is basically the same, while the amplitude is slightly different, which indicates

that the internal gas pressure has limited effects on fuel deformation in power operation conditions, when the coolant pressure is high enough.

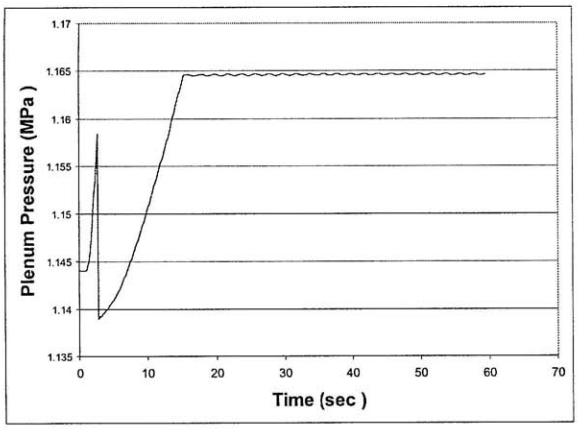

(a) Plenum Pressure

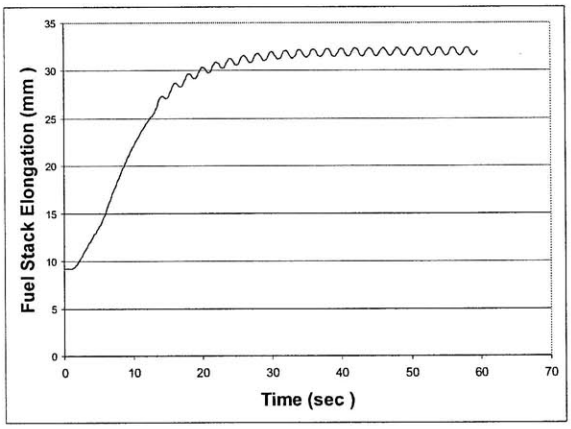

(b) Fuel Stack Axial Elongation

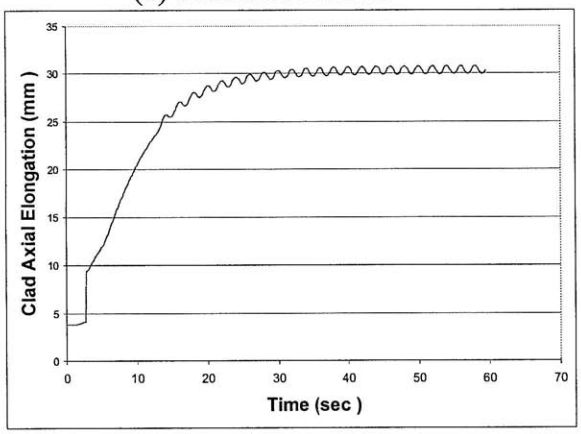

(c) Clad Axial Elongation

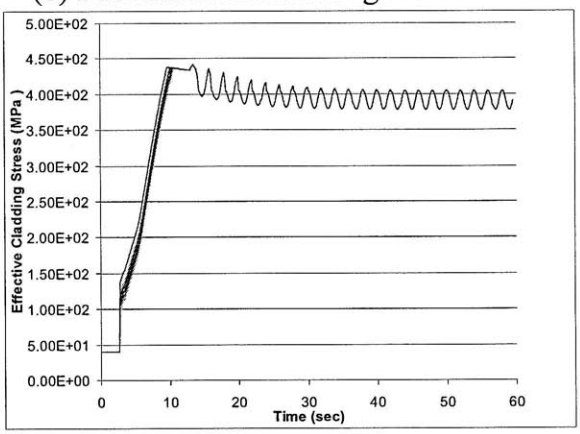

(d) Effective Cladding Stress

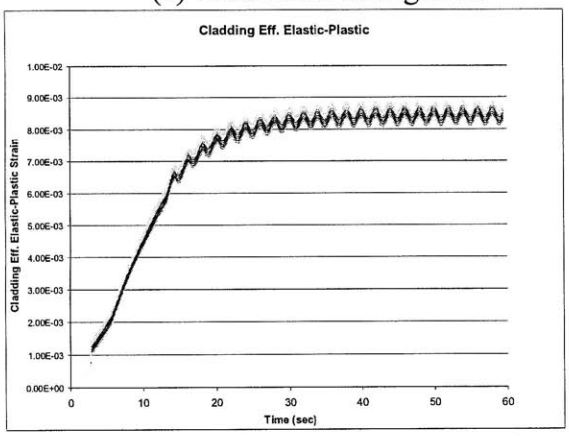

(e) Cladding Effective Strain

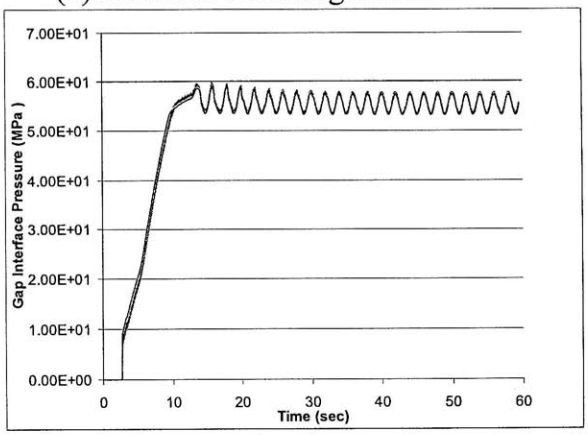

(f) Gap Interface Pressure

Figure 11.10. FRAPTRAN simulation results for BWR power oscillation (4), different internal gas pressure

11.4.3 Cladding Stress and Strain Analysis

1. Cladding Stress Criterion

Where creep is significant, the *ASME B&PV Code Section III Article NH-3000* specifies that the strain limiting criteria, rather than stress limiting criteria are applied. However, simplified methods can be used to establish conservative limits for stress.

(1) *Sm* = min. of {2/3 *Sy* at ambient (room) temperature, 2/3 *Sy* at service temperature, 1/3 *Su* at ambient (room) temperature, 1/3 *Su* at service temperature}

(2) *St* = min. of {100 % of the stress to cause 1% strain, 80% of the stress to initiate tertiary creep, 67% of the minimum stress to cause rupture}

The time independent stress limits for the load categories are as follows with: *Pm*, primary membrane stress (pressure difference across the cladding and PCMI); *Pl* primary local stress (stress raiser due to pellet cracking and bambooing); *Pb*, primary bending stress (bowing or PCI gradients); and *Q*, secondary stress (thermal stresses)

- $Pm < 1.0\ Sm$
- $Pm + Pl < 1.5\ Sm$
- $Pm + Pl + Pb < 1.5\ Sm$
- $Pm + Pl + Pb + Q < 3.0\ Sm$

The stress adder *Q* is included to assure that the transient thermal stresses do not exceed stresses which could exhaust the deformation capability of materials

It should be noticed that typical fuel performance codes (like FRAPTRAN) calculate *Pm* and *Q*, but not *Pl* and *Pb*.

2. Cladding Strain Criterion

The total permanent uniform strain shall not exceed:

- 1 % membrane strain (limiting)
- 2 % bending strain
- 5 % local strain

The intent of this requirement is to limit cladding damage due to slow rate strain accumulation at which the stress does not reach the stress limit (yield stress). The clad loading mechanism is the rod internal differential pressure with the system pressure and clad straining by the pellet expansion and PCMI. A bending strain and local strain are not calculated by FRAPTRAN and the limits are not applied at this time.

In this section, we followed the limiting criteria discussed above to examine if the cladding is failed under power oscillations. The results are shown in Table 11-5.

Table 11-5: Simulation results applying to the design criterion

Design Criterion	Simulation Results	Criteria Values	If Satisfy
Pm< 1.0 Sm	$Pm = \sigma_{tresca} = \lvert \sigma_\theta - \sigma_r \rvert$, $Max(Pm) = 300MPa$	$Sy \approx 500MPa$, $Sm = 2/3Sy = 333MPa$	Yes
Pm+Q<3.0 Sm	$Max(Q) = 160MPa$, $Pm + Q = 460MPa$	$3Sm = 1000MPa$	Yes
1% membrane strain	$Max(\varepsilon_{eff}) = 0.0103$ $Overall, \varepsilon_z = 0.008$	1%	No (by a very small value)

It should be mentioned that the thermal stress Q achieved its maximum value when the fuel rod increased its power form zero to rated power before power oscillation started, which may not happen in the real plants. Although the 1% membrane strain criteria is not satisfied, we still have enough confidence that the fuel rod would not fail as we can see the cladding strain and permanent axial and hoop strain did not change with power oscillations from Figures 11.9a and 11.9b.

It can be concluded that under a certain amount of undamped power oscillation cycles, the cladding would not fail and the fuel integrity is not violated.

Table 11-6: Fatigue threshold stress in the literature for Zircaloy-4 cladding

References	Test condition	Fatigue threshold stress
[Soniak et al., 1994]	350 °C and 1Hz	350Mpa, unirradiated 210MPa at EOL
[Joseph, 1997]	350 °C, varying frequencies between 0.5 Hz and 2Hz	350Mpa, unirradiated 210MPa (at EOL with 95% confidence level) 250MPa (at EOL with best estimate fitting)
[Kim et al., 2007]	350 °C	344.7Mpa, unirradiated at 1Hz load 300Mpa, unirradiated at 0.5Hz load

Thus, the BWR would not have cladding fatigue problems under the assumed power oscillations, since the allowed number of cycles is greater than 10^6 (more than 23 days) under the alternating load.

The small amplitude of the alternating stress S_{alt} can be explained as follows: 1) the pin thermal time constant is relatively large (on the order of 3-5 seconds) so that the heat flux change due to the power oscillation is attenuated; and 2) the heat flux in case of boiling is proportional to the 3rd to 4th power of temperature difference between the wall and the coolant. Thus, the cladding temperature changes at the hot spots are expected to be very small, unless dryout takes place. The average cladding temperature change in the power oscillations in Section 11.4.2 is shown here in Figure 11.11, in which the average cladding temperature oscillation was only around 2°C.

11.5 Cladding Fatigue Analysis

Cladding fatigue failure is an unlikely failure mode for a reactor in base load operation, and it is omitted in Section 11.4, as there are only 24 cycles in the oscillation calculation. But under hypothetical unstable power oscillations arising during ATWS, the oscillations could persist for thousands of times, given the short interval of 2 seconds between each cycle. Thus, cladding fatigue problem under long time power oscillation is examined in this section.

According to ASME criteria for stressed metals [ASME, 1998], cumulative number of strain cycles shall be less than the design fatigue lifetime with appropriate margins. A safety factor of 2 on stress amplitude is applied in this analysis.

Under power oscillation conditions, the alternating stress is the thermal stress, $S_{alt} = 1/2\Delta\sigma_{\max,Tresca}$. From Figures 11.9c and 11.9d: $S_{alt} \le 20MPa$ under the oscillation conditions calculated in Section 11.4. By using Soderberg Criterion:

$$\frac{K_t\sigma_a}{S_N} + \frac{\sigma_m}{S_y} \le 1 \tag{11-4}$$

In which, $\sigma_a = 20MPa, \sigma_m = 400MPa, S_y = 500MPa, K_t = 2$, we can calculated $S_N = 200MPa$.

Although the issue of deformation behavior of Zircaloy-4 cladding under cyclic load in the reactor environment is not closed yet, many stress-life diagrams have been reported in the literature. The calculated equivalent stress of *200 MPa* is smaller than the threshold stress (above which the infinite fatigue life could be expected) in [O'Donnell and Langer, 1964], [Soniak et al., 1994], [Joseph, 1997], and [Kim et al., 2007], as shown in Table 11-6.

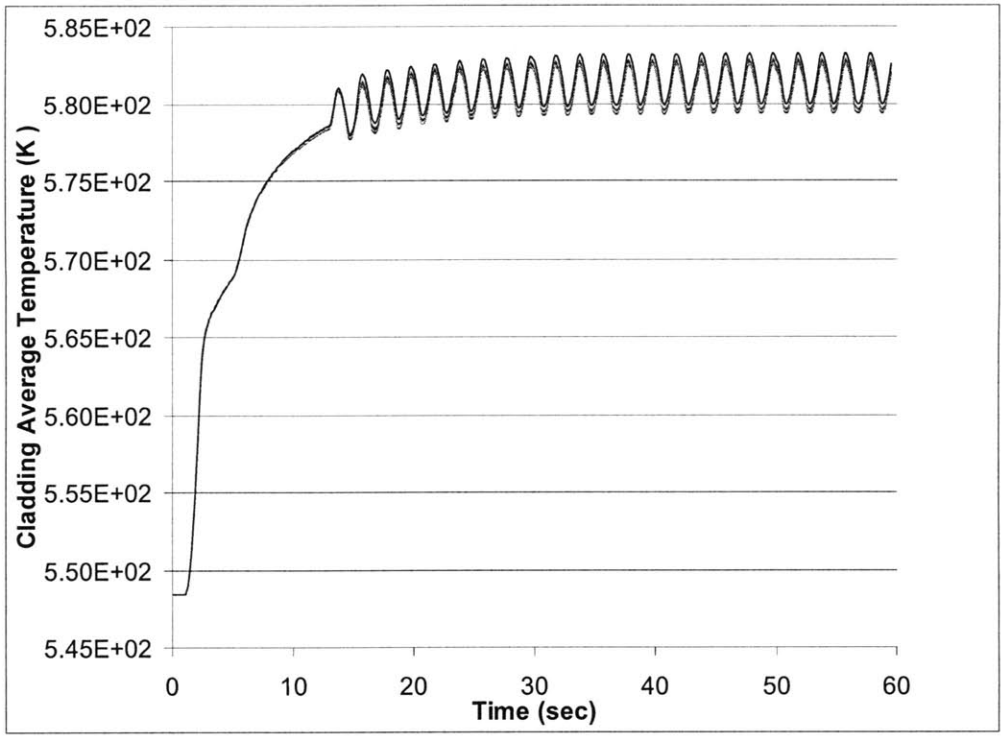

Figure 11.11: Cladding Average Temperature Changes in Power Oscillations

11.6 Summary

In summary, the fuel integrity under power oscillations with ATWS was examined in this work using FRAPTRAN code. Based on the analysis, the following conclusions can be drawn from consideration of the stress-strain criterion and thermal fatigue:

(1) The FRAPTRAN code can be used to analyze fuel performance under BWR power oscillations. The FRAPTRAN code results for a test case FK-11 were in good agreement with experiments.

(2) The fuel deformation was mainly caused by PCMI and was roughly proportional to the fuel enthalpy. Enhanced cladding deformation due to ratcheting was not found.

(3) The cladding can satisfy the design criterion (stress-strain criterion) in ASME Code under power oscillation conditions, which means it could maintain the fuel integrity.

(4) The fission gas release (internal gas pressure) is of importance to tests under cold zero power conditions, but not for the normal power operating conditions.

(5) Cladding thermal fatigue is not an issue under power oscillations, unless dryout takes place.

12. Summary and Conclusions

12.1 Summary of Conclusions

This work is meant to contribute to understanding of the conditions leading to the BWR instability phenomena, addressing a wide range of issues associated with the design to ensure advanced BWR stability and the use of appropriate models to predict the margin for stability. In particular four aspects of the BWR stability are assessed: 1) flashing-induced instability and natural circulation BWR startup; 2) stability of the BWRs with high power density designs; 3) modeling assumptions and approximations in stability analysis methods; and 4) clad performance during power oscillations. The major conclusions concerning the above four aspects are individually summarized below.

12.1.1 Flashing-Induced Instability and Natural Circulation BWR Startup

1. Development of FISTAB code

Both experimental and analytical studies in the literature have shown that BWRs are susceptible to flashing-induced instabilities during natural circulation start-up. To capture the effect of flashing on density wave oscillations at low pressure during the startup conditions, a code named FISTAB was developed in the frequency domain in this work.

The code incorporates pressure dependent water/steam thermodynamic properties, from which the evaporation due to flashing can be captured. A thermal-hydraulic non-homogeneous equilibrium model (NHEM) along with a lumped fuel dynamics model was adopted in the work. The Maier-Coddington drift-flux model was implemented to evaluate the phase slip, since this model was shown to perform very well for a wide range of experimental data. An iterative solution scheme was developed to calculate the steady state coolant flow conditions under zero loop pressure drop boundary condition for the equations depicting the flow in the water circulation path.

For linear stability analysis, a perturbation calculation approach for pressure oscillation through the flow channels was developed along with an efficient scheme to solve the resulting perturbation equations. A globally-convergent Newton method was developed in this work to solve the system characteristic equation.

The functionality of the FISTAB code was confirmed by comparison to the experimental results at the SIRIUS-N facility. Both stationary and perturbation results agree well with the experimental results.

2. NCBWR start-up

To examine the stability characteristics of NCBWRs during startup, the proposed ESBWR start-up procedure were examined by the FISTAB code. It was confirmed that the examined operating points along the ESBWR start-up trajectory, simulated with TRACG, were stable.

However, the FISTAB code was based on linear perturbation theory, and the transition from single-phase to two-phase natural circulation flow induced by flashing could not be modeled in FISTAB. To avoid the instability resulting from the transition from single-phase natural circulation to two-phase circulation, a simple criterion was proposed for the NCBWRs start-up. Under the criterion, the flashing was only allowed to occur above the riser and below the steam line (in essence above the vessel water level) when the steam dome pressure is still low.

12.1.2 Stability Analyses of Advanced BWR Designs

1. High power density BWR with advanced fuel designs

Using the frequency domain code STAB developed at MIT, stability performance of the large assembly with small pins (LASP) concept and of the cross shape twisted fuel rods (CST) have been investigated and compared with a traditional BWR reference core.

Single channel thermal-hydraulics oscillation, neutronic regional out-of-phase oscillation and neutronic core-wide in-phase oscillation were considered as instability modes.

Both the LASP and the CST designs were proposed to increase the core power by 20% with a similar increase of core flow; other operating conditions are fixed at the reference BWR design, such as the core inlet temperature, system pressure, core power distribution, and core power to flow ratio.

In all oscillation modes, the decay ratios of the CST design under rated conditions were somewhat smaller than those of the reference BWR, due to the reduction of the overall friction pressure loss and the reduction in the ratio of two-phase pressure loss to single-phase pressure loss, which indicates more robust stability margin. It was also seen that the decay ratios under uprated conditions were similar or slightly smaller than those under rated conditions, indicating that the stability performance is dependent on the power-to-flow ratio. Power uprate does not have important effects on stability performance when the power-to-flow ratio is maintained, and the void feed back coefficients are maintained.

Due to its larger void reactivity coefficient and smaller pin diameter, the decay ratios of the LASP design were much larger than those of the reference BWR in the coupled regional and core-wide stability analyses. However, they were still below the design limit of $DR=0.8$. To enhance the stability performance of the large assembly design, an increase of inlet orifice coefficient can be considered.

Furthermore, for the LASP core and the reference core, decay ratio sensitivities were evaluated against the void coefficient, Doppler coefficient, inlet orifice coefficient, coolant flow rate, and reactor thermal power. For the evaluated three instability modes, both cores showed similar sensitivities. The decay ratios were much smaller than stability limits within the considered parameter ranges.

It is concluded that good stability performance of the LASP core and the CST core can be expected under nominal conditions, even though they have 20 % higher reactor thermal power and flow rate than the reference core. However, further investigation would be still required for the LASP core startup and the operation procedures in the regions with high power but low flow rate.

2. Reduced moderation (highly voided) RBWR designs

Three types of density wave oscillations: single-channel, out-of-phase, and in-phase oscillations were examined for the reduced moderation RBWR-AC and RBWR-TB2 designs with the STAB code. In order to achieve the hard neutron spectrum (for higher conversion ratios) and the negative void reactivity coefficients in the RBWR designs, the hexagonal tight-lattice fuel rod arrangement and very high core average void fraction are adopted; and the core is designed to be short and flat.

It was found in the single-channel stability analysis that the shorter core length speeds up transient response, thus improving the overall stability performance of the RBWR-AC. It could also be concluded that the coupled neutronic stability performance was not an issue for the RBWR-AC because of its small neutronic feedback coefficients. However, the values of the coefficients under powering-up or -down need to be ascertained to ensure satisfactory performance during such operations.

RBWR-TB2 has smaller stability margin to single-channel type instability compared to a typical BWR due to its higher power-to-flow ratio and high friction pressure drop in the upper reflector. Although the shorter core length helps speed up the transient response, the smaller flow velocity reduces its effects. Coupled neutronic stability performance should be further addressed for RBWR-TB2 since it has a comparable void feedback coefficient to regular BWR and worse thermal-hydraulic stability performance. The stability performance could be greatly enhanced if the inlet orifice coefficient was increased and the void coefficient could be designed to be less negative.

Both the RBWR-AC and RBWR-TB2 designs are viable from stability performance point of view, even though their core exit qualities are around 3 times the exit quality in a traditional BWR. The RBWRs shift more flow to the high power region by better orifice design, narrow inter-assembly gaps, and more flat radial power distribution; thus, improving the stability performance. The active coolant flow rates in the hottest assemblies of RBWRs are shown in Table 6-12, with comparison to the reference BWR.

12.1.3 Stability Analysis Approach, time domain vs. frequency domain

A wide variety of codes and models can be used to assess the stability conditions, ranging from sophisticated system codes, able to calculate an overall plant behavior, to very simple models for a single heated channel. All of them have the capability to quantify stability, although their reliability may be different. In fact, the objectives of qualification and the level of approximation, thus the reliability of results, are different for the various models. Multipurpose codes solving multi-dimensional equations both for neutronics and thermal-hydraulics have become available recently. On the other hand, simplified codes based on one-dimension Homogeneous Equilibrium Model (HEM) for the two-phase flow are still used in the same framework. The NRC's latest coupled thermal-hydraulics and neutron kinetics code, TRACE/PARCS, and the frequency domain code, STAB, developed at MIT, were applied in this work to simulate the Ringhals 1 Stability Test.

1. TRACE modeling effects on stability predictions

Various modeling effects on TRACE stability analysis were assessed in this work, including time-spatial discretization, numerical schemes, channel grouping, neutronics modeling, and control system modeling.

It was found that numerical damping when using the Semi-Implicit (SI) method with adjusted axial mesh size, decreased when the time step size was increased; and the numerical damping for SI was minimized when the step size reached the material courant limits. Conversely, the SETS method was not very sensitive to the time step size; and the

numerical damping slightly decreased when the step size was decreased. The results from the SETS and the SI method became closer when the time step size was small. It can be concluded that the stability analysis by using TRACE (and other similar 1D thermal-hydraulics system codes) is sensitive to the time-space discretization scheme, and that numerical diffusion should be carefully controlled. The SI method with adjustable mesh-size was successful in minimizing the numerical diffusion in this work and produced reasonably good agreements with the Ringhals stability test. However, its fidelity in a large transient is still in question. It would be impossible to allow the Courant number to approach unity all the time for all the cells in all channels.

Five patterns of core region mapping using 6-, 10-, 20-, 50- and 325-CHANs were used to investigate the channel grouping effects. Some differences were observed in the coupled steady state results and the radial power distributions among different lumped channel schemes. The calculated DRs from the power response signals after control rod perturbations were somewhat different (±0.06 from the reference value, within the model uncertainties). It can be concluded that the transient response is somewhat sensitive to the lumped channel scheme in the coupled TRACE/PARCS simulation. But a clear tendency for the damping ratio with the channel number was not observed.

The coupled TRACE/PARCS 3D simulation was compared with TRACE stand alone point kinetics models in pressure perturbation transients. It was found that the power responses of the 3D PARCS model and the reference point kinetics model were very different, although the void coefficient in the point kinetics model was calculated based on the PARCS 3D neutronics model. Both the oscillation amplitude and frequency in the 3D model were higher than those in the reference point kinetics model, which indicated that the neutronics feedback was attenuated by the point kinetics model in TRACE.

Although the control systems would regulate some reactor variables (such as the recirculation pump speed, turbine pressure, feedwater flow rate and temperature), their effects on stability performance and transient responses were negligible in small perturbation initiated oscillations (control rod perturbation and pressure perturbation in

this work). Thus, it is acceptable to neglect the control systems while investigating the static stability performance of the plant. However, significant differences were found in the simulated recirculation pump trip events for the cases with and without control systems. Very low-frequency oscillations due to control system instability were also observed. So, the control systems are significant to the transient behavior and stability performance of BWR in large transients, and cannot be neglected in these simulations.

2. Ringhals 1 stability benchmark and modeling uncertainties

By using the SI scheme and the appropriate nodalization scheme to minimize numerical diffusion, the TRACE/PARCS analysis results were in reasonably good agreement with the experimental results, considering that there were some uncertainties in deriving the oscillation decay ratios from the transient signals of the plant due to the selected time window and the time series analysis methods. The STAB code predictions of the stability parameters also agreed reasonably well with the experimental results. The biases for the predicted global decay ratio were about 0.07 in TRACE results, and -0.04 in STAB results. However, the standard deviations of decay ratios were both large, around 0.1, indicating large uncertainties in both analyses. The predictions of oscillation frequencies agreed better with the reference values in all cases.

The major modeling uncertainties in stability analysis with the STAB code and TRACE code were summarized in Table 10-8. Although TRACE code used more sophisticated models, the modeling uncertainty was not less than that of the STAB code. The benchmark results for Ringhals stability test were at the same level of accuracy from both codes. Since the frequency domain approach is generally fast and can be applied efficiently to conduct parametric sensitivity studies; while the time domain approach has the capability to capture the non-linear features and transient behavior of BWRs, they are both useful for BWR stability analysis.

12.1.4 Clad Performance under Power Oscillations

The fuel integrity under power oscillations without reactor scram was examined in this work by using the FRAPTRAN code, with consideration of allowable stress-stain criterion and thermal fatigue.

The FRAPTRAN code ability to analyze fuel performance under BWR power oscillations was tested. The FRAPTRAN code predictions were in good agreement with FK-11 test results in NSRR in Japan. In the simulation of FK-11 test, the fuel deformation was mainly caused by PCMI and was roughly proportional to the fuel enthalpy. Enhanced cladding deformation due to ratcheting was not found.

Under assumed power oscillation conditions for a high burnup fuel in a traditional BWR, the cladding can satisfy the allowable stress-strain conditions according to the ASME Code. Also, the equivalent alternating stress is below the fatigue threshold stress. Thus the fatigue limit criterion is not violated, and the allowed number of cycles is above 10^6 (which would occur over 23 days). It can be concluded that under a large amount of undamped power oscillation cycles, the cladding would not fail and the fuel integrity is not compromised.

12.2 Recommendations for Future work

1. Stability of the advanced BWR designs

Further investigation of the NCBWRs start-up with a system code, such as RELAP5 or TRACE, would be necessary to examine the transient responses under various start-up procedures.

For the RBWRs, there are uncertainties in the models used in this work, since we have limited knowledge about the thermal-hydraulics of the tight triangular fuel lattice, and the neutronics behavior in these highly heterogeneous cores. Detailed thermal-hydraulics (more lumped channels) and neutronics (3D feedback on axial/radial power distribution)

modeling would be required for stability analysis to capture the heterogeneity effects in the core.

If the exclusion region in the power-to-flow map due to stability concern is not allowed to increase in the evolutionary and innovative BWR designs, comparing to the reference BWR/4, the stability performance of the advanced designs under high-power and low-flow conditions require further investigation; and some design modifications may be required.

2. Stability analysis methods

1) 3D capability

Given the current tendency to apply multi-dimensional, multi-physics and multi-resolution simulation in nuclear engineering, coupled 3D analysis should be favored for future development of stability analysis methods. Therefore, a frequency domain code with 3D modeling capability in thermal-hydraulics and neutronics should be developed and verified against a wide range of conditions; while the time domain approach with 3D capability should focus on minimizing the numerical diffusion for stability prediction in the future development.

2) Ways to interpret stability (analysis results)

Most of the stability analyses focus only on the decay ratio and oscillation frequency. However, the decay ratio is based on linear stability theory and is only perfectly valid for a second order system. It may not be appropriate under certain circumstances in a BWR. Better ways to interpret the analysis results (transient signals in the time domain or perturbation variables in the frequency domain), such as the phasor (i.e. phase vector), are required for enhancing the reliability of the predictive methods.

3) Quantifying the uncertainty

Large uncertainties exist in the code predictions for both the frequency domain and time domain approaches. The uncertainties in the stability analysis should be addressed, including the modeling uncertainty, correlation uncertainty, and parameter uncertainty.

Until such capabilities are developed, the allowable design values for the decay ratio should remain significantly away from the limiting condition of 1.0, perhaps continuing the 0.8 value used in past GE efforts.

3. Fuel performance during power oscillation

A better fission gas release and swelling model are required for the transient fuel performance analysis, such as FRAPTRAN.

It may be also interesting to examine the possibility of the boiling transition during the power and flow oscillations.

References:

Ambrosini W., and Ferreri J.C., "Analysis of Basic Phenomena in Boiling Channel Instabilities with Different Flow Models and Numerical Schemes," *ICONE-14*, Miami, Florida, USA, July 17-20, 2006.

Andersen J.G., Inada F., Klebanov L.A., "TRACG Analyses of Flashing Instability during Start-up," *ICONE-3*, April 23-27, Kyoto, Japan, 1995.

Askari, B., "An advanced Frequency-Domain Code for Boiling Water Reactor Stability Analysis and Design", PhD thesis, Swiss Federal Institute of Technology (ETH), Zurich, Switzerland, 2008.

ASME, "1998 ASME Boiler & Pressure Vessel Code III Devision 1," 1998.

Bouré, J. A., Bergles, J. E., and Tong, L. S., "Review of Two-Phase Flow Instability", *Nuclear Engineering Design*, 25:165–192, 1973

Carmichael, L.A., and Niemi, R.O., "Transient and Stability Tests at Peach Bottom Atomic Power Station Unit 2 at end of Cycle 2", EPRI NP-564, Electric Power Research Institute, 1978.

Chatfield C. "The analysis of time series: an introduction," 6th ed., CRC Press LLC, Florida, 2003.

Cheung, Y.K., et al. "Design Evolution of Natural Circulation ESBWR," *ICONE-6*, May 1998.

Cheung Y.K., and Rao A.S., "Startup Simulation of a Natural Circulation Plant -ESBWR," *ICONE-8*, April 2-6, Baltimore, MD, USA, 2000.

Chiang, J. H., Aritomi, M., and Mori, M. et al., "Fundamental Study on Thermo-Hydraulics during Start-up in Natural Circulation Boiling Water Reactors, (III)", *J. Nucl. Sci. Technol.*, 31, 9, 883-893 1994.

Coddington, P., and Macian, R., "A study of the performance of void fraction correlations used in the context of Drift-flux two-phase flow models", *Nuclear Engineering and Design*, 215, 199-216, 2002.

Conboy T. M., P. Hejzlar, and M.S. Kazimi, "Thermal-Hydraulic Analysis of Cross Shaped Fuel for High Power Density BWRs", MIT-NFC-TR-093, July 2007.

D'Auria, F., et al., "State of the Art Report on Boiling Water Reactor Stability", OECD/GD(97)13, 1997.

D'Auria F., Lombardi-Costa A., and Bousbia-Salah A., "The Boiling Water Reactor Stability," IAEA-TECDOC-1474, Annex 10, 2005.

D'Auria F., Lombardi-Costa A., and Bousbia-Salah A., "The Boiling Water Reactor Stability – Updated," INL-IAEA Course on Natural Circulation, Idaho Falls, ID USA, May 19-23, 2008.

Downar T., Greenspan E., Kazimi M., et al., "Technical Evaluation of the HITACHI Resource-Renewable BWR (RBWR) Design Concept Phase II Interim Progress Report." Prepared for Electric Power Research Institute, June 15, 2009.

Downar T.J., et al., "PARCS v2.6 U.S. NRC Core Neutronics Simulator - User Manual," 2004.

Downar T.J., "Coupled Neutronics/Thermal-Hydraulics Nuclear Reactor Analysis," ANS Seminar at MIT, October 26, 2009.

Frost, B. T., "Nuclear Fuel Elements," Pergamon Press, New York, 1982.

Fukahori T., et al., "Development of an analysis system for fuel integrity evaluation and application to BWR core instabilities", 2005 Water Reactor Fuel Performance Meeting, Paper number: 1091, Kyoto, Japan, October 2-6, 2005.

Furuya, M., Inada, F., and Van der Hagen, T. H. J. J.. "Flashing-Induced Density Wave Oscillations in a Natural Circulation Loop with a Chimney - Mechanism of Instability and Stability Map". *Nuclear Engineering Design*, 235(15):1557–1569, 2004.

Furuya M., "Experimental and Analytical Modeling of Natural Circulation and Forced Circulation BWRs", PhD thesis, Delft University of Technology, Delft, The Netherlands, 2006.

Gartia et al., "A Comparative Study of Different Start-Up Procedures for Two-Phase Natural Circulation Based Reactors," *NUTHOS-7,* Seoul, Korea, October 5-9, 2008.

GE Nuclear Energy, "The ABWR Plant General Description", a CD description, January 2000.

GE-Hitachi Nuclear Energy, "ESBWR Design Control Document", Rev. 5, 2008.

Gialdi E., et al., "Core Stability in Operating BWR: Operational Experience," *Prog. Nucl. Energy*, 15, 447, 1985.

Hanggi, P., "Investigating BWR Stability with a New Linear Frequency-Domain Method and Detailed 3D Neutronics," a Ph.D. dissertation submitted to the Swiss Federal Institute of Technology, Zurich, 2001.

Hinds, D., and Maslak, C., Next-generation nuclear energy: The ESBWR, *Nuclear News*, 35-40, January 2006.

Hitachi Ltd., Presentation file, "Resource-Renewable BWR for Long-term Energy Supply and Effective Use of Transuranic Elements (RBWR-AC/BDBA) Rev. 1," April 27, 2009a.

Hitachi Ltd., Presentation file, "RBWR-TB2/BDBA Rev. 1," June 1, 2009b.

Hitachi Ltd., Presentation file, "Resource-Renewable BWR for Long-term Energy Supply and Effective Use of Transuranic Elements (RBWR-AC/MNVC)," Oct. 2008.

Hotta A., Honma M., Ninokata H., and Matsui Y., "BWR regional instability analysis by TRAC/BF1-ENTREE-I: application to density-wave oscillation," *Nuclear Technology*, vol. 135, no. 1, pp. 1–16, 2001a.

Hotta A., Zhang M., and Ninokata H., "BWR Regional Instability Analysis by TRAC/BF1-ENTREE-II: Application to Ringhals Unit-1 Stability Test," *Nuclear Technology*, vol. 135, no. 1, pp. 17–38, 2001b.

Hu R. and Kazimi, M.S., "Stability Analysis of Natural Circulation in BWRs at High Pressure Conditions", MIT-ANP-TR-118, Cambridge, Massachusetts, October 2007.

IAEA, "Status of advanced light water reactor designs," IAEA -TECDOC-1391, May 2004.

Inada, F., Furuya, M., Yasuo, A., "Thermo-hydraulic instability of boiling natural circulation loop induced by flashing (analytical consideration)," *Nuclear Engineering Design*, 200, 187-199, 2000.

Inoue M., Maeda K., Katsuyama K., Tanaka K., Mondo K., and Hisada M., "Fuel-to-Cladding Gap Evolution and Its Impact on Thermal Performance of High Burnup Fast Reactor Type Uranium-Plutonium Oxide Fuel Pins," *Journal of Nuclear Materials*, Vol. 326, pp. 59-73, 2004.

Iwamura T., et al., "Concept of innovative water reactor for flexible fuel cycle (FLWR)," *Nuclear Engineering and Design*, 236, 1599-1605, 2006.

Jiang S.Y., Zhang Y.J., Bo J.H., and Wang F., "Conversion from single to two-phase operation in a natural circulation nuclear reactor," *Kerntechnick*, **63**, 132-138 (1998).

Joseph J., "Framatome creep fatigue-damage modelling on irradiated fuel cladding and its use for fuel design," Transaction of the 14th International Conference on Structural Mechanics in Reactor Technology (SmiRT 14), Lyon, France, August 17-22, 1997.

Karahan A., J. Buongiorno, and M.S. Kazimi, "An Evolutionary Fuel Assembly Design For High Power Density BWRs," MIT-NFC-PR-092, July 2007.

Karahan A., and Buongiorno J., "Modeling of Thermo-Mechanical and Irradiation Behavior of Metallic and Oxide Fuels for Sodium Fast Reactors," MIT-NFC-TR-110, August 2009.

Kazimi, M.S., et al., "Core Design Options for High Power Density BWRs", MIT-NFC-PR-089, December 2006.

Kazimi, M.S., et al., "Core Design Options for High Power Density BWRs", MIT-NFC-PR-097, November 2007.

Kim J.H., Lee M. H., Choi B.K., and Jeong Y.H., "Deformation Behavior of Zircaloy-4 Cladding under Cyclic Pressurization," *Journal of Nuclear Science and Technology*, Vol. 44, No. 10, p. 1275-1280, 2007.

Kozlowski T., Roshan S., Dinh T., "Evaluation of Coupled Codes Relap5/PARCS Capability for BWR Global Stability Prediction," *NURETH-12*, Pittsburgh, Pennsylvania, USA, September 30 – October 4, 2007.

Lahey, R. T., Jr., and Moody, F. J., "The Thermal Hydraulics of a Boiling Water Nuclear Reactor", Chapter 7, American Nuclear Society, La Grange Park, IL, 1993.

Lefvert T., "Ringhals 1 Stability Benchmark, Specifications," NEA/NSC/DOC(94) 15, 1994.

Lefvert T., "Ringhals 1 Stability Benchmark, Final Report," NEA/NSC/DOC(96) 22, 1996.

Liu W., and Kazimi M.S., "Modeling of High-Burnup LWR Fuel Response to Reactivity-Initiated Accidents," MIT-NFC-TR-096, October 2007.

Lu, Shanlai. "GE Simplified Boiling Water Reactor Stability Analysis in Time Domain," Ph.D. Thesis, The Pennsylvania State University, May 1997.

Mahaffy J.H., "Numerics of Codes: Stability, Diffusion, and Convergence," *Nuclear Engineering and Design*, 145, 131-145, 1993.

Manera, A., and van der Hagen, T.H.J.J., "Stability of natural-circulation-cooled Boiling Water Reactors during startup: experimental results", *Nuclear Technology*, 143, 77-88, 2003.

Manera, A., "Experimental and Analytical Investigations on Flashing-Induced Instabilities in Natural Circulation Two-Phase Systems", PhD thesis, Delft University of Technology, Delft, The Netherlands, 2003.

March-Leuba, J., Cacuci D.G., and Perez R.B., "Nonlinear Dynamics and Stability of Boiling Water Reactors, Part I: Qualitative Analysis", *Nucl. Sci. Eng.*, 93, 111-123, 1986a.

March-Leuba, J., Cacuci D.G., and Perez R.B., "Nonlinear Dynamics and Stability of Boiling Water Reactors, Part II: Quantitative Analysis", *Nucl. Sci. Eng.*, 93, 124-136 1986b.

March-Leuba J., and Blakeman E.D., "A Mechanism for Out-of-Phase Power Instabilities in Boiling Water Reactors", *Nuclear Science and Engineering*, 107, 173-179, 1991.

March-Leuba, J., and Rey, J.M., "Coupled Thermohydraulic-Neutronic instabilities in boiling water nuclear reactors: a review of the state of the art." *Nuclear Engineering and Design*, 145, No. 1-2, 97-111, 1993.

March-Leuba, J., "An Introduction to the Mechanisms Leading to Density Wave Instabilities in BWRs", *NUTHOS-6*, Nara, Japan, October 4-8, 2004.

Muñoz-Cobo, J.L., and Verdú G., "Application of Hopf Bifurcation Theory and Variational Methods to the Study of Limit Cycles in Boiling Water Reactors", *Ann. Nucl. Energy*, 18, No. 5, 269, 1991.

Munoz-Cobo, J. L., Podowski, M.Z., and Chiva, S., "Parallel channel instabilities in boiling water reactor systems: boundary conditions for out of phase oscillations", *Annals of Nuclear Energy*, 29, pp.1891-1917, 2002.

Murase, et al., "The Development of the Evolutionary BWR", *ICONE-14*, Miami, Florida, USA, July 2006.

NakaMura T., et al., "Irradiated Fuel Behavior under Power Oscillation Conditions," *Journal of Nuclear Science & Technology*, Vol. 40, No. 5, p. 325-333, 2003.

NakaMura T., et al., "NSRR High Burnup Fuel Tests for RIAs and BWR Power Oscillations without Scram," NSRC 2002, Washington D.C., USA, Oct. 29, 2002.

Nayak A., "Study on the stability of natural circulation for the design of Advanced Heavy Water Reactor," Doctoral dissertation, Tokyo Institute of Technology, Japan, 2000.

Nissen W.H.M., van der Voet J., and Karuza J., "The start-up of the Dodewaard natural circulation Boiling Water Reactor – experiences," *Nuclear Technology*, **107**, 93-102, 1994.

NIST, Reference Fluid Thermodynamic and Transport Properties Database (REFPROP): Version 7.0, http://www.nist.gov/srd/nist23.htm, 2007.

O'Donnell W. J. and Langer B. F., "Fatigue design basis for Zircaloy Components," *Nucl. Sci. and Eng.*, 20, 1-12, 1964.

Olander D., "Fundamental Aspects of Nuclear Reactor Fuel Elements - Chapter 21," Springfield, VA: Technical Information Center, Office of Public Affairs, Energy Research, and Development Administration, 1976.

Otaduy P., and March-Leuba J., "LAPUR User's Guide," NUREG/CR-5421, 1989.

Paniagua J., Rothagi U.S., Prasad V., "Modeling of Thermal Hydraulic Instabilities in Single Heated Channel Loop During Startup Transients," *Nuclear Engineering Design*, Vol. 193, 207, 1999.

Peng S.J., Podowski M.Z., Lahey R.T. Jr. and Becker M., "NUFREQ-NP: A Computer Code for the Stability Analysis of Boiling Water Nuclear Reactors," *Nucl. Sci. Eng.*, 88, 404-411, 1984.

Podowski, M. Z., "Modeling and analysis of two-phase flow instabilities", *NURETH-10*, Seoul, Korea, October 5-9, 2003.

Saha, P. "Thermally Induced Two-Phase Flow Instabilities, Including the Effect of Thermal Non-Equilibrium between the Phases", Ph.D. Thesis, School of Mechanical Engineering, Georgia Institute of Technology, Atlanta, Georgia, June 1974.

Schuster C., Ellinger A., Knorr J., "Analysis of Flow Instabilities at the Natural Circulation Loop DANTON with regards to Non-linear Effects," *Heat and Mass Transfer*, 36, 557, 2000.

Sinha R.K. and Kakodkar A., "Design and development of the AHWR—the Indian thorium fuelled innovative nuclear reactor," *Nuclear Engineering and Design*, 236, 683-700, 2006.

Soniak A., Lansiart S., Royer J., Mardon J. P., Waeckel N., "Irradiation effect on fatigue behavior of Zircaloy-4 cladding tubes," *Zirconium in the Nuclear Industry, 10th Int. Symp.*, 549 - 558, 1994.

Takeda R., et al., "General Features of Resource-Renewable BWR (RBWR) and Scenario of Long-term Energy Supply," Proc. of International Conference on Evaluation of Emerging Nuclear Fuel Cycle Systems - *GLOBAL'95*, Versailles, France, September, 1995a.

Takeda R., et al., "Conceptual Core Design of a Resource-Renewable BWR and Long-term Energy Supply," *Trans. Am. Nucl. Soc.*, 72, 389, 1995b.

The MathWorks Inc., "MATLAB V7.0.4 Code Help," Massachusetts, 2004.

Todreas, N. E., and Kazimi, M. S., "Nuclear System I, Thermal Hydraulic Fundamentals", Hemisphere Publishing Corporation, 1990.

Tong, L.S., "Boiling Heat Transfer and Two-Phase Flow", Chapter 6, Taylor & Francis, 1997.

Tsuji, M., Nishio K., and Narita M., "Stability Analysis of BWRs Using Bifurcation Theory", *J. Nuc. Sci. and Tech.*, 30, 11, 1107-1119, 1993.

USNRC, "TRACE V5.0 - Theory Manual," Washington, DC, 2008.

USNRC, "FRAPTRAN: A Computer Code for the Transient Analysis of Oxide Fuel Rods", NUREG/CR-6739, August 2001.

Van Bragt, D.D.B., et al., "Analytical modeling of flashing-induced instabilities in a natural circulation cooled boiling water reactor," *Nuclear Engineering and Design*, 215, 199-216, 2002.

Woo, et al. "Experimental Study on Stability of Natural Circulation Boiling Water Reactor during Start-up Transient", *NURETH-12*, Pittsburgh, Pennsylvania, USA, 2007.

Wulff, W., et al., "High-Speed BWR Power Plant Simulations on the Special-Purpose Peripheral Processor AD10," BNL-NUREG-34167, International Conference on Simulation for Nuclear Reactor Technology, Cambridge, England, April 9-11, 1984.

Xu Y., et al., "Application of TRACE/PARCS to BWR Stability Analysis," *Annals of Nuclear Energy*, 36, 317-323, 2009.

Yadigaroglu, G. and Askari, B., "Boiling water reactor stability revisited: The effects of flashing", *Nuclear Engineering and Design*, 235, 1093-1105, 2005.

Yang W.S., Initial Implementation of Multi-Channel Thermal-Hydraulic Capability to Frequency Domain SCWR Stability Analysis Code SCWRSA, ANL-GENIV-056, September 2005.

Zhao, J., Saha, P., and Kazimi, M.S., "Stability Analysis of Supercritical Water Cooled Reactors", MIT-ANP-TR-108, Cambridge, Massachusetts, September 2005.

Zuber, N., and Findlay, J. A., "Average Volumetric Concentration in Two-Phase Flow Systems", *Journal of Heat Transfer*, Vol. 87, pp. 453-468, 1965.

Nomenclature

English

A_c : Fuel assembly cross sectional flow area (m^2)

C_{den} : Density reactivity coefficient

C_{dop} : Doppler reactivity coefficient

C_k : Kinematics wave velocity (m/s), $C_k = j + V_{gj}$

C_o : Void distribution parameter

c_p : Specific heat at constant pressure [kJ/(kgK)]

D_e : Hydraulic Diameter (m)

f : Friction factor in single-phase liquid region

f_m : Friction factor in two-phase mixture region

G : Mass flux (kg/m^2s)

h : Enthalpy (kJ/kg)

j : Volumetric flux density (m/s)

K_{in} : Inlet orifice coefficient

k_f : Fuel thermal conductivity [W/(m K)]

k : Thermal conductivity [W/(m K)], or neutron multiplication factor

L : Length of fuel rod heated region (m)

L_{nod} : Length of fuel rod lower unheated plenum (m)

L_{nou} : Length of fuel rod upper gas plenum (m)

$\dot{m}$: Flow rate (kg/s)

N_{sub} : Subcooling Number

N_{pch} : Phase Change Number

N_{flash} : Flashing Number

Nu: Nusselt number

ΔP : Pressure drop (MPa)

P : Pressure (MPa)

P_b : Primary bending stress

P_l : Primary local stress

P_m : Primary membrane stress

P_h : Heating parameter of the fuel rods per assembly (m)

Pr: Prandtl number

q'' : Surface heat flux (kW/m^2)

q'''_v : Volumetric heat flux (kW/m^3)

$\dot{Q}$: Reactor power

Q: Secondary stress

r : Radius of the fuel pin (m)

R_1 : Fuel pellet radius (m)

R_2 : Fuel cladding inside radius (m)

R_3 : Fuel cladding outside radius (m)

Re: Reynold number

s : Variable of Laplace Transformation

T_o : Fuel centerline temperature (K)

T_f : Fuel temperature (K)

T_c : Fuel cladding temperature (K)

$\overline{T}_{pin}$: Average temperature of the fuel pin (K)

T_w : Wall temperature (K)

T_∞ : Bulk fluid temperature (K)

t : Time (s)

u : Coolant velocity (m/s)

v : Specific volume (m^3/kg)

V_{gj} : Vapor drift velocity (m/s)

$X(t)$: Vector of state variables

x: Flow quality

x_{eq}: Equilibrium quality

$x_{eq,exit}$: Equilibrium quality at channel exit

z: Axial coordinate.

Greek letters

ρ: Coolant density (kg/m^3)

δ: Perturbation

ξ: Fuel pin non-dimensional radius, $\xi = \frac{r}{R_1}$; or water density to enthalpy derivative at constant pressure, $\xi = \frac{\delta\rho}{\delta h}\Big|_p$

η: Fuel cladding non-dimensional radius, $\eta = \frac{r - R_2}{R_3 - R_2}$; or water density to pressure derivative at constant enthalpy, $\eta = \frac{\delta\rho}{\delta P}\Big|_h$

σ: Real part of eigenvalue

ϖ: Imaginary part of eigenvalue

λ_i: Eigenvalues

λ: Length of heated single-phase liquid region (m)

α: Vapor void fraction

Γ: Vapor generation rate (kg/m^{3}s), or velocity to pressure transfer function

Π: Transfer function of the inlet flow oscillation to the total pressure drop oscillation across the channel

λ_i: Decay constant of ith-group precursors,

β_i: Fraction of neutrons in ith delayed group,

λ_m: m^{th} mode reactivity

ϕ_m: m^{th} neutron flux mode

Σ_f : Fission cross section

v : Number of neutrons per fission

Λ_m : Neutron generation time of the m^{th} mode

Subscripts

in : Channel inlet

exit : Channel outlet

f : Saturated liquid, or Fuel

g : Saturated vapor

fg : Difference between values of vapor and liquid at saturation

ext : External

m : Two phase mixture

λ : Properties at net vapor generation point

i : Inlet

k : Axial node number

C: Channel

e: Exit

dc: Downcomer

grav: Gravity

acc: Acceleration

sp: Separator

tot: Total

t: Total

F : Feedback

ori : Orifice

c : Coolant

nod : Lower non-heating fuel part

nou : Upper non-heating fuel part

1: Heated single-phase liquid region

2: Heated two-phase mixture region

Acronyms

ABWR: Advanced Boiling Water Reactor

ATWS: Anticipated Transient Without Scram

BOC: Beginning of Cycle

BOP: Balance of Plant

BWR: Boiling Water Reactor

CST: Cross Shape Twisted

DR: Decay Ratio

DWO: Density Wave Oscillations

EOC: End of Cycle

EPRI: Electric Power Research Institute

ESBWR: Economical Simplified Boiling Water Reactor

FISTAB: code for Flashing Induced Stability Analysis of BWR

GE: General Electric

HEM: Homogenous Equilibrium model

IAEA: International Atomic Energy Agency

LASP: Large Assembly with Small Pins

NCBWR: Natural Circulation Boiling Water Reactor

NHEM: Non-Homogenous Equilibrium model

NF: Natural Frquency

NK: Neutron Kinetics

NPP: Nuclear Power Plant

NRC: Nuclear Regulatory Commission

PCMI: Pellet-Cladding Mechanical Interaction

RBWR: Resource-renewable Boiling Water Reactor

STAB: code for Stability Analysis of BWR

TH: Thermal-Hydraulics

TRU: Transuranics

Appendixes

Contents

Appendixes 291
A. Supplementary Model Descriptions in FISTAB Code 292
A.1 General Drift Flux Model 292
A.2 Vapor Generation Model due to Flashing 293
A.3 Chen's Correlation 295
References of Appendix A 297
B. A Global Newton Method to Solve the Characteristic Equation in Frequency Domain Linear Stability Analysis 298
B.1. Introduction 298
B.2. System Characteristic Equation 298
B.3. Review of Root-finding algorithms 299
B.4 The Global Newton Method for the Characteristic Equation 302
B.5 Results and Discussions 306
B.5.1. Real algebraic equations 307
B.5.2. Complex algebraic equation 307
B.5.3. System Characteristic Equation in linear stability analysis 308
B.5.4. Addressing the drawbacks of the Newton Method 309
B.6 Summary 311
References for Appendix B 312
C. Peach Bottom 2 Low Flow Stability Test Benchmark with STAB code 313
C.1 Brief Description of the PB2-LFST 313
C.2 Discussion of Results 315
References for Appendix C 318
D. Neutronic Model Description 319
D.1 Neutronic equations 319
D.2 Lamda modes expansion method 320
D.3 Neutroinc feedback 323
References for Appendix D 324
E. Decay Ratio Evaluation Methods for Stability Analysis in the Time Domain 325
References for Appendix E 329
F. The Semi-Implicit Scheme and Numerical Dissipation 330
References for Appendix F 331

A. Supplementary Model Descriptions

A.1 General Drift Flux Model

The drift flux model is to compute the void fraction distribution at a plane and the slip in two-phase flow needed to obtain the relative velocity between the phases, originally developed by Zuber and Findlay [Zuber and Findlay, 1965]. The description of the general drift-flux model can be also found in [Todreas and Kazimi, 1990].

In the drift-flux model, the local vapor velocity is defined as the sum of the two-phase local volumetric velocity (j) and the local drift velocity of the vapor (V_{gj}).

$$u_g = j + V_{gj} \tag{A-1}$$

Hence,

$$j_g = \alpha u_g = \alpha j + \alpha(u_g - j) \tag{A-2}$$

Then, the void fraction α can be obtained as a function of the total and vapor superficial velocities, j and j_g, a phase distribution parameter C_0 and a drift velocity V_{gj}. The C_0 represents the global effect due to radial non-uniform void and velocity profiles, and V_{gj} represents the local relative velocity effect between the phases.

$$\alpha = \frac{j_g}{C_o j + V_{gj}}. \tag{A-3}$$

The void fraction may be also predicted from the drift flux model based on the flow quality, as:

$$\alpha = \frac{x}{C_o\left(x\frac{\rho_{fg}}{\rho_f} + \frac{\rho_g}{\rho_f}\right) + \frac{\rho_g V_{gj}}{G_m}}. \tag{A-4}$$

And the phase slip can be obtained as:

$$S = C_o + \frac{(C_o - 1)x\rho_f}{(1-x)\rho_g} + \frac{\rho_f V_{gj}}{(1-x)G_m} \tag{A-5}$$

Other useful relationships among the phase velocities (u_f, u_g), superficial velocities (j_f, j_g, j), and mixture velocity (u_m) include:

$$u_g = u_m + \frac{\rho_f}{\rho_m} V_{gj} \tag{A-6}$$

$$u_f = u_m - \frac{\alpha\rho_g}{(1-\alpha)\rho_m} V_{gj} \tag{A-7}$$

$$j_g = \alpha u_g = \alpha(u_m + \frac{\rho_f}{\rho_m} V_{gj}) \tag{A-8}$$

$$j_f = (1-\alpha)u_f = (1-\alpha)u_m - \frac{\alpha\rho_g}{\rho_m} V_{gj} \tag{A-9}$$

$$u_m = j - (\frac{\rho_f}{\rho_m} - 1)V_{gj} \tag{A-10}$$

In which,

$$u_m = \frac{G_m}{\rho_m} \tag{A-11}$$

$$\rho_m = (1-\alpha)\rho_f + \alpha\rho_g \tag{A-12}$$

Various drift-flux correlations are available in the literature, with different procedures to compute C_0 and the drift velocity V_{gj}.

A.2 Vapor Generation Model due to Flashing

Considering the flashing effects, the vapor generation rate Γ_{tot} in two-phase saturation region could be derived from the mixture mass conservation equation, liquid/vapor phase mass conservation equation, and mixture energy conservation equation [Todreas and Kazimi, 1990], as:

Mixture mass conservation equation:

$$\frac{\partial((1-\alpha)\rho_f + \alpha\rho_g)}{\partial t} + \frac{\partial}{\partial z}((1-\alpha)\rho_f u_f + \alpha\rho_g u_g) = 0 \quad \textbf{(A-13)}$$

Liquid phase mass conservation equation:

$$\frac{\partial((1-\alpha)\rho_f)}{\partial t} + \frac{\partial((1-\alpha)\rho_f u_f)}{\partial z} = -\Gamma_{tot} \quad \textbf{(A-14)}$$

Mixture energy conservation equation:

$$\frac{\partial}{\partial t}(\rho_m h_m - p) + \frac{\partial}{\partial z}(G_m h_m^+) = u_m \frac{\partial p}{\partial z} + \frac{P_h}{A_c} q''(z,t) \quad \textbf{(A-15)}$$

In which,

$$h_m = \frac{(1-\alpha)\rho_f h_f + \alpha\rho_g h_g}{\rho_m} \quad \textbf{(A-16)}$$

$$h_m^+ = \frac{(1-\alpha)\rho_f u_f h_f + \alpha\rho_g u_g h_g}{G_m} \quad \textbf{(A-17)}$$

Combining Eq. (A-15), (A-16), and (A-17), and neglecting the pressure work term, $\frac{u_m}{h_{fg}}\frac{\partial p}{\partial z}$, we obtain:

$$\frac{\partial}{\partial t}((1-\alpha)\rho_f h_f + \alpha\rho_g h_g) + \frac{\partial}{\partial z}((1-\alpha)\rho_f u_f h_f + \alpha\rho_g u_g h_g) = \frac{\partial p}{\partial t} + \frac{P_h}{A_c} q''(z,t) \quad \textbf{(A-18)}$$

Multiplying h_g to Eq. (A-13), we obtain,

$$(h_f + h_{fg})\left(\frac{\partial((1-\alpha)\rho_f)}{\partial t} + \frac{\partial}{\partial z}((1-\alpha)\rho_f u_f)\right) + h_g\left(\frac{\partial(\alpha\rho_g)}{\partial t} + \frac{\partial}{\partial z}(\alpha\rho_g u_g)\right) = 0 \quad \textbf{(A-19)}$$

Subtracting the liquid mass conservation Eq. (A-14) from Eq. (A-19), we obtain,

$$h_f\left(\frac{\partial((1-\alpha)\rho_f)}{\partial t} + \frac{\partial}{\partial z}((1-\alpha)\rho_f u_f)\right) + h_g\left(\frac{\partial(\alpha\rho_g)}{\partial t} + \frac{\partial}{\partial z}(\alpha\rho_g u_g)\right) = \Gamma_{tot} h_{fg} \quad \textbf{(A-20)}$$

Then, subtracting Eq. (A-20) from Eq. (A-18), we have

$$(1-\alpha)\rho_f \frac{\partial h_f}{\partial t} + \alpha\rho_g \frac{\partial h_g}{\partial t} + (1-\alpha)\rho_f u_f \frac{\partial h_f}{\partial z} + \alpha\rho_g u_g \frac{\partial h_g}{\partial z} = \frac{\partial p}{\partial t} + \frac{q'' P_h}{A_c} - \Gamma_{tot} h_{fg} \quad \textbf{(A-21)}$$

Set, $\frac{\partial h_f}{\partial t} = \frac{\partial h_f}{\partial p}\frac{\partial p}{\partial t} = h'_f \frac{\partial p}{\partial t}$, $\frac{\partial h_g}{\partial t} = h'_g \frac{\partial p}{\partial t}$, $\frac{\partial h_f}{\partial z} = h'_f \frac{\partial p}{\partial z}$, $\frac{\partial h_g}{\partial z} = h'_g \frac{\partial p}{\partial z}$,

Eq. (A-21) can be written as:

$$\Gamma_{tot} = \frac{q''_w P_h}{A_c h_{fg}} + \frac{1}{h_{fg}}\left(\frac{\partial p}{\partial t}(1-\alpha\rho_g h'_g - (1-\alpha)\rho_f h'_f) - \frac{\partial p}{\partial z}(\rho_g j_g h'_g + \rho_f j_f h'_f)\right) \quad \textbf{(A-22)}$$

Therefore, it is shown in Eq. (A-22) that the total vapor generation rate Γ_{tot} has contributions from both heating, Γ_{heat}, and from flashing, Γ_{flash}:

$$\Gamma_{heat} = \frac{q''_w P_h}{A_c h_{fg}} \quad \textbf{(A-23)}$$

$$\Gamma_{flash} = \frac{1}{h_{fg}}\left(\frac{\partial p}{\partial t}(1-\alpha\rho_g h'_g - (1-\alpha)\rho_f h'_f) - \frac{\partial p}{\partial z}(\rho_g j_g h'_g + \rho_f j_f h'_f)\right) \quad \textbf{(A-24)}$$

A.3 Chen's Correlation

The two-phase flow heat transfer coefficient for saturation boiling is defined as:

$$h = h_{NB} + h_c \quad \textbf{(A-25)}$$

where h_{NB} is related to nucleate boiling and h_c is due to convection heat transfer.

In the widely used Chen's correlation [Todreas and Kazimi], the convective term is expressed in the form of a modified Dittus-Bolter correlation, as shown in Eq. (A-26):

$$h_C = 0.023\left[\frac{G(1-x)D_e}{\mu_f}\right]^{0.8}\left[\frac{\mu Cp}{k}\right]_f^{0.4}\left(\frac{k_f}{D_e}\right)F \quad \textbf{(A-26)}$$

And the nucleation part is based on the Forster-Zuber correlation, in the form of:

$$h_{NCB} = 0.00122\left[\frac{k_f^{0.79} C_{pf}^{0.45} \rho_f^{0.49}}{\sigma^{0.5} \mu_f^{0.29} h_{fg}^{0.24} \rho_g^{0.24}}\right] \Delta T_{sat}^{0.24} \Delta P_{sat}^{0.75} S \qquad \textbf{(A-27)}$$

The factors F and S are fitted as follows:

$$F = \begin{cases} 1.0 & X_{tt}^{-1} \le 0.10 \\ 2.35(X_{tt}^{-1} + 0.213)^{0.736} & X_{tt}^{-1} > 0.10 \end{cases} \qquad \textbf{(A-28)}$$

$$S = \frac{1}{1 + 2.53 \times 10^{-6} \,\mathrm{Re}^{1.17}} \qquad \textbf{(A-29)}$$

Where, $\mathrm{Re} = \mathrm{Re}_f F^{1.25}$ and X_{tt} is the Lockhart-Martinelli parameter:

$$\frac{1}{X_{tt}} = \left(\frac{x}{1-x}\right)^{0.9} \left(\frac{\rho_f}{\rho_g}\right)^{0.5} \left(\frac{\mu_g}{\mu_f}\right)^{0.1}. \qquad \textbf{(A-30)}$$

A.4 CISE-4 Correlation

The CISE-4 correlation is widely used to estimate the critical power in high quality water flow. It is based on the quality-boiling length concept and was optimized in the flow range of 1000<G<4000kg/m^2 s.

The correlation is expressed by the following equations:

$$x_{cr} = \frac{D_e}{D_h}\left(a \frac{L_{cr}}{L_{cr} + b}\right) \qquad \textbf{(A-31)}$$

Where $a = \dfrac{1}{1 + 1.481 \times 10^{-4} (1 - p/p_{cr})^{-3} G}$, if $G \le G^*$

and $a = \dfrac{(1 - p/p_{cr})}{(G/1000)^{1/3}}$, if $G \ge G^*$

where $G^* = 3375(1 - p/p_{cr})^3$; p_{cr}=critical pressure (MPa); L_{cr} = boiling length to CHF (m); and:

$$b = 0.199(p_{cr}/p - 1)^{0.4} G D^{1.4}$$

Where G is in kg/m^{2}s and D is in meters (m).

References of Appendix A

Todreas, N. E., and Kazimi, M. S., "Nuclear System I, Thermal Hydraulic Fundamentals," Hemisphere Publishing Corporation, 1990.

Zuber, N., and Findlay, J. A., "Average Volumetric Concentration in Two-Phase Flow Systems", *Journal of Heat Transfer*, Vol. 87, pp. 453-468, 1965.

B. A Global Newton Method to Solve the Characteristic Equation in Frequency Domain Linear Stability Analysis

B.1. Introduction

In frequency domain stability analysis methods, such as STAB and FISTAB, the system stability performance is characterized by the decay ratio (DR), which is solved from the dominant root of the characteristic equation. The dominant root of the characteristic equation is the crucial indicator of the system stability behavior. Thus, it is very important to find the accurate dominant roots from the system characteristic equation, which is usually a very high order algebraic equation (on the order of N, where N is the total node numbers for steady-state finite difference schemes).

The objective of this part of the present work is to find an effective scheme to solve the system characteristic equation. The character of the equation is first discussed. After a review of the general root solving algorithms, a global Newton method is suggested. Then, the matrix form algorithms of the Newton-Raphson method and the proposed global Newton method are described and implemented in MATLAB. Finally, the global Newton method is examined by some simple equations and the actual system characteristic equation. It is demonstrated that the improved Newton method satisfies the goal of rapid convergence and is globally convergent.

B.2. System Characteristic Equation

As described in Chapter 3, the characteristic equation is just the transfer function between the inlet flow oscillation and the total pressure drop oscillation across the channel. It is then worthwhile to discuss the perturbation equation to understand the character of the system characteristic equation. As discussed in Chapter 3 and indicated in Figure B.1, the perturbation equations are solved numerically along the axial computational nodes.

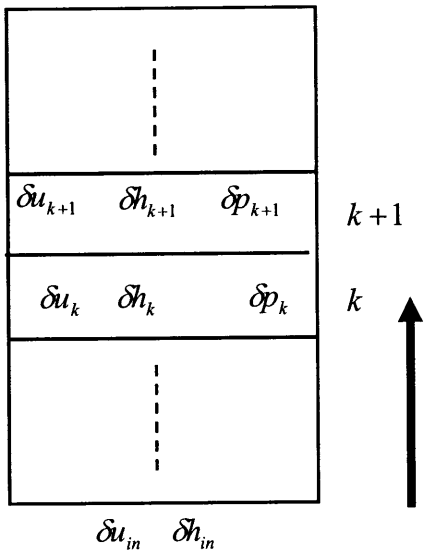

Figure B.1: Transient channel perturbation calculation by marching up the nodes

For each axial node k, the coolant perturbation equations could be expressed in the matrix form:

$$sE_k \delta X_k = A_k \delta X_k + B_k \delta X_{k-1} + C_k \delta q''_{k-1} + D_k \qquad \textbf{(B-1)}$$

Where s is the Laplace transformation variable; δX_k is the vector representing the enthalpy, pressure, and velocity perturbations in the node k and is defined as

$$\delta X_k(t) = [\delta h_k(t), \delta P_k(t), \delta u_k(t)]^T \qquad \textbf{(B-2)}$$

A_k, B_k, C_k, D_k, and E_k are the coefficient matrices, and can be calculated from the steady state parameters for coolant channel nodes.

So, for the transfer function between the inlet flow oscillation and the total pressure drop oscillation $\Pi(s)$, it is a very complex non-linear function with the order of total nodes number N_{totoal} in the numerical form.

B.3. Review of Root-finding algorithms

To find an effective numerical scheme to solve the characteristic equation, it is necessary to review the general root-finding algorithms.

As studied in numerical analysis, root-finding algorithms perform best when they take advantage of known characteristics of the given function. Thus, an algorithm to find isolated real roots of a low-degree polynomial in one variable may bear little resemblance to an algorithm for complex roots of a "black-box" function which is not even known to be differentiable. The performance of a root-finding algorithm includes the ability to separate close roots, robustness in achieving reliable answers despite inevitable numerical errors, and the rate of convergence.

The simplest root-finding algorithm is the bisection method. It works when f is a continuous function and it requires previous knowledge of two initial guesses, a and b, such that $f(a)$ and $f(b)$ have opposite signs. Although it is reliable, it converges slowly, adding one good bit with each iteration.

Newton-Raphson method is widely used if the function f to have a continuous derivative. Newton's method may not converge if one starts too far away from a root. However, if it does converge, it is faster than the bisection method. Convergence is usually quadratic, so the number of good bits doubles with each iteration. Newton's method is also important because it readily generalizes to higher-dimensional problems, in which the Jacobian matrix and the LU decomposition may be required.

Broyden's method is a quasi-Newton method for the numerical solution of nonlinear equations in more than one variable. Newton's method for solving the equation $f(x) = 0$ uses the Jacobian J at every iteration. However, computing this Jacobian may be a difficult and expensive operation. The idea behind Broyden's method is to compute the whole Jacobian only at the first iteration, and to do a rank-one update at the other iterations. Other variation of Newton's methods include chord method and Shamaskii method, both have the advantages in saving the LU decomposition in the process of Newton's method.

Replacing the derivative in Newton's method with a finite difference yields the secant method. This method does not require the computation (nor the existence) of a derivative, but the price is a slower convergence (the order is approximately 1.6).

The false position method is like the secant method. However, instead of retaining the last two points, it makes sure to keep one point on either side of the root. The false position method is faster than the bisection method and more robust than the secant method.

The secant method also arises if one approximates the unknown function f by linear interpolation. When quadratic interpolation is used instead, one arrives at Müller's method. It converges faster than the secant method. A particular feature of this method is that the iterates x_n may become complex. This can be avoided by interpolating the inverse of f, resulting in the inverse quadratic interpolation method. Again, convergence is asymptotically faster than the secant method, but inverse quadratic interpolation often behaves poorly when the iterates are not close to the root.

Finally, Brent's method is a combination of the bisection method, the secant method and inverse quadratic interpolation. At every iteration, Brent's method decides which method out of these three is likely to do best, and proceeds by doing a step according to that method. This gives a robust and fast method, which therefore enjoys considerable popularity. Actually, the embedded MATLAB function *"fzero"* applies the Brent's method to solve the non-linear equation with a single variable.

As the objective equation in our analysis is an equation in the complex domain, the methods required to know the signs of the function are not suitable, as the bisection method, false position, and the Brent's method. The variations of Newton's method, chord/Shamaskii/Broyden, are not necessary as the calculation of the Jacobian matrix and the LU decomposition are not a burden for 2×2 matrices. So, an improved Newton-Raphson, with the property of globally convergent and fast convergence, is very desirable, as the one suggested in the next section.

B.4 The Global Newton Method for the Characteristic Equation

The system characteristic equation described in Section B.2 can be represented by a nonlinear equation in complex domain as:

$$F(s) = X(s) + iY(s) = 0 \tag{B-3}$$

where $s = \sigma + j\omega$.

This equation can be solved using the Newton-Raphson method, which derives from the Taylor series expansion of a function in the neighborhood of the present point,

$$F(s + \delta s) = F(s) + F'(s)\, s\, \delta s + \frac{1}{2} F''(s)\delta s^2 + \cdots. \tag{B-4}$$

For small enough values of δs, and for well-behaved functions, the terms beyond linear are unimportant, hence $F(s + \delta s) = 0$ implies:

$$\delta s = -\frac{F(s)}{F'(s)} \tag{B-5}$$

By evaluating this Newton step at a trial solution s_i, the next trial solution is determined as:

$$s_{i+1} = s_i + \delta s_i \tag{B-6}$$

until this change becomes negligible.

Since an analytic function satisfies the Cauchy-Riemann equation, the derivative $F'(s)$ is given by:

$$F'(s) = \frac{\partial X}{\partial \sigma} + i\frac{\partial Y}{\partial \sigma} = \frac{\partial Y}{\partial \omega} - i\frac{\partial X}{\partial \omega} \tag{B-7}$$

Thus, the Newton step is explicitly determined only with the derivatives with respect to the frequency as:

$$\delta s = \delta\sigma + i\delta\omega \tag{B-8}$$

where

$$\delta\sigma = -\frac{1}{|F'(s)|^2}\left(\frac{\partial Y}{\partial \omega}X - \frac{\partial X}{\partial \omega}Y\right) \tag{B-9}$$

$$\delta\omega = -\frac{1}{|F'(s)|^2}\left(\frac{\partial X}{\partial \omega}X - \frac{\partial Y}{\partial \omega}Y\right) \tag{B-10}$$

$$|F'(s)|^2 = \left(\frac{\partial X}{\partial \omega}\right)^2 + \left(\frac{\partial Y}{\partial \omega}\right)^2 \tag{B-11}$$

When a trial solution s_i differs from the true root s by ϵ_i. The deviation of the trial solution can be determined as:

$$\varepsilon_{i+1} = s_{i+1} - s = s_i + \delta s_i - s = \varepsilon_i - \frac{F(s)}{F'(s)} = -\frac{\varepsilon_i^2}{2}\frac{F''(s)}{F'(s)} \quad \textbf{(B-12)}$$

This shows that the Newton-Raphson method converges quadratically near a root, and hence the number of significant digits approximately doubles with each step.

The general procedures of Newton-Raphson method could be expressed as [Heinkenschloss 2008]:

Input: Function F, Initial valuex_0,
tolerance *tol*, maximum number of iterations *maxit*

Output: approximation of the root
For $k = 0, \cdots, maxit$ do
Compute $F'(x_k)s_k = F(x_k)$. (LU-decomposition)
Compute $x_{k+1} = x_k + s_k$
Check for truncation/ tolerance
End

However, as discussed in Section B.3, far from a root where the higher order terms are important, the Newton-Raphson method can give grossly inaccurate, meaningless corrections. For instance, the initial guess for the root might be so far from the true root that it allows the search interval to include a local maximum or minimum of the function. If iteration places a trial guess near such a local extreme, so that the first derivative nearly vanishes, then Newton-Raphson sends its solution off to a limbo, with vanishingly small hope of recovery. In other words, its global convergence property is poor, and hence it often diverges if the initial guess is not sufficiently close to the root. Therefore, it is desirable to combine the rapid local convergence of Newton's method with a globally convergent strategy that will guarantee some progress towards the solution at each iteration step.

The characteristic equation given in Eq. (B-3) is equivalent to the equation $|F(s)| = 0$. However, when the old point s_i is not close enough to the root, taking the full Newton step δs_i may not results in the new point s_{i+1} with reduced $|F|$ and being closer to the root. Therefore, in order to guarantee some progress towards the solution at each iteration step, the new step is determined such that it decreases$|F|$. This is the same requirement we would impose if we were trying to minimize the function:

$$f(s) = \frac{1}{2}|F(s)|^2 \tag{B-13}$$

Every solution to Eq. (B-3) minimizes Eq. (B-13), but there may be local minima of Eq. (B-13) that are not solutions to Eq. (B-3).

Representing the complex variable s and the characteristic function $F(s)$ as two dimensional vectors as:

$$s = (\sigma, \omega)^T \tag{B-14}$$
$$F(s) = [X(s), Y(s)]^T \tag{B-15}$$

The Newton step for this set of equations is given by:

$$\delta s = (\delta\sigma, \delta\omega)^T = -J^{-1} \cdot F \tag{B-16}$$

Here J is the Jacobian matrix:

$$J = \begin{bmatrix} \frac{\partial X}{\partial \sigma} & \frac{\partial X}{\partial \omega} \\ \frac{\partial Y}{\partial \sigma} & \frac{\partial Y}{\partial \omega} \end{bmatrix} = \begin{bmatrix} \frac{\partial Y}{\partial \omega} & -\frac{\partial X}{\partial \omega} \\ \frac{\partial X}{\partial \omega} & \frac{\partial Y}{\partial \omega} \end{bmatrix} \tag{B-17}$$

In this representation, the function $f(s)$ defined in Eq. (B-13) is given by:

$$f(s) = \frac{1}{2} F \cdot F \tag{B-18}$$

A global method, some variations from that in [Yang, 2005], can be developed to minimize $f(s)$ along the Newton direction δs in Eq. (B-16) by taking Newton steps designed to bring F to zero. To utilize the quadratic convergence of Newton method near the root, the full Newton step is first tried. However, it is checked at each iteration that the proposed step reduces f. If not, the Newton direction is backtracked until an

acceptable step is found. In other words, a new point along the Newton direction δs is determined as:

$$s_{i+1} = s_i + \lambda \delta s_i, 0 < \lambda \leq 1 \tag{B-19}$$

by finding λ so that $F(s_{i+1})$ has decreased sufficiently. It is guaranteed to find an acceptable step by backtracking, since the Newton step is a descent direction for f.

$$df = \nabla f \cdot \delta s = (F \cdot J) \cdot (-J^{-1} \cdot F) = -F \cdot F < 0 \tag{B-20}$$

The parameter λ can be determined such that it exactly minimizes f in the direction δs. However, it is extremely wasteful of function evaluation. A better strategy is obtained by requiring the average rate of decrease of f to be at least some fraction, α, of the initial rate of decrease $\nabla f \cdot \delta s$:

$$f(s_{i+1}) \leq f(s_i) + \alpha \nabla f \cdot (s_{i+1} - s_i) \tag{B-21}$$

and by requiring the rate of decrease of f at s_{i+1} to be greater than some fraction of the rate of decrease of f at s_i.

By defining a function $g(\lambda)$:

$$g(\lambda) = f(s + \lambda \delta s) \tag{B-22}$$

so that

$$g'(\lambda) = \nabla f \cdot \delta s \tag{B-23}$$

A practical backtracking algorithm is derived as follows:

(1) The first step is always the Newton step, $\lambda = 1$.

(2) If this step is not acceptable, $g(\lambda)$ is approximated by a quadratic polynomial. Using available values $g(0) = F(s_i), g'(0) = \nabla f(s_i) * \delta s_i < 0$, and $g(1) = F(s_{i+1})$, $g(\lambda)$ is approximated as:

$$g(\lambda) = [g(1) - g(0) - g'(0)]\lambda^2 + g'(0)\lambda + g(0) \tag{B-24}$$

(3) λ is determined by minimizing this quadratic form:

$$\lambda = -\frac{g'(0)}{2[g(1)-g(0)-g'(0)]} \tag{B-25}$$

Since the Newton step failed, $g(1) > g(0) + \alpha g'(0)$ and hence $\lambda < \frac{1}{2(1-\alpha)}$. However, we need to guard against too small a value of λ to avoid taking steps that are too small. Set $\lambda_{min} = 0.1$.

(4) Set $s_{i+1} = s_i + \lambda \delta s_i$. If $f(s_{i+1}) > f(s_i)$, a second backtracks of Newton iteration may be required, go to step (2); Else, go to step (1).

The procedure of the global Newton method is schematically shown on Figure B-2:

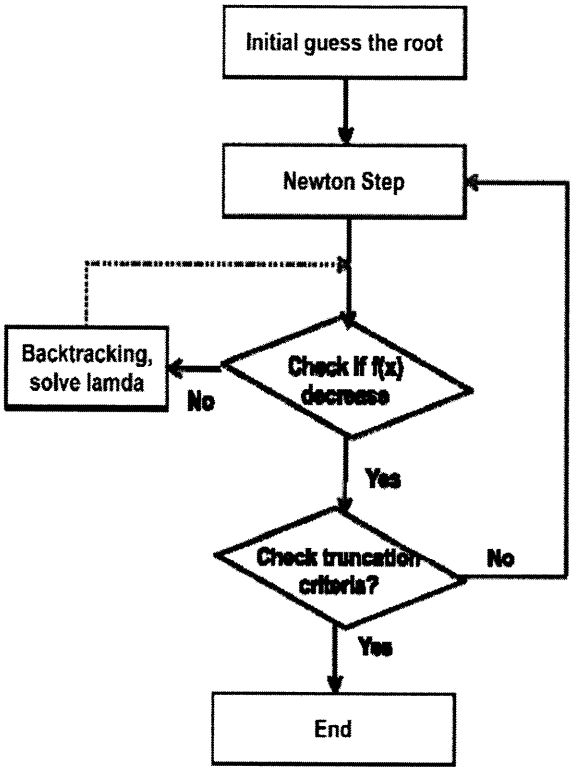

Figure B.2: The scheme of the global Newton method

B.5 Results and Discussions

The proposed global Newton method is implemented in FISTAB in the MATLAB platform, modified from the regular Newton-Raphson solver in [Kelley C. T., 2003]. The global Newton solver is tested on sample equations to verify its global convergence and the convergent speed.

B.5.1. Real algebraic equations

For the algebraic equation $f(x) = (x+2)(x+3)(x+4)(x+5) = 0$, the roots are $x = -2, -3, -4, -5$. The equation is also solved numerically by the implemented MATLAB code of the global Newton's method, the iteration steps of the $x_k, f(x_k)$, and s_k are listed in the Table B-1.

Table B-1: Output of iteration steps, real algebraic equation

k	x_k	$f(x_k)$	s_k
0	-2.3	0.9639	1.0569
1	-1.2431	13.7735	0.1057
1'	-2.1943	0.7931	0.3339
2	-1.8604	1.0684	0.0334
2'	-2.1609	0.705	0.2423
3	-1.9186	0.5647	-0.0714
4	-1.9899	0.0614	-0.0099
5	-1.9998	0.0011	-0.0002
6	-2	0	0

It is shown in the above table that the Newton-Raphson step does not converge (reduce the value of $|f(x)|$ at step 1 and step 2. However, with the backtracking along the Newton step (with the prime), the value of $|f(x)|$ is reduced, and the scheme of the global Newton method converges to the right root of $x = -2$.

B.5.2. Complex algebraic equation

Also, for the algebraic equation in complex domain, such as:
$f(x) = (x+2)(x+3)(x+4)(x+5)(x+i)(x-i) = 0$, the roots are $x = -2, -3, -4, -5, \pm i$. The equation is also solved numerically by the global Newton's method, the iteration steps of the $x_k, \|f(x_k)\|$, and s_k are listed in the Table B-2.

It is again shown that the normal Newton step does not converge at step 3 and step 4, but the global Newton method converges to the right roots of $x = -2$, with the backtracking along the Newton step.

Table B-2: Output of iteration steps, complex algebraic equation

k	x_k	$\|f(x_k)\|$	s_k
0	-2.4000 + 1.0000i	49.4983	-0.0442 - 0.4477i
1	-2.4442 + 0.5523i	17.2483	-0.0479 - 0.4120i
2	-2.4920 + 0.1403i	7.4106	-0.2200 - 0.8075i
3	-2.7121 - 0.6671i	21.3189	0.0723 - 0.1262i
3'	-2.4197 + 0.0141i	6.8142	2.5331 - 0.9799i
4	0.1134 - 0.9657i	38.8324	0.2533 - 0.0980i
4'	-2.1664 - 0.0838i	4.6283	0.1851 + 0.1382i
5	-1.9813 + 0.0543i	1.7613	-0.0210 - 0.0520i
6	-2.0023 + 0.0023i	0.0969	0.0023 - 0.0023i
7	-2.0000 - 0.0000i	0.0003	0.0000 + 0.0000i
8	-2.0000 + 0.0000i	0	0

B.5.3. System Characteristic Equation in linear stability analysis

The actual system characteristic equation in the linear stability analysis is also solved by the proposed global Newton method, with the initial guess of $x_0 = [-0.3\ 0.3]^T$. The iteration steps of the $\|x_k\|$, $\|f(x_k)\|$, and $\|s_k\|$ are listed in the Table B-3, which again demonstrate the convergence improvement in the step 1, 2, 3, and 4 by proposed global Newton method.

Table B-3: Output of iteration steps, system characteristic equation

k	$\|\|x_k\|\|$	$\|\|f(x_k)\|\|$	$\|\|s_k\|\|$
0	0.42	5428786	35.42
1	35.82	2.97E+12	3.54
1'	3.95	4472797	10.83
2	7.08	16555886	1.49
2'	2.59	4001454	14.23
3	13.66	39326356	1.42
3'	2.54	3558133	8.23
4	10.41	3747123	0.82
4'	3.25	3129612	5.13
5	8.17	1894099	1.84
6	6.37	180449.4	0.16
7	6.46	780.54	0
8	6.46	0.02	0

From all the three test equations, the proposed global Newton method shows very good convergence. Also, the convergence speed is very fast, on the same order of Newton-Raphson method. The convergence speed of the global Newton method is obviously assured, since it is in essence a regular Newton-Raphson method with possible backtracking at each step.

B.5.4. Addressing the drawbacks of the Newton Method

It is well known that the Newton's method does not work well under the condition of multi-roots, zero derivatives, etc. Therefore, it is necessary to address those drawbacks with the proposed global Newton method.

(1) Inflection point

For function $f(x)=(x-1)^3=0$, with initial guess value of $x_0=-1$ and iteration stop criteria $\epsilon = 10^{-6}$, the iteration steps are listed in Table B-4, and the figure below.

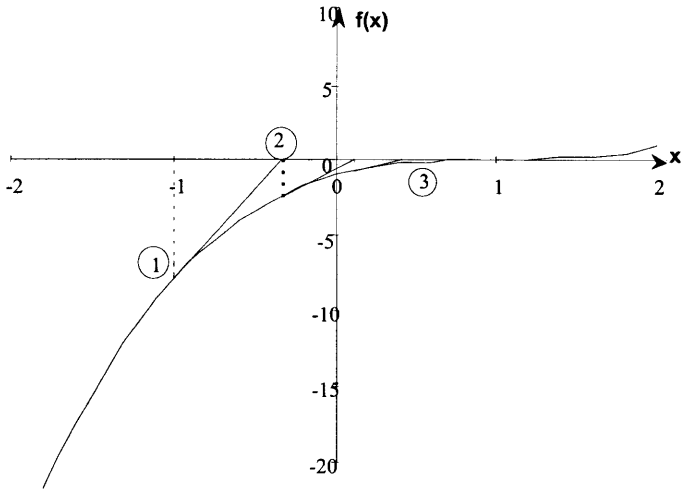

Table B-4: Output of iteration steps, inflection point

k	x_k	$f(x_k)$	s_k
0	-1	8	0
1	-0.3333	2.37E+00	0.6667
2	0.1111	0.7023	0.4444
3	0.4074	0.2081	0.2963
4	0.6049	0.0617	0.1975
5	0.7366	0.0183	0.1317
6	0.8244	0.0054	0.0878
7	0.8829	0.0016	0.0585
8	0.922	0.0005	0.039
9	0.948	0.0001	0.026
10	0.9653	0	0.0173
11	0.9769	0	0.0116
12	0.9846	0	0.0077

(2) Division by zero

For function $f(x)= x^3 - 0.03x^2 + 2.4\text{x}10^{-6} = 0$, with initial guess value of $x_0 = 0.0201$, the iteration steps are listed in Table B-5, and the figure below.

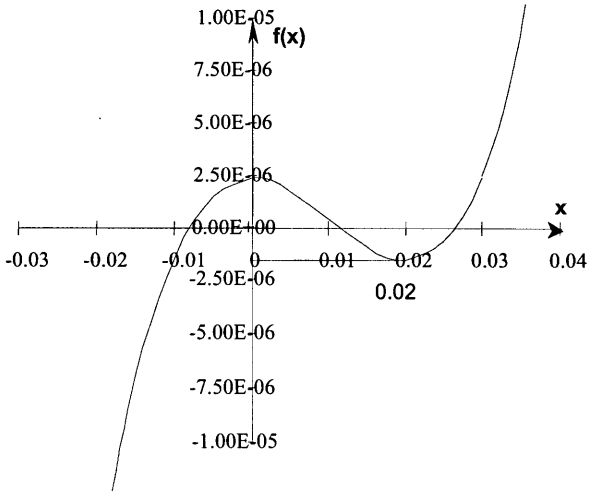

Table B-5: Output of iteration steps, division by zero

k	x_k	$f(x_k)$	s_k
0	0.0201	0	0
1	0.2854	0.0208	0.2653
1′	0.0466	0.0000385	0.0265
2	0.0363	0.0000106	-0.0104
3	0.0303	0.0000026	-0.006
4	0.0274	0.0000004	-0.0028
5	0.0267	0.00000003	-0.0008
6	0.0266	0	-0.0001
7	0.0266	0	0

(3) Root Jumping

For function $f(x)=\sin(x)$, with initial guess value of $x_0 = 7.54$, the iteration steps are listed in Table B-6. The iteration steps of Newton-Raphson method is shown in the figure at the left.

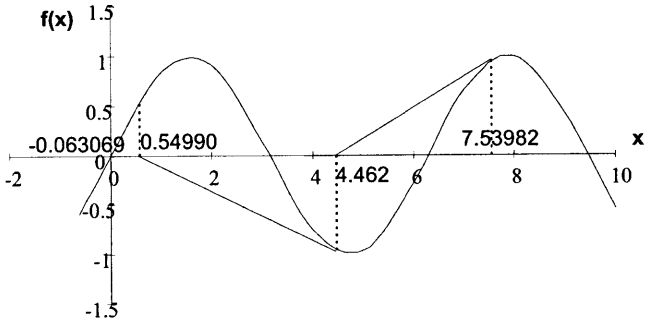

Table B-6: Output of iteration steps, root jumping

k	x_k	$f(x_k)$	s_k
0	7.54	0.9511	0
1	4.4605	0.9684	-3.0795
1′	7.232	0.8128	-0.308
2	5.837	0.4315	-1.395
3	6.3154	0.0322	0.4783
4	6.2832	0	-0.0322
5	6.2832	0	0

For all the above equations, the global Newton method would converge to one root of the equation, showing good global convergence. However, in the case of inflection point, the global Newton method follows Newton-Raphson method at every step, and it did not improve the convergence speed; also the final solution , $x = 0.9846$, is a little far from the actual root $x = 1$ under the stop criteria of $\epsilon_{abs} = 10^{-6}$ and $\epsilon_{relative} = 10^{-6}$.

Nonetheless, the problems of root jumping and dividing by zero derivatives are improved by the global Newton method, as shown in the backtracking at step $1'$ in both Tables B-5 and B-6.

B.6 Summary

Numerous methods exist in literature to solve various types of non-linear equations. The numerical root-finding algorithms perform best when they take advantage of known characteristics of the given function. To assure good convergence, a global Newton method is proposed and implemented to solve the characteristic equation, which is a very high order nonlinear equation in the complex domain, in the frequency domain linear stability analysis code FISTAB. The proposed method is in essence a Newton-Raphson

method with backtracking to guarantee some progress towards the solution at each iteration step.

The tests of some example equations and the actual characteristic equation demonstrate both good global convergence and fast convergent speed of the new method. Some drawbacks of Newton's method were also addressed with the proposed global Newton method. The proposed method improved the performance for the problems of zero derivatives and root jumping, but did not improve the performance around the inflection points.

References for Appendix B

Heinkenschloss M., Numerical Solution of Nonlinear Equations, CAAM353 Computational Numerical Analysis Course Materials, Rice University, Spring 2008.

Kelley C. T., "Solving Nonlinear Equations with Newton's Method", Society for Industrial and Applied Mathematics, 2003.

Yang W.S., Initial Implementation of Multi-Channel Thermal-Hydraulic Capability to Frequency Domain SCWR Stability Analysis Code SCWRSA, ANL-GENIV-056, September 2005.

C. Peach Bottom 2 Low Flow Stability Test Benchmark with STAB code

Zhao et al. [2005] applied the STAB (originally called SAB) code to the Low Flow Stability Test (LFST) at Peach Bottom 2 (BWR/4) NPP. However, the code has been updated significantly since then. It is necessary to evaluate the reliability of the updated STAB code for BWR stability analysis. Thus, the updated STAB code is benchmarked against the Peach Bottom 2 Low Flow Stability Test in this work.

Major modifications for the original STAB code include:

1) Changing the axial power shape from uniform to non-uniform;
2) Grids (lower/upper tie-plates and spacers) are included in the analysis.
3) Adding the capability of calculating the flow distribution in the lumping channels (with different power peaking factor) in the code;
4) Including the effect of the mixing of the bypass flow and the active coolant flow above the core;
5) Changing the treatment of equations in the non-heated region, from analytic integration to numerical integration;

C.1 Brief Description of the PB2-LFST

Four series of Low-Flow Stability Tests (PT1, PT2, PT3 and PT4) have been performed at Peach Bottom Unit 2 in 1977 at the end of cycle 2 (EOC-2) by using a pressure perturbation technique. The LFST were intended to measure the reactor core stability margins at the limiting conditions used in design and safety analyses. Four test conditions for the stability tests were planned to be as close as possible to one of the following reactor operating conditions, as shown in Figure C.1.

(1) Points along the rated power-flow control line (PT1 and PT2);
(2) Points along the natural circulation power-flow control line (PT2, PT3 and PT4). However, the minimum core flow that could be achieved at test conditions PT2,

PT3, and PT4 was limited to that corresponding to about 20% of rated recirculation pump speed, rather than natural circulation core flow.

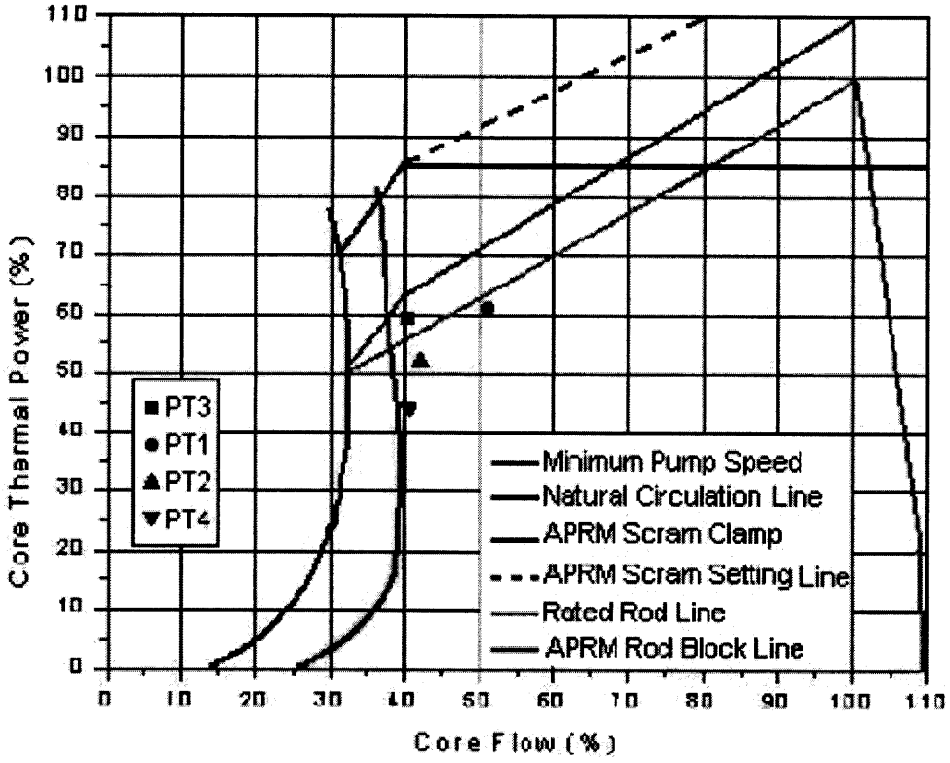

Figure C.1: Test Points in the Peach Bottom-2 Low-Flow Stability Tests, [Costa, 2007]

The tests results and important parameters are listed in Table C-1 below. The axial power distributions at each test point are shown in Figure C.2.

Table C-1: Peach Bottom test results and conditions at the end of cycle 2 (from [Carmichael and Niemi, 1978])

Tests number		Core Pressure (MPa)	Power (% rated)	Flow rate (% rated)	Core inlet enthalpy (kJ/kg)	Experimental	
						Freq. (*HZ*)	DR*
Cycle 2	PT1	7.06	60.6	52.3	1184.6	0.439	0.259
	PT2	7.01	51.7	43.8	1187.7	0.441	0.303
	PT3	7.098	59.2	40.4	1184.6	0.424	0.331
	PT4	7.056	43.5	40.3	1183.8	0.383	0.271

*: Decay ratio

For the neutronic feedback, no much information was available. Avoiding using a neutronic code to determine those neutronic feedback coefficients, simple assumptions are applied: (1) a constant Doppler coefficient; (2) a quadratic form for Void coefficient, $C_v = C_1 + C_2\overline{\alpha} + C_3\overline{\alpha}^2$, were $\overline{\alpha}$ is the core average void fraction.

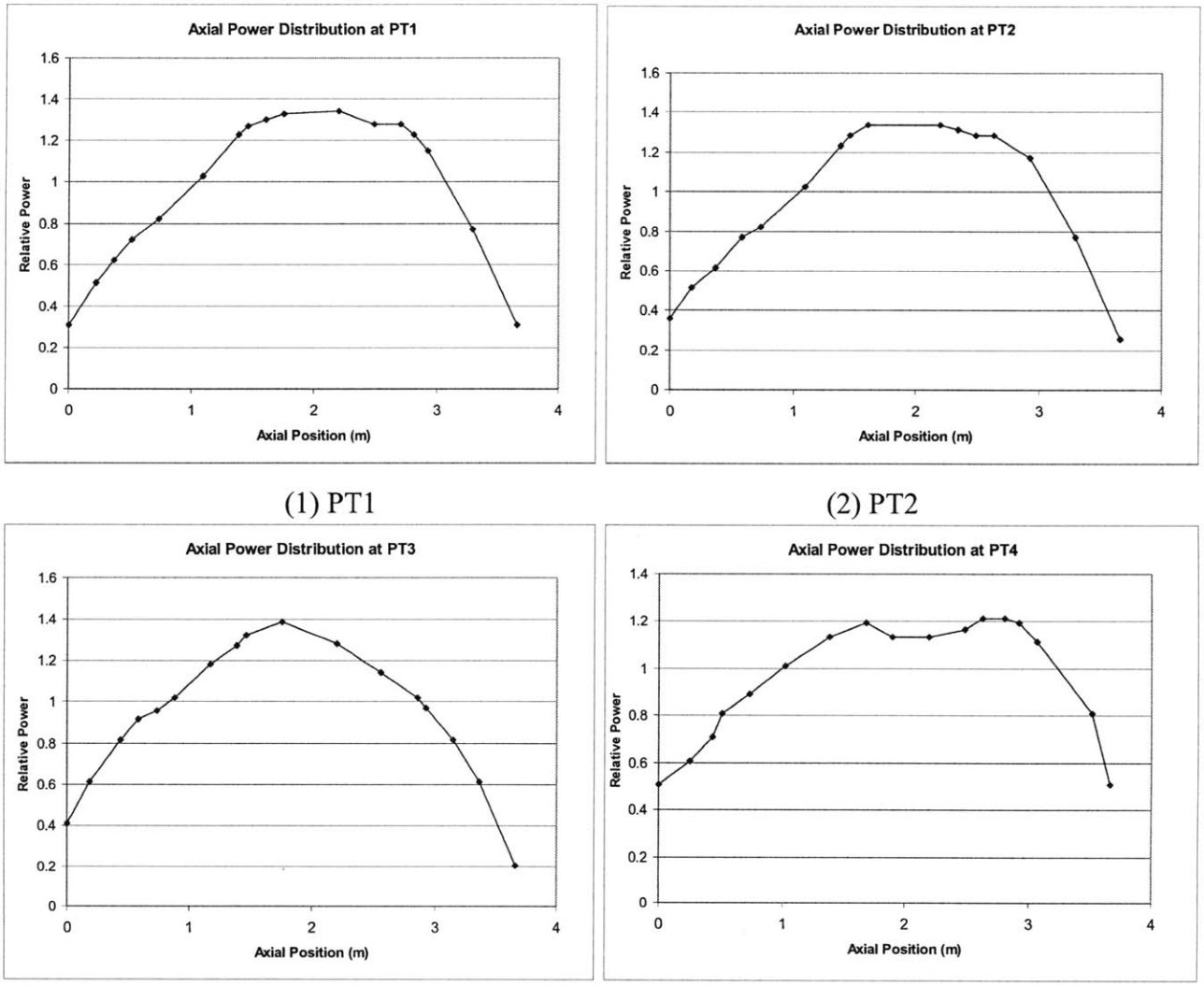

(1) PT1 (2) PT2

(3) PT3 (4) PT4

Figure C.2: Axial power distributions at the four Test Points

C.2 Discussion of Results

Comparison of the STAB predicted results and the experimental data is given in Table C-2, and they are graphically illustrated as shown in Figure C.3 and Figure C.4.

Table C-2: Comparison of the experimental and the predicted results

Tests number	Experimental Results		Calculated Results	
	Freq. (*HZ*)	Decay ratios	Freq. (*HZ*)	Decay ratios
PT1	0.439	0.259	0.463	0.324
PT2	0.440	0.303	0.489	0.377
PT3	0.424	0.331	0.455	0.405
PT4	0.383	0.271	0.355	0.312

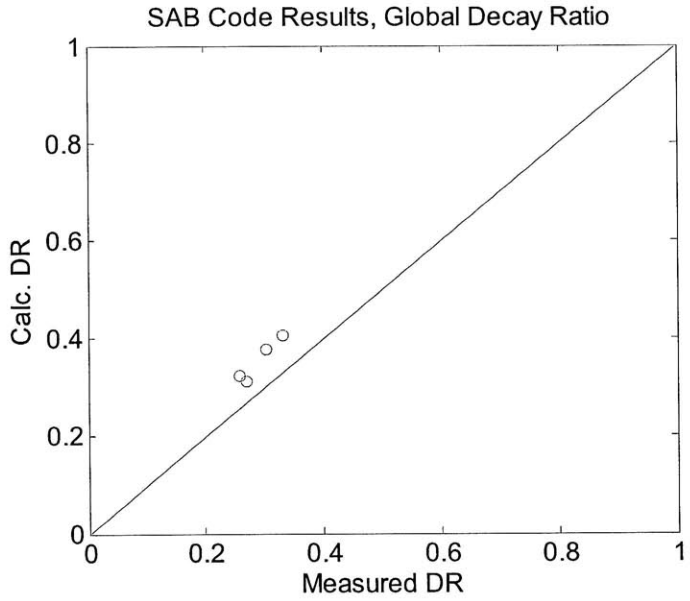

Figure C.3: Comparison of decay ratios, LFST benchmark

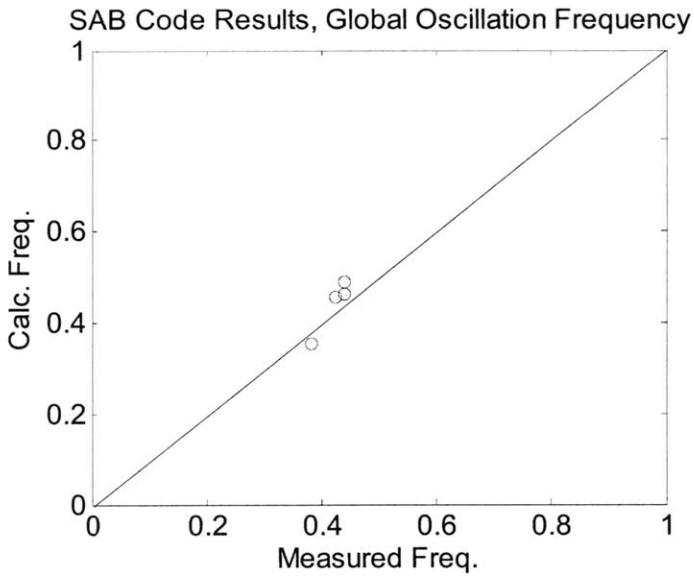

Figure C.4: Comparison of oscillation frequencies, LFST benchmark

Defining the biases and the standard deviations for the decay ratios and frequencies as:

$$\widetilde{E}_{DR} = \frac{\sum_{n=1}^{n_{\exp.}} (DR_{pre.} - DR_{\exp.})_n}{n_{\exp.}}, \quad \widetilde{E}_{Frq.} = \frac{\sum_{n=1}^{n_{\exp.}} (F_{pre.} - F_{\exp.})_n}{n_{\exp.}}$$

$$\sigma_{DR} = \sqrt{\frac{\sum_{n=1}^{n_{\exp.}} (DR_{pre.} - DR_{\exp.})_n^2}{n_{\exp.}}}, \quad \sigma_{Frq.} = \sqrt{\frac{\sum_{n=1}^{n_{\exp.}} (F_{pre.} - F_{\exp.})_n^2}{n_{\exp.}}}$$

Where $n_{\exp.}$ is the number of the examined points.

It can be found that the biases for the predicted decay ratio and frequency are about 0.063 and 0.019 respectively; while the standard deviations for them are about 0.065 and 0.034.

Therefore, it can be concluded that the current STAB code predictions match the experimental data reasonably well and the predicted results are a little more conservative as the conservative assumptions used in the model.

References for Appendix C

Carmichael L. A., and Niemi R. O., "Transient and Stability Tests at Peach Bottom Atomic Power Station Unit 2 at End of Cycle 2," EPRI Report NP-564, 1978.

Costa A.L., "BWR Instability Analysis by Coupled 3D Neutron-Kinetic and Thermal-Hydraulic Codes", PhD Dissertation, University of Pisa, 2007.

Zhao, J., Saha, P., and Kazimi, M.S., "Stability Analysis of Supercritical Water Cooled Reactors", MIT-ANP-TR-108, Cambridge, Massachusetts, September 2005.

D. Neutronic Model Description

The detailed description of the neutronics model in the STAB code can be found in [Zhao et al., 2005] and [Hu and Kazimi, 2007], as summarized in this Appendix.

D.1 Neutronic equations

The time dependent multi-group diffusion equation is widely used to model the dynamic neutron flux distribution inside a reactor core. However, it uses time dependent and space dependent cross-sections, which are determined by the reactor local thermal-hydraulic conditions and control rod positions. As a result, the equation becomes non-linear and too difficult to solve. For simplicity, the point kinetics equation is used in the STAB code.

The point kinetics method assumes that the spatial and time dependent neutron flux and delayed neutron precursor concentration are separable functions of time and space. The neutron energy spectrum, the normalized flux and delayed neutron precursor space distribution functions are independent of the time. These assumptions greatly simplify the multi-group diffusion equations. The point kinetics neutron density equation is then given as:

$$\frac{dn}{dt} = (\frac{\rho(t) - \beta}{\Lambda})n(t) + \sum_{i=1}^{6} \lambda_i C_i(t) \qquad \text{(D-1)}$$

and the delayed neutron precursor density equation is:

$$\frac{dC_i}{dt} = \beta_i \frac{k}{\Lambda} n(t) - \lambda_i C_i(t) \qquad \text{(D-2)}$$

The above equations also predict the reactor transient behavior reasonably well, if the reactor normalized spatial neutron flux distribution does not change significantly during a transient.

To take into account the reactor thermal-hydraulic feedback, instead of calculating the local cross section change, the point kinetics method uses the feedback reactivity. The feedback reactivity represents the overall effect of changing thermal-hydraulic conditions throughout the whole reactor core. The two major feedback mechanisms are the moderator density change and the fuel Doppler effects. There are weighting schemes to calculate the appropriate overall feedback reactivity due to changing local thermal-hydraulic conditions.

Because of its simplicity, the point kinetics model has been widely used to predict the reactor kinetics behavior and the onset of the instability. The disadvantage of the point kinetics model is that it cannot predict local power distribution changes during a reactor transient. However, during an out-of-phase instability, the high harmonic neutron spatial distribution modes are excited even if the fundamental mode is stable. To obtain the dynamic features of the high harmonic modes, a modal expansion method is used.

D.2 Lamda modes expansion method

The basic idea of the modal expansion method is to approximate the unknown space and time related neutron flux function by a linear combination of known space functions with time-depended coefficients. Therefore, the modal expansion method includes two steps: (1) define the space functions (2) derive the time-dependent coefficients.

The Lamda modes expansion model can be expressed as:

$$L^o\phi_m(r,E) = \frac{1}{\lambda_m} M^o\phi_m(r,E) \tag{D-3}$$

In which,

L^o : the steady-state destruction operator,

M^o : the steady-state production operator,

λ_m : m^{th} mode reactivity

ϕ_m : m^{th} neutron flux mode

For a bare homogenous cylindrical reactor with radius R and height H, it can be shown that the fundamental and first subcritical modes can be described as:

$$\phi_o(r,z,\theta) = J_o(2.40r/R)\sin(\pi z/H)$$
$$\phi_1(r,z,\theta) = J_1(3.83r/R)\sin(\pi z/H)\sin(\theta) \quad \text{(D-4)}$$

The shapes of these two modes are illustrated in Figure D.1.

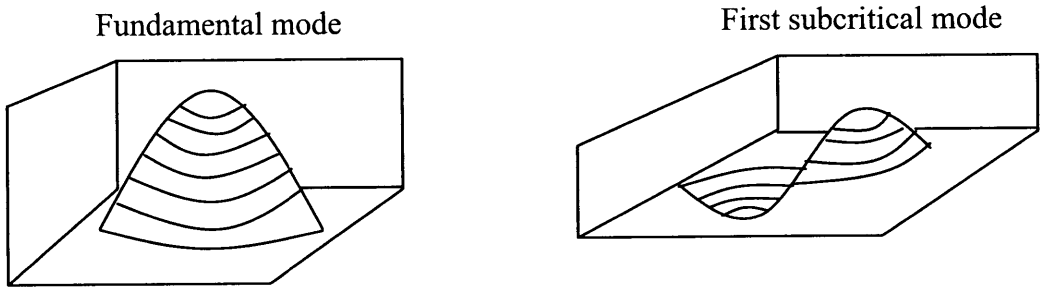

Figure D.1: Shapes of the fundamental and first subcritical modes

During out-of-phase oscillations, the excited first subcritical mode coupled to a stable fundamental mode generates an out-of-phase dynamics feature. The total neutron flux is the combination of these two dominant neutron flux modes and can be illustrated as:

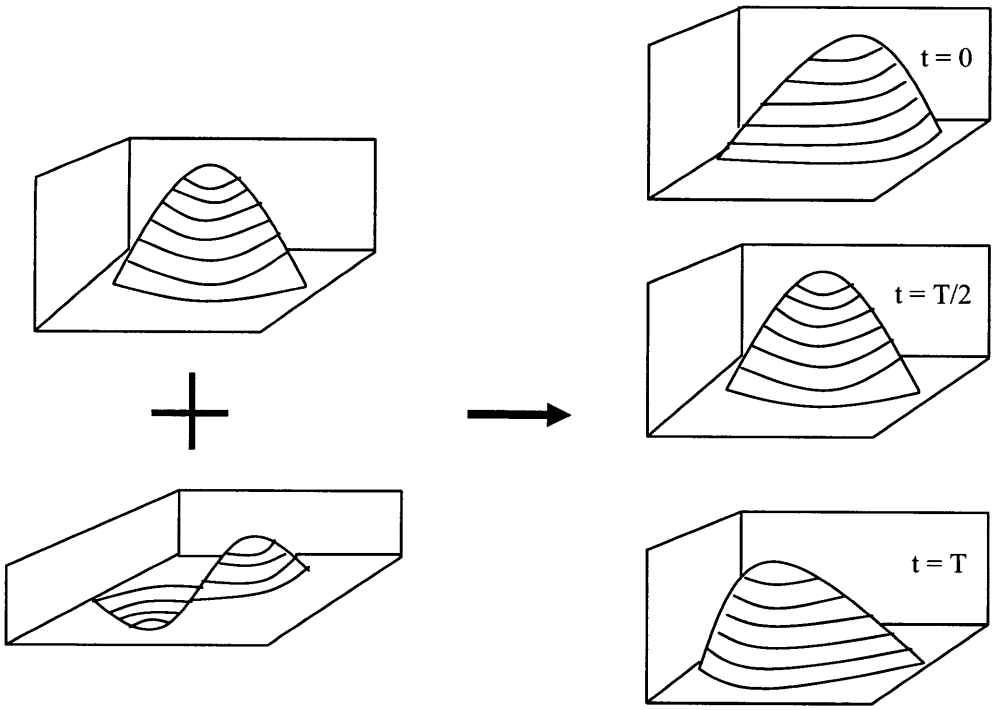

Figure D.2: Total neutron flux dynamics during out-of-phase oscillation

The adjoint equations of ϕ_m can be described as:

$$L^{oT}\phi_m^*(r,E) = \frac{1}{\lambda_m} M^{oT}\phi_m^*(r,E) \tag{D-5}$$

And the ϕ_m together with its adjoint eigenvectors ϕ_m^* have the relation:

$$< \phi_m^*, M^o \phi_k >= 0, \text{ for } m \neq k \tag{D-6}$$

Using the λ modal expansion method, the modal point kinetic equation can be obtained. Neglecting the non-linear terms and tiny parts, the simplified equations are listed below.

$$\frac{dn_m}{dt} = \frac{\rho_m^s - \beta}{\Lambda_m} n_m + \frac{\rho_{m0}}{\Lambda_m} + \sum_{i=1}^{6} \lambda_i c_{i,m} \tag{D-7}$$

$$\frac{dc_{i,m}}{dt} = \frac{\beta_i}{\Lambda_m} n_m - \lambda_i c_{i,m} \tag{D-8}$$

Where,

ρ_m^s : the subcritical reactivity of the mth mode, which can be defined as:

$$\rho_m^s = 1 - 1/\lambda_m \tag{D-9}$$

ρ_{mn}: the excitation reactivity of the m[th] mode, which is introduced by a net change in the n[th] mode reaction rate. It can be described as:

$$\rho_{mn} = < \phi_m^*, (\delta M - \delta L)\phi_n > / < \phi_m^*, M_o \phi_m > \tag{D-10}$$

Λ_m: the neutron generation time of the m[th] mode, which can be described as:

$$\Lambda_m = < \phi_m^*, 1/V\phi_m > / < \phi_m^*, M_o \phi_m > \tag{D-11}$$

The subcritical reactivity ρ_m^s can be calculated using the formula derived by [March-Leuba and Blakeman, 1991]:

$$\rho_m^s = D\nabla B^2 / \nu\Sigma_f \tag{D-12}$$

Where,

D: diffusion coefficient

Σ_f: fission cross section

ν : number of neutrons per fission

∇B^2: the geometric buckling difference between the fundamental and m[th] mode

Applying Perturbation and Laplace transformations to the above equations, the so called zero-power transfer function of the m[th] harmonic mode can be derived:

$$\delta q''' = \Phi_m(s)\delta\rho_{m0} \tag{D-13}$$

$$\Phi_m(s) = q_o'''(s\Lambda_m - \rho_m^s + \sum_{i=1}^{6} \frac{\beta_i s}{s+\lambda_i})^{-1} \tag{D-14}$$

D.3 Neutroinc feedback

The void-reactivity and the fuel temperature-reactivity are two important reactivities that link the thermal-hydraulics and the neutronics. Generally, they are specified with reactivity coefficients which show the change in the reactivity due to change in the feedback parameter, either the void fraction or the fuel temperature.

The neutronic feedback is controlled by the whole core average properties. The oscillations of the core average parameters are obtained by adding up the weighted contributions for all of the nodes, radial and axially through out of the core. If the core has N channels and one channel has M nodes axially, the average core density and fuel temperature oscillations can be expressed as:

$$\delta\tilde{\rho}_c = \delta w_{in}\sum_{j=1}^{N}\sum_{i=1}^{M} W_{j,i}U_{den}^{j,i} + \delta q_o'''\sum_{j=1}^{N}\sum_{i=1}^{M} W_{j,i}Q_{den}^{j,i} = U_{den}\delta w_{in} + Q_{den}\delta q_o''' \tag{D-15}$$

$$\delta\tilde{t}_f = \delta w_{in}\sum_{j=1}^{N}\sum_{i=1}^{M} W_{j,i}U_{f}^{j,i} + \delta q_o'''\sum_{j=1}^{N}\sum_{i=1}^{M} W_{j,i}Q_{f}^{j,i} = U_{f}\delta w_{in} + Q_{f}\delta q_o''' \tag{D-16}$$

W_n is the weighting factor at each node, which is usually taken in the form:

$$W_{j,i} = \frac{P_{j,i}^2}{\sum_{j=1}^{N}\sum_{i=1}^{M} P_{j,i}^2} \tag{D-17}$$

Therefore, the reactivity feedback oscillation can be obtained as:

$$\begin{aligned}\delta\rho_F &= C_{den}\delta\tilde{\rho}_c + C_{dop}\delta\tilde{t}_f \\ &= (C_{den}U_{den} + C_{dop}U_f)\delta w_{in} + (C_{den}Q_{den} + C_{dop}Q_f)\delta q_o'''\end{aligned} \tag{D-18}$$

References for Appendix D

Hu R. and Kazimi, M.S., "Stability Analysis of Natural Circulation in BWRs at High Pressure Conditions", MIT-CANES-ANP-PR-118, Cambridge, Massachusetts, October 2007.

March-Leuba J., and Blakeman E.D., "A Mechanism for Out-of-Phase Power Instabilities in Boiling Water Reactors", *Nuclear Science and Engineering*, 107, 173-179, 1991.

Zhao, J., Saha, P., and Kazimi, M.S., "Stability Analysis of Supercritical Water Cooled Reactors", MIT-CANES-ANP-TR-108, Cambridge, Massachusetts, September 2005.

E. Decay Ratio Evaluation Methods for Stability Analysis in the Time Domain

Decay ratio can be calculated from the transient signal, its autocorrelation function (ACF), and the impulse response function (IRF) calculated using an autoregressive moving-average model (ARMA) or an autoregressive model (AR) to fit the behavior of the system.

When the system is characterized as a second-order oscillator, it can be introduced in the form:

$$\ddot{x} + 2\alpha\dot{x} + (\alpha^2 + \omega^2)x = 0 \tag{E-1}$$

The general solution for the system is:

$$x(t) = Ae^{-\alpha t}\cos(\omega t + \phi) \tag{E-2}$$

The DR parameter is defined as the ratio between two consecutive maxima of the signal and gives a measurement of the damping of the system. For the second order system, it is a constant and given by:

$$DR = e^{-\frac{2\pi\alpha}{\omega}} \tag{E-3}$$

Signals obtained during transients initiated by small perturbations may be approximated with second order systems. The autocorrelation function of transient signals can be also used for evaluating the Decay Ratio. However, noise signals cannot be fitted with a second order system. The impulse response function can be extract from both transient signals and stationary noises and then used for evaluate Decay Ratio.

Five ways to define Decay Ratio for any transient signal, its ACF and IRF for transient signal and noise can be defined and are being described hereafter.

1) For a second order system, the DR would be defined as the ratio of two consecutive maxima of these functions. As the system is not strictly second order system, this definition gives not a constant. So, the average of first two ratios is used to improve the results:

$$\boldsymbol{DR = \frac{1}{2}\left(\frac{A_2}{A_1} + \frac{A_3}{A_2}\right)} \qquad \textbf{(E-4)}$$

where A_i are the local maxima, as can be seen in the Figure E.1 [D'Auria et al., 1997] below.

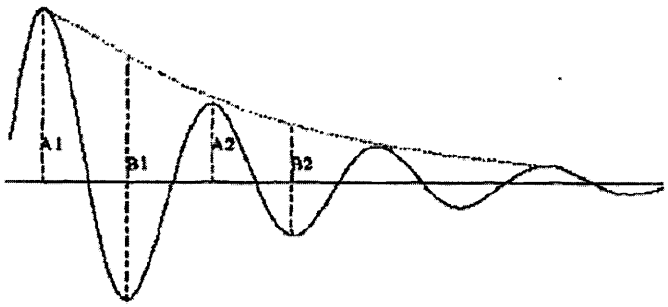

Figure E.1 Diagram for definitions of the decay ratio

2) To avoid any disturbance due to the influence of the parasitic noise or the time series finiteness. An alternative definition is considered.

$$DR = \frac{1}{2}\left(\frac{B_2}{B_1} + \frac{B_3}{B_2}\right) \qquad \text{(E-5)}$$

In order to obtain the points B_i, the following steps are considered. The first four maximums of the ACF or IRF, denoted by (t_{Mi}, x_{Mi}), are identified. Once these points are obtained, one fits them by 3rd order polynomial, which uses Lagrange Interpolating Polynomial formula:

$$P(t) = \sum_{i=1}^{4}\sum\left\{\left(\prod_{j=1}^{4}\frac{t - t_{Mj}}{t_{Mi} - t_{Mj}}\right)x_{Mi}\right\} \qquad \text{(E-6)}$$

After this, the first three minima are identified (t_{Mi}, x_{Mi}), and the image points, $P(t_{Mi})$, of the fitted polynomial can be characterized. Thus, B_i are given by:

$$B_i = P(t_{Mi}) - x_{Mi} \tag{E-7}$$

3) AR-Lyapunov Approximation

It is assumed that the reactor behavior can be fitted to a second order model with transfer Function of the form:

$$H(s) = \frac{1}{(s-\gamma)(s-\gamma^*)} \tag{E-8}$$

The system oscillation period can be calculated from the imaginary part of γ and is given by $L = 2\pi/Im(\gamma)$. And the DR, defined as the quotient between the amplitude of two points separated by L, has the form:

$$DR = e^{Re(\gamma)/Im(\gamma)} \tag{E-9}$$

4) Direct Curve fitting

For each of the three types of functions, it is with a damped sinusoidal form:

$$x(t) = c_0 + ce^{-\alpha t}\cos(\omega t + \varphi) \tag{E-10}$$

If least square fitting is successful, the DR and NF of the system are given as:

$$DR_f = e^{-2\pi\alpha/\omega} \tag{E-11}$$

$$Fr_f = \omega/(2\pi) \tag{E-12}$$

This definition of DR and NF is appropriate for transients with short perturbations, but not for the noise signal.

5) ARMA-AR Model

It is based on the impulse response obtained from parametric models of the system, either autoregressive or autoregressive moving-average ones. Once the IRF is available, using the expression:

$$h_j = \sum_{i=1}^{p} \beta_i^j \, \omega_i \tag{E-13}$$

The DR can be calculated as the quotient between two consecutive maxima of the impulse response:

$$DR_j = h_{L+j}/h_j \tag{E-14}$$

Where j is the instant corresponding to the maximum of the function and L represents the 'lag', or length between two consecutive maxima. Approximating the behavior of the system by a continuous second order model, L is given by $L = 2\pi/Im(\gamma)$, where γ is the dominant pole of the transfer function in the continuous s-plane.

Forsmark stability benchmark

A recommendation of the Ringhals 1 benchmark was to study the different time series analysis methods in order to obtain a unified methodology to detect and suppress the oscillations during reactor operation, as well as better qualification of the applied noise analysis methods. A follow-up benchmark, Forsmark stability benchmark [OECE/NEA, 2001], was thus proposed, dedicated to the analysis of time series data and including the evaluation of both global and regional stability.

The activity was focused on the analysis of time series data by means of noise analysis techniques in the time domain. Several cases were studied as, for example, the importance of the time duration of measured data, APRM data containing more than one natural frequency of the core, data with a mixture between a global oscillation mode and a regional (half core) oscillation, and others. Table E-1 presents the several methods used by the participants to obtain results to DR and NF.

Table E-1: Participants and methods used in the Forsmark Stability Benchmark

Method	Organization	Country
Auto-regressive methods and dominant poles	PSI UPV/CSN SIEMENS	Switzerland Spain Germany/USA
Auto-regressive methods and impulse response	TOSHIBA JAERI IRI/TU-Delft PSU	Japan, Japan, Netherlands, USA
Auto-correlation	TOSHIBA	Japan
Recursive auto-correlation	SIEMENS	Germany/USA
ARMA (plateau method)	PSI	Switzerland
Power spectrum estimation	CSNNS	Mexico
LAPUR (frequency domain)	PSU	USA

References for Appendix E

D'Auria F. et al., "State of the art report on BWR stability," OECD/GD(97)13, 1997.

OECE/NEA, "Forsmark 1 & 2 Boiling Water Reactor Stability Benchmark - Time Series Analysis Methods for Oscillation during BWR Operation," NEA/NSC/DOC(2001)2, 2001.

F. The Semi-Implicit Scheme and Numerical Dissipation

The following discussion of the numerical dissipation and the Semi-Implicit (SI) scheme in the TRACE code is summarized from [Xu et al., 2009].

Previous studies [Mahaffy, 1993] have suggested the potential for numerical damping in the SETS method, which is the primary numerical solution method in TRACE. Because of these concerns, the semi-implicit method option in TRACE was used for stability analysis in this work. However, when the semi-implicit method is used for stability analysis, it is important to achieve a material Courant limit (or CFL) near unity in order to minimize numerical dissipation:

$$CFL: c = v\Delta t / \Delta x; \tag{F-1}$$

where v is coolant velocity, Δx is mesh size and Δt is time step size.

The potential numerical dissipation in the SI scheme can be demonstrated using the single-phase mass continuity equation:

$$\rho_t + v\rho_x = 0 \tag{F-2}$$

The explicit and implicit upwind finite differencing of Eq. (F-2) can be written as Eqs (F-3) and (F-4), respectively:

$$\frac{\rho_j^{n+1} - \rho_j^n}{\Delta t} + \frac{v_{j-1}\rho_{j-1}^n - v_j\rho_j^n}{\Delta x} = 0 \tag{F-3}$$

$$\frac{\rho_j^{n+1} - \rho_j^n}{\Delta t} + \frac{v_{j-1}\rho_{j-1}^{n+1} - v_j\rho_j^{n+1}}{\Delta x} = 0 \tag{F-4}$$

The modified equation for the explicit and implicit upwind finite difference of mass continuity equation can be written as:

$$\rho_t + v\rho_x = v\Delta x(1 \mp c)\rho_{xx}/2 + O[\Delta x^2, \Delta t^2] \tag{F-5}$$

where the right hand side of equation (F-5) is the error introduced by finite differencing. The leading team is the artificial viscosity and the sign $\mp$ is negative for the explicit scheme and positive for the implicit scheme.

The numerical diffusion of the explicit or implicit upwind difference scheme is the result of two sources of error. The spatial differencing error can be written as: $v\Delta x\rho_{xx}/2$ and the time differencing error can be written as: $\mp\Delta t\rho_{tt}/2 = \mp cv\Delta x\rho_{xx}/2$.

In the implicit method, the two errors always enhance each other, and the minimum dissipation occurs at the smallest time step size. However, in the explicit method, the two errors cancel each other. If CFL = 1, numerical dissipation would disappear. However, if CFL<1 then numerical dissipation will increase with decreasing time step, and if CFL>1, then numerical dissipation is negative and false viscosity will destabilize the solution.

If the upwind scheme is used for spatial finite differencing, then the implicit method is numerically more stable than the explicit method. However, the implicit method has potentially more numerical dissipation then the explicit method for practical applications. For stability analysis in this work, the explicit method with larger time step sizes was preferred. However, the time step size was chosen to match the courant limit as closely as possible. In this manner, the potential for numerical instability was minimized which would compromise the accuracy of the solution.

References for Appendix F

Mahaffy J.H., "Numerics of Codes: Stability, Diffusion, and Convergence," Nuclear Engineering and Design, 145, 131-145, 1993.

Xu Y., et al., "Application of TRACE/PARCS to BWR Stability Analysis", *Annals of Nuclear Energy*, 36, 317-323, 2009.